

**ELUCIDATING THE HMG-COA REDUCTASE REACTION  
MECHANISM USING PH-TRIGGERED TIME-RESOLVED X-RAY  
CRYSTALLOGRAPHY**

by

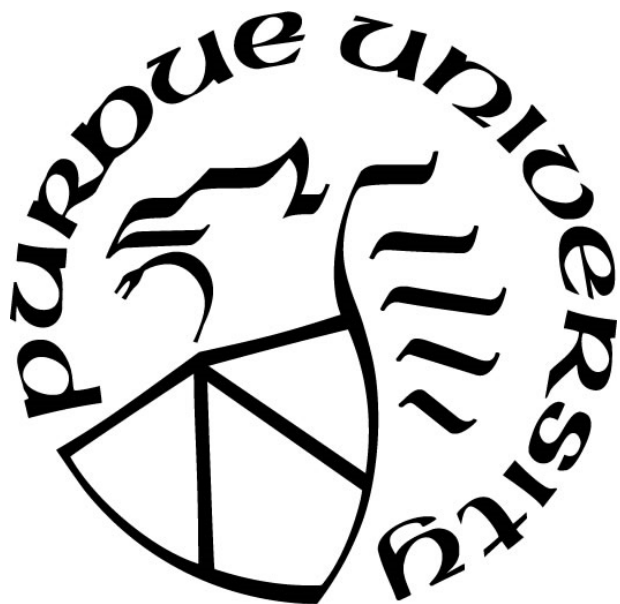
**Vatsal Purohit**

**A Dissertation**

*Submitted to the Faculty of Purdue University*

*In Partial Fulfillment of the Requirements for the degree of*

**Doctor of Philosophy**



Department of Biological Sciences

West Lafayette, Indiana

December 2021

**THE PURDUE UNIVERSITY GRADUATE SCHOOL**  
**STATEMENT OF COMMITTEE APPROVAL**

**Dr. Cynthia Stauffacher, Chair**

Department of Biological Sciences

**Dr. Carol Post**

Department of Medicinal Chemistry and Molecular Pharmacology

**Dr. Andrew Mesecar**

Department of Biochemistry, Department of Biological Sciences

**Dr. Angeline Lyon**

Department of Chemistry, Department of Biological Sciences

**Approved by:**

Dr. Jason Cannon

and

Dr. Janice P. Evans



*For my grandfather, Niranjan Swaroop Bohra*

## **ACKNOWLEDGMENTS**

I would like to first thank my graduate advisor Dr. Cynthia Stauffacher for being the most supportive mentor I could ever ask for. I owe all my progress to her constant guidance on several aspects of research training and her belief in me. I would also like to thank Dr. Nic Steussy who has also been extremely instrumental in helping me navigate various technical aspects of my research project. In addition, I would like to thank Tim Schmidt for all the training I have acquired from him in crystallography. I am also grateful for the mentorship I received from all my advisory committee members – Dr. Andrew Mesecar, Dr. Carol Post and Dr. Angeline Lyon. They offered me a lot of advice over the years with respect to working on, writing about, and presenting my research. I learnt and grew a lot with various lab members in the Stauffacher Research Group that I shared space with and would like to thank them for extending their help to me at various stages of my project. I would also like to thank members of Dr. Paul Helquist and Dr. Olaf Wiest's group at the University of Notre Dame who I had a chance to work in collaboration with on several interdisciplinary aspects of this project. I would finally like to thank my friends and family for their emotional support and encouragement during my years of graduate research.

## TABLE OF CONTENTS

LIST OF TABLES.....	10
LIST OF FIGURES .....	11
KEYWORDS.....	15
ABSTRACT.....	16
CHAPTER 1. INTRODUCTION .....	18
1.1 Objectives .....	18
1.1.1 Overall goal of the research.....	18
1.1.2 Research Objectives.....	19
1.2 Organization.....	19
CHAPTER 2. BACKGROUND .....	20
2.1 Role of <i>Pm</i> HMGR in the mevalonate pathway .....	20
2.2 <i>Pm</i> HMGR enzyme architecture.....	22
2.3 <i>Pm</i> HMGR reaction mechanism .....	22
2.4 Structural studies on <i>Pm</i> HMGR .....	23
2.4.1 <i>Pm</i> HMGR active site.....	23
2.4.2 Flap domain configurations in <i>Pm</i> HMGR structures .....	25
2.4.3 <i>Pm</i> HMGR ligand-enzyme interactions.....	26
2.5 Turnover in <i>Pm</i> HMGR crystals.....	28
2.6 Obtaining time-resolved crystallographic data to study <i>Pm</i> HMGR reaction mechanism	29
2.7 Observing enzyme turnover and other biological processes using time-resolved crystallography.....	30
2.7.1 Development of time-resolved data collection methods .....	30
2.7.2 Development of sample delivery methods in time-resolved crystallography .....	31
2.7.3 Use of caged-NAD <sup>+</sup> cofactors for time-resolved crystallography studies of <i>Pm</i> HMGR .....	32
2.7.4 Application of a pH-jump method for time-resolved crystallographic studies of <i>Pm</i> HMGR.....	35
CHAPTER 3. STUDYING THE FACTORS LIMITING MEVALONATE OXIDATION IN THE <i>PM</i> HMGR CRYSTALLIZATION ENVIRONMENT.....	37
3.1 Introduction.....	37
3.2 Methods.....	39

3.2.1	Measuring the effect of the <i>Pm</i> HMGR crystallization environment on enzymatic activity .....	39
3.2.1.1	Obtaining the <i>Pm</i> HMGR crystal structure bound to mevalonate, CoA and NAD <sup>+</sup> .....	39
3.2.1.2	Obtaining anomalous diffraction from rubidium bound <i>Pm</i> HMGR crystals.....	40
3.2.1.3	Crystallographic data analysis.....	40
3.2.1.4	pH profile measurements in the crystallization buffer .....	41
3.2.1.5	Measuring the effect of ionic concentration on enzymatic activity in the crystallization buffer .....	42
3.2.1.6	Comparing the effect of the precipitant ions in the crystallization buffer .....	42
3.2.2	K <sub>m</sub> and K <sub>cat</sub> measurements in crystallization conditions.....	43
3.2.3	pKa calculations of active site residues and ligands.....	44
3.3	Results.....	44
3.3.1	Structure obtained with mevalonate, CoA and NAD <sup>+</sup> .....	44
3.3.2	pH-rate profile measurements in crystallization conditions .....	47
3.3.3	Determining changes in the enzyme kinetic parameters in the crystallization environment .....	48
3.3.4	Effect of precipitant ions in the <i>Pm</i> HMGR crystallization environment .....	50
3.3.5	Investigation of the effects of ions on <i>Pm</i> HMGR turnover.....	51
3.3.6	Turnover in <i>Pm</i> HMGR in the absence of ammonium.....	52
3.3.7	Turnover at a high ionic concentration in the absence of the crystallization salt.....	53
3.3.8	Effect of ammonium sulfate outside the crystallization buffer .....	54
3.3.9	Calculated pKa values of catalytic residues in the crystal structure.....	55
3.3.10	Utilization of Rb <sub>2</sub> SO <sub>4</sub> to identify NH <sub>4</sub> <sup>+</sup> binding sites in <i>Pm</i> HMGR: .....	56
3.4	Discussion.....	57
3.4.1	Inhibition of mevalonate oxidation in the <i>Pm</i> HMGR crystallization environment ..	57
3.4.2	Turnover in the crystallization environment is dependent on ionic concentration....	58
3.4.3	Utilizing kinetic characteristics in the crystallization environment to develop a reaction triggering method.....	61
CHAPTER 4. DEVELOPMENT OF A PH-JUMP METHOD TO TRIGGER THE <i>PM</i> HMGR REACTION IN CRYSTALS.....		63
4.1	Introduction.....	63
4.2	Materials and Methods.....	64
4.2.1	Protein purification and crystallization.....	64
4.2.2	Preparation of freeze-trapped crystals post reaction-initiation in a pH-jump buffer.	65

4.2.3	UV-Vis absorbance measurements in ligand-bound enzyme crystals.....	66
4.2.4	Room temperature absorbance measurements in <i>Pm</i> HMGR crystals.....	67
4.3	Results.....	68
4.3.1	Absorption spectra of freeze trapped HMGR crystals after the pH jump: .....	68
4.3.2	Absorption spectra of <i>Pm</i> HMGR crystals at room temperature after a pH jump .....	72
4.4	Discussion.....	73
4.4.1	Freeze-trapped time-resolved absorption spectra in <i>Pm</i> HMGR crystals .....	73
4.4.2	Absorption spectra of <i>Pm</i> HMGR crystals at room temperature after a pH jump .....	76
CHAPTER 5. TIME-RESOLVED DIFFRACTION MEASUREMENTS.....		77
5.1	Introduction.....	77
5.2	Materials and methods .....	78
5.2.1	pH-jump diffraction experiments .....	78
5.2.2	Acquisition of <i>Pm</i> HMGR mutant structures .....	78
5.2.3	Structure comparisons .....	79
5.2.3.1	Structure alignments of regions with minimum RMSD variation .....	79
5.2.3.2	Structure alignment of <i>Pm</i> HMGR core-helix regions.....	80
5.2.4	Comparing changes in the electron density at the ligand-bound region.....	80
5.2.5	Measuring angles between helices in the <i>Pm</i> HMGR flap domain.....	81
5.2.6	Calculating interhelical volume in <i>Pm</i> HMGR flap domain .....	82
5.3	Results.....	82
5.3.1	Comparison of quaternary complex structure to other ligand bound structures.....	83
5.3.2	pH jump experiments in <i>Pm</i> HMGR crystals .....	90
5.3.2.1	Observed electron density changes in <i>Pm</i> HMGR crystals after buffer exchange ..	90
5.3.2.2	Changes in the thioester region between mevalonate and CoA .....	91
5.3.2.3	Movements observed in post pH-jump structures associated with thioester bond formation and product release: .....	93
5.3.2.4	Conformational changes observed in the flap domain in post pH-jump structures .....	108
5.3.3	Changes in the NAD <sup>+</sup> and mevalonate interaction site .....	111
5.3.3.1	Comparing changes in the electron density and distance between ligands at the <i>Pm</i> HMGR active site within the first minute of reaction initiation .....	115
5.3.3.2	Changes in the adenine-ribose region of NADH in structures obtained within the first minute of reaction initiation: .....	123

5.3.4	Movements observed in the <i>Pm</i> HMGR active site in structures obtained within the first minute of reaction initiation .....	124
5.3.5	Movements observed in the <i>Pm</i> HMGR active site in structures obtained within the first minute of reaction initiation .....	127
5.3.5.1	Changing conformation of the <i>Pm</i> HMGR flap domain .....	128
5.3.5.2	Changing contacts between the <i>Pm</i> HMGR flap domain and CoA binding site. ..	134
5.3.5.3	Comparing contacts between the <i>Pm</i> HMGR flap domain and the NAD <sup>+</sup> binding site .....	137
5.3.5.4	Interhelical movements in the flap domain .....	139
5.3.6	Effect of <i>Pm</i> HMGR flap mutations on ligand-binding and flap closure .....	148
5.3.7	Movement in the <i>Pm</i> HMGR small domain .....	152
5.3.8	Movement in the <i>Pm</i> HMGR large domain .....	155
5.4	Discussion .....	156
5.4.1	Comparison of the <i>Pm</i> HMGR quaternary complex to various ligand-bound structures .....	157
5.4.2	Application of the pH-jump triggering method to observe reaction initiation in <i>Pm</i> HMGR crystals .....	163
5.4.3	Conformational changes in the flap domain associated with ligand and small domain movements .....	168
5.4.4	Comparison of polder maps at the mevalonate-NAD <sup>+</sup> interaction site within the first minute of reaction initiation .....	171
5.4.5	Comparison of simulated annealing omit maps at the mevalonate-NAD <sup>+</sup> interaction site within the first minute of reaction initiation .....	173
5.4.6	Movement of ligands at the <i>Pm</i> HMGR active site within the first minute of reaction initiation .....	174
5.4.7	Observed changes in the NAD <sup>+</sup> adenine-ribose binding region within the first minute of reaction initiation .....	176
5.4.8	Movement of <i>Pm</i> HMGR active site residues within the first minute of reaction initiation .....	176
5.4.9	Changes in flap domain configuration .....	179
5.4.10	Changing contacts of the flap domain at the ligand binding site .....	182
5.4.11	Changes in interhelical contacts in the flap domain region .....	183
5.4.12	Exploring key <i>Pm</i> HMGR flap mutant structures .....	185
5.4.13	Movements observed in the small domain region adjacent to the NAD <sup>+</sup> /NADH binding site .....	186

5.4.14	Movements observed in the large domain region adjacent to the CoA binding site...	187
5.5	Limitations in our application of the pH-jump method .....	188
5.6	Future Directions .....	192
REFERENCES: .....		195
APPENDIX.....		202

## LIST OF TABLES

Table 2.1 Flap orientation in the presence of different <i>Pm</i> HMGR substrate and cofactors .....	27
Table 3.1 Crystallographic refinement statistics for the HMGR structure soaked with mevalonate, NAD <sup>+</sup> and CoA. ....	46
Table 3.2 K <sub>m</sub> and K <sub>cat</sub> measurements in the crystallization buffer. ....	48
Table 3.3 Turnover of <i>Pm</i> HMGR at pH 7 and pH 9 in sodium chloride. ....	54
Table 3.4 pK <sub>a</sub> values obtained for catalytic residues. ....	55
Table 5.1 Structures obtained with <i>Pm</i> HMGR and various permutations of ligands.....	84
Table 5.2 Wilson Scale Factor obtained for the structures before and after a pH-jump.....	121
Table 5.3 Distance between mevalonate, CoA and NAD <sup>+</sup> in time-resolved <i>Pm</i> HMGR structures. ....	122
Table 5.4 Angle measurements between flap domain helices .....	133
Table 5.5 Volume measurements of the <i>Pm</i> HMGR flap.....	133



## LIST OF FIGURES

Figure 1.1 Proposed reaction steps for conversion of mevalonate into HMG-CoA in <i>Pm</i> HMGR .....	16
Figure 2.1 Sequence alignment of Class II HMGRs.....	21
Figure 2.2 <i>Pm</i> HMGR bound to mevalonate, CoA and NAD <sup>+</sup> .....	22
Figure 2.3 <i>Pm</i> HMGR enzymatic reaction mechanism .....	23
Figure 2.4 <i>Pm</i> HMGR active site.....	24
Figure 2.5 Active site of <i>Pm</i> HMGR with dithio-HMGCoA and NADH. ....	25
Figure 2.6 <i>Pm</i> HMGR flap interactions with NAD <sup>+</sup> and CoA .....	27
Figure 2.7 <i>Pm</i> HMGR active site interactions. ....	28
Figure 2.8 <i>Pm</i> HMGR catalytic reaction scheme .....	29
Figure 2.9 N-2-Nitrobenzyl Nicotinamide Adenine Nucleotide.....	33
Figure 3.1 <i>Pm</i> HMGR reaction mechanism with the hydride transfer steps marked in red .....	41
Figure 3.2 <i>Pm</i> HMGR active site crystal structure. ....	45
Figure 3.3 pH-rate profile of <i>Pm</i> HMGR in crystallization buffer .....	47
Figure 3.4 Michaelis Menten and Lineweaver-Burk plots for NAD <sup>+</sup> , mevalonate and CoA.....	49
Figure 3.5 Turnover in <i>Pm</i> HMGR at different ammonium sulfate concentrations.....	50
Figure 3.6 pH-rate profile of <i>Pm</i> HMGR in the presence of ammonium salts.....	51
Figure 3.7 pH-rate profile of <i>Pm</i> HMGR in the presence of sodium sulfate and lithium sulfate..	52
Figure 3.8 pH-rate profile of <i>Pm</i> HMGR in a potassium sulfate and rubidium sulfate.....	53
Figure 3.9 pH-activity profile of <i>Pm</i> HMGR with ammonium sulfate in enzymatic assay buffer	55
Figure 3.10 Anomalous Rb density from <i>Pm</i> HMGR structures.....	57
Figure 3.11 HMG-CoA and dithio-HMG-CoA orientations in the presence of NAD <sup>+</sup> in <i>Pm</i> HMGR .....	58
Figure 3.12 Sulfate binding sites in Apo <i>Pm</i> HMGR .....	61
Figure 4.1 <i>Pm</i> HMGR hydride transfer reaction steps .....	64
Figure 4.2 Time-resolved UV-Vis absorbance spectra (Control Experiment) .....	69
Figure 4.3 Time-resolved UV-Vis spectra from 0.4 mm <i>Pm</i> HMGR crystals. ....	70
Figure 4.4 Time-resolved UV-Vis spectra from 0.1 mm <i>Pm</i> HMGR crystals .....	71

Figure 4.5. Room temperature time-resolved UV-Vis spectra .....	73
Figure 5.1 RMSD calculations for structure alignment .....	79
Figure 5.2 <i>Pm</i> HMGR homodimer structure bound to mevalonate, CoA and NAD <sup>+</sup> .....	80
Figure 5.3 Ligand bound structures compared to the <i>Pm</i> HMGR quaternary complex .....	87
Figure 5.4 Distance between HIS 381 and CoA in HMG-CoA and NAD <sup>+</sup> / CoA and NAD <sup>+</sup> structures .....	89
Figure 5.5 Active site of the quaternary complex in pH-jump buffer. ....	90
Figure 5.6 Time-resolved omit and 2Fo-Fc maps for structures obtained 20 second – 10 minutes after reaction initiation .....	92
Figure 5.7 Structure comparisons 20 seconds after reaction initiation .....	94
Figure 5.8 Structure comparisons 1 minute after reaction initiation .....	96
Figure 5.9 Structure comparisons 2 minute 20 seconds after reaction initiation .....	98
Figure 5.10 Structure comparisons 4 minutes after reaction initiation .....	99
Figure 5.11 Structure comparisons 5 minutes after reaction initiation .....	100
Figure 5.12 Structure comparisons 8 minutes after reaction initiation. ....	103
Figure 5.13 Structure comparisons 10 minutes after reaction initiation. ....	105
Figure 5.14 Changes in CoA adenine 2Fo-Fc density 10 minutes after reaction initiation .....	107
Figure 5.15 Changes in flap domain 2 Fo-Fc density between H 385 – I 392 before and 10 minutes after reaction initiation .....	107
Figure 5.16 Flap domain comparisons 20 seconds – 10 minutes after reaction initiation .....	109
Figure 5.17 2Fo-Fc electron density for interhelix region between helix 1 and 2 of <i>Pm</i> HMGR flap .....	110
Figure 5.18 NAD <sup>+</sup> carboxamide orientation 20 seconds and 1 minute after reaction initiation .....	112
Figure 5.19 Movement of mevaldehyde 20 seconds and 1 minute after reaction initiation .....	112
Figure 5.20 Mevaldehyde carboxyl end orientation 20 seconds / 1 minute after reaction initiation. ....	113
Figure 5.21 Distance between mevaldehyde and NADH 20 seconds and 1 minute after reaction initiation. ....	113
Figure 5.22 Distance between mevalonate and CoA 20 seconds / 1 minute after reaction initiation .....	113
Figure 5.23 Polder map comparisons for ligands within first minute of reaction initiation .....	117

Figure 5.24 Simulated annealing composite omit map comparisons within first minute of reaction initiation .....	118
Figure 5.25 Distance comparisons at the active site within first minute of reaction initiation...	119
Figure 5.26 Changes in NAD <sup>+</sup> and NADH adenine, ribose and phosphate region density .....	123
Figure 5.27 Distance comparisons for <i>Pm</i> HMGR ligands within first minute of reaction initiation .....	126
Figure 5.28 B-factor comparisons for ligands within first minute of reaction initiation .....	127
Figure 5.29 Flap domain conformation comparisons within the first minute of reaction initiation .....	131
Figure 5.30 RMSD comparisons of flap domain within the first minute of reaction initiation.....	132
Figure 5.31 B-factor flap domain comparisons within the first minute of reaction initiation. ..	134
Figure 5.32 Changing conformations of flap domain residues near CoA phosphate region within first minute of reaction initiation. ....	136
Figure 5.33 Flap domain and NAD <sup>+</sup> interactions within first minute of reaction initiation .....	138
Figure 5.34 Changing distances between ARG 379 (flap helix 1) and HIS 411 (flap helix 2) within first minute of reaction initiation .....	141
Figure 5.35 Interhelical distance between A 383, A386 and V 408 within first minute of reaction initiation .....	142
Figure 5.36 Changing distance in the interhelical region between flap helix 1 and 2 within first minute of reaction initiation.....	143
Figure 5.37 Conformational changes in residues between flap helix 2 and 3 before and after reaction initiation. ....	145
Figure 5.38 Changing distance between flap helix 2 (L 407) and 3 (A 418) within first minute of reaction initiation .....	146
Figure 5.39 Changing distance between helix 2 (V 403) and helix 3 (L 422) within the first minute of reaction initiation.....	147
Figure 5.40 <i>Pm</i> HMGR E399A mutant RMSD comparisons (with closed flap domain).....	149
Figure 5.41 Structure comparisons of E399A with wild type <i>Pm</i> HMGR .....	150
Figure 5.42 <i>Pm</i> HMGR E399A RMSD and structure comparisons (without flap domain). ....	151
Figure 5.43 <i>Pm</i> HMGR (WT) and E399A flap domain alignments .....	151
Figure 5.44 <i>Pm</i> HMGR L407S RMSD and structure comparisons.....	152
Figure 5.45 Small domain movement comparisons within first minute of reaction initiation. ..	153
Figure 5.46 Large domain movement comparisons within first minute of reaction initiation. ..	155

Figure 5.47 Flap and small domain interactions in Mevalonate-NAD <sup>+</sup> and CoA-NAD <sup>+</sup> structures. .....	161
Figure 5.48 CoA and HMG-CoA binding sites compared to quaternary complex and mevalonate - <i>Pm</i> HMGR interactions.....	162

## KEYWORDS

KEYWORD	FULL FORM
HMG-CoA	3-hydroxy-3-methylglutaryl-CoA
MEV	Mevalonate
CoA	Coenzyme A
NAD	Nicotinamide Adenine Dinucleotide
MVD	Mevaldehyde
QM/MM	Quantum Mechanics / Molecular Mechanics

## ABSTRACT

HMG-CoA reductase from *Pseudomonas mevalonii* (*Pm*HMGR) catalyzes the oxidation of mevalonate and mevaldyl-CoA to form HMG-CoA using CoA-SH and two NAD<sup>+</sup> cofactors. While the enzyme has been used extensively as a drug target in humans to treat hypercholesterolemia, its pathway has also been found to be critical for the survival of antibiotic resistant gram-positive bacteria. Structural studies using non-productive and slow-substrate binary complexes as well as biochemical studies using half and full reactions led to the proposal that the conversion of mevalonate to HMG-CoA occurs through the generation of two intermediates, mevaldehyde and mevaldyl-CoA (Shown in Fig 1.1). However, several intermediary changes along the *Pm*HMGR reaction pathway remain unclear. By gathering information about the enzyme's intermediate states via structural studies, we could identify potential allosteric sites that further the reaction mechanism. Using this knowledge, we could design enzyme inhibitors that act as novel antibacterials. The application of time-resolved crystallographic methods would provide structural information about transitory states in the *Pm*HMGR reaction mechanism. The *Pm*HMGR crystal has been shown to be suitable for time-resolved crystallographic measurements for the reaction steps resulting in mevaldyl-CoA formation. However, our structural investigations of the mevalonate, CoA and NAD<sup>+</sup> complex that are expected to result in the formation of mevaldehyde (Fig 1.1) do not show any changes corresponding to a turnover in the crystal environment.

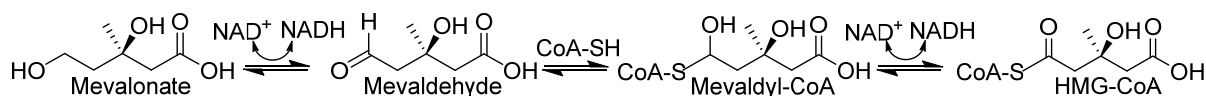


Figure 1 Proposed reaction steps for conversion of mevalonate into HMG-CoA in *Pm*HMGR

To investigate the factors limiting enzymatic activity in the crystal, we investigated the effects of pH and specific ions in the crystallization environment. Kinetic studies indicated a strong *Pm*HMGR inhibition in the crystallization buffer that is dependent on the concentration of the crystallization precipitant ammonium sulfate. These studies also indicated an increase in enzyme turnover with increasing pH. Utilizing the ionic concentration and pH-dependent

properties of the enzyme in the crystallization environment, we have developed a reaction triggering approach using pH changes for *PmHMGR* crystals.

We have demonstrated our application of this ‘pH-jump’ method by observing changes in *PmHMGR* crystals after reaction initiation. Changes in the density of mevalonate, CoA and NAD<sup>+</sup> have indicated mevaldehyde and mevaldyl-CoA formation. Additionally, the appearance of a unique NADH absorbance peak after the pH-change has also highlighted the initiation of the *PmHMGR* reaction and the occurrence of a hydride transfer step. Our analysis of the movements using time-resolved structures post reaction-initiation have also highlighted structural changes and inter-domain contacts in the small and flap domain that would allow cofactor exchange and product release. The pH-jump method can hence be utilized as a novel approach for triggering the *PmHMGR* reaction in crystals and further studying transitory states along its reaction pathway.

# CHAPTER 1. INTRODUCTION

## 1.1 Objectives

### 1.1.1 Overall goal of the research

The field of time-resolved crystallography currently faces many scientific challenges that need to be overcome to make it a viable approach across biomolecular systems. For a time-resolved crystallographic experiment to be developed to study enzymatic reaction mechanisms requires the application of a reliable reaction triggering approach and the data collection capabilities to capture the onset of changes associated with reaction initiation. With significant variability in enzymatic mechanisms, approaches that cater to individual biological systems need to be developed for reaction-triggering and time-resolved data collection. Extending the application of time-resolved crystallographic methods to novel systems can lead to further development of new approaches to acquire time-resolved structural information.

There is a lack of transitory intermediate state information in enzymatic systems running multi-step reactions like *PmHMGR*. Additionally, the ability of this enzyme to undergo large scale conformation changes and turnover within the crystal environment make it uniquely suited for studying by time-resolved crystallographic methods<sup>[1, 2]</sup>. With factors exclusively limiting the oxidation of mevalonate in the crystal environment, we have not been able to observe turnover in a mevalonate, CoA and NAD<sup>+</sup> bound quaternary complex. With the quaternary complex being inactive, we are unable to observe the changes that lead to the formation of mevaldehyde and subsequently facilitate the formation of a thioester bond between mevaldehyde and CoA. Given that *PmHMGR* primarily runs its enzymatic reaction converting mevalonate to HMG-CoA, observing the changes that it undergoes in running a reaction in this direction would be beneficial in fully understanding its mechanism. Hence, the goal of this research project has been to develop and apply an approach to obtain time-resolved crystallographic information about the *PmHMGR* reaction mechanism. By identifying certain factors that limit and affect the turnover of *PmHMGR* in the crystal, we have been able to design a novel method using pH changes to trigger a non-photoactivatable multi-step reaction thus adding to the approaches to study complex enzymatic mechanisms using time-resolved crystallography.



### 1.1.2 Research Objectives

The set of objectives in this research project pertain to developing time-resolved methods to study the intermediary changes that make up the *Pm*HMGR mechanism of mevalonate oxidation to form HMG-CoA. First, we needed to develop a reaction-triggering method for which we had to determine the factors limiting mevalonate oxidation and determine how they can be overcome in the crystallization environment. We also wanted to obtain a timeframe within which we could capture different intermediate stages of the reaction. With the intent of observing the formation of reaction intermediates via structural studies, our aim then was to develop a reaction-triggering approach and observe the progression of the *Pm*HMGR reaction with the oxidation of mevalonate.

Information obtained through time-resolved methods can provide novel insight into the energetics and structural features that govern multistep reactions. The development of this methodology can act as a proof-of-concept which can also be applied to other similar enzymes. Our goal is to capture reaction intermediates starting from a mevalonate, CoA and NAD<sup>+</sup> *Pm*HMGR complex, thereby understanding the structural and biochemical changes that facilitate the reaction steps needed to carry out 2 hydride transfer steps, a thioester bond formation and product release.

## 1.2 Organization

The thesis is organized into five parts. The first and second chapters introduce the research problem, aims and the background of the project. The third chapter details the studies conducted to understand the effect of pH and crystal environment on enzymatic activity. The fourth chapter explores the application of the pH-jump method to trigger enzymatic activity within the crystal environment as documented via time-resolved UV-Vis measurements. The fifth chapter describes crystal structures obtained via the application of the pH-jump method. These structures are compared with each other to determine the changes that are observed with time after the reaction initiation. A structural comparison of a pre pH-jump structure of *Pm*HMGR bound to mevalonate, CoA and NAD<sup>+</sup> to other ligand bound structures has also been documented.

## CHAPTER 2. BACKGROUND

### 2.1 Role of *Pm*HMGR in the mevalonate pathway

HMG-CoA reductase is the rate limiting enzyme of the mevalonate pathway and is involved in isoprenoid biosynthesis in humans and is a drug (vastatin) target for patients suffering from hypercholesterolemia<sup>[3]</sup>. The mevalonate pathway has also been found to be crucial for the survival of low G-C gram positive bacteria and found to reduce virulence in knockout mice without the mevalonate synthase (MvaS) gene and is therefore thought to be a suitable target for novel antibiotics<sup>[4]</sup>. HMG-CoA reductase in *P. mevalonii* (*Pm*HMGR) utilizes mevalonate as a carbon source to generate HMG-CoA via a two-electron oxidation-reduction reaction<sup>[5-7]</sup>. The mammalian membrane bound and soluble low G-C pathogenic bacterial homologues of HMGR belong to two different classes of HMGRs, Class I and II respectively<sup>[8]</sup>. *Pm*HMGR belongs to class II HMGRs along with various other HMGRs from other bacteria such as *Staphylococcus aureus*, *Enterococcus faecalis*, *Streptococcus pneumoniae*, *Burkholderia cenocepacia* and *Listeria monocytogenes*, some *Streptomyces* bacteria and Archaea *Archaeoglobus fulgidus*<sup>[3, 9-15]</sup>. *Pm*HMGR has been extensively studied as a model system for Class II HMGRs. Biochemical studies have shown that *Pm*HMGR can run the HMGR enzymatic reaction in the direction of mevalonate oxidation and HMG-CoA reduction<sup>[5]</sup>. While the production of mevalonate by various HMGRs results in the production of metabolite isopentenyl-diphosphate, *Pm*HMGR also utilizes mevalonate to produce Acetyl-CoA as a carbon source in the citric acid cycle.

*Pm*HMGR sequences have shown to overlap with sequences of various other Class II HMGRs in gram-positive and gram-negative bacteria, particularly in regions associated with NAD<sup>+</sup>, CoA and mevalonate binding and catalysis (Fig 2.1). Here, the regions associated with NAD<sup>+</sup> binding starting from D 683 – N 688 in *P. mevalonii* are conserved across organisms. Similarly, the residues associated with CoA (SER 85) and mevalonate (ARG 261, ASN 271) placement at the active site are found to be conserved. Catalytic residues associated with hydride transfer between mevalonate and NAD<sup>+</sup> (GLU 83 and LYS 267) and deprotonation of CoA-SH for thioester bond formation (HIS 385) are also conserved. Hence, understanding the mechanism of *Pm*HMGR can give us insight into the catalytic mechanism of several other antibiotic resistant

gram-positive bacteria. Detailed information about the *Pm*HMGR mechanism can be used to generate novel antibacterials.

L. Delbrueckii	PMTTE	ASVVAAANHGMSVFAKAGGVKATSQRDGIYGVQIVLEVTEAFS-LA-GFKKEFPA	121
F. Bacterium	PMAIE	SSVVAAASKAAKFWLNRGGFKTKVRSTVKSQVHIMYNGLHGEMDAFYAFKAD	180
C. Gingivalis	PMVLE	SSVVAAVSKAAKFWSEQGGFLCQVRSMEKVGHIHLFFEGDKHELQFFSTIEPL	135
S. Aureus	PMMVE	PSVVAAASYGAKLVNQTTGGFKTVSSERIMIGQIVFDGVDDTEKLSADIKALEKQ	135
L. Pneumophila	PLAVE	ETIIAALS KSAKWIRQHGEINTWVHGECILGQIQLAKVKDFHRFSDLFNKNRQY	141
P. Mevalonii	PLVVE	PSIVAAASYMAKLARANGGFTTSSSAPLMHAQVQIVGIQDPLNARLSLLRRKDE	137
D. Acidovorans	PMAVE	PSVVAAASYMAKLARE DGGFQTSSTLPLMRAQVQVLGVTDPHGARLAVLQARAQ	137
E. Facaelis	PLVVE	PSIVAAASYMAKLA---QGFKTVNQRLMRGQIVFYDVADAESLIDELQVRETEIFQQ	521
L. Delbrueckii		YIKEANKE-FASLIRHGGGLKDLTARQEA----DLVYLLALVDPAEA	175
F. Bacterium		LLQSVQS-INASMKKRGGGLDLQLINKTDVLA-GYYQLHATFETK	238
C. Gingivalis		LYEQQTQG-ITENMRKGGGSSIIKDMTDSLE-HYYQVFVFTLTG	193
S. Aureus		IHKIADEA-YPSIKARGGGYQRIADTFPE---QQLLSLKVFVDTK	191
L. Pneumophila		FIEIANKDVAANMVKRGGGVTDLQVRHLKREDGQDMAVIHLMNSC	201
P. Mevalonii		IIELANRK-DQLNSLGGGCRDIEVHTFADTPRGPMPLVAHLVDVR	196
D. Acidovorans		IIERANSR-DKVLIGLGGGCKDIEVHVFPDTPRGPMPLVHUVDR	196
E. Facaelis		AELSYPSIVKRGGGLRDLQYRAFDES-----FVSVDFLVDVK	573
L. Delbrueckii	KKMALLAKIGSSDPYRAVTNN	KGIMNGVDAVMLATGNDYRAVEAACHAYAASGEYRSL	286
F. Bacterium	RKFTRAVDIATVEPYRAVTHN	KGIMNGIDAVVIATGNDYRAVEAGVHAYAARDGQYRSLT	357
C. Gingivalis	TDFTRAIVANADVYRAVTHN	KGVMNGIDAVVIATGNDYRAVEAAVHAYAAGEGRYKSLT	309
S. Aureus	KRMERASVLAQVDIIRAAATHN	KGVMNGIHAVVLATGNDYRGAEASAHAYASRDGQYRGIA	301
L. Pneumophila	QKLQEASLFAEIDPYRAATHN	KGVMNGIDPVLIATGNDYRAVEAGIHSYAARSQGYKAIT	302
P. Mevalonii	EGILDAYAFAAVDPYRAATHN	KGIMNGIDPLIVATGNDYRAVEAGAHAYACRSGHYGSLT	305
D. Acidovorans	EGVLDAYTFAAIDPYRAATHN	KGIMNGIDPVIVATGNDYRAVEAGAHAYASRSGSYTSLT	305
E. Facaelis	EKIVLASRYASLDPYRAVTHN	KGIMNGIEA VVLATGNDYTRAVSASCHAFVKEGRYQGLT	680
L. Delbrueckii	NFAALSAISTKGIQAGH	IMRLQSRNVVQTLPASAEKAAVYQMMISQGYGE---TAAKN	400
F. Bacterium	NFAALHSLVTTGIQAGH	IMKMHVLNMLEQIGANDDEKLLKKAFQDKTPSF----SGLRE	470
C. Gingivalis	NFAAVSSLVTYGIQKGH	IMKMHLANILNQLGATPAQKQEIAYFKDKTVSH----SEVVQ	422
S. Aureus	NFAACRALVSEGIQKGH	IMSLQYKSLAIVVGAKGDEIAQVAEALKQEPRANT----QVAER	417
L. Pneumophila	NLGALKALCTDGIQGH	IMKLHIDNLLL VAGANENEMPVLKEKLQEWLNLNKRVS LNAYD	420
P. Mevalonii	NLGAMRALATEGIQRGH	IMALHARNIAVVAGARGDEV DWVARQLVEYHDVRA---DRAVA	420
D. Acidovorans	NLGALRALATEGIQRGH	IMALHARNIALVAGATGDEVDAVARQLAAEHDVRT---DRALE	420
E. Facaelis	NLAALRALVSEGIQKGH	IMALQARSLAMTVGATGKEVEAVAQQLKRQKTMNQDRALA	796

Figure 2.1 Sequence alignment of Class II HMGRs. Overlapping regions in the NAD<sup>+</sup> binding region (yellow), catalytic site (GLU 83 – Light Purple, LYS 267 – Red, HIS 381 – Dark Purple) and enzyme regions H-bonding to CoA (SER 85 – Green), mevalonate (ARG 261 – Teal, ASN 271 – Dark Blue) and NAD<sup>+</sup> (ASP 283 - Brown) in *Pm*HMGR are highlighted.

## 2.2 *Pm*HMGR enzyme architecture

The structure of the enzyme in *P. Mevalonii* was first obtained at 3 Å in 1995 by Lawrence et. al and indicated that the enzyme exists as a homodimer (90,000 g /mol) with an active site at the dimer interface<sup>[16, 17]</sup>. *Pm*HMGR crystals have a cubic symmetry (I4<sub>1</sub>32) with equal unit cell dimensions of 226 Å and 2 molecules per asymmetric unit.

Each monomer has a domain region that binds to cofactors CoA (large domain) and NAD<sup>+</sup> (small domain) with the substrate mevalonate binding at the homodimer interface<sup>[18, 19]</sup>(Fig 2.2). Movement of the 50-residue C-terminal region of the enzyme comprising of 3 helices, termed the flap domain, has been found to be essential in the formation of the enzyme's active site. In the presence of the substrates and cofactor, the flap domain is found to close in on the active site and position a critical catalytic residue HIS 381 adjacent to CoA-SH<sup>[19]</sup>.

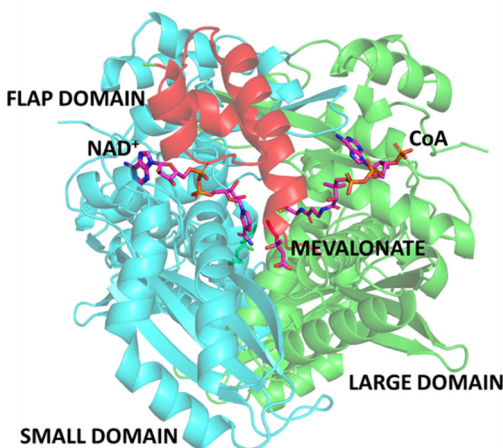


Figure 2.2 *Pm*HMGR bound to mevalonate, CoA and NAD<sup>+</sup>

## 2.3 *Pm*HMGR reaction mechanism

The class II enzyme utilizes two successive NAD<sup>+</sup> cofactors that perform hydride transfers and accept electrons from the substrate (mevalonate) and intermediate (mevaldyl-CoA) along the reaction pathway.

The prokaryotic enzyme has been found to catalyze the same reaction steps as the mammalian enzyme in both forward and reverse directions (Shown in Fig 2.3 a.)<sup>[5]</sup>. The conversion has been shown to occur with the production of the intermediate mevaldehyde after a hydride

transfer between the hydroxyl of mevalonate and  $\text{NAD}^{+}$ <sup>[5, 20]</sup> (Shown in Fig 2.3 b.). Additional studies by Retey et. al have identified a second intermediate in the HMGR reaction in yeast where the enzyme converts mevaldehyde into a thiohemiacetal (mevaldyl-CoA)<sup>[21]</sup> (Shown in Fig 2.3 c.).

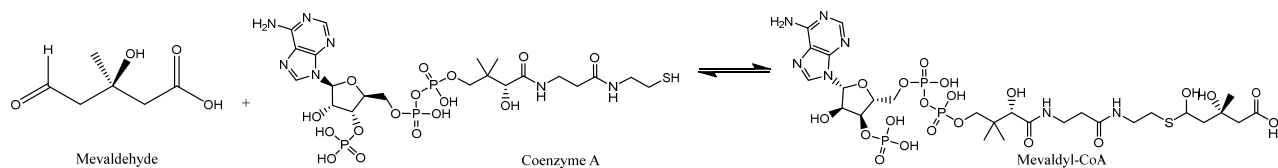
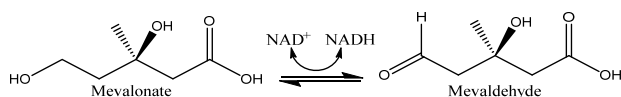
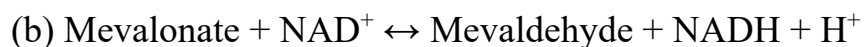
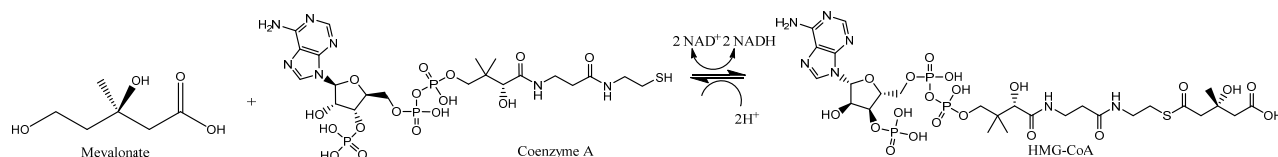


Figure 2.3 *Pm*HMGR enzymatic reaction mechanism A. Conversion of mevalonate to HMG-CoA B. Mevalonate oxidation step in the *Pm*HMGR enzymatic reaction C. Thioester bond formation step between mevaldehyde and CoA in the *Pm*HMGR enzymatic reaction

While the cofactor CoA is chemically involved as a substrate that forms a thioester bond with mevalonate to form HMG-CoA, its binding also plays a structural role in the *Pm*HMGR mechanism by increasing the rate of conversion of mevaldehyde to mevalonate 1.5-2.5 fold<sup>[5, 20]</sup>.

## 2.4 Structural studies on *Pm*HMGR

### 2.4.1 *Pm*HMGR active site

Several site-directed mutagenesis studies in *Pm*HMGR have also indicated that the residues GLU 83 and LYS 267 are crucial for the enzyme's active site<sup>[22, 23]</sup>. Crystal structures and QM/MM

simulations have subsequently shown that GLU 83 and LYS 267 act as a proton acceptor and oxyanion-hole respectively for the hydride transfer step with  $\text{NAD}^+$  that is proposed to convert mevalonate into mevaldehyde (Fig 2.4)<sup>[1, 19, 24]</sup>. The presence of GLU 82 and ASP 783 have been shown to position the GLU 83 and LYS 267 at the enzyme active site<sup>[19]</sup>. Site-directed mutagenesis studies in *PmHMGR* have indicated that HIS 381 acts as a general base and allows the deprotonation of CoA-SH for the cofactor to form a thioester bond with mevaldehyde resulting in the production of mevaldyl-CoA<sup>[25]</sup> (Fig 2.4). Similar functional studies with Syrian Hamster HMGR further validate the role of a catalytic HIS acting as a general base involved in the deprotonation of CoA-SH resulting in the acylation of mevaldehyde to form mevaldyl-CoA<sup>[26, 27]</sup>. The positioning of the thiol before the breaking of the thioester bond in mevaldyl-CoA has been observed in the structure obtained with *PmHMGR* bound to NADH and dithio-HMG-CoA obtained by Steussy et. al<sup>[1]</sup>(Shown in Fig 2.5). In this experiment, dithio-HMG-CoA has been observed to act as a slow substrate and stall the reaction after the first hydride transfer step converting dithio-HMG-CoA to dithio-hemiacetal (Fig 2.5).

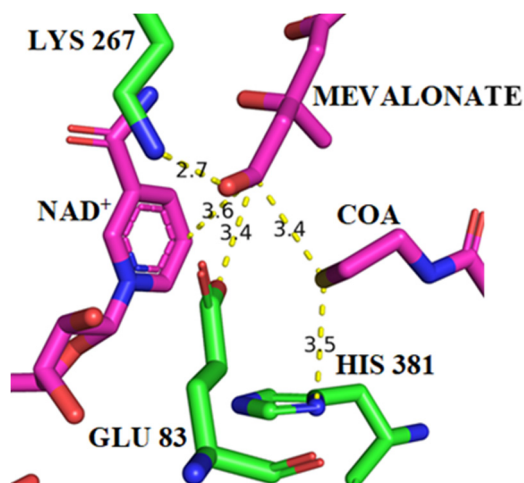


Figure 2.4 *PmHMGR* active site showing interactions with Glu 83, Lys 267 and HIS 381 with mevalonate, CoA and  $\text{NAD}^+$

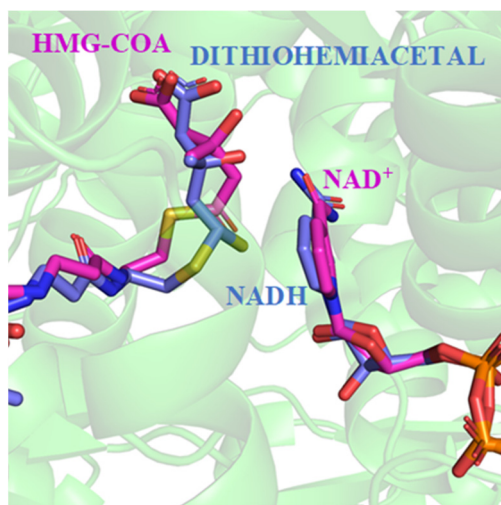


Figure 2.5 Active site of *PmHMGR* with dithio-HMGCoA and NADH (blue, PDB: 4I4B) superposed with the structure observed with HMG-CoA (violet, PDB: 1QAX).

#### 2.4.2 Flap domain configurations in *PmHMGR* structures

The binary and ternary complexes of this enzyme have been studied by Tabernero et. al (1999) and Steussy et. al (2015)<sup>[1, 19]</sup>. Crystal structures of *PmHMGR* complexes bound to HMG-CoA-NAD<sup>+</sup>, mevalonate-NADH and CoA-NAD<sup>+</sup>-mevalonate also show the closure of the flap domain not observed in the apo enzyme structure. Additionally, QM/MM and kinetic studies have also shown increased rigidity in the flap domain residues L407, E399 and E396 in the enzyme's transition state. The reduced dynamics of this region indicates that the conformation adopted by these residues in the enzyme's transition state has an allosteric effect on the *PmHMGR* hydride transfer step<sup>[28]</sup>.

Variations in the degree of flap-domain closure have been observed depending on the ligands bound at the active site. The binding of specific ligands and intermediates has hence been shown to affect the conformation of the flap domain. The presence of the flap domain has been studied in the presence of other combinations of ligands. Depending on the presence of substrate or cofactor, the flap domain has been observed to be found in either an open, closed or partially open (disordered states). The presence of the flap domain in the presence of various substrate/cofactor combinations has been summarized in the Table 2.1.

Studies by Duncan et. al have shown that in binary complexes soaked with only mevalonate / mevaldehyde and NAD<sup>+</sup> / NADH, a partial closure of the flap has been observed. Maximum closure of the flap domain is only observed when all the substrates are present. In the presence of

natural substrates and cofactors, the full flap domain is only observed in structures that have CoA / HMG-CoA and NAD<sup>+</sup> / NADH present.

### 2.4.3 *Pm*HMGR ligand-enzyme interactions

The binary and ternary complexes of this enzyme have been studied by Tabernero et. al (1999) and Steussy et. al (2015)<sup>[11, 16]</sup>. Crystal structures of *Pm*HMGR complexes bound to HMG-CoA-NAD<sup>+</sup>, mevalonate-NADH and CoA-NAD<sup>+</sup>-mevalonate also show the closure of the flap domain not observed in the apo enzyme structure. Additionally, QM/MM and kinetic studies have also shown increased rigidity in the flap domain residues L407, E399 and E396 in the enzyme's transition state. The reduced dynamics of this region indicates that the conformation adopted by these residues in the enzyme's transition state has an allosteric effect on the *Pm*HMGR hydride transfer step<sup>[18]</sup>.

The presence of the flap domain has been studied in the presence of other combinations of ligands. Depending on the presence of substrate or cofactor, the flap domain has been observed to be found in either an open, closed or partially open (disordered states). The presence of the flap domain with various substrate/cofactor combinations has been summarized in the Table 2.1<sup>[2]</sup>.



Table 2.1 Flap orientation in the presence of different *Pm*HMGR substrate and cofactors

Structure	Open Flap Entrance Disordered Flap	Closed Flap Entrance Disordered Flap	Closed Flap Entrance Partially Ordered Flap	Closed Flap Entrance Ordered Flap
Apoenzyme	X			
(dithio) HMG-CoA	X			
Dithiohemiacetal NAD <sup>+</sup>				X
Thiohemiacetal		X		
Mevalonate	X			
Mevaldehyde	X			
Mevaldehyde NAD(H)	X			
Thiovalonate, CoA and NAD <sup>+</sup>				X
Mevalonate NAD <sup>+</sup>		X	X	
Mevalonate NADH		X	X	
CoA	X			
NAD	X			
CoA and NAD				X
CoA and NAD(H)				X
HMG-CoA and NAD			X	
HMG-CoA and NAD(H)			X	

The regions between the phosphate portion of NAD<sup>+</sup> and the thiol portion of CoA are shown to make contacts with the first helix in the flap domain region of *Pm*HMGR (Shown in Fig 2.6).

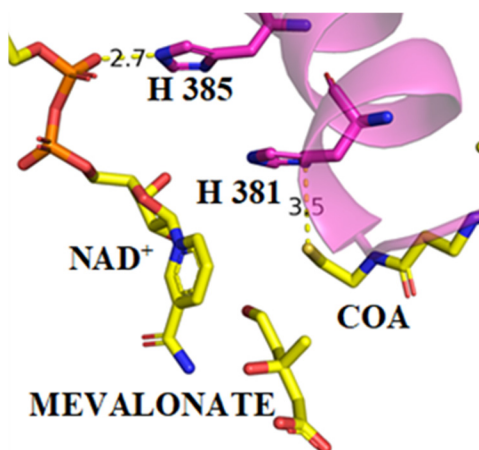


Figure 2.6 *Pm*HMGR flap interactions with NAD<sup>+</sup> and CoA

Studies by Duncan et. al have also documented conformational changes in the small domain region that forms contacts with  $\text{NAD}^+$  and full closure of the flap domain upon CoA binding<sup>[2]</sup>. These changes indicate that the binding of CoA could induce conformational changes resulting in the full formation of the enzyme's active site and the subsequent hydride transfer step that takes place between mevalonate and  $\text{NAD}^+$ .

The formation of the enzyme's active site is shown to take place after binding of the substrates and cofactor with a hydrogen bond network forming between the large domain (SER 85) to the active site with CoA and the amide atom in the pantothenic acid region of CoA. Additional interactions are formed between the small domain residue ASN 688 and the phosphate oxygen atoms in  $\text{NAD}^+$ . Flap domain residues HIS 381 and HIS 385 also form contacts with the CoA-thiol and  $\text{NAD}^+$  Phosphate Oxygen respectively (Shown in Fig 2.7).

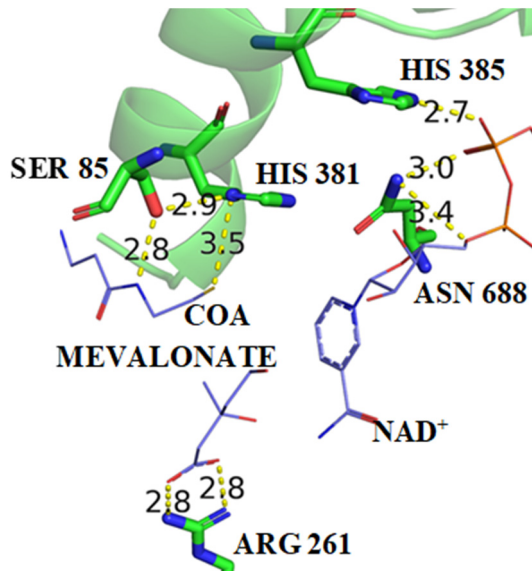


Figure 2.7 Residues in the large, small and flap domain forming interactions with  $\text{NAD}^+$ , mevalonate and CoA at the *PmHMGR* active site.

## 2.5 Turnover in *PmHMGR* crystals

As outlined above, the study of productive complexes in *PmHMGR* has shown that the enzyme is capable of undergoing turnover within the crystal. Studies of crystal structures of binary and ternary productive complexes by Duncan et. al have provided major insight into the mechanistic changes in the enzyme<sup>[2]</sup>. The binary complex structure solved with the intermediate mevaldehyde and CoA showed the formation of hemiacetal, indicating the ability of the enzyme

to be active within the crystal or facilitating the interaction of the 2 ligands by placing them in proximity<sup>[2]</sup>. The formation of mevaldyl-CoA with mevaldehyde and CoA bound at the enzyme's active site further indicated that the thiohemiacetal can also be produced as a reaction intermediate if a hydride transfer first converts mevalonate into mevaldehyde. Additionally, the formation of mevaldyl-CoA in *Pm*HMGR has also been observed using a slow substrate dithio-HMG-CoA and NADH. In this productive complex with the slow substrate, the observed thioester region is shown to change from a flat  $sp^2$  configuration to a pyramidal  $sp^3$  configuration indicating the formation of a thiohemiacetal<sup>[1]</sup>.

## 2.6 Obtaining time-resolved crystallographic data to study *Pm*HMGR reaction mechanism

While standard crystallographic studies have used the ability to observe turnover and large-scale conformational changes in the *Pm*HMGR crystals to map out different steps in the proposed reaction mechanism using non-productive and slow substrate complexes (Shown in Fig 2.8).

However, details pertaining to the mechanistic changes that the enzyme undergoes during the formation of the first proposed intermediate mevaldehyde, the conversion of mevaldehyde into mevaldyl-CoA,  $NAD^+$  exchange and product release are still unknown. These details can only be studied by capturing dynamic information about the enzyme for which we need to be able to capture time-resolved structural data with *Pm*HMGR.

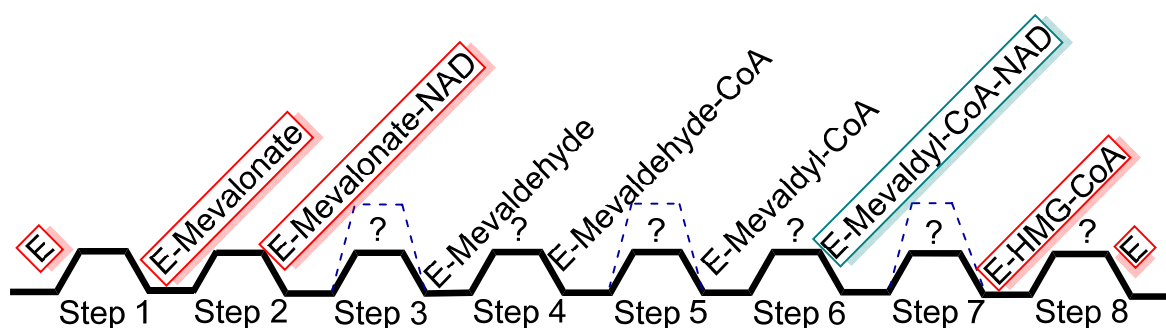


Figure 2.8 Map showing the different steps within the HMG-CoA reductase catalytic reaction. Structures were obtained with substrates, cofactors and products (red) and the ones that show evidence for intermediates with slow-substrates (green). Steps in the reaction pathway with higher activation energy are also indicated (dashed-blue).

In classical enzyme crystallography, we have been largely accustomed to understanding mechanisms by observing static structures that showcase enzyme-ligand interactions. While these structures illustrate the regions of the enzyme involved in activity and the comparison of apo and ligand-bound structures can tell us a lot about the structure-function relationships of the enzyme, the role of enzyme dynamics during catalysis remained largely unexplored. Additionally, we were unable to obtain structural information about various intermediate transitory states that play a key role in the enzyme's reaction pathway using static ligand bound structures.

The *Pm*HMGR cubic crystals are particularly well suited for dynamic studies as the active site is solvent exposed and can allow binding of the substrate using direct soaking techniques. The resulting conformational changes also do not disturb the crystal lattice, thereby permitting turnover to take place within the crystal. Additionally, the lack of structural information for reaction intermediates along the *Pm*HMGR reaction pathway make it a particularly good target for time-resolved crystallographic methods.

## **2.7 Observing enzyme turnover and other biological processes using time-resolved crystallography**

Enzyme turnover in crystals with changes in electron density has been observed several decades ago with the introduction of substrates in elastase, glycogen phosphorylase crystals and with caged-GTP and caged-NADP in Ha-Ras p21 protein and isocitrate dehydrogenase respectively<sup>[29-32]</sup>. To further study enzymatic processes that facilitate turnover, several methods to obtain time-resolved structural information have been developed in crystallography.

### **2.7.1 Development of time-resolved data collection methods**

Initial efforts in time-resolved crystallography have been largely focused on systems that are light-driven because these processes can be regulated via an external light source. The steps that can be initiated by photon absorption have largely appeared to be locally driven at the absorption site given that they often affect the electronic configuration and coordination state of metal clusters in various biomolecules or bring about a photochemical like isomerization resulting in a rapid biological process. Therefore, these changes appear within extremely fast timescales ranging from femtoseconds to picoseconds. The ease of triggering these processes has made the

advent of time-resolved crystallographic methods largely centered towards adapting to these timescales.

Data collection methods starting with Laue Crystallography and subsequently serial femtosecond crystallography using X-ray free electron lasers have aimed at achieving complete datasets in an extremely shorter amount of time as compared to standard crystallographic methods. Using a polychromatic X-ray source, Laue diffraction has been able to obtain time-resolved structural information of several enzymes with a very short X-ray exposure time. This method has been used to tap into time-scales ranging from milliseconds – picoseconds. Relying on light-driven reaction triggering, Laue diffraction experiments have been often coupled with pump-probe laser setups. This approach has been applied to obtain dynamic information of several light-driven natural processes with photo-active yellow protein (PYP) and Photosystem II<sup>[33, 34]</sup>. Additionally, it has also been utilized to observe ligand photodissociation and the subsequent interactions with a myoglobin-CO complex and hemoglobin<sup>[35, 36]</sup>. However, Laue diffraction has also faced some limitations, particularly the introduction of spatial overlaps in diffraction patterns because of high crystal mosaicity or crystal disorder because of reaction initiation or from high intensity Laue radiation. This eventually becomes a hurdle in Laue data processing<sup>[37]</sup>. These limitations were subsequently overcome with the use of X-ray free electron lasers and microcrystals which provided a narrower bandwidth of radiation to overcome the effects of crystal disorder while achieving a high degree of observed changes within smaller crystals<sup>[38, 39]</sup>.

### **2.7.2 Development of sample delivery methods in time-resolved crystallography**

To match advances in data collection, we have also seen various developments in sample delivery with the use of microjet injectors that maintain a stream of microcrystals in an XFEL beam and can also handle viscous samples<sup>[40, 41]</sup>. Additional recent approaches towards sample delivery include fixed-target systems and drop-on-tape setups using acoustic droplet ejection<sup>[42-44]</sup>. In the process of designing new sample delivery systems, the field has also made several advances in the mixing apparatus that is coupled with sample delivery. The use of mixing / diffusion techniques allows us to apply a reaction initiation approach in biological systems that are not photosensitive. This is usually done by introducing a ligand or ion that would mediate or act as a substrate for an enzymatic reaction. The process of diffusion also allows us to observe the formation of key interactions that take place before the reaction such as the accommodation of

ligands into an enzyme active site that is coupled with several allosteric and local conformational changes that allow the enzyme to function after reaction initiation. Mixing initiation has been used in injectors with cytochrome C-oxidase microcrystals that had been reduced using dithioinlite and subsequently soaked with CO-saturated buffer prior to data collection<sup>[45]</sup>. The development of ‘Hit and return (HARE)’ system devices has also been suited for the introduction of ligands into microcrystals. Ligand solutions are introduced via a piezo-driven droplet injector that is synchronized with the data collection step on a fixed target system thereby coordinating reaction initiation and sample mounting. This approach has been demonstrated with the introduction of GlcNac<sub>3</sub>, a Lysozyme inhibitor<sup>[46]</sup>. The uses of HARE systems can also be further modified for optical excitation with pump-probe devices. This has been displayed with the cleavage of photocaged fluoroacetate to observe the catalytic mechanism of FacD (Flouroacetate dehalogenase) using time-resolved serial synchrotron crystallography<sup>[47]</sup>. The use of the mix-and-diffuse method to observe ligand-binding has also been incorporated into tape drive sample delivery systems with the introduction of the inhibitor chitotriose to lysozyme crystals<sup>[48]</sup>.

### **2.7.3 Use of caged-NAD<sup>+</sup> cofactors for time-resolved crystallography studies of *PmHMGR***

While ligand diffusion is a potential way to observed time-resolved changes in *PmHMGR* crystals to understand its reaction mechanism, this process requires long soaking times of several hours with a small concentration of ligands to preserve crystal order that is otherwise lost due to excessive cracking of the crystals during ligand entry. Therefore, having substrate-soaked enzyme crystals before reaction initiation would be more suitable for rapid time-resolved data collection. This indicates the need to have an inactive *PmHMGR* ligand-bound complex that can be subsequently triggered by releasing it from its trapped inactive conformation which has been conventionally done with the use of photocaged ligands. We initially attempted the use of caged-NAD<sup>+</sup> cofactors with a mevalonate and CoA bound *PmHMGR*. Here the caged-NAD<sup>+</sup> acts as an inactive cofactor that binds in the same location as NAD<sup>+</sup> but only becomes functional after the attached moiety modifying NAD<sup>+</sup> (cage) is removed with an external stimulus. Photocaged-NAD<sup>+</sup> was synthesized using an N-2-nitrobenzyl group (Fig 2.9) ( $\lambda_{\text{excitation}} = 308 \text{ nm}$ ,  $\Phi_{\text{yield}} = 0.19$ ) by Dr. Jeremy Weitgenant using a previously established protocol<sup>[49]</sup>.

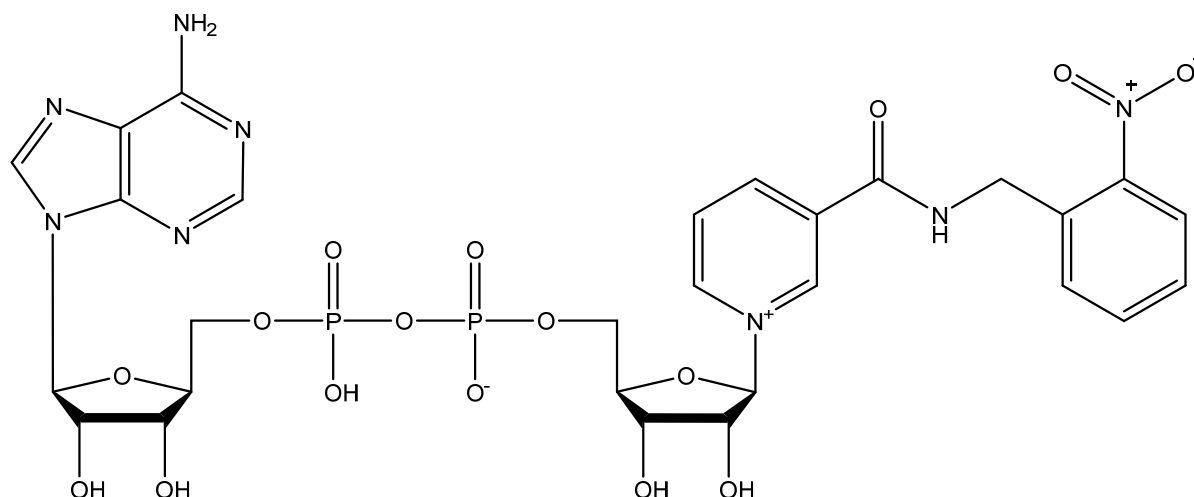


Figure 2.9 N-2-Nitrobenzyl Nicotinamide Adenine Nucleotide

Structural studies after binding photo caged-NAD<sup>+</sup> with mevalonate, CoA and were conducted by Dr. Chandra Duncan, Dr. Nicklaus Steussy, Tim Schmidt and Dr. Jeremy Weitgenant. While we don't observe full occupancy for the photo-caged cofactor in the ribose and phosphate regions, these structures showed electron density in the nicotinamide, ribose, phosphate and adenine portions. The mevalonate was observed to have an occupancy in the crystal structure that is equivalent to the rest of the enzyme. However, the increased mobility of the bound caged-cofactor has been shown to interfere with CoA binding.

This structure indicated that NAD<sup>+</sup> that had been photocaged with 2-nitrobenzaldehyde would be suitable for having the enzyme locked in an inactive conformation and for triggering the *Pm*HMGR reaction upon uncaging. However, it also indicated some limitations. These structures also showed additional binding of 2-nitrobenzyl-nicotinamide in the small domain which was then predicted to be a result of cleavage from the molecule. Since the cleavage was not photo-triggered, this indicated a lack of stability for the caged NAD<sup>+</sup> use in a time-resolved experiment<sup>[2]</sup>. It could have also occurred due to the binding of N-2-nitrobenzyl photocage which happened to present with the caged-NAD<sup>+</sup> that was introduced into *Pm*HMGR crystals for this experiment.

The use of this caged-NAD<sup>+</sup> for a time-resolved experiment was previously attempted with Laue time-resolved crystallography in *Pm*HMGR. The Laue x-ray crystallographic method was first tested on *Pm*HMGR with HMG-CoA only soaked into the crystals. While the ligand-bound structure of the enzyme could be solved using this technique, this experiment also indicated that the substrate undergoes lysis in the thioester bond region as has been previously observed in other

HMG-CoA bound structures (PDB: 1DQ8, 1R31)<sup>[50]</sup>. Additionally, it was determined that the reduced cofactor NADH could not be photocaged due to the added photocage rearranging to make a light insensitive molecule. This initially suggested that the mevalonate, CoA and NAD<sup>+</sup> bound complex might be better suited for time-resolved crystallographic studies for the reaction mechanism leading up to the thiohemiacetal formation (Fig 1.1). However, subsequent studies have since shown the lack of mevalonate oxidation in this quaternary complex crystal environment needs to be overcome before time-resolved data collection of its reaction mechanism can be achieved. In this study a Laue time-resolved crystallographic experiment was also attempted with caged-NAD<sup>+</sup>, mevalonate and CoA-SH using Nd:Yag ( $\lambda = 355$  nm) and an Nd:Yag OPO laser ( $\lambda = 320$  nm) to cleave the photocage for reaction initiation. Difference maps generated using pre and post laser-triggered Laue diffraction amplitudes indicated no change in the caged-NAD<sup>+</sup> indicating no lysis of the photocage in the *Pm*HMGR crystal environment. The lack of reaction initiation was attributed to the lack of laser power at required wavelength of 308 nm for the photoexcitation of the N-2-nitrobenzyl photocage. Laser triggering at wavelengths ranging from 320 – 355 that were used to obtain higher laser power while targeting the tail end of the caged-NAD<sup>+</sup> excitation spectrum were speculated to be too far away<sup>[2]</sup>.

To obtain photocages with a higher excitation wavelength, BHC-nicotinamide photocages were synthesized by Dr. Pauline Bourbon in Dr. Paul Helquist's group at University of Notre Dame. These photocages had a modified coumarin ring giving them a higher excitation wavelength between 330 – 370 nm, depending on the polarity of the solvent. Time-dependent density function theory calculations further indicated the optimal stability of a carbamate linker<sup>[51]</sup>. However, under solvent conditions necessary for the crystals, the observed quantum yield for the photocage was extremely low (0.036).

Work on the design of photocages and on the synthesis of caged-NAD<sup>+</sup> was continued by Dr. Farbod Salahi in Dr. Paul Helquist's group at the University of Notre Dame to overcome some of the previous challenges. After synthesizing several nicotinamide photocages, his work identified a p-hydroxyphenacyl (pHP) photocage attached to nicotinamide via a carbamate linker to have the most favorable solubility, photolytic efficiency (quantum yield - 11 %) in organic solvents and water at pH 7. The photocage was also observed to show photocleavage at a suitable wavelength of 330 nm at pH 7.9<sup>[52]</sup>. However, enzyme exchange reactions with all the synthesized photocages (which included BHC-nicotinamide and pHP) and NAD<sup>+</sup> using the enzymes NADase or ADP-



ribosyl-cyclase failed to produce the caged-NAD<sup>+</sup> as was done with N-2-Nitrobenzaldehyde, presumably due to their bigger sizes<sup>[53, 54]</sup>. Hence, a novel approach for synthesizing NAD<sup>+</sup> molecules and modifying pyridinium moieties has been explored by Dr. Salahi which can be extended<sup>[55, 56]</sup>. Increased susceptibility of the carbamate linker to nucleophilic attack in the crystallization environment has prevented the synthesis of a caged-NAD<sup>+</sup> with a carbamate linked pHP chromophore.

Currently approaches to cage the substrates HMG-CoA and mevalonate are being developed by Ryan OConnell in Dr. Paul Helquist's group and attempts to substitute the carboxylate region of the substrates with a pHP photocage using a carbamate linker are underway.

#### **2.7.4 Application of a pH-jump method for time-resolved crystallographic studies of *Pm*HMGR**

As an alternative to using caged-ligands and while exploring the factors limiting activity in a mevalonate, CoA and NAD<sup>+</sup> crystal, we arrived at the application of a pH-jump as a technique to do time-resolved crystallography. This technique had also been employed by Singer et. al to study the mechanism of Trypsin by using pH changes to probe the deacylation of guanidinobenzyl Trypsin. The use of a pH jump in these crystals results in the removal of the guanidinobenzyl group allowing the trypsin to catalyze the hydrolysis of peptides<sup>[57]</sup>. A pH-jump has also been utilized to observe  $\alpha$ -helix folding and coiled coil formation in leucine zippers by releasing protons from o-nitrobenzaldehyde upon shining UV light using time-resolve infrared spectroscopy measurements<sup>[58]</sup>. O-nitrobenzaldehyde has also been utilized to observe helix formation in poly-L-glutamic acid, changing active site conformation and protonation state to form an enzyme intermediate and subsequent unfolding in cytochrome C using time-resolved x-ray scattering<sup>[59, 60]</sup>. Additional approaches to using o-nitrobenzaldehyde for pH-jump experiments include observing volumetric changes in Apomyoglobin to detect folding intermediates and the rate-limiting steps that lead to native folded states using photoacoustic measurements<sup>[61]</sup>. In addition to utilizing pH-jumps, temperature jumps and external electric fields have also been employed to capture untapped dynamic and / or unfolded states of enzymes<sup>[62-67]</sup>. While pH changes have been demonstrably introduced by uncaging protons from different molecules to regulate pH, the pH-jump has also been employed with crystals by introducing them directly to a higher pH buffer and changing their internal pH via diffusion. This has been attempted with a porcupine pancreatic elastase bound to a

$\gamma$ -lactam derived inhibitor where the change in pH is shown to change the inhibitor conformation and the neighboring sidechains due to the deacylation of the acyl-enzyme complex<sup>[68]</sup>. However, due to these crystals being unstable and dissolving at higher pH, the pH-jump method could only capture the early stages of the deacylation process and not the subsequent intermediates. 1-(2-Nitrophenyl)ethyl-(NPE)-sulfate has also been utilized to conduct a UV-laser triggered pH jump in order to observe the proton transfer mechanism of an M2 proton channel<sup>[69]</sup>.

The use of a pH-jump method to observe turnover in *PmHMGR* was previously explored by Dr. Chandra Duncan, who identified that by modifying the *PmHMGR* crystal environment and changing crystal pH, one can observe enzyme turnover. The quaternary crystal structure of *PmHMGR* indicates no activity in the mevalonate, CoA and NAD<sup>+</sup> bound structure. However, the factors limiting activity at crystallization pH (pH 6.7) and in the *PmHMGR* crystal environment were not fully understood. Previous structural studies have also indicated that the reaction intermediate mevaldehyde and CoA can form a thioester bond in the enzyme crystal indicating that in this case it is the mevalonate oxidation that is inhibited<sup>[2]</sup>. In further investigating the factors that limit enzyme turnover in the crystallization environment we have been able to identify inhibitive effects of the crystal precipitant salt and pH-dependent properties of the enzyme. These have subsequently allowed us to utilize the ion-dependent inhibition and pH-dependent activity to our benefit to design a novel reaction triggering method. The use of our ‘pH-jump’ method allows us to transition a mevalonate, CoA and NAD<sup>+</sup> bound *PmHMGR* from an inactive to an active state in crystals. While this method triggers activity, it also slows down the reaction rate in order for us to observe subsequent changes within a time-frame of minutes allowing us to use freeze-trapping methods to observe post reaction intermediate states. Using pH, we can further regulate the rate of enzyme turnover and hence adapt it to suit other data collection techniques.

In addition to identifying factors significantly inhibiting mevalonate oxidation in *PmHMGR* crystals and developing a pH-jump reaction triggering protocol, we have subsequently focused on the application of the pH-jump method in observing post-reaction intermediates. Using structural information from various time-resolved structures obtained after reaction initiation, we have described several intermediate states along the enzyme’s reaction pathway and the structural and chemical changes that facilitate intermediate formation, cofactor exchange and product release.

## CHAPTER 3. STUDYING THE FACTORS LIMITING MEVALONATE OXIDATION IN THE *PmHMGR* CRYSTALLIZATION ENVIRONMENT

### 3.1 Introduction

The ability to obtain structural information about post-reaction intermediates can help us further understand the mechanism that facilitates the oxidation of mevalonate to its subsequent intermediate followed by a thioester bond formation with CoA. Capturing structural data from post-reaction intermediates can also potentially validate previously established models for the *PmHMGR* catalytic mechanism. Observing turnover in a crystalline environment requires that the enzyme can undergo conformational changes that facilitate catalysis within a crystal without disturbing the crystal lattice. The crystal environment must also be chemically suitable for the enzyme to facilitate a biochemical reaction. Additionally, one needs to have temporal control over the enzymatic reaction in the crystal environment in order to synchronize the initiation of activity with the collection of structural data at different stages of the reaction. In order to utilize crystallography to observe structural changes that facilitate the *PmHMGR* reaction mechanism, one must first understand the effect of the crystallization environment on enzymatic activity.

An effective way to gauge the potential activity of the enzyme in a crystal is to measure the enzyme's turnover in a crystallization buffer thereby measuring the effect of the constituents of the crystallization environment on *PmHMGR* activity. High salt concentrations have been shown to reduce enzyme activity by altering enzyme structure<sup>[70]</sup>. Earlier studies with bovine pancreatic Ribonuclease have shown an inhibitive effect of the crystallization salt, ammonium sulfate. These studies show a ~100 fold inhibition of the enzyme at a concentration of 1-2 M followed by an increase in activity at 3 M<sup>[71, 72]</sup>. The inhibitory effect of ammonium sulfate was also investigated in Ribonuclease A and Ribonuclease 5 based on their structures grown from high salt crystallization buffers with concentrations of 30 % and 2 M ammonium sulfate respectively. In the case of Ribonuclease A, the inhibition was found to be due to the binding of sulfate ions at the enzyme's active site by binding to the catalytic residue HIS 119 and disrupting its interactions with ASP 121. The binding of sulfates was also shown to affect the conformation of active site residues Lys 14, Lys 41 and Lys 66 and formation of salt bridges in the Ribonuclease A<sup>[73]</sup>. In the case of Ribonuclease 5 (Angiogenin), the sulfate was found to bind in the peripheral regions, however disrupting essential waters that disrupted the conformation of Arg 66, a key residue in

the Angiogenin cell binding domain and therefore disrupt other key interactions at the enzyme's ribonucleotide binding active site<sup>[73, 74]</sup>. High salt concentrations have also shown to influence coulombic enzyme-substrate interactions in Ribonuclease A<sup>[75]</sup>.

In addition to the crystallization buffer salt, protonation of the side chains that make up the active site, residues that regulate ligand movement as well as the substrate and cofactor also affect the turnover of the enzyme. Hence, the turnover of the enzyme observed in the crystallization buffer environment is significant dependent on its pH.

Therefore, to understand the effect of the crystallization precipitant salt and pH on the turnover of *PmHMGR*, an pH-rate profile was measured in the crystallization buffer in the pH range 4-11. A direct comparison may not be able to be made when comparing the activity in a pre-soaked crystal where the substrates are already situated in the active site with a solution-based assay where the substrate-enzyme contacts need to be established before activity can be observed. However, the crystallization solution can act as a good mimic to determine significant changes in enzyme activity.

To test the inhibitive effect of the ionic concentration in the crystallization buffer, we measured the salt-rate profile of the enzyme at different ionic concentrations. To determine if the inhibitive effect is from a specific ionic interaction in the crystallization environment and if it affects the pH-dependent kinetic properties of the enzyme, the pH-rate profile of the enzyme was measured in the presence of different salts testing the inhibitory effect of ammonium and sulfate ions. The inhibitive effect of ammonium sulfate was also tested by adding it to the enzymatic assay buffer used for pH-rate profile measurements keeping the concentration of salt the same as that of the crystallization buffer. To test the inhibition in the absence of ammonium and sulfate ions, we measured the pH-rate profiles of the enzyme in the presence of various ammonium and sulfate salts. By doing so, we have been able to separate the inhibitive effects of both salt ions in the crystallization buffer environment. We also tested the inhibitive effect of a high salt concentration in the absence of both ammonium and sulfate ions. Additionally, the effects of pH on the protonation states of the many catalytic residues and the bound ligands at the enzyme active site was investigated by calculating their pK<sub>a</sub> values. By obtaining a new understanding of the effects of ionic concentration and pH in the *PmHMGR* environment, we were able to develop a pH-dependent reaction triggering approach that allows us to capture transitory states of the enzyme using freeze-trapping methods.

## 3.2 Methods

### 3.2.1 Measuring the effect of the *Pm*HMGR crystallization environment on enzymatic activity

#### 3.2.1.1 Obtaining the *Pm*HMGR crystal structure bound to mevalonate, CoA and NAD<sup>+</sup>

Using a modified version of previously established protocol, purification of *Pm*HMGR was done by expressing the enzyme in BL21 cells via a pKK177-3-RED plasmid. Following steps of protein expression, the cells and subsequent centrifugation, the cell suspension was washed in potassium phosphate, EDTA, Glycerol and PMSF buffer. A cell lysate was obtained by passing the suspension through a French pressure cell several times. After extracting the soluble protein via centrifugation, *Pm*HMGR was separated via an Ammonium Sulfate fractionation step. The *Pm*HMGR enzyme was then separated via an anionic exchange on a DEAE-sepharose column using KCl<sup>[6]</sup>. To crystallize the apo-enzyme, a 0.25 x 0.25 x 0.1 mm crystals were used as a seed and a sitting-drop solution was set up with 1.2 M (NH<sub>4</sub>)<sub>2</sub>SO<sub>4</sub> and 100 mM ADA (crystallization buffer) and 95  $\mu$ M HMGR (10  $\mu$ L of 20  $\mu$ g/ $\mu$ l HMGR). 0.9  $\mu$ l of seeding solution with dilutions ranging from  $3.16 \times 10^{-4}$  –  $3.16 \times 10^{-6}$  were added to the crystallization drop. The crystallization drops also contained 2.5  $\mu$ l of dI H<sub>2</sub>O and 10  $\mu$ l of the crystallization buffer. Apo crystals of the size 0.4 x 0.4 x 0.2 mm picked for structure determination<sup>[1]</sup>. The crystals were cryoprotected by gradually replacing the reservoir solution with 1.2 M ammonium sulfate, 100 ADA and 32% glycerol and letting the crystals sit overnight. The ligands mevalonate, NAD and CoA were then soaked into the crystal by gradually replacing the cryoprotectant solution with a soaking solution containing 1.2 M Ammonium Sulfate, 100 mM ADA and 32% Glycerol and 5 mM mevalonate, 1 mM NAD and 1 mM CoA. An initial dataset was obtained using a home source, a Rigaku RU-200 rotating anode generator equipped with confocal mirrors and a RaxisIV++ detector, to confirm diffraction. A 2.0 Å dataset was subsequently obtained at the Advanced Photon Source (Argonne National Laboratory) at beamline 23-ID-D using a wavelength of 1.013 Å. The diffraction images were obtained on Dectris Pilatus3-6M detector. Data collection and refinement statistics are shown in Table 3.1.

### 3.2.1.2 Obtaining anomalous diffraction from rubidium bound *PmHMGR* crystals

To map potential binding sites for an ammonium ion ( $\text{NH}_4^+$ ) in *PmHMGR*, we decided to introduce rubidium (Rb) into the crystal environment. The size of  $\text{NH}_4^+$  ions make them different to differentiate from  $\text{H}_2\text{O}$  molecules in a 2.0 - 2.5 Å crystal structure. Hence, by replacing them with  $\text{Rb}^+$  which has the same valency, we wanted to map out potential  $\text{NH}_4^+$  ion binding sites. To do so, we soaked in 0.6 M  $\text{RbSO}_4$ , 100 mM ADA and 30 % glycerol into a *PmHMGR* crystal of the size 0.4 x 0.4 x 0.2 µm for 3 hours. The crystal was then frozen and diffracted with a 15.22 / 15.35 keV beam that had been calibrated to observed be at the absorption edge of Rb. The diffraction data was obtained at the 23-ID-D beamline at the Advanced Photon Source, Argonne National Laboratory. In order to obtain this diffraction data, we used a Pilatus 6M detector keeping a beam to detector distance of 500 mm.

### 3.2.1.3 Crystallographic data analysis

The collected datasets were indexed, integrated, and scaled using HKL2000 with the programs Denzo and Scalepack<sup>[76]</sup>. The program Scalepack2MTZ was used to generate a reflection file in the CCP4 suite of programs<sup>[77, 78]</sup>. Phasing information for the structure was obtained using the phaserMR program on CCP4<sup>[79]</sup>. A high-resolution native structure (PDB ID: 4I64) was used as a search model for the structure. Structure and parameter files for the ligands were obtained using a small molecule library Phenix suite of programs<sup>[80-82]</sup>.

LigandFit from Phenix was used to fit new ligand molecules in the generated 2Fo-Fc density generated after the molecular replacement structure had been sufficiently refined<sup>[81, 83, 84]</sup>. In order to do the refinement, we used a rigid body refinement using the program *refmac5* in CCP4 followed by a simulated annealing (Cartesian) refinement using the *phenix.refine* function<sup>[78, 85]</sup>. The liganded structure was then subjected to several refinements using *phenix.refine* after using Molprobability to correct Ramachandran and rotamer outliers. Additionally, mismatches with electron density were also corrected using real-space correlation outliers in *phenix.refine*. These cycles of refinement were repeated until convergence of *R*work and *R*free values was observed<sup>[86, 87]</sup>. The program *composite\_omit\_map* in Phenix was used to generate omit maps for the ligands at the enzyme active site<sup>[88]</sup>. TLS refinement was used in the final iterations of the refinement process<sup>[77]</sup>.

To analyze anomalous diffraction in *PmHMGR* crystals soaked with RbSO<sub>4</sub>, ADA and glycerol buffer, a molecular replacement solution was first obtained from the diffraction data using apo-HMGR (PDB: 4I64) as a search model using the ccp4 program phaserMR<sup>[1, 79]</sup>. The program autosol was subsequently used to generate a single anomalous diffraction solution and identify Rb binding sites<sup>[89]</sup>.

#### 3.2.1.4 pH profile measurements in the crystallization buffer

To determine the effect of pH and crystallization constituents on *PmHMGR*, we measured the pH-rate profile of the enzyme. The pH-rate profile of *PmHMGR* was obtained by measuring the rate of hydride transfer in solution from pH 4-11. The hydride transfer steps take place during the formation of mevaldehyde from mevalonate and HMG-CoA from mevaldyl-CoA in the HMG-CoA reductase mechanism (Shown in Fig 3.1).

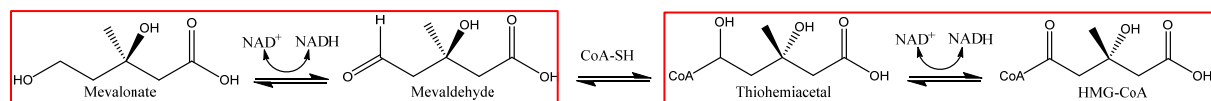


Figure 3.1 HMGR (*P. Mevalonii*) reaction mechanism with the hydride transfer steps marked in red

The enzymatic reaction was run using the substrate mevalonate (4 mM) and cofactors CoA (0.51 mM) and NAD (2 mM) in the crystallization buffer (1.2 M Ammonium Sulfate, 100 mM ADA and 32 % Glycerol) stepping through the pH range 4-11<sup>[19]</sup>. The ligands in this assay were kept at saturated concentrations referred to in previous assay measurements of mevalonate oxidation<sup>[90]</sup>. Individual reactions were set up in a 96-well plate with 5  $\mu$ L of 20 mg/mL purified *PmHMGR* added. A solution comprising of ligands, crystallization buffer and water was added to each well to obtain a total volume of 100  $\mu$ L. The dilution with water was adjusted to obtain 1.2 M Ammonium Sulfate, 100 mM ADA and 32 % Glycerol which is the concentration of constituents present in the crystallization buffer. The reaction was monitored using a BioTek Synergy H1 Hybrid Reader by plotting the increasing in absorbance of NADH after the reduction of NAD<sup>+</sup> with mevalonate. The formation of NADH can be observed from its unique absorbance at 340 nm due to the change in the electronic configuration of a reduced nicotinamide. These measurements were compared to the pH-rate profile measured in an enzymatic assay buffer made

up of 100 mM Tris, Potassium Phosphate and Glycine which are the assay conditions used in a pH-profile characterization study with *Pseudomonas mevalonii* HMG-CoA reductase<sup>[90]</sup>. The enzymatic assay buffer was designed to have a stable pH range from 5.8 - 10.6 with a combination of Potassium Phosphate (pH range 5.8 – 8.0), Tris (pH 7.0 – 9.0) and Glycine (pH 8.8 – 10.6) and is hence an effective buffer for obtaining a pH profile of the enzyme which can act as a standard for comparison. Seven replicate measurements and one control without the enzyme were obtained at each of the pH values that were tested in both the crystallization and enzymatic assay buffer conditions. An average of the seven replicates was used to determine the final turnover at each pH.

#### *3.2.1.5 Measuring the effect of ionic concentration on enzymatic activity in the crystallization buffer*

To measure the effect of the ions from the precipitant in the crystallization buffer on enzymatic activity, we measured the production of NADH by *PmHMGR* at different concentrations of ammonium sulfate ranging from 0.2 – 1.8 M. This range covers the concentration of ammonium sulfate used in the crystallization buffer (1.2 M). In all the measurements, the concentrations of the other crystallization buffer constituents, ADA and glycerol were kept at the same concentration of 100 mM and 32 % respectively. Seven replicate measurements and one control without the enzyme were obtained at each of the concentrations of ammonium sulfate that were tested. An average of the seven replicates was used to determine the final turnover at each ammonium sulfate concentration.

#### *3.2.1.6 Comparing the effect of the precipitant ions in the crystallization buffer*

The inhibitive effect of the crystallization salt ammonium sulfate was measured by adding 1.2 M ammonium sulfate to an enzymatic assay buffer comprising of 100 mM tris, potassium phosphate and glycine.

The inhibitive effects of  $\text{NH}_4^+$  ions on pH-dependent turnover were measured in 1.2 M ammonium chloride, 100 mM ADA and 32 % glycerol and 1.2 M ammonium acetate, 100 mM ADA and 32 % PEG-400 buffer. Additionally, the inhibitive effect of the presence of sulfate ions ( $\text{SO}_4^{2-}$ ) was measured in the presence of 1.2 M sodium sulfate, 100 mM ADA and 32 % glycerol and 1.2 M lithium sulfate, 100 mM ADA and 32 % glycerol. While the same concentration of salt could not be achieved, we also measured the pH-rate profile of the enzyme in the presence of 0.27



M potassium sulfate, 100 mM ADA and 32 % glycerol and 0.6 M rubidium sulfate, 100 mM ADA and 32 % glycerol. The effect of the absence of both the ions ( $\text{NH}_4^+$  and  $\text{SO}_4^{2-}$ ) was also tested by measuring the turnover of the enzyme in the presence of 1.2 M sodium chloride, 100 mM ADA and 32 % glycerol.

The concentration of produced NADH was calculated using the Beer-Lambert law where  $\text{conc}_{\text{NADH}} = \frac{\Delta A_{340}}{T_f - T_i}$ . Here,  $\Delta A_{340}$  is defined as the maximum change in absorbance observed when the enzyme is mixed with the substrates defined as the plateau value after a linear increase.  $T_i$  and  $T_f$  are defined as the initial and final time points respectively for the absorption measurement. Using the Beer-Lambert law,  $A_{340}_T = \epsilon_{\text{NADH}} l \text{conc}_T$  where  $A_{340}_T$  and  $\text{conc}_T$  are defined as the absorbance and concentration of NADH at time point T. Here,  $\epsilon_{\text{NADH}}$  is the extinction coefficient of NADH ( $6022 \text{ M}^{-1} \text{cm}^{-1}$ ) and  $l$  (0.3 cm) is the path length of the microplate reader well.  $\Delta A_{340} = A_{340}_{T_f} - A_{340}_{T_i}$  where  $A_{340}_{T_i}$  and  $A_{340}_{T_f}$  are the initial and maximum measured absorbance values observed over the period of first-order linear increase.

The turnover of the enzyme was then measured using the following equation:

$$\text{Turnover} = \frac{(\text{conc. NADH} \times \text{MW}_{\text{enzyme}})}{(\text{mg. of enzyme used} \times \text{Vol. of well} \times 10^{-3})}$$

The molecular weight of enzyme is 90,000 g/mol and the total volume of the reaction well in the 96-well plate is 100  $\mu\text{L}$ .

### 3.2.2 $K_m$ and $K_{\text{cat}}$ measurements in crystallization conditions

Purified HMGR for  $K_m$  measurements was obtained from Dr. C. Niclaus Steussy, who purified the enzyme using the published methods referred to in Section 3.2.1. To determine the  $K_m$  and  $K_{\text{cat}}$ , the specific activity in  $\mu\text{mol} / \text{min} / \text{mg}$  was measured at different concentrations for NAD, CoA and mevalonate. The concentration ranges used for each ligand were 0-0.25 mM, 0-2.0 mM and 0-2.0 mM for CoA, NAD and mevalonate respectively. For the  $K_m$  and  $K_{\text{cat}}$  measurements for each substrate, we kept the concentration of the other ligands at a constant saturated concentration of 0.51 mM, 2 mM and 4 mM for CoA, NAD and mevalonate respectively. The enzyme concentration was also kept to 5.6  $\mu\text{M}$  for all the measurements. The data was plotted and fit using a Michaelis Menten and Lineweaver-Burk plot using the Sigma Plot 14.0 software to calculate the  $K_m$  of each ligand.

### 3.2.3 pKa calculations of active site residues and ligands

To investigate the effect of the protonation states of the catalytic residues and ligands on the enzymatic reaction in the crystal environment, we calculated the pKa of each residue using the propka3.4.1 program developed by the Jensen Research Group<sup>[91, 92]</sup>.

The pKa values obtained for the catalytic residues Glu 83, Lys 267 and His 381 in the quaternary complex structure with mevalonate, CoA and NAD<sup>+</sup> were compared to the ones generated using propKa with the structure of the apoenzyme, the enzyme bound to mevalonate and NAD<sup>+</sup> (PDB ID: 1QAY) only and the structure with the enzyme bound to dithio-HMG-CoA and NAD<sup>+</sup> (PDB ID: 4I4B)<sup>[1, 19]</sup>.

## 3.3 Results

### 3.3.1 Structure obtained with mevalonate, CoA and NAD<sup>+</sup>

In comparison to other structural studies with mevaldehyde and CoA or dithio-HMG-CoA and NADH, where the formation of the thioester bond was observed, an examination of the active site of the structure obtained with mevalonate, CoA and NAD surprisingly indicated no biochemical interaction between ligands<sup>[1, 18]</sup>. *PmHMGR* crystallizes as an obligate homodimer. In the 2.0 Å structure (statistics in Table 3.1) obtained with mevalonate, CoA and NAD<sup>+</sup> obtained with *PmHMGR*, we observe only one site fully occupied and the other only bound to mevalonate due to blockage by crystal contacts<sup>[19]</sup>. What we observe at the active site in Fo-Fc Omit maps (Fig 3.2) is strong electron density for mevalonate, CoA and NAD showing what appears to be the pre-turnover state from mevalonate to HMG-CoA.

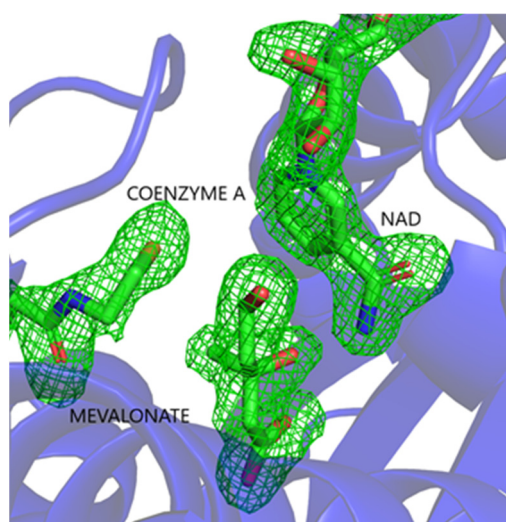


Figure 3.2 Active site region with  $3\sigma$  Fo-Fc omit map density from a 2.0 Å X-ray structure obtained from *PmHMGR* crystals soaked with mevalonate, CoA and  $\text{NAD}^+$ .

Table 3.1 Crystallographic refinement statistics for the HMGR structure soaked with mevalonate, NAD<sup>+</sup> and CoA. Highest resolution statistics in parentheses.

	Mevalonate, CoA and NAD <sup>+</sup>
Space group	I4(1)32
Unit cell dimensions	
a, b, c (Å)	226.04
$\alpha = \beta = \gamma$ (deg)	90
resolution (Å)	46.1 – 2.0 Å
no. of unique reflections	66,670
Rmerge (%)	2.9 (19.8)
Mean I/ $\sigma$ I	16.4 (0.8)
Completeness (%)	100.0 (99.9)
Data redundancy	16.3
	Refinement
Rwork (%)	18.1
Rfree (%)	22.5
r.m.s.d bond lengths (Å)	0.016
r.m.s.d bond angles (deg)	1.81
No. of protein residues	795
No. of water molecules	390
Average B. factor, protein (Å <sup>2</sup> )	32.3
Average B factor, ligand (Å <sup>2</sup> )	35.5
Average B factor, water (Å <sup>2</sup> )	37.1
Residues in Ramachandran plot regions (%)	
Most favored	96.23
Additional allowed	3.77
Outliers	0.00

### 3.3.2 pH-rate profile measurements in crystallization conditions

The study of the mevalonate, CoA and NAD reaction complex is essential to understanding the conversion of mevalonate into the first reaction intermediate mevaldehyde. The lack of activity that was observed in the mevalonate, CoA and NAD<sup>+</sup> bound crystal structure prompted us to determine the effect of the crystallization environment on the enzyme's activity in this catalytic direction. Understanding the factors resulting in the reduced activity could be utilized in developing approaches to overcome inhibition in *PmHMGR* crystals. In addition to the crystallization components, we also wanted to understand the effect of the crystallization pH (pH 6.7) on the activity observed in the crystallization environment. Upon measuring the rate of NADH production in the crystallization buffer in comparison to the enzymatic assay buffer, we find that at crystallization pH the turnover of the enzyme is observed to decrease by 92.7 % from  $270.99 \pm 20.88 \text{ min}^{-1}$  in the enzymatic assay buffer to  $19.8 \pm 3.3 \text{ min}^{-1}$  in the crystallization buffer (Fig 3.3).

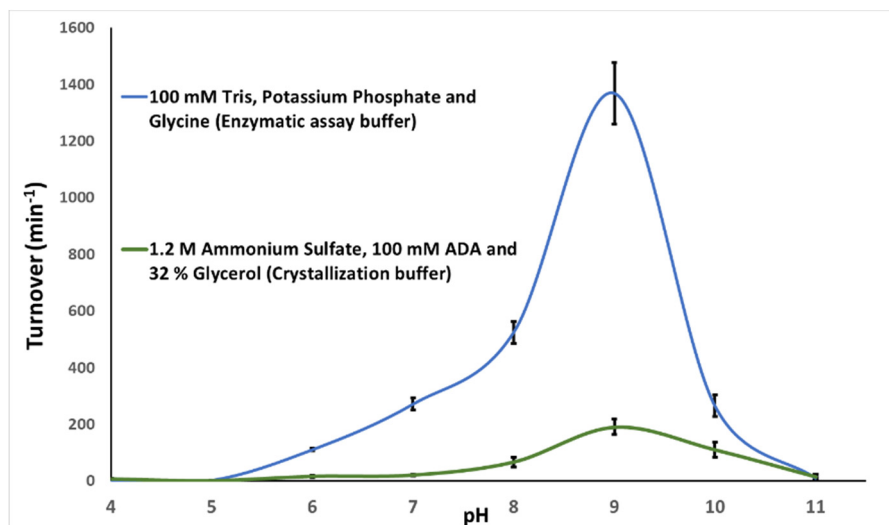


Figure 3.3 pH profile of *PmHMGR* in the crystallization buffer (green) in comparison with the enzymatic assay buffer (blue)

The pH-rate profile also indicates that the maximum turnover of the enzyme is observed to decrease by 86.1 % in the crystallization buffer in comparison to the enzymatic assay buffer while maximum turnover is observed at pH 9 in both environments (Fig 3.3). Around pH 11, we see a sharp fall and disappearance of enzyme activity. These turnover measurements further indicate that the crystallization environment drastically reduces enzyme activity and showcases pH-dependent effects on enzyme turnover.

### 3.3.3 Determining changes in the enzyme kinetic parameters in the crystallization environment

The effect of the crystallization environment on *Pm*HMGR enzyme kinetics was further characterized by measuring the  $K_m$  and  $K_{cat}$  values for each of the ligands involved in mevalonate oxidation (CoA, NAD and mevalonate) in the crystallization buffer. The measured values are shown in Table 3.2. These values show a drastic reduction in  $K_{cat}/K_m$  in comparison to the ones obtained at assay conditions optimized for mevalonate oxidation with 0.1 M Tris, 0.1 M KCl buffer at pH 9 in previously published studies<sup>[1]</sup>.

Table 3.2  $K_m$  and  $K_{cat}$  measurements for CoA, NAD and Mevalonate in the crystallization buffer (1.2 M ammonium sulfate, 100 mM ADA and 32 % glycerol, pH 7.0) and optimized enzymatic assay buffer (0.1 M KCl, 0.1 M Tris, pH 9.0) where activity is derived from  $V_{max}$  measurements at saturated substrate concentrations<sup>[1]</sup>.

	CoA (mM)	NAD (mM)	Mevalonate (mM)
$K_m$ (crys buffer)	$0.03 \pm 0.004$	$0.05 \pm 0.01$	$0.03 \pm 0.01$
$K_{cat}$ (crys buffer)	$20.95 \pm 0.85$	$13.36 \pm 0.48$	$20.50 \pm 0.75$
$K_{cat} / K_m$ (crys buffer)	$775.93 \pm 119.21$	$272.61 \pm 61.99$	$732.21 \pm 159.16$
$K_m$ (assay buffer)	$0.09 \pm 0.02$	$0.24 \pm 0.00$	$0.12 \pm 0.02$
$K_{cat} / K_m$ (assay buffer)	38000	14250	28500
Ratio $K_{cat} / K_m$ for Assay / Crys	49:1	52:1	40:1

The Michaelis-Menten and Lineweaver-Burk plots obtained from different concentrations of mevalonate, CoA and  $NAD^+$  are shown in Fig 3.4.

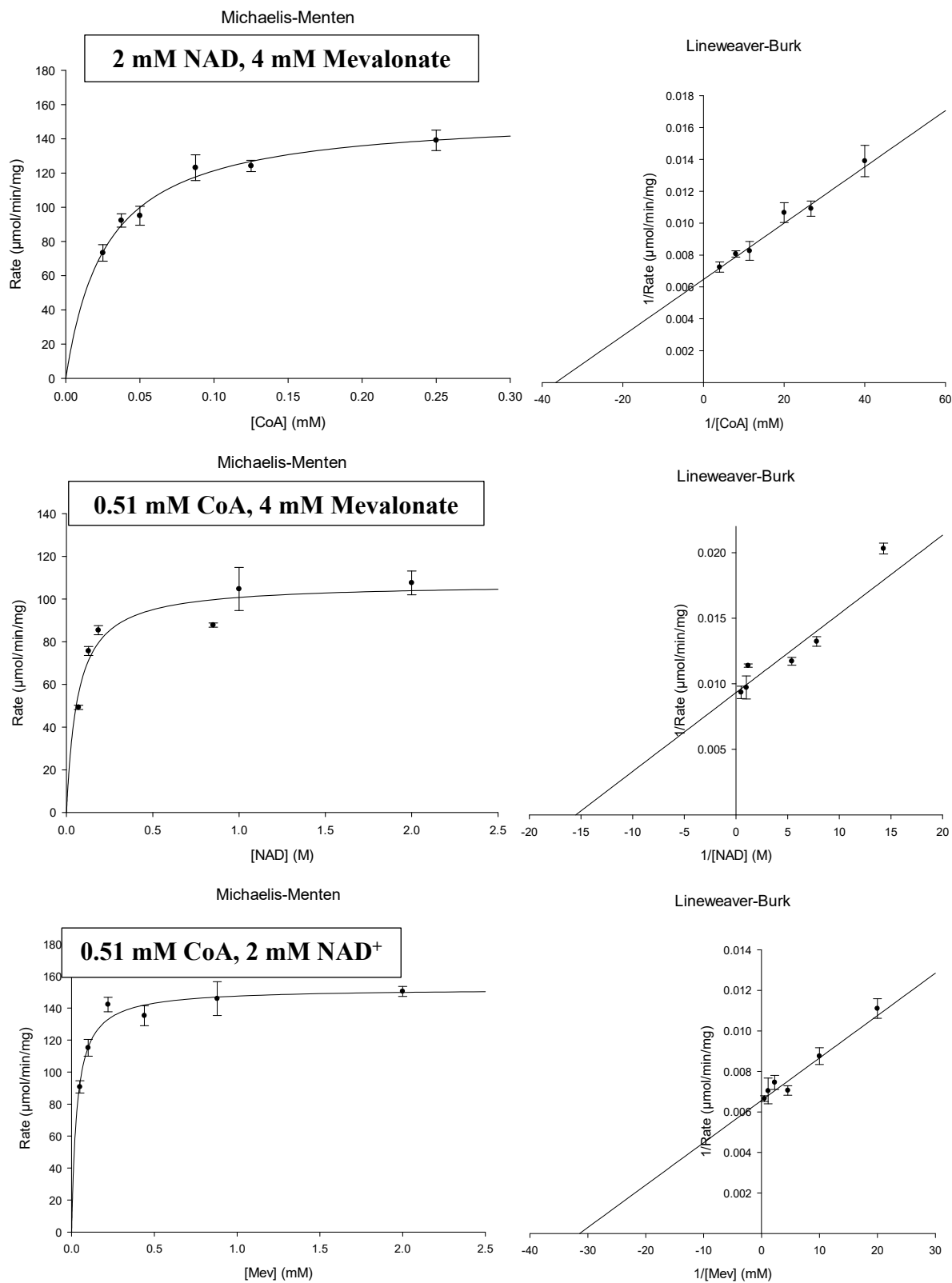


Figure 3.4 Michaelis Menten and Lineweaver-Burk plots for NAD and Mevalonate in the presence of CoA used to determine  $K_m$  in the Crystallization buffer (pH 7)

### 3.3.4 Effect of precipitant ions in the *Pm*HMGR crystallization environment

The lack of activity that was observed in the mevalonate, CoA and NAD bound crystal structure and pH-rate profile in the crystallization environment alluded to the possibility of ligand interactions being affected by a high ionic concentration. This has been observed in other crystal environments with a large concentration of ammonium sulfate as in the case of ribonucleases where the inhibition was found to be due to the binding of  $\text{SO}_4^{2-}$  ions<sup>[71-75]</sup>. It prompted us to determine the effect of the ionic concentration in the crystallization environment on the enzyme activity in this catalytic direction.

The effect of the ions in the crystallization environment was tested on *Pm*HMGR by measuring its activity at different concentrations of ammonium sulfate ranging from 0.02 – 1.8 M keeping the pH and other crystallization buffer constituents ADA and glycerol constant (pH 6.7). A decline in enzymatic activity was clearly observed with increasing ammonium sulfate concentration from 0.2 – 1.8 M with the activity decreasing by ~97 % going from the lowest concentration to the highest concentration (Fig 3.5). This steady decline in activity indicates an inhibition that is dependent on the large concentration of ions in the crystallization environment.

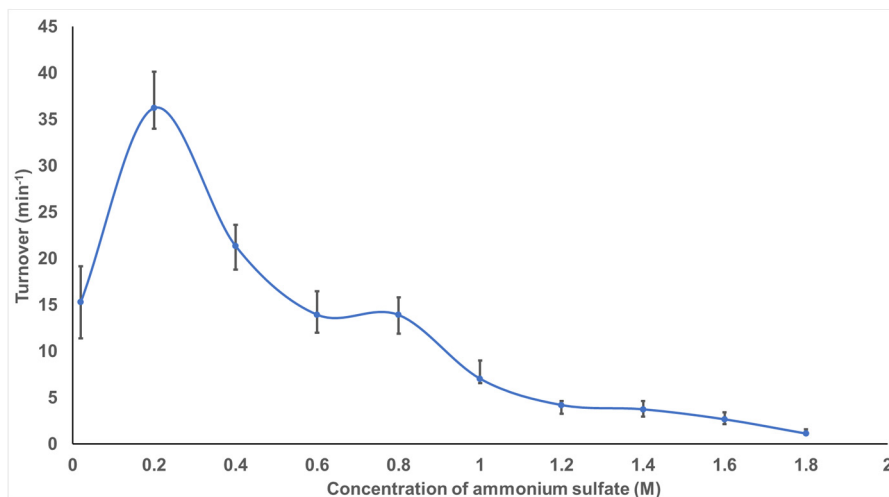


Figure 3.5 Turnover in *Pm*HMGR at different ammonium sulfate concentrations ranging from 0.2 – 1.8 M.



### 3.3.5 Investigation of the effects of ions on *Pm*HMGR turnover

Our insight into the effect of ionic concentration on *Pm*HMGR turnover in the crystal environment also led us investigate the effect of the specific individual ions  $\text{NH}_4^+$  and  $\text{SO}_4^{2-}$  in the crystallization buffer. To understand the effect of the  $\text{NH}_4^+$  ion in the crystallization salt, we measured the pH-rate profile with a set of alternate non-sulfate ammonium salts in the presence of other crystallization buffer constituents, ADA and glycerol. The observed pH profile with 1.2 M ammonium chloride, 100 mM ADA and 32 % Glycerol also indicated a significant inhibition in comparison to the enzymatic assay buffer between pH 7-11. The reduction of maximum turnover in the presence of ammonium chloride ( $\sim 79.8\%$ ) was found to be comparable to that observed in ammonium sulfate ( $\sim 86.1\%$ ). Inhibition of the enzyme was also observed in a 1.2 M ammonium acetate, 100 mM ADA and 32 % PEG-400 environment (Shown in Fig 3.6.) which is an alternate crystallization environment found to prevent lysis of the thioester bond in both human and bacterial HMG-CoA soaked crystals (PDB ID: 1DQ8, PDB ID: 1R31), the reasons for which are unclear<sup>[1]</sup>. The enzyme was found to have a higher degree of inhibition across the entire pH range in this ammonium environment with a  $\sim 97.2\%$  reduction in maximum turnover. Our measurements indicated that a significant degree of inhibition in *Pm*HMGR can be observed in the absence of sulfate salts and in the presence of various ammonium salts. The measured pH-rate profiles with different ammonium salts showed some variation in turnover depending on the anioinic counterion present in the salt.

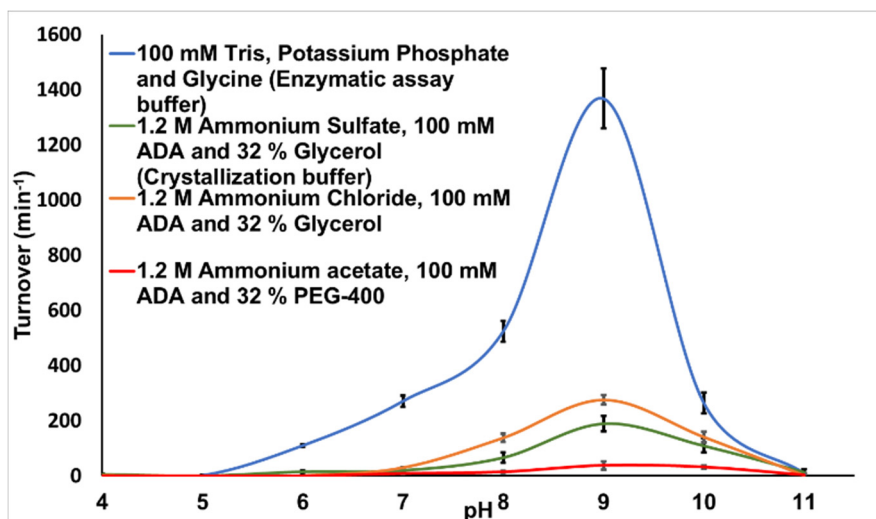


Figure 3.6 pH-rate profile of *Pm*HMGR in ammonium chloride, ADA and glycerol (Orange), ammonium acetate, ADA and glycerol in comparison to the crystallization buffer (green) and enzymatic assay buffer (blue).

### 3.3.6 Turnover in *Pm*HMGR in the absence of ammonium

The inhibitory effect of the counter ion in the crystallization buffer salt,  $\text{SO}_4^{2-}$  was then tested by measuring the pH-rate profile of *Pm*HMGR with lithium sulfate and sodium sulfate in comparison to the crystal precipitant salt ammonium sulfate. Both the buffers had the same concentration of salt, ADA and glycerol as the crystallization buffer. A significant reduction in turnover was observed in both the pH-rate profiles across pH 4-11. The percent of inhibition at the pH of maximum turnover (lithium sulfate – 89 %, sodium sulfate – 92.04 %) was equivalent to that measured in the presence of ammonium salts. This indicated that the reduced activity in the crystal environment could be due to the presence of both ammonium and sulfate ions (Fig 3.7), each of which could have a separate effect on the enzyme.

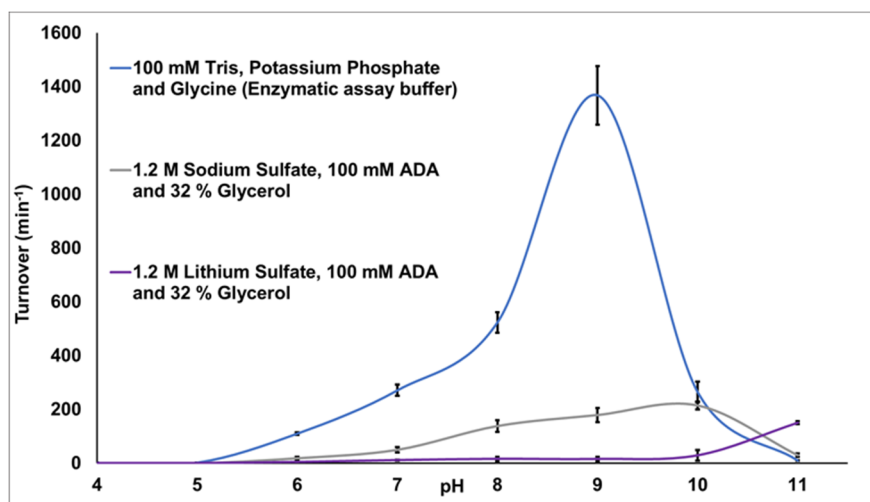


Figure 3.7 pH-rate profile of *Pm*HMGR in the presence of tris, potassium phosphate and glycine buffer (enzymatic assay buffer; blue), sodium sulfate, ADA and glycerol buffer (grey) and lithium Sulfate, ADA and glycerol buffer (purple).

Alternatively, these results also suggested that the observed inhibition could be independent of ionic composition and entirely dependent on ionic concentration. The effect of ionic concentration was also evident in the pH-rate profile of the enzyme in the presence of 0.6 M rubidium sulfate and 0.27 M potassium sulfate. Since the highest salt concentration in the buffer could only be 0.6 M and 0.27 M with rubidium sulfate and potassium sulfate respectively, in contrast to the ammonium salts, the degree of inhibition was significantly reduced across pH 4-12 (Fig. 3.8).

A peculiar increase in turnover is observed at pH 11 in the potassium and rubidium sulfate buffers in comparison to the enzymatic assay and crystallization buffer where no activity is observed. This rise in activity is observed outside the characterized pH-range for enzymatic activity (Fig 3.8).

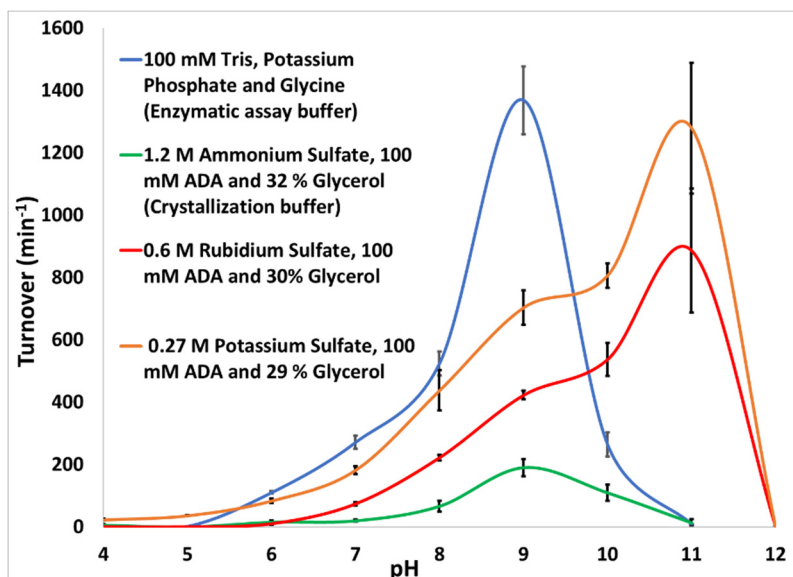


Figure 3.8 pH-rate profile of *PmHMGR* in a potassium sulfate, ADA and glycerol (orange) and rubidium sulfate, ADA and glycerol buffers (red) in comparison to the enzymatic assay buffer (blue) and crystallization buffer (green).

### 3.3.7 Turnover at a high ionic concentration in the absence of the crystallization salt

To test the effect of a high ionic concentration in the absence of the crystallization salt ions  $\text{NH}_4^+$  and  $\text{SO}_4^{2-}$ , we measured the turnover of *PmHMGR* at pH 7 and pH 9 in the presence of 1.2 M sodium chloride. A degree of inhibition of the same order of magnitude as the crystallization buffer is observed in the sodium chloride environment indicating that the reduction in activity in the crystallization environment is independent of ionic composition (Table 3.3).

Table 3.3 Turnover of *Pm*HMGR at pH 7 and pH 9 in various buffers testing the inhibitive effect in the presence of sodium chloride in comparison to the enzymatic assay conditions in contrast to the inhibition observed in the crystallization buffer. Degree of inhibition in the presence of ammonium sulfate and sodium chloride also included with turnover values.

Buffer conditions (pH 7)	Turnover pH 7 (min <sup>-1</sup> )	Turnover pH 9 (min <sup>-1</sup> )
100 mM Tris, 100 mM Potassium Phosphate, 100 mM Glycine (Enzymatic assay buffer)	271.0 ± 20.9	1368.0 ± 108.9
1.2 Ammonium Sulfate, 100 mM ADA and 32 % Glycerol (Crystallization buffer)	19.8 ± 3.3 (0.93)	190.1 ± 27.4 (0.86)
1.2 M Sodium Chloride, 100 mM ADA and 32 % glycerol	36.9 ± 9.6 (0.86)	124.4 ± 14.3 (0.90)

### 3.3.8 Effect of ammonium sulfate outside the crystallization buffer

To test the effect of ammonium sulfate outside the crystallization buffer, we also measured the pH-activity profile of *Pm*HMGR in the enzymatic assay buffer with 1.2 M ammonium sulfate. The addition of ammonium sulfate in enzymatic assay buffer does reduce enzyme activity from pH 4-9 however the degree of inhibition is smaller in comparison to that observed in the crystallization buffer (Fig 17.). The maximum turnover in the pH-rate profile in the enzymatic assay buffer at pH 9 is shown to decrease by 73.4 % with the addition of (NH<sub>4</sub>)<sub>2</sub>SO<sub>4</sub> to an enzymatic assay environment. This percent of inhibition is very close to that observed at pH 9 in the crystallization buffer (86.1 %) indicating that inhibitory effect of (NH<sub>4</sub>)<sub>2</sub>SO<sub>4</sub> is present between pH 4-9 even outside the crystallization environment indicating that it plays a key role in the reduction of turnover in the crystal environment. In contrast to the pH-rate profiles measured with other ammonium salts maximum turnover is observed at pH 11 in the presence of ammonium sulfate in the enzymatic assay buffer environment (Fig 3.9).

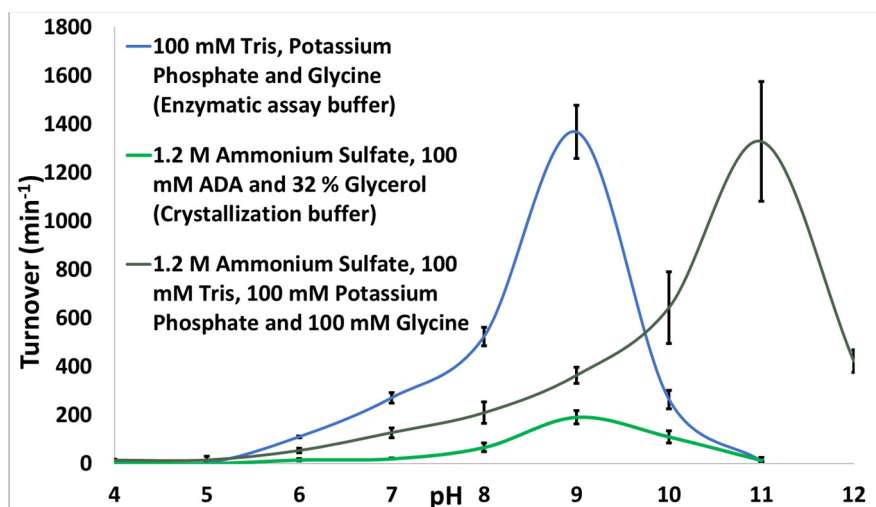


Figure 3.9 pH-activity profile of *PmHMGR* in enzymatic assay buffer (blue) in contrast with the activity observed in the enzymatic assay buffer with 1.2 M ammonium sulfate.

### 3.3.9 Calculated pKa values of catalytic residues in the crystal structure

To computationally predict the effect of the crystallization pH and environment on the pKa of the enzyme ligands and catalytic residues, we calculated the pKa values from the apo enzyme and various ligand-bound crystal structures of *PmHMGR*. The values obtained for the pKa values with the quaternary complex structure with mevalonate, CoA and NAD are shown in table 3.4. The values calculated from the crystal structure of the apoenzyme, structure with mevalonate and NAD<sup>+</sup> and structure with dithio-HMG-CoA and NAD<sup>+</sup> have also been included for comparison.

Table 3.4 pKa values obtained for catalytic residues and substrates with different ligand combinations.

Structure ( <i>PmHMGR</i> )	Glu 83	Lys 267	His 381
Apo	4.44	11.88	-
Mevalonate, NAD <sup>+</sup>	0.07	10.59	3.92
Mevalonate, CoA, NAD <sup>+</sup>	1.11	11.27	7.45
Dithio-HMG-CoA, NAD <sup>+</sup>	3.58	13.16	5.21

In the presence of mevalonate and  $\text{NAD}^+$ , the pKa value of Glu 83 is observed to drop drastically from 4.44 to 0.07. When CoA is added to the model, the pKa value is found to increase (1.11) but is still significantly lower than the pKa value obtained for the apoenzyme. The value for pKa in Glu 83 is found to be closest to the apo-enzyme in the structure with dithio-HMG-CoA (3.58) which shows a trapped post-hydride transfer conformation after HMG-CoA is converted into mevaldyl-CoA.

The pKa value of Lys 267 is also found to fluctuate with and without the presence of CoA. The pKa is shown to increase with the addition of CoA in *PmHMGR* also bound to mevalonate and  $\text{NAD}^+$  from 10.59 to 11.27 which is close to that obtained with the apoenzyme. The pKa is observed to increase even post-hydride transfer from 11.27 to 13.16 in the presence of a dithiohemiacetal in the presence of a deprotonated Glu 83.

In the presence of CoA, the pKa of His 381 is observed to increase from 3.92 to 7.45. It is observed to decrease again in the post-hydride transfer state to 5.21. The pKa of His 381 in the mevalonate, CoA and  $\text{NAD}^+$  bound complex determines the concentration of deprotonated His 381 in this quaternary complex. Using the Henderson-Hasselbach equation the concentration of deprotonated His381 can be calculated as 18% that of protonated His 381. With a rise in pH, we can expect the concentration of deprotonated His 381 to increase to 93 %.

### **3.3.10 Utilization of $\text{Rb}_2\text{SO}_4$ to identify $\text{NH}_4^+$ binding sites in *PmHMGR*:**

To determine potential  $\text{NH}_4^+$  binding sites in the *PmHMGR* crystal to obtain insight into how ionic interactions inhibit the enzymatic reaction, we soaked the *PmHMGR* crystals in  $\text{Rb}_2\text{SO}_4$ , ADA and glycerol solution and obtained an anomalous diffraction dataset. The anomalous dataset shows one potential binding site in the  $\text{NAD}^+$  phosphate region (Fig 3.10). However, it is not in proximity to the region where  $\text{NAD}^+$  is interacting with the enzyme. Since we observe cofactor density in ligand-soaked structures, we know that the  $\text{NH}_4^+$  ion cannot prevent ligand binding. Hence, the presence of the Rb density in the  $\text{NAD}^+$  binding region could be just a result of it being solvent exposed since that is a predominant area for binding in Rb-soaking experiments<sup>[93]</sup>.

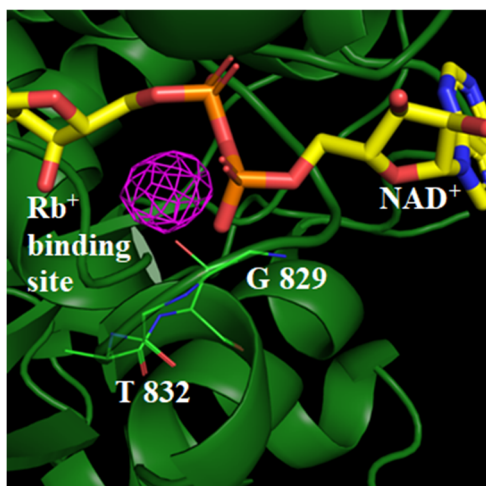


Figure 3.10 Anomalous Rb density from *PmHMGR* structures soaked in  $\text{Rb}_2\text{SO}_4$ , ADA and glycerol buffer

### 3.4 Discussion

#### 3.4.1 Inhibition of mevalonate oxidation in the *PmHMGR* crystallization environment

The turnover of *PmHMGR* has been observed in the crystal environment in the presence of dithio-HMG-CoA and NADH where the dithioester bond is shown to reorient the CoA and HMG portions of the product from a flat to a pyramidal geometry indicating a change from an  $\text{sp}^2$  orbital present in dithioHMG-CoA to an  $\text{sp}^3$  orbital present in dithiohemiacetal. This change in configuration is an indicator of reduction upon hydride transfer from NADH to dithio-HMG-CoA in order to form a dithiohemiacetal<sup>[1]</sup>. With the reconfiguration of the thioester bond, the distance between HMG-CoA (C1) and  $\text{NAD}^+$  (C4) is shown to decrease from 4.0 Å to 3.2 Å. The  $\text{sp}^3$  orbital of the dithioester bond is also shown to be oriented parallel to an oxidized  $\text{NAD}^+$  (Fig 3.11 B) in the dithio-HMG-CoA and NADH soaked structure in comparison to an HMG-CoA bound structure where the thioester bond is rotated up towards  $\text{NAD}^+$  (Fig 3.11 A). This rearrangement of the ligands at the active site indicates reaction initiation with the slow substrate dithio-HMG-CoA and NADH with the reaction progressing towards the formation of the thiohemiacetal intermediate within the *PmHMGR* crystalline environment.

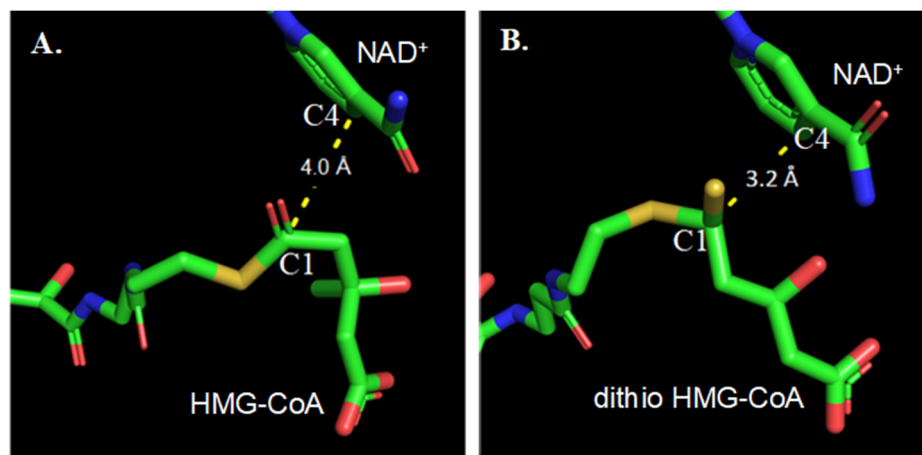


Figure 3.11 A. Distance between HMG-CoA (C1) and NAD<sup>+</sup>(C4) B. Distance between dithio HMG-CoA (C1) and NAD<sup>+</sup>(C4)

Similarly structural studies by Duncan et. al have shown that a complex of mevaldehyde and CoA only with the enzyme results in the formation of a thioester bond, indicating that a reaction between the first proposed intermediate and CoA is feasible in the crystallization environment<sup>[2]</sup>. However, the quaternary complex structure comprising of mevalonate, CoA and NAD<sup>+</sup> shows no sign of any reaction, with no observable density formed between the two substrates, even with the appropriate cofactor for activity. With no signs of thioester bond formation with the substrate mevalonate, we must conclude that the crystal environment inhibits the hydride transfer and oxidation of mevalonate to mevaldehyde.

### 3.4.2 Turnover in the crystallization environment is dependent on ionic concentration

We investigated the effect of the crystallization constituents and pH on the enzyme's turnover and identified that the *Pm*HMGR turnover is significantly inhibited due to a high concentration of ammonium sulfate in the crystallization buffer. We also identified that this inhibition is not dependent on the ionic composition of the precipitant salt. In addition to investigating the salt-induced inhibition, we also captured various pH-dependent variations in the turnover of the enzyme under different ionic environments. We identified an increase in activity with pH within a pH-range under different ionic environments with the maximum turnover being observed between pH 9-11. In contrast, the turnover at the crystallization (pH 6.7) environment



with these salts was significantly lowered. In the presence of some salts (ammonium acetate and lithium sulfate), the enzyme appeared to be inactive at crystallization pH.

The pH-dependent properties of *PmHMGR* have previously been documented in pH-rate profile measurements in optimized conditions. The optimum activity was observed at pH 9 which was shown to be an effect of CoA-SH that has a known pKa of 9.6 for the thiol atom. At high alkaline pH, we expect to have a significant deprotonation of the SH group in CoA-SH which has shown to inhibit mevalonate oxidation, thereby resulting in reduced activity at higher pH<sup>[90]</sup>.

Similar pH-dependent properties were also observed in the presence of the crystallization buffer where the optimal activity was again observed around pH 9. In the case of the crystallization buffer, the calculated pKa values for the catalytic residues provided additional insight about pH-dependent effects on various reaction steps. Our propKa calculations predict that the pKa of HIS 381 (7.45) would result in a higher concentration of the deprotonated residue (from 18 to 93 %) with an increase in pH (Table 3.4). Since deprotonated HIS 381 facilitates the deprotonation of CoA-SH, the increase in pH would result in further CoA-S<sup>−</sup> formation and therefore, the formation of a thioester bond between mevaldehyde and CoA. This change in the protonation state of HIS 381 with pH would explain the increase in turnover rate with pH. The pKa of Lys 267 is also predicted to be 11.27 the deprotonation of which would result in reduced turnover due to the lack of formation of electrostatic interactions that would facilitate mevalonate oxidation (Table 3.4). Based on this predicted value the concentration of deprotonated Lys 267 is expected to increase from 5.4 to 54 % which could partly explain the steady drop in activity with increasing pH in the crystallization buffer.

While the degree of inhibition observed in the crystallization environment appears to be largely dependent on salt concentration in the crystallization environment, our testing of different ammonium and sulfate salts to separate their independent effects on enzyme turnover indicate pH-dependent characteristics that are particular to each counterion. In the presence of other crystallization buffer constituents, ADA and glycerol, all the ammonium salts tested show optimal activity at pH 9. However, in the case of all the tested sulfate salts, we observe optimal activity at pH 10 and 11. In the case of ammonium sulfate, we find that it shows optimal activity at pH 9 and pH 11 depending on the other constituents present. Hence, it is possible that both ammonium and sulfate ions from the crystal precipitant salt have an underlying effect that influences pH-dependent properties of the enzyme but not the degree of inhibition.

In the case of ammonium ions in the crystal, it is possible that in the inhibitive effects of an ammonium ion interaction with the enzyme are reduced because of ammonium ion deprotonation at high pH. Since  $\text{NH}_4^+$  has a pKa value of 9.25 (Eq 1), we expect to observe a deprotonation and formation of  $\text{NH}_3$  at higher pH resulting in reduced interaction with these ions (Eq 1).



Therefore, this could be an additional underlying factor resulting in optimal activity at pH 9 in all the ammonium salts tested. Identifying specific ammonium interaction sites would be beneficial in understanding the *Pm*HMGR interactions that get affected in the presence of a high concentration of ammonium ion. While no key interaction sites could be mapped using isopropyl ammonium or rubidium salt binding, other salts with the same cationic properties could also be tried.

An increased pKa for the catalytic residues HIS 381 and LYS 267 in various sulfate salt environments could shift the optimal activity to a higher pH. Further experiments would be needed to determine any specific effect of these salts on the pKa of *Pm*HMGR residues. Like in the case of ribonucleases, structural studies of the quaternary complex of *Pm*HMGR have also identified various sulfate binding sites. We've also observed the binding of  $\text{SO}_4^{2-}$  ions replacing phosphates in the ligand binding site in the apo enzyme (PDB ID: 4164) (Fig 3.12). While the binding of these ions should not prevent the oxidation of mevalonate completely, as is observed in the crystal structure, they could reduce the turnover observed in the crystal environment by reducing ligand binding (Fig 3.2).

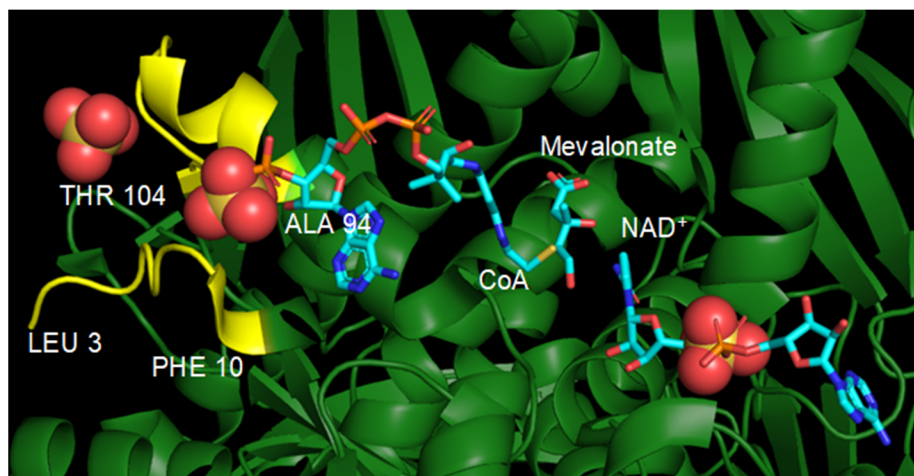


Figure 3.12 Sulfate binding sites in Apo HMGR. SO<sub>4</sub> binding site in the large domain marked in red. PmHMGR ligands (teal) are super imposed from quaternary ligand-bound structure.

From calculating the pK<sub>a</sub> values of the residues in the enzyme, we find that the residues Glu 83 and Lys 267 that are associated with the hydride transfer step are found to have pK<sub>a</sub> values that would lend them to exist in their anionic and cationic states respectively at pH 6.7 in the crystallization buffer. The strong reduction in the pK<sub>a</sub> for Glu 83 that is observed in the presence of mevalonate, CoA and NAD in comparison to the apo enzyme and the structure with dithio-HMG-CoA and NAD indicate that the enzyme is present in a pre-hydride transfer state in the crystal structure of the quaternary complex. The shift in the pK<sub>a</sub> of Glu 83 from the mevalonate-NAD<sup>+</sup> bound structure (0.07) to the DithioHMG-CoA and NAD<sup>+</sup> bound structure is expected since in the former the sidechain is situated to enable a proton transfer from mevalonate to Glu 83. ONIOM and QM/MM calculations by Quinn et. al have also demonstrated that a neutral glutamate is more favorable for the reduction of HMG-CoA which would make its anionic properties in the crystal environment more favorable to convert a thiohemiacetal intermediate into HMG-CoA<sup>[94]</sup>.

### 3.4.3 Utilizing kinetic characteristics in the crystallization environment to develop a reaction triggering method

Our understanding of concentration dependent inhibition from various salts in the crystal environment and its variation with pH could be utilized to trigger the *Pm*HMGR enzymatic reaction. Based on the pH-rate profiles that we have recorded, the measurements made in an

Ammonium Acetate, ADA and PEG-400 environment have seemed suitable to initiate reaction turnover at a rate that would be amenable to observing different stages of the reaction within the crystal using flash-freezing techniques. The utilization of a flash-freezing method offers a simple and modest approach to the design of a time-resolved experiment since it does not rely on any external apparatus or data collection techniques to obtain post-turnover diffraction datasets from the protein crystals.

The utilization of the pH-rate profiles in an Ammonium Acetate, ADA and PEG-400 for the triggering of mevalonate oxidation in *PmHMGR* can be conceptualized as a pH-jump experiment where the enzyme is kept inactive at crystallization pH and subsequently transferred to a higher pH environment to initiate activity. Evidence for the lack of activity at the crystallization pH can be determined based on the recorded pH-rate profiles in an ammonium acetate, ADA and PEG-400 buffer where negligible turnover is observed between pH 6 and 7 which is not expected to translate into significant product formation in the crystal environment. With this expectation, the ligands mevalonate, CoA and NAD<sup>+</sup> at pH 6.7 can be introduced in a *PmHMGR* crystal that has been modified by exchanging its crystallization constituents with ammonium acetate, ADA and PEG-400 (pH-jump buffer constituents). This would ensure that we have obtained a ligand-bound enzyme that would represent an inactive enzyme conformation in the crystal environment. The subsequent transfer of these crystals to a higher pH would then trigger the enzymatic reaction. The utilization of this method would be beneficial in time-resolved approaches that can be used to obtain information about transitory states in the enzymatic reaction pathway.

## CHAPTER 4. DEVELOPMENT OF A PH-JUMP METHOD TO TRIGGER THE *PmHMGR* REACTION IN CRYSTALS

### 4.1 Introduction

The use of time-resolved methodologies to study any system requires the use of a triggering method to obtain temporal control over the biological process that is being investigated. Photoactivatable enzymes have the advantage of being triggered through light and thus have a method for reaction initiation that is accessible without any modifications to the biological system. To initiate non-photoactivatable biological processes several other methods have been developed such as the use of caged-ligands, mixing and diffusion of ligands or oxidizing / reducing agents, pH-jumps, temperature jumps and the application of external electric fields (Detailed in Chapter 2 - 2.5.1, 2.5.2). HMG-CoA reductase, being a non-photoactivatable enzyme also requires the use of a novel approach to trigger its enzymatic activity. Previous attempts of utilizing caged-NAD<sup>+</sup> cofactors to trigger mevalonate oxidation in *PmHMGR* crystals have also been documented (Detailed in Chapter 2 – 2.5.3).

We have also considered the possibility of using direct diffusion to introduce the ligands into a *PmHMGR* crystal. However, our methods for soaking ligands into the *PmHMGR* crystals established by Tim Schmidt indicate that rapid introduction of all ligands necessary for the full enzymatic reaction at high concentrations (> 5 mM) can be destructive and result in rapid cracking and dissolution. To obtain substrate and cofactor bound enzyme structures after soaking crystals at lower concentrations, requires a long soaking time of several hours. Therefore, having substrate-soaked enzyme crystals before reaction initiation would be more suitable for rapid time-resolved data collection.

pH-dependent kinetic properties of *PmHMGR* have been previously documented in optimized pH-rate profile conditions in the presence of mevalonate, CoA and NAD<sup>+</sup>. These studies showed an increase in turnover between pH 4 – 9<sup>[90]</sup>. By characterizing the pH-dependent effects in the crystallization environment (Documented in Chapter 3 – 3.3.2), we have also identified that these pH-dependent changes in turnover of mevalonate are preserved. What is affected however is the rate of turnover due to a significant inhibition from a high concentration of precipitant salt, ammonium sulfate. Like the inhibition is observed in the presence of other salts, the pH-dependent properties remain similar as well. In the presence of other ammonium salts (ammonium acetate

and ammonium chloride), we also observe an increase in turnover between pH 4 – 9 and maximum activity at pH 9. In the presence of sodium sulfate and lithium sulfate, we see a similar trend of increasing activity with pH but the optimal pH for activity at pH 10 and 11 respectively.

As had been previously identified in studies by Dr. Chandra Duncan, our pH-rate profile measurements of *Pm*HMGR in an ammonium acetate, ADA and PEG-400 buffer also indicated the lack of turnover at crystallization pH (6.7). The observance of this pH-rate profile indicated that if one were to introduce the substrates and cofactor to *Pm*HMGR crystals at crystallization pH after exchanging their environment with an ammonium acetate, ADA, PEG-400 buffer and then subsequently introduce them to a pH 9 environment, it could trigger the enzymatic reaction in the crystal.

Based on the enzymatic reaction in HMG-CoA reductase and its proposed mechanism, NADH is produced in the two hydride transfer steps that produced mevaldehyde and HMG-CoA respectively (Fig 4.1). Given that the timeline of the reaction progression in crystals was unknown, observing the production of NADH via its unique spectroscopic signature at 340 nm could be the simplest way to detect the onset of turnover and validate the pH-jump method.

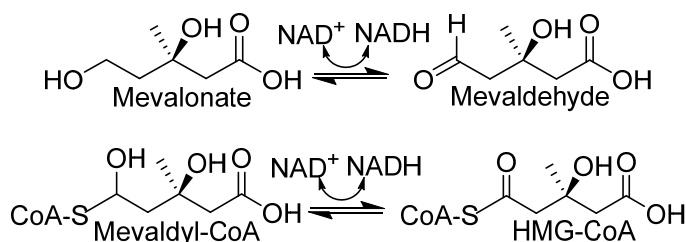


Figure 4.1 Enzymatic reaction steps indicating a hydride transfer in the HMG-CoA reductase reaction

## 4.2 Materials and Methods

### 4.2.1 Protein purification and crystallization

HMG-CoA reductase was purified and crystallized using a previously described method described in section 3.2.1.1<sup>[16, 95]</sup>. Crystals of the size range 0.05 x 0.05 x 0.025 mm to 0.5 x 0.5 x 0.25 mm were obtained within 2-3 weeks in a 1.2 M ammonium sulfate and 100 mM ADA environment. To establish the optimum conditions for obtaining absorption data, two different thicknesses of crystal samples were tested. A control sample of 0.25 x 0.25 x 0.1 mm was used to

obtain the absorbance of a ligand-bound crystal at pH 6.7. Several crystals of the size 0.1 x 0.1 x 0.05 mm were picked because they had the ideal sample thickness for obtaining a UV-Vis absorbance signal. Larger crystals of size 0.4 x 0.4 x 0.2 mm were also used since they were found to be more stable at higher pH conditions. Hence, we were able to test for both crystal stability and thickness in our absorbance measurements.

#### **4.2.2 Preparation of freeze-trapped crystals post reaction-initiation in a pH-jump buffer**

*Pm*HMGR crystals had been cryoprotected by introducing a cryoprotectant solution containing 1.2 M ammonium sulfate, 100 mM ADA and 32 % glycerol using a step-wise approach, outlined by Tim Schmidt. For this approach, a small volume (3  $\mu$ L) of the cryoprotectant solution is initially added to a 23.4  $\mu$ L crystal drop. This added cryoprotectant volume is slowly ramped up to 20  $\mu$ L (following a gradual sequence of added volume – 5  $\mu$ L, 5  $\mu$ L, 10  $\mu$ L, 10  $\mu$ L, 20  $\mu$ L, 20  $\mu$ L and 20  $\mu$ L) keeping a minimum wait time of 5 minutes between subsequent additions. Before adding 20  $\mu$ L of cryoprotectant solution, the same volume is removed from the drop and this step is repeated at least 3 times. The crystallization drop with added cryoprotectant solution is left to equilibrate overnight (for 16-20 hours). Using this method, a final cryoprotectant concentration of 32 % glycerol is achieved in the crystal environment. The same approach is utilized to incrementally add 1.2 M (NH<sub>4</sub>)CH<sub>3</sub>COO, 100 mM ADA and 30% PEG-400 solution at pH 6.7 (pH-jump buffer). While adding this solution and for subsequent additions, even smaller volumes like 3  $\mu$ L are first removed from the crystal drop before being replaced with the pH-jump buffer solution. Following this step, the crystal drop is left to equilibrate for 8 hours. The ligands for the enzymatic reaction – mevalonate, CoA and NAD<sup>+</sup> were then introduced at a 5mM, 1mM and 1mM concentration respectively in the pH-jump buffer by gradually introducing and replacing the current solution in the sitting drop with the ligand-soaking solution. Because of the pH used (pH 6.7), the enzyme is kept inactive when the ligands are added. Crystals with dimensions 0.4 x 0.4 x 0.2 mm remained in the soaking solution for four hours before being scooped out and placed in another well with the pH-jump buffer at pH 9 consisting of 1.2 M (NH<sub>4</sub>)CH<sub>3</sub>COO, 100 mM ADA and 30% PEG-400. The transfer of these crystals to a higher pH initiates enzyme activity. These crystals were soaked for different time periods ranging from 80 seconds to 10.5 minutes in the pH 9 environment. The crystals were then scooped out and frozen in liquid nitrogen to freeze-trap the

overall post-reaction state captured in the pH 9 soaked crystal. Crystals of the size 0.25 x 0.25 x 0.1 mm were used as a control to obtain a ligand-bound sample at pH 6.7. For crystals of this size, a soaking time of 2 hours was used to introduce the ligands mevalonate, CoA and NAD<sup>+</sup>. An additional control sample of this size was also acquired after being soaked in a pH 9 (pH-jump buffer) environment for 3.5 minutes before being frozen. Additionally, several crystals of a smaller size of 0.1 x 0.1 x 0.05 mm were also used. After slowly introducing the ligands in these crystals in the pH-jump buffer for a soaking time of 1 hour, the crystals were transferred to a pH 9 pH-jump buffer solution for a soaking time of 65 seconds to 30.5 minutes before being frozen in liquid nitrogen. By utilizing a range of samples, our aim was to optimize their width to obtain the best absorbance signal.

A speculative timeline of 30 minutes was initially established for crystals of both sizes (0.1 and 0.4 mm) tested given the significantly low rate of turnover in the pH-jump at pH 9. This significant lowering of reaction timescales is also supported by the 1000-fold reduction of turnover in the crystalline environment of carboxypeptidase in comparison to its activity measurement in solution<sup>[96]</sup>. Diffusion-based triggering experiments in cytochrome C oxidase that showed turnover in crystals have also indicated a timescale of minutes thereby supporting the assumption for a similar reaction timeframe to be expected in *PmHMGR* crystals<sup>[48]</sup>. While a set of samples soaked for time points from 60 seconds – 30 minutes were initially prepared for both sizes of crystals measured (0.1 mm and 0.4 mm), 0.4 mm crystals soaked at pH 9 for time periods ranging from 15 – 30 minutes were lost due to robot malfunctions while obtaining diffraction data at the APS synchrotron source and therefore only UV-Vis data until the first 10.5 minutes could be compared.

#### **4.2.3 UV-Vis absorbance measurements in ligand-bound enzyme crystals**

UV-Vis spectra were collected on the frozen crystal samples at the Stanford Synchrotron Radiation Lightsource (Beamline 9-2). The crystals were mounted in front of a UV-Vis microspectrophotometer and kept frozen using a liquid nitrogen stream. To reduce the formation of ice on the samples, a process termed cryo-annealing was used where the liquid nitrogen stream used to keep the samples frozen was turned off for a predetermined amount of time (30 seconds) to allow the ice present on the crystal surface to melt. This step was effective in reducing the ice on our crystal samples and greatly improved the observed signal. UV-Vis spectra were collected in the wavelength range 250 – 900 nm using a Hamamatsu deuterium and halogen lamp and an



Ocean Optics QE65000 Spectrum Analyzer. A 50  $\mu\text{m}$  light source is used to obtain the absorbance spectra. A dark spectrum was first obtained to obtain a measure of background intensity in the absence of lamp illumination. Additionally, a reference spectrum measuring maximum intensity from the light source in the absence of sample was also obtained. Both dark and reference spectra were used to calculate the sample absorbance using the following equation:

$$A = \log_{10} \left[ \frac{R - D}{S - D} \right]$$

Here, A is the calculated sample absorbance at wavelength  $\lambda$  (AU). S is the sample transmitted intensity wavelength  $\lambda$  (counts). D is the background intensity at wavelength  $\lambda$  (counts) and R is the reference incident intensity at wavelength  $\lambda$  (counts). The phi-rotation mode was utilized in order to find the best orientation to obtain UV-Vis spectra. This helped with reducing artifacts due to ice, cracks, nylon loop and internal reflections from the frozen mother liquor while measuring the absorbance. To use this feature, a phi rotation range was defined from 0 to 360 degrees with a 5-10 degree step size to sample areas around the entire crystal. The best spectra obtained was then utilized for our comparisons. All the spectra obtained were compared after identifying the lowest absorbance value in each of the spectral measurements (at wavelengths greater than 600 nm) and setting it to zero absorbance by subtracting it from all absorbance values across the wavelength spectrum in that dataset.

#### 4.2.4 Room temperature absorbance measurements in *Pm*HMGR crystals

The *Pm*HMGR crystal used for this measurement was cryoprotected and pre-soaked with the pH-jump buffer and ligands mevalonate, CoA and  $\text{NAD}^+$  at pH 6.7 using the protocol outlined in section 4.2.2. The crystal samples were then transported in a room temperature shipper. The shipping container was able to maintain humidity in a sealed environment with the use of foam pieces pre-soaked with the crystallization mother liquor.

At the SSRL beamline, the humidity of the sample was controlled for these measurements using an Arinax HC-lab instrument to blow humid air onto the crystal sample. This method allows us to directly mount the crystal at room temperature without the need for capillary mounting. A relative starting humidity for crystals was estimated from previously recorded values for different cryoprotectants<sup>[97]</sup>. It was then measured for the crystallization and pH-jump buffer by centering

empty loops with the respective buffers on them. The humidity was adjusted until the drop size was found to remain stable with time. This humidity value was then used for subsequent diffraction and UV-Vis absorption measurements.

To obtain UV-Vis spectra, a control absorption spectrum from 215-900 nm was measured for the crystal sample. The crystal was then transferred to a droplet of the pH-jump buffer with 1.2M ammonium acetate, 100 mM ADA and 32 % PEG-400 at pH 9 on a glass slide for 3 minutes and then mounted again for a continuous time-resolved absorption measurement after reaction initiation that was obtained over several minutes.

## 4.3 Results

### 4.3.1 Absorption spectra of freeze trapped HMGR crystals after the pH jump:

By measuring changes in the UV-Vis spectroscopic signature of mevalonate, CoA and NAD<sup>+</sup> bound *Pm*HMGR crystals transferred to a higher pH (pH 9) environment, we were able to observe the onset and timeframe of turnover. The unique absorbance peak of NADH at 340 nm helped us detect the reduction of NAD<sup>+</sup> obtained as a cumulative result of the oxidation of mevalonate and mevaldyl-CoA. By observing changes in NADH, NAD<sup>+</sup> and Adenine absorbance, we can determine the timeframe of the reaction steps in the crystal starting with mevalonate oxidation and ending with product release.

Based on the pH-rate profile observed in an ammonium acetate, ADA and PEG-400 environment (Section 3.3.5, Fig 3.6), we should expect the onset of enzymatic activity after we move the crystals into a pH 9 environment. Given that this solution has a buffering range of 4.75 and 9 from ammonium acetate and 6.0-7.2 from ADA, we can expect the desired pH of the solution to be preserved during the soaking and transfer steps at both crystallization (pH 6.7) and higher pH (pH 9).

No absorbance signal for NADH is observed in a 0.25 x 0.25 x 0.1 mm crystal (used as a control) that has been exchanged in an Ammonium Acetate, ADA and PEG-400 buffer and soaked with mevalonate, CoA and NAD at pH 6.7. (Shown in Fig 4.2-4.4). No difference was observed in the absorbance signal at 340 nm with and without annealing (Fig 4.2). A peak for NADH absorbance was also observed in 0.25 x 0.25 x 0.1 mm crystals exchanged in the Ammonium

Acetate, ADA and PEG-400 buffer (pH 6.7) and soaked with mevalonate, CoA and NAD<sup>+</sup> and then further soaked in pH-jump buffer (pH 9) for 3.5 minutes (Fig 4.2).

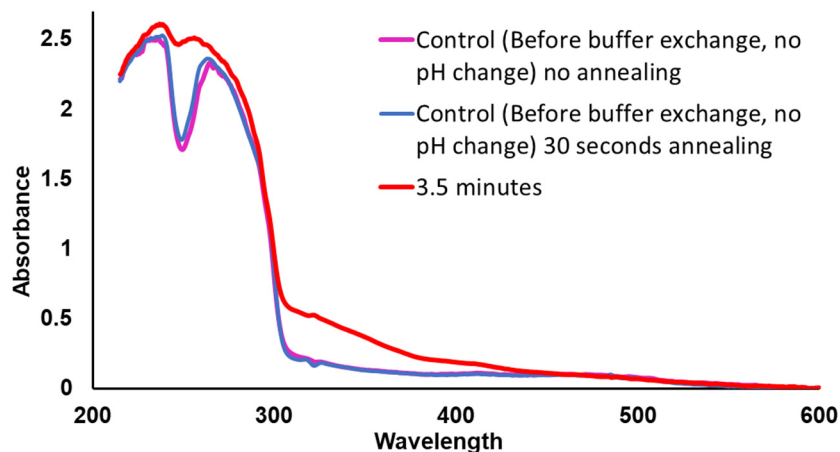


Figure 4.2 UV-Vis absorbance spectra for 0.25 x 0.25 x 0.1 mm crystals before and after a pH change (at pH 9)

The UV-Vis spectra obtained at different time points after the crystals were transferred to a pH 9 buffer and freeze-trapped are shown in Figure 4.3. The absorption spectra from the 0.4 x 0.4 x 0.2 mm crystals that were picked to optimize crystal stability at high pH conditions indicate the emergence of an absorbance peak for NADH at 340 nm ( $A_{340}$ ) after the crystal was transferred into a pH 9 buffer. The peak observed at 340 nm is shown to increase from 80 seconds to 8.5 minutes. While an increase in absorbance is observed at several time points, we also see a drop in absorbance at 340 nm after 3.5 minutes at 5.5 minutes and another drop after 8.5 minutes at 10.5 minutes that is greater in magnitude.

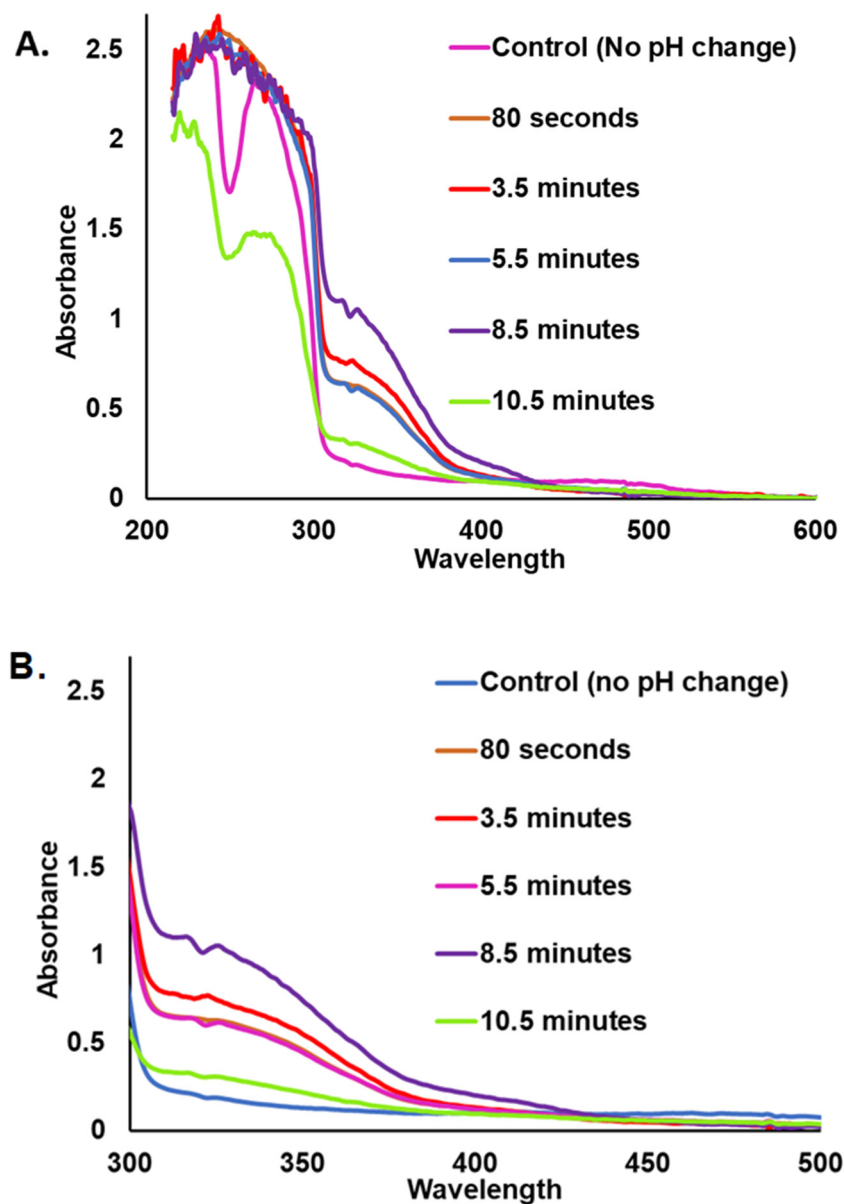


Figure 4.3 UV-Vis spectra from A. 200-600 nm B. 300 – 450 nm for freeze-trapped HMGR crystals (0.4 x 0.4 x 0.2 mm) after a pH change from 80 seconds – 10.5 minutes (at pH 9). Time after the pH change is indicated in the legend.

This experiment was also conducted using crystals with different dimensions (0.1 x 0.1 x 0.05 mm) with the intent of obtaining better quality absorbance data in thinner crystals. The absorbance data obtained is shown in Fig 4.4.

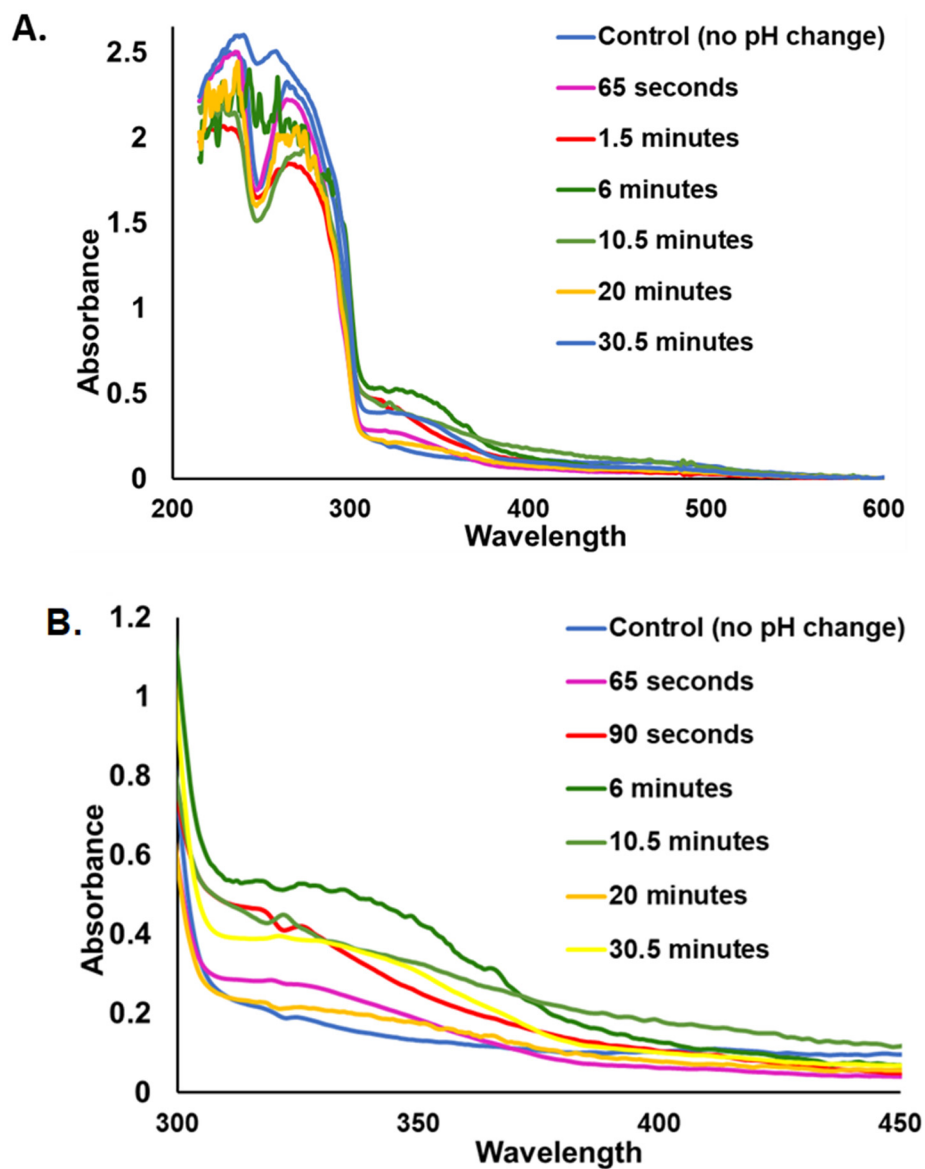


Figure 4.4 UV-Vis absorbance data obtained for A. 200 – 600 nm and B. 300 – 450 nm for different substrate-soaked 0.1 x 0.1 x 0.05 mm crystals soaked at a higher pH 65 seconds – 30.5 minutes

The absorbance data shows a similar trend with an increase in absorbance from 65 seconds to 6 minutes and a subsequent decrease in absorbance after 10 minutes indicating the production and release of NADH. The trend of decreasing absorbance at long time points is also observed at 20 minutes. However, 30.5 minutes following a pH change, the absorbance is found to increase again. The maximum increase in absorbance observed in crystals that are 0.1 x 0.1 x 0.05 mm in size is ~ 53% of that observed in crystals that are 0.4 x 0.4 x 0.2 .

The absorbance spectra obtained in the range of 220 – 280 nm for NAD<sup>+</sup> nicotinamide (220 nm), Adenine (260 nm) and the aromatic amino acids, Tryptophan and Tyrosine (275-280 nm) was unfortunately muddled by what appears to be a poor transmittance at these lower wavelengths perhaps as a results of large crystal size in the case of 0.4 mm crystals and / or ice formation. In the case of the crystals of size 0.4 x 0.4 x 0.2 mm, the peaks at these wavelengths appear to merge or appear too noisy to distinguish due to their high (> 2) absorbance values. It is only at the pre pH-jump or 10.5 minute post pH-jump time points that we can draw some comparison with the absorbance in this region decreasing significantly for both the NAD<sup>+</sup> and adenine absorbance region after a long soaking time at high pH.

In the case of smaller crystals of size 0.1 x 0.1 x 0.05 mm, we continue to observe this high absorbance value 6 minutes and 20 minutes after the change in pH. However, an initial drop in the absorbance of NAD<sup>+</sup> and adenine absorbance is observed following 1.5 minutes after being introduced to a pH 9 environment. This continues until 20 minutes. At 30.5 minutes, we observe an increase in absorbance that is greater than that observed in control sample at pH 6.7.

#### **4.3.2 Absorption spectra of *Pm*HMGR crystals at room temperature after a pH jump**

To determine if the onset of enzymatic activity after a pH jump can also be measured from the same ligand-bound crystal, we measured the changes in NADH absorption in *Pm*HMGR crystals at room temperature. It was observed that the crystal measured showed an absorbance peak for NADH after being soaked for 3 minutes at pH 9 (Shown in Fig 4.5). The NADH absorbance peak was also observed to merge with the adenine and protein absorbance at 260-280 nm.

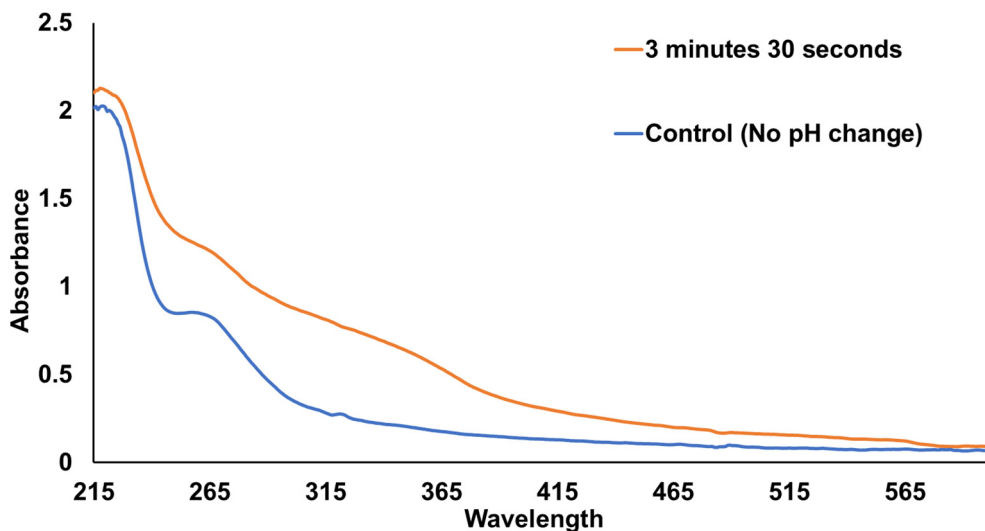


Figure 4.5. Absorption spectra observed before and after transitioning *PmHMGR* crystals into a pH 9 buffer at room temperature

## 4.4 Discussion

### 4.4.1 Freeze-trapped time-resolved absorption spectra in *PmHMGR* crystals

Using UV-Vis measurements, we were able to determine the onset of turnover in *PmHMGR* crystals that had been pre-soaked with pH-jump buffer, mevalonate, CoA and NAD<sup>+</sup> at pH 6.7 and subsequently transferred to a pH 9 environment. The lack of an absorbance peak at pH 6.7 indicates an estimated lack of turnover at the crystallization pH for *PmHMGR* crystals in the pH-jump buffer environment. The observed absorbance peaks at pH 9 further indicate that a subsequent pH change in the pH-jump buffer is necessary to observe turnover in *PmHMGR* crystals.

The increase in NADH absorbance at time points between 80 seconds to 8.5 minutes indicates an ongoing hydride transfer and a production of NADH in the crystal with time. The drop in absorbance between the 3.5 minute and 8.5 minute time points in the spectra collected with 0.4 mm crystals could allude to a decrease in NADH production between the formation of mevaldehyde from mevalonate and HMG-CoA from mevaldyl-CoA during the thiohemiacetal formation step for the NAD<sup>+</sup> exchange to occur. Alternatively, it could also be due to a difference in the concentration of cofactor bound within the *PmHMGR* crystal samples. Because the pH-change also relies on the efficiency of soaking across several crystals, minor variations in internal

crystal pH after a pH-change might occur. This could be an alternative factor resulting in a sudden dip in absorbance 5.5 minutes after a pH change. Repeated measurements within this timeframe would be essential to see if this intermittent drop in absorbance is reproducible to be certain about the changing concentration of NADH.

The eventual and significant reduction in NADH absorbance 10.5 minutes after a pH change is speculated to be due to the release of reduced NAD<sup>+</sup> cofactor out of the catalytic site and back into the reservoir thereby effectively leaving the crystal that is scooped and frozen for the absorbance measurement. This eventual release of NADH can be attributed to the lack of ligands in the pH 9 solution which would result in a shift in equilibrium after the pH jump and thus a diffusion of the cofactor back into the solution. Hence, what is captured in the spectra is the NADH peak from the cofactor that is still left in the crystal.

Several spectra obtained between 200-300 nm for 0.4 mm *Pm*HMGR crystals are difficult to distinguish due to the poor transmittance and merging of absorbance peaks. However, the overall reduction in the absorbance amplitude for NAD<sup>+</sup> nicotinamide at 220 nm at 10.5 min in comparison to the pre pH-jump sample is indicative of the conversion of NAD<sup>+</sup> to NADH and the subsequent release of the cofactor. We also observe a reduction in the absorbance from 250-290 nm. This could indicate a possible reduction in adenine absorbance at 260 nm in NAD<sup>+</sup>, NADH, CoA and HMG-CoA again because of ligand release. This region also includes the absorbance wavelength in Tyrosine and Tryptophan residues (280 nm). While we do not expect a shift in protein stability at higher pH considering that we observe maximum activity in the pH-jump buffer environment at pH 9, a change in pH could result in a conformational change in the mevalonate, CoA and NAD<sup>+</sup> bound enzyme. If these changes affect its secondary, tertiary or quaternary structure resulting in a change in the solvent exposure of the adenine portion of the bound NAD<sup>+</sup> and CoA, it might also translate to a shift in the protein absorbance thereby factoring into the overall drop in absorbance between 250-290 nm.

A change in absorbance at 340 nm was also observed in smaller sized crystals (0.1 mm) with an increase in absorbance within the first 6 minutes indicating the production of NADH followed by a decreasing absorbance from 10-20 minutes which indicated a diffusion of the cofactor out of the crystal. The increase in absorbance observed at 30 minutes which appears to be an outlier could be attributed to a backward diffusion of NADH into the crystal after a prolonged period of soaking.



While the smaller sized crystals also had indistinguishable spectra at 200-300 nm owing to the presence of ice that could not be reduced with the use of annealing at 6 minutes and 20 minutes, several time points following a pH-change (65 seconds, 1.5 minutes and 10.5 minutes) showed distinguishable absorbance peaks from 215-240 nm and 250-290 nm. The spectra obtained at 220 nm 65 seconds following a pH change matched that observed in the pre pH-jump sample indicating that while there was NADH production following the pH-jump indicated by the emergence of a peak at 340 nm, the overall concentration of  $\text{NAD}^+$  was not significantly affected. However, at subsequent time points (1.5 and 10.5 minutes), this absorbance is observed to drop further in comparison to the pre pH-jump structure. This change in absorbance at 220 nm between the post pH-jump structures at 65 seconds and 1.5 minutes following a pH change appears to be indicative of a conversion of  $\text{NAD}^+$  to NADH at 1.5 minutes considering the simultaneous increase in NADH absorbance at 340 nm. However, the difference in absorbance between the post pH-jump structures at 6 minutes and 10.5 minutes following a pH change appears to be a result of  $\text{NAD}^+$ /NADH release considering a drop in both their nicotinamide peaks at 220 nm and 340 nm respectively.

The absorbance in the 260-270 nm region was observed to reduce slightly 65 seconds after a pH-change. Considering that this region is a lot closer to the absorbance peak of adenine, it is possible that its change is a result of a changing orientation and exposure of adenine from CoA and  $\text{NAD}^+$ /NADH at the active site after reaction initiation. The further drop in absorbance in this region 1.5 minutes after a pH change could also be further indicative of this change in the ligand-bound crystal. Structural studies of the ligand-bound enzyme from this type of sample might elucidate whether this interpretation of observed changes is plausible. The drop in adenine absorbance in this region at the 10.5-minute post pH-jump structure in comparison to the previously observed time point of 6 minutes in conjunction with the reduction in NADH absorbance is indicative of the release of  $\text{NAD}^+$  / NADH and / or CoA and HMG-CoA in the smaller sized crystals.

The overall reduction in NADH absorbance in the 0.1 mm crystals in comparison to the bigger 0.4 mm crystals indicates that the absorbance changes observed in the crystal are also dependent on enzyme concentration, which in this case correlates to crystal size. The changes in absorbance in all the crystals studied that signify reaction initiation and product release indicate a turnover time that is in the order of minutes. Given that we observe NADH absorbance 65 and 80 seconds after a pH change in 0.1 and 0.4 mm sized crystals respectively, we can expect to observe

crystallographic changes associated with mevalonate oxidation within this time after reaction initiation. By identifying this timeframe, we can now design a time-resolved crystallographic experiment where we can expect to observe potential conformational and biochemical changes associated with the first hydride transfer step. Similarly, with decreasing absorbance at 10.5 minutes in both 0.1 and 0.4 mm crystals, we expected to observe the release of ligands after several minutes. This indicated that other reaction steps such as thioester bond formation between mevaldehyde and CoA and the exchange of NADH with another  $\text{NAD}^+$  cofactor for HMG-CoA formation could be observed within this time frame after a pH change.

Given that we only have sparse time points for both 0.4 mm and 0.1 mm crystals, we can estimate the onset and timescale of turnover in *PmHMGR* crystals with a lot more certainty than the incremental changes in concentration of ligands between time points. More closely spaced time points would be required to capture additional changes in ligand-bound states of the enzyme after reaction initiation and before product release. Additionally, we might be able to better capture changes in the 200-300 nm region with smaller (lesser than 0.1 mm) crystals and better freezing conditions that prevent ice formation.

#### **4.4.2 Absorption spectra of *PmHMGR* crystals at room temperature after a pH jump**

The appearance of an absorbance peak for NADH at 340 nm in a ligand-bound *PmHMGR* crystal after a pH change indicated that the changes observed in our freeze-trapped samples can also be seen within a single crystal. Additionally, it indicated that the pH changes can also be introduced within crystals at room temperature for time-resolved diffraction and absorbance measurements. The observed broadening of the NADH absorbance spectra could also be due to the increase in temperature which has been previously recorded with  $\text{NAD(P)H}^{[98]}$ . This experimental setup can hence be modified using a flow cell or dropper to introduce pH changes and capture real-time absorbance data over the course of the enzymatic reaction.

## CHAPTER 5. TIME-RESOLVED DIFFRACTION MEASUREMENTS

### 5.1 Introduction

With several ligand binding domains and dynamic regions forming the catalytic site for the multi-step reaction catalyzed by HMG-CoA reductase, we expect several conformational and chemical changes to facilitate each reaction step. These changes can now be characterized with the ability to observe the reaction taking place within the crystal. With the development of a triggering method, we have now demonstrated the ability to initiate the *Pm*HMGR reaction in crystals. Our kinetic and absorption spectroscopy studies provide estimates for the reaction rate within the crystal. Using this information, we can determine the timeframe within which we can expect to observe the effects of turnover in *Pm*HMGR crystals. Using this tested reaction triggering pH-jump method we can now obtain structural information along the reaction pathway and observe trapped reaction intermediates. This can be done via time-resolved diffraction experiments on *Pm*HMGR crystals after reaction initiation following a pH-jump.

By comparing diffraction datasets at different time points, we can confirm and expand upon the current reaction models for the enzyme. With the availability of several ligand-bound structures from previous studies, which include binary, ternary, slow-substrate and proposed intermediate bound structures that indicate the structural changes to be observed at several time points, we have an additional means of identifying and confirming the changes observed along the reaction pathway (Previously described in section 2.4). With a time-resolved experiment, we aim to also characterize changes that have not yet been observed in crystal structures such as the structural changes that characterize the formation of mevaldehyde, the exchange of NAD<sup>+</sup> leading to the subsequent formation of HMG-CoA and product release.

The structures obtained post reaction-initiation in *Pm*HMGR crystals can be compared to pre-pH jump structures to study changes in enzyme conformation and ligand placement to determine movements that advance the reaction. We can also detect changes in electron density of ligands that would indicate intermediate / product formation and cofactor exchange to further understand different states along the reaction pathway.

## 5.2 Materials and methods

### 5.2.1 pH-jump diffraction experiments

To do this experiment, we obtained *Pm*HMGR crystals using the same methods described in section 3.2.1.1 and 4.2.1. We utilized crystals of the size 0.4 x 0.4 x 0.2 mm after testing various sizes for their stability and diffraction quality after being introduced at a higher pH environment. Crystals of this size were found to be ideal for utilizing the pH-jump method. Mevalonate, CoA and NAD<sup>+</sup> bound *Pm*HMGR crystals were obtained and then introduced to a pH 9 environment before being freeze-trapped at various time points between 20 seconds – 10 minutes. This step was conducted using the cryoprotection, soaking and pH-jump protocol outlined in Section 4.2.2. Diffraction data for these crystals was obtained at beamline 23-ID-D at the Advanced Photon Source, Argonne National Laboratory. The structures obtained were solved via molecular replacement using the quaternary complex as the search model. Each dataset was subsequently refined using the method described in section 3.2.1.3. Since the coordinate and parameter files for mevaldehyde and HMG-CoA could not be utilized from the PHENIX library, they were built and obtained using the PHENIX program eLBOW<sup>[99]</sup>. For structures obtained between 20 seconds – 1 minute after a pH-change, we used a CC<sub>1/2</sub> of 0.3 which should give us a reliable cutoff to incorporate statistically significant reflection data into our model<sup>[100]</sup>.

### 5.2.2 Acquisition of *Pm*HMGR mutant structures

*Pm*HMGR mutant (E399A and L407S) enzymes prepared by Dr. Nic Steussy and Dr. Taylor Quinn were crystallized using a seeding method using a wild type 0.25 × 0.25 × 0.1 μm apo HMGR crystals. E399A crystals grew to 0.1 × 0.1 × 0.05 μm and L407S crystals grew to 0.3 x 0.3 crystals in 4-6 weeks. The crystals were cryoprotected and soaked with ligands mevalonate, CoA and NAD<sup>+</sup> using the same protocol outlined for wild type crystals in section 3.2.1.1. A 1.66 Å and 1.79 Å dataset was obtained for E399A and L407S respectively at the 23-ID-B beamline at the Advanced Photon Source, Argonne National Laboratory. Crystallization for the E396A *Pm*HMGR enzyme was also attempted using the same method but did not yield any crystals.

### 5.2.3 Structure comparisons

#### 5.2.3.1 Structure alignments of regions with minimum RMSD variation

An initial set of structural comparisons were done to identify conformational differences between various ligand-bound structures and the mevalonate, CoA and NAD<sup>+</sup> bound quaternary complex at pH 6.7. Additionally, we also compared various ligand-bound structures to the quaternary complex. For both these set of structures, the RMSD of each residue was calculated between the reference (quaternary complex at pH 6.7) structure and the structure we were interested in comparing. The acquired RMSD values were subsequently plotted. To avoid influencing the structure comparison, the structures were not aligned prior to calculating RMSD. This is because structure alignments modify regions to achieve best superposition. The transformed structures produced from this alignment could hide the variations in enzyme conformation that might be present. Due to differences in the reference cartesian coordinates of each structure, the magnitude of the minimum calculated RMSD varied for each structure comparison. While this value varied depending on the structure compared, the calculated plot for each structure showed regions with significantly low variation from the baseline RMSD. Fig 5.1 illustrates an example of 2 of the structures compared to the quaternary complex. Regions of minimum RMSD variation were identified from each plot and subsequently aligned using the LSQ superimpose feature COOT.

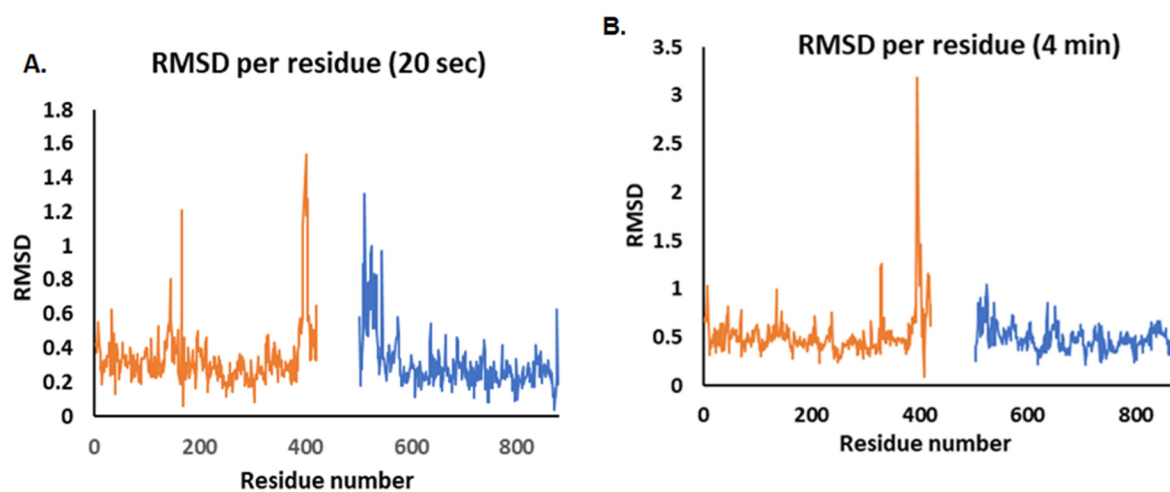


Figure 5.1 RMSD comparison of the structures obtained at different time points (A. 20 sec, B. 4 min)

### 5.2.3.2 Structure alignment of *PmHMGR* core-helix regions

While comparing movements in our set of closely spaced post pH-jump structures acquired 20 seconds – 1 minute after being introduced to a pH 9 environment, we aligned 4 helical regions in the protein core (258-298 and 758-798) (Fig 5.2). Our initial structural studies indicated that this time range was largely associated with changes leading up to and after the first hydride transfer step. Our assessment of their movements indicated that this core-helix region shows minimal movement and hence its alignment allowed us to capture more drastic changes that are present in other portions of the enzyme. By comparing this region for these set of structures, we were also able to keep our alignment constant without significantly affecting the conformation of compared structures. The set of structures compared using this alignment were studied in greater detail.



Figure 5.2 *PmHMGR* homodimer with each monomer indicated in cyan and violet and the core helices depicted in yellow

### 5.2.4 Comparing changes in the electron density at the ligand-bound region

*PmHMGR* structures obtained from crystals that have undergone a pH-jump are expected to show changes at the active site associated with  $\text{NAD}^+$  reduction and thioester bond formation between CoA and mevaldehyde. In order to compare changes in the density of  $\text{NAD}^+$  and in substrate bound regions, we generated polder maps using the phenix.polder program in the phenix suite of programs. The advantage of utilizing polder maps is that by excluding the bulk solvent, the map can help visualize weak electron densities thereby showcasing all the changes associated with ligands in the post-turnover structures<sup>[101]</sup>. The ‘map sigma level comparison’ program was

utilized to compare different polder maps<sup>[80-82, 99, 102]</sup>. This program utilizes a novel ‘rank scaling’ approach to determine an appropriate contour level for visually comparing two electron density maps between a common set of grid points in real space. It offers a better way to visualize these differences in comparison to a constant  $\sigma$  cutoff since that can vary in the number of grid nodes utilized for generating each map leading to an unequal comparison<sup>[103-106]</sup>.

Utilizing this program, we were able to determine an appropriate  $\sigma$  value to compare 2 structures keeping the polder map of the reference structure at 3  $\sigma$ . The structure obtained after exchanging the crystal with the pH-jump buffer (1.2 M Ammonium Acetate, 100 mM ADA and 32 % PEG-400) had the best resolution and was hence used as a reference structure for the  $\sigma$  level comparison. 2Fo-Fc density maps obtained before refinement with ligand models were also used to observe drastic changes in ligand bounded regions. The ‘map sigma level comparison tool’ was also used to compare these maps.

Lastly, refined composite omit maps with and without simulated annealing have been used to compare changes in the electron density in the ligand bound region<sup>[88, 107]</sup>. In contrast to the polder maps that can pick up the weakest signals of electron density, the composite simulated omit maps stringently remove any phase bias by using simulated annealing refinement in the generation of the maps. Hence, the analysis of polder maps and simulated annealing composite omit maps provide a complementary view of changes occurring at the enzyme’s active site in areas with subtle changes in electron density. Since the ‘sigma map level comparison’ could not recognize the simulated annealing composite omit maps generated, we used a conventional cutoff value of 3 $\sigma$  to compare these maps. The use of complementary methods helps differentiate changes in electron density that could be noise in comparison to ones that are a result of biochemical changes in the *Pm*HMGR crystal environment.

### **5.2.5 Measuring angles between helices in the *Pm*HMGR flap domain**

To compare changes in the angles between flap domain helices before and after reaction initiation at different time points, we used the PyMol command ‘angle\_between\_helices’ that generates a helical axis for 2 specified residue regions and measures the angles between them.

### 5.2.6 Calculating interhelical volume in *Pm*HMGR flap domain

Changes in the inner volume of the *Pm*HMGR flap domain before and after reaction initiation at different time points was also calculated using the program ProteinVolume<sup>[108]</sup>. This program utilizes a ‘flood fill algorithm’ to determine the Van Der Waal and void (Cavity) volume from a *Pm*HMGR structure using a calculated solvent-excluded volume of the enzyme. Protonated PDB files of the *Pm*HMGR flap domain obtained before and several time points after reaction initiation were utilized for this calculation.

## 5.3 Results

With the use of a pH-jump triggering method, our intent is to observe the onset of turnover in the enzyme and the changes along the reaction pathway that allow the reaction to occur. Our testing of the pH-jump method using UV-Vis spectra measurements in *Pm*HMGR crystals indicated to us that this method was applicable in initiating reaction turnover and carrying forward the complete *Pm*HMGR reaction in crystals. However, the biochemical changes that are associated with mevalonate oxidation and thioester bond formation between mevaldehyde and CoA had not been structurally observed. Obtaining structural information of post reaction-initiated intermediates would identify the transitory conformational changes that the enzyme undergoes along its reaction pathway. Movement of key residues and ligands at different stages of the enzymatic reaction would also indicate the changes that advance individual reaction steps. Hence, an experiment was conducted to obtain diffraction data from *Pm*HMGR crystals that had been freeze trapped at several time points after reaction initiation using the pH-jump method. These time points ranged across the time period of 10 minutes within which we also observed changes in UV-Vis spectra that indicated reaction initiation and product release. Subsequent analysis of these structures indicated the time periods within which we could expect to observe mevalonate oxidation and NAD<sup>+</sup> reduction, thioester bond formation and product release. Given that we have very little structural information centered around the formation of the first reaction intermediate mevaldehyde after the oxidation of mevalonate and it being the first step of the reaction, we decided to center the rest of this structural study on this step by obtaining several closely spaced structures centered around this reaction event. In addition to having several structures obtained after reaction initiation using the pH-jump method, we also had several ligand-bound structures



that served as markers of several intermediate steps along the reaction pathway. These structures were previously collected via several experiments conducted by Dr. Nic Steussy, Dr. Chandra Duncan and Tim Schmidt<sup>[1, 2]</sup>. By comparing our newly acquired structure of *Pm*HMGR bound to mevalonate, CoA and NAD<sup>+</sup> that served as a starting point for this enzymatic reaction to these structures, we could anticipate some of the structural changes that would occur along the reaction pathway. This comparison also helped us identify the key ligand-enzyme interactions and conformational changes that take place upon ligand binding and how they might change after the conversion of the substrate and cofactors into the reaction intermediates, during cofactor exchange and product release.

### **5.3.1 Comparison of quaternary complex structure to other ligand bound structures**

The mevalonate, CoA and NAD<sup>+</sup> bound structure acquired was compared to other ligand-bound structures by determining and aligning the low RMSD regions. Regions in each of the ligand-bound structures that showed movement in comparison to the quaternary complex were highlighted. By observing the range of conformational changes in the presence and absence of different combinations of ligands, we were able to identify which ligand-interactions lead to the conformation observed in the quaternary complex. By identifying the regions influenced by different ligand binding sites, we were also able to determine the regions where we would expect movements due to substrate to intermediate conversion, ligand movement and release.

The ligand-bound *Pm*HMGR structures compared to the quaternary complex are shown in the table below:

Table 5.1 Structures obtained with *Pm*HMGR and various permutations of ligands for the enzymatic reaction and substrate / cofactor analogs

#	Ligands in structure	Resolution	PDB ID
1	Apo-enzyme	1.75 Å, 2.2 Å	4I64
2	HMG-CoA	1.85 Å	4I6A
3	R-Mevalonate	1.45 Å	4I6Y
4	Mevaldehyde and CoA	1.8 Å	-
5	Dithio-HMG-CoA and NAD <sup>+</sup>	2.8 Å	4I4B
6	NADH	2.3 Å	-
7	CoA	2.3 Å	-
8	Mevalonate and NAD <sup>+</sup>	2.8, 2.4 Å	-
9	CoA and NAD <sup>+</sup>	2.3 Å	-
10	HMG-CoA and NAD <sup>+</sup>	2.8 Å	-

In comparison to the apo-enzyme (PDB ID: 4I64), we see movements in the small domain binding region of the quaternary complex near the NAD<sup>+</sup> binding site in the neighboring small (HIS 613 - ARG 721) and large domain (VAL 825 - THR 834) regions in the same monomer (Fig 5.3 A). We find these regions moving closer to the active site after the binding of NAD<sup>+</sup>. The binding of ligands brings these neighboring regions closer to the ligand-binding site. No significant movement was observed in the CoA binding site after the co-substrate is bound (Shown in Fig 5.3 A.).

However, the movement of regions neighboring the NAD<sup>+</sup> binding site is observed in the absence of the cofactor in the structure of *Pm*HMGR bound to HMG-CoA (PDB ID: 4I6A). The small domain neighboring the NAD<sup>+</sup> bound region in this structure is still found to overlap closely with the quaternary complex. However, variations in the extent of ligand induced movements in the HMG-CoA bound structure are observed in the small domain (ILE 618 – GLY 670 and ALA 687 – LEU 714) and large domain (VAL 825 – A 838 (HMG-CoA)) in comparison to the quaternary complex (Fig 5.3 B). Movement of the small domain region is further observed when the quaternary complex structure is compared to the structure obtained with mevalonate (PDB ID: 4I6Y; Fig 5.3 C.). Our comparisons also show that the movements in the small domain and large domain regions are greater in the mevalonate-bound complex in comparison to the apo-enzyme and closely match that of the HMG-CoA bound structure. The extent of movement in comparison to the quaternary complex is observed to vary in a slightly larger region in the mevalonate-bound

complex (GLY 620 – HIS 662, HIS 676 – R 721 in the small domain and VAL 825 – PRO 836 in the large domain) (Shown in Fig 5.3 C.).

The structure of the enzyme obtained with mevaldehyde and CoA which has been shown to undergo turnover with the formation of a thiohemiacetal has a conformation like the dithio-HMG-CoA and HMG-CoA bound enzyme. With the mevalonate and CoA regions occupied, we also observe variations in the conformation of regions spanning the small domain residues ILE 621 – VAL 661, ALA 675 – THR 705 and the large domain residues GLY 826 – THR 705 in comparison to the quaternary complex. However, even in the absence of NAD<sup>+</sup>/NADH, we observe conformational changes in the small domain region near the cofactor binding site. The variation in the adopted conformation appears to be greater near the NAD<sup>+</sup> adenine-ribose binding site (Fig 5.3 D).

The effects of the absence of mevalonate are observed in the *Pm*HMGR structure bound to NADH where movement of the small domain regions near mevalonate (ARG 628 – VAL 661, PRO 664 – MET 672 and GLY 686 – SER 715) away from the active site is observed in comparison to the quaternary complex. While the presence of the NADH does move the neighboring large domain region (LEU 827 – LEU 837) in the conformation close to that observed in the quaternary complex unlike the apo enzyme, HMG-CoA and mevalonate bound structures, we still do observe a slight deviation in its position (Fig 5.3 E).

The individual binding effects of CoA can be observed in our comparison of the quaternary complex with a CoA bound *Pm*HMGR structure. Greater conformational deviations from the quaternary complex are observed in comparison to NAD<sup>+</sup> and mevalonate bound structures in small (ASN 626 – GLU 660, ALA 665 – ARG 669 and GLY 686 – ALA 718) and large (LEU 827 – ALA 838) domain regions (Shown in Fig. 5.3 F.).

In the absence of CoA, with the enzyme bound to mevalonate and NAD<sup>+</sup>, the ternary complex is observed to move slightly closer to the ligand-binding site in the CoA (LEU 3 – GLY 40) and NAD<sup>+</sup> (ASN 643 – GLY 655) binding regions (Fig 5.3 G) in comparison to the quaternary complex. The flap domain is also observed in this mevalonate-NAD<sup>+</sup> complex in the absence of CoA. Conformational changes are observed in the flap domain in the Mevalonate-NAD<sup>+</sup> bound structure in comparison to the quaternary complex with CoA. With the presence of CoA in the quaternary complex, the flap domain is shown to move away from the ligand-binding region in comparison to the mevalonate and NAD<sup>+</sup> bound complex. These movements are shown to increase

significantly after the MET 382 residue along the domain spanning between GLU 375 – ALA 418. Therefore, flap regions close to the enzyme active site do not appear to be affected with and without the presence of CoA. This lack of difference can be observed in the active site region with the distance between the catalytic histidine (HIS 381) and the thiol atom in CoA only changing by 0.2 Å with the addition of CoA (Fig 5.4 A, B). The quaternary complex was also compared to additional mevalonate and NAD<sup>+</sup> bound complexes where the flap closure was not observed. These complex structures were obtained with lower ligand concentrations and soaking times which we believe reduced the propensity for flap closure. The nucleotide-mevalonate bound structure doesn't show significant movement in the CoA binding region in the presence and absence of the flap domain with slight movement in the same regions in the absence of CoA (LEU 3 – LEU 13) (Fig 5.3 H.). However, we do observe more movement of the NAD<sup>+</sup> binding domain away from the active site in the absence of the flap (Fig 5.3 H.).

With the addition of NAD<sup>+</sup>/NADH to CoA and in the absence of mevalonate, the structure closely resembles the quaternary complex with minimal deviations in the small domain region. Movements are also observed in solvent exposed and flexible regions of the flap domain (Fig 5.3 I).

Minimal conformational differences in the large and small domains are also observed in the structure obtained with the non-productive complex with HMG-CoA and NAD<sup>+</sup> (Fig 5.3 J) in comparison to the quaternary complex. The flap domain is observed from GLU 375 – ALA 420, much like in the quaternary complex with mevalonate, CoA and NAD<sup>+</sup>. Like in the case of the structure obtained with CoA and NAD/NADH, localized changes are observed in the flap domain regions VAL 408 – ASP 412 and ALA 393 - VAL 400.

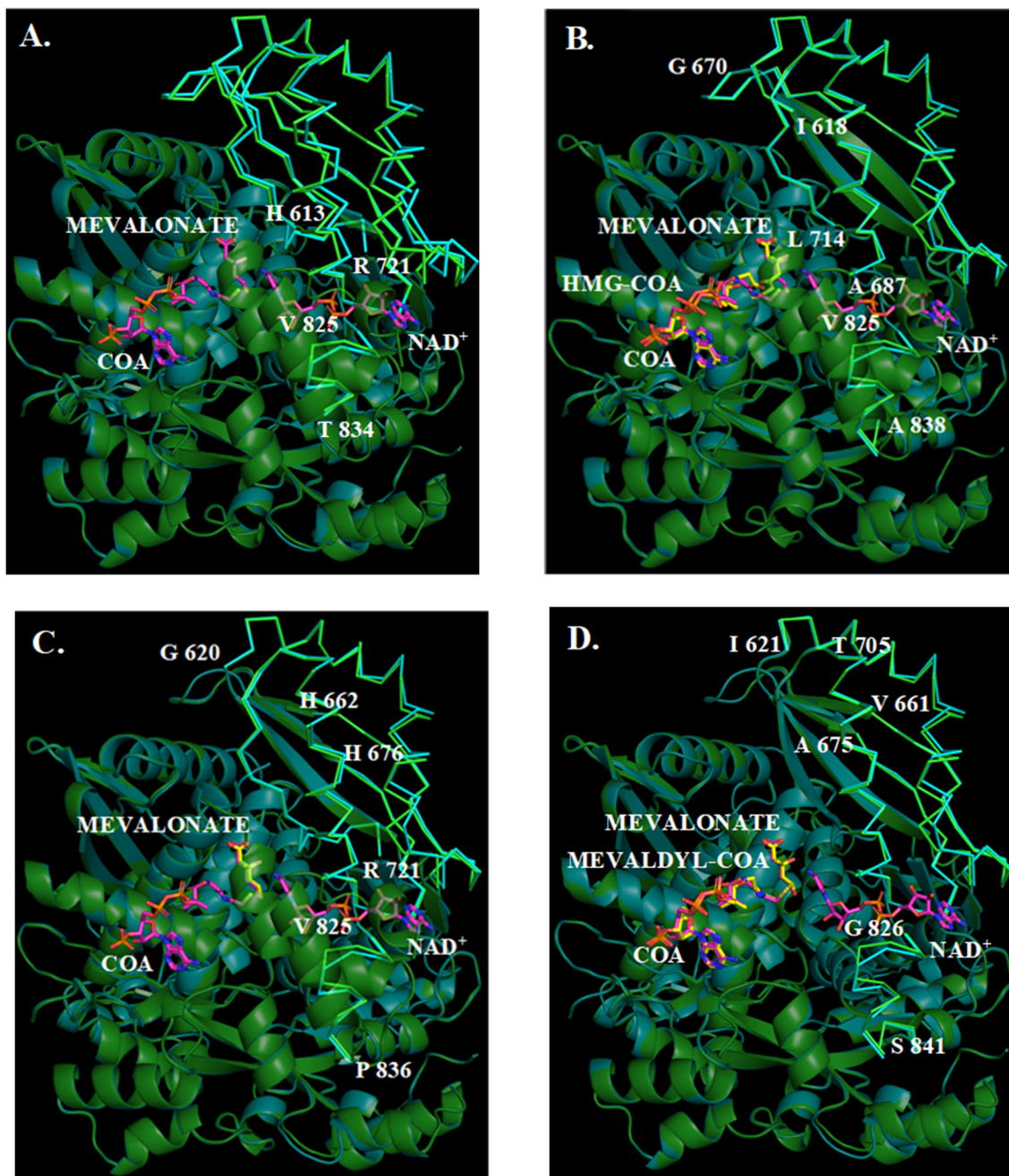


Figure 5.3 Changes observed in the quaternary structure with mevalonate, CoA and NAD<sup>+</sup> (green) in comparison to the A. apoenzyme (teal) and structure with B. HMG-CoA C. Mevalonate, D. Mevaldyl-CoA E. NADH, F. CoA, G. Mevalonate and NAD<sup>+</sup>, H. Mevalonate and NAD<sup>+</sup> (without flap), I. CoA and NAD, J. HMG-CoA and NAD<sup>+</sup>

Figure 5.3 continued

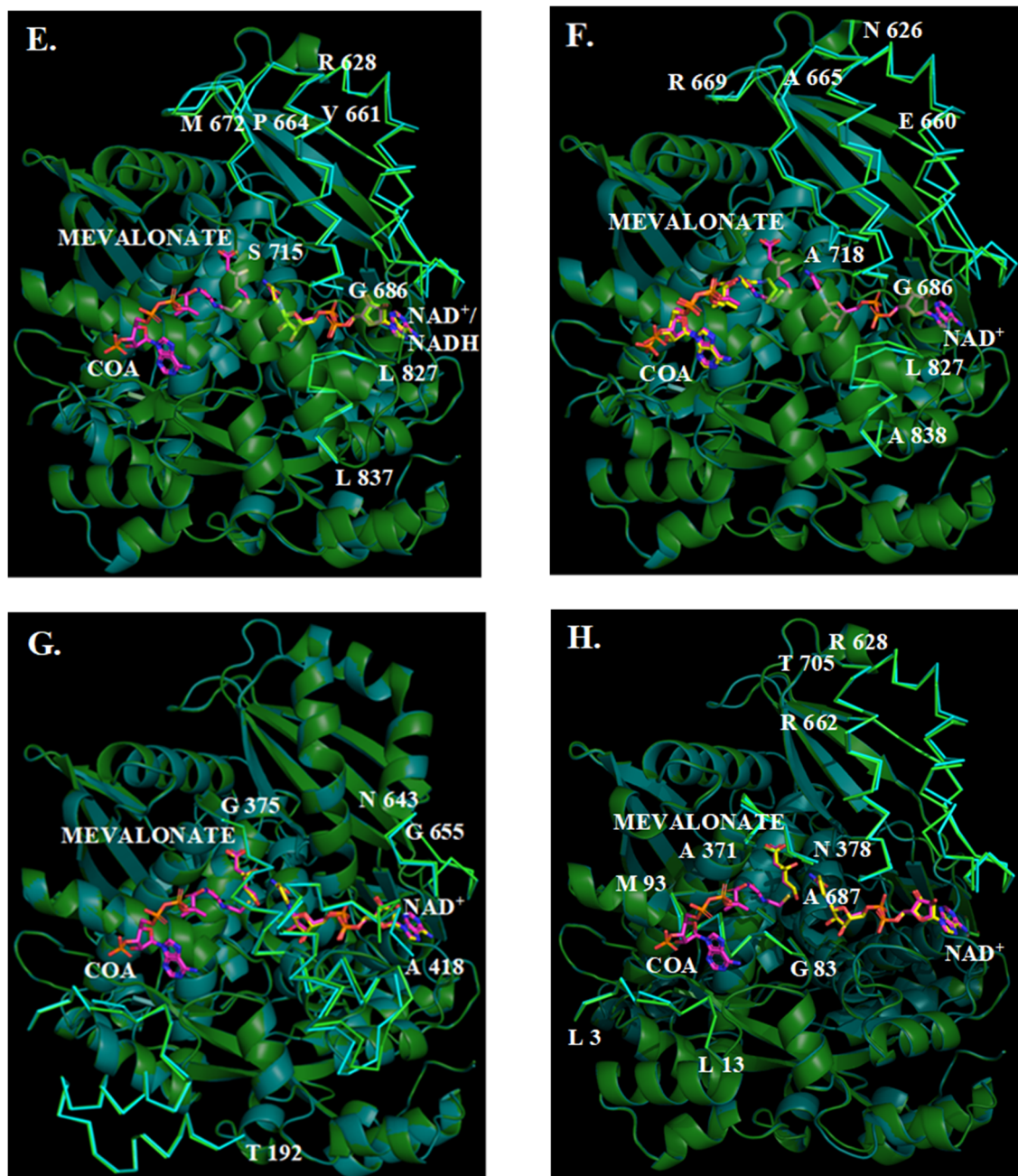




Figure 5.3 continued

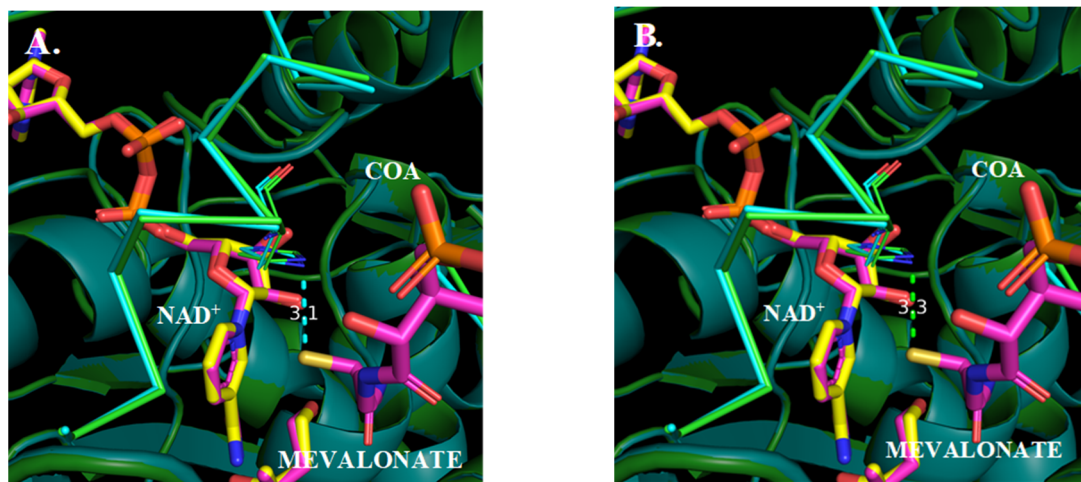
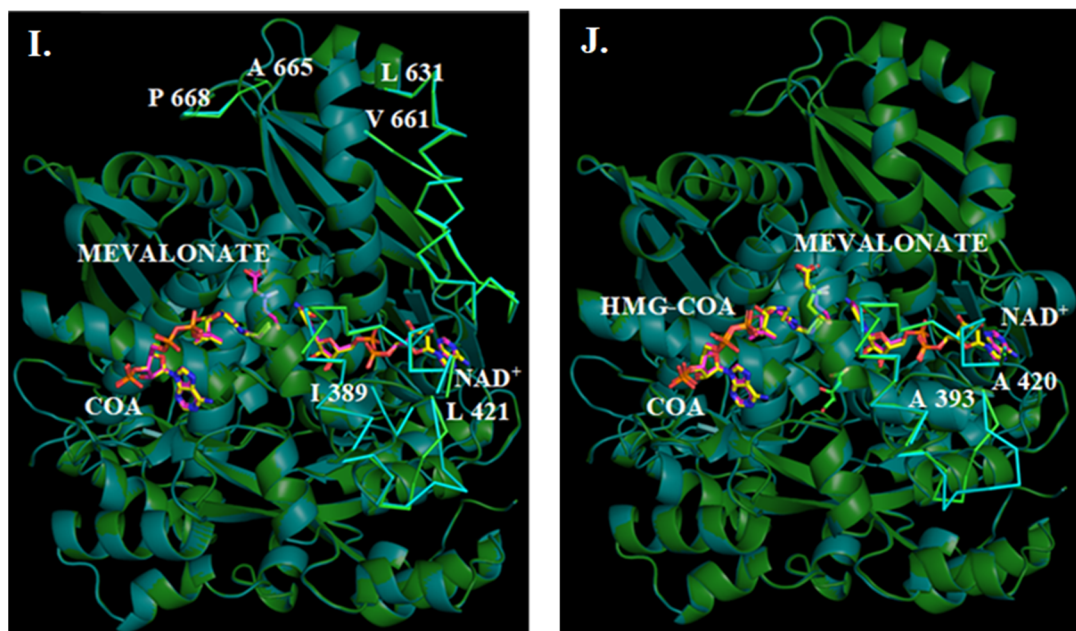


Figure 5.4 A. Changes observed in the active site between the catalytic histidine (HIS 381) and CoA in the quaternary complex (purple / green) and B. Mevalonate and NAD (yellow / teal) bound ternary complex.

### 5.3.2 pH jump experiments in *Pm*HMGR crystals

To capture changes that occur in the mevalonate, CoA and NAD<sup>+</sup> bound enzyme after reaction initiation the pH-jump triggering approach was utilized. As was demonstrated, in 0.4 mm crystals using the spectral signature of NADH in Chapter 4 (Section 4.3.1), the time range for observing the progression of the *Pm*HMGR from reaction initiation to product release was identified to be 10 minutes. Using this rationale, we prepared several *Pm*HMGR crystals after slowly introducing the pH-jump buffer and the ligands mevalonate, CoA and NAD<sup>+</sup> at pH 6.7 and subsequently transferring them to pH 9 before being freeze trapped. A set of crystal samples that had been soaked at pH 9 at sparse time points ranging from 20 seconds – 10 minutes was prepared. Diffraction data from these crystals were obtained with resolutions ranging from 2.06 Å – 2.5 Å.

#### 5.3.2.1 Observed electron density changes in *Pm*HMGR crystals after buffer exchange

The crystals were soaked in an ammonium acetate, ADA and PEG-400 (pH-jump buffer) environment at pH 6.7 to introduce the ligands in an inactive crystal environment as was inferred from the pH-rate profile and UV-Vis spectroscopy experiments (Fig 3.6, 4.2). The crystallographic structure obtained in *Pm*HMGR crystals after being slowly soaked with the pH-jump buffer at pH 6.7 indicated the presence of NAD<sup>+</sup>, CoA and mevalonate. The structure also showed the lack of thioester bond formation or NAD<sup>+</sup> reduction as is observed in the polder maps generated in the mevalonate, CoA and NAD<sup>+</sup> region (Fig 5.5).

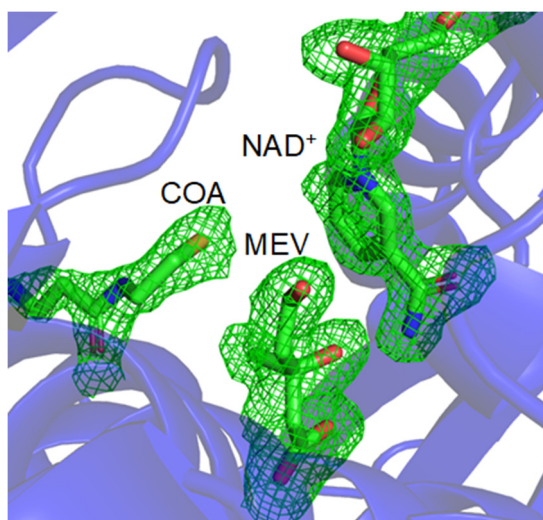


Figure 5.5 Active site region with 3 $\sigma$  Fo-Fc omit map density from a 1.93 Å X-ray structure obtained from *Pm*HMGR crystals soaked with mevalonate, CoA and NAD after being pre-soaked in pH-jump buffer.



### 5.3.2.2 Changes in the thioester region between mevalonate and CoA

The thioester region between the substrate mevalonate and cofactor Coenzyme A was compared at different time points after *Pm*HMGR crystals were soaked at pH 9 and then diffracted. Changes in this region would indicate the formation of the intermediate, mevaldyl-CoA and eventually the product HMG-CoA. We compared the changes in omit map Fo-Fc density after modelling HMG-CoA at the active site in these structures and observed that after long soaking times between 4-5 minutes (Fig 5.6 C-D), we observe the appearance of a thioester bond density between the mevalonate and CoA portions. Additionally, we also observed that at longer soaking times (8-10 minutes) (Fig 5.6 G), we observe a disappearance of thioester bond density and a reduction of the electron density in the entire molecule (10 minutes) (Fig 5.6 H). We also observe a steady decrease in negative (red) Fo-Fc density in the thioester bond region going from the pre-pH jump structure to the one where we observe strong density for the thioester bond region indicating an increasing proclivity and rearrangement of the ligands to allow formation of the second intermediate. Additionally, we also observe a slow build up of thioester bond density while comparing 2Fo-Fc maps in thioester bond region from 1 minute – 5 minutes (Fig 5.6 I-L).

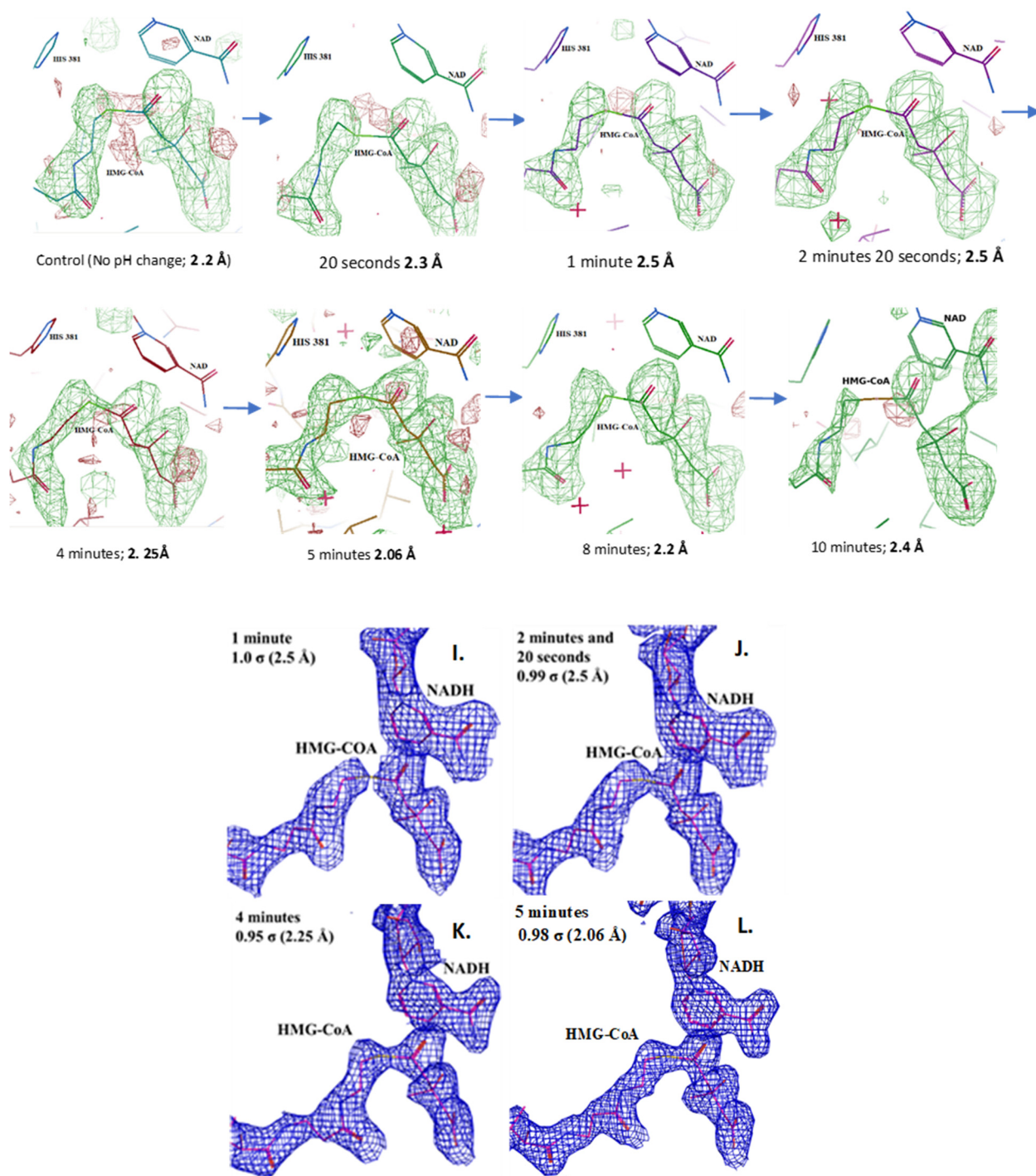


Figure 5.6 Changes in refined omit maps in the thioester bond region before (A.) and after a change from 20 seconds – 10 minutes after being introduced to a pH 9 environment (B-H). Changes in thioester bond density observed in 2Fo-Fc maps from 2 minute 20 seconds to 5 minutes after *Pm*HMGR crystals are introduced to a pH 9 environment (I-L)

An initial analysis on movements in the protein molecule across the different time points observed was conducted across the different sparse data points. To do this analysis, we compared the structures obtained at different time points after the pH jump with the quaternary complex crystal structure in the crystallization buffer at pH 6.7.

### **5.3.2.3 Movements observed in post pH-jump structures associated with thioester bond formation and product release:**

Given that thioester bond formation between mevalonate and CoA is only observed 5 minutes after the enzyme is introduced to pH 9, we wanted to follow the changes that it undergoes prior to that step in the reaction mechanism. These changes include the hydride transfer step with mevalonate and NAD<sup>+</sup> resulting in the formation of mevaldehyde, NAD<sup>+</sup>/NADH exchange and changes leading up to thioester bond formation.

Following a transfer of *Pm*HMGR crystals to a higher pH environment, we studied the significant movements obtained at different time points at higher pH in comparison to structures obtained at pH 6.7. At the 20 second time point, a shift in the flap position (Fig 5.7 A.) is observed that correlates with a change in the position of adenine in NAD<sup>+</sup> (Fig 5.7 A – marked in red, B). Distances between VAL 392 (CG1 and O) and the Adenine (C8A) position were also found to increase by 0.3 Å and 0.5 Å respectively. A change in the nicotinamide position (Fig 5.7 A – marked in yellow, C) is also observed with the amide nitrogen of nicotinamide moving towards Mevalonate by 0.4 Å after 20 seconds. The distance between Mevalonate and Coenzyme A is found to increase by 0.2 Å at 20 seconds (Fig 5.7 A – marked in blue, D).

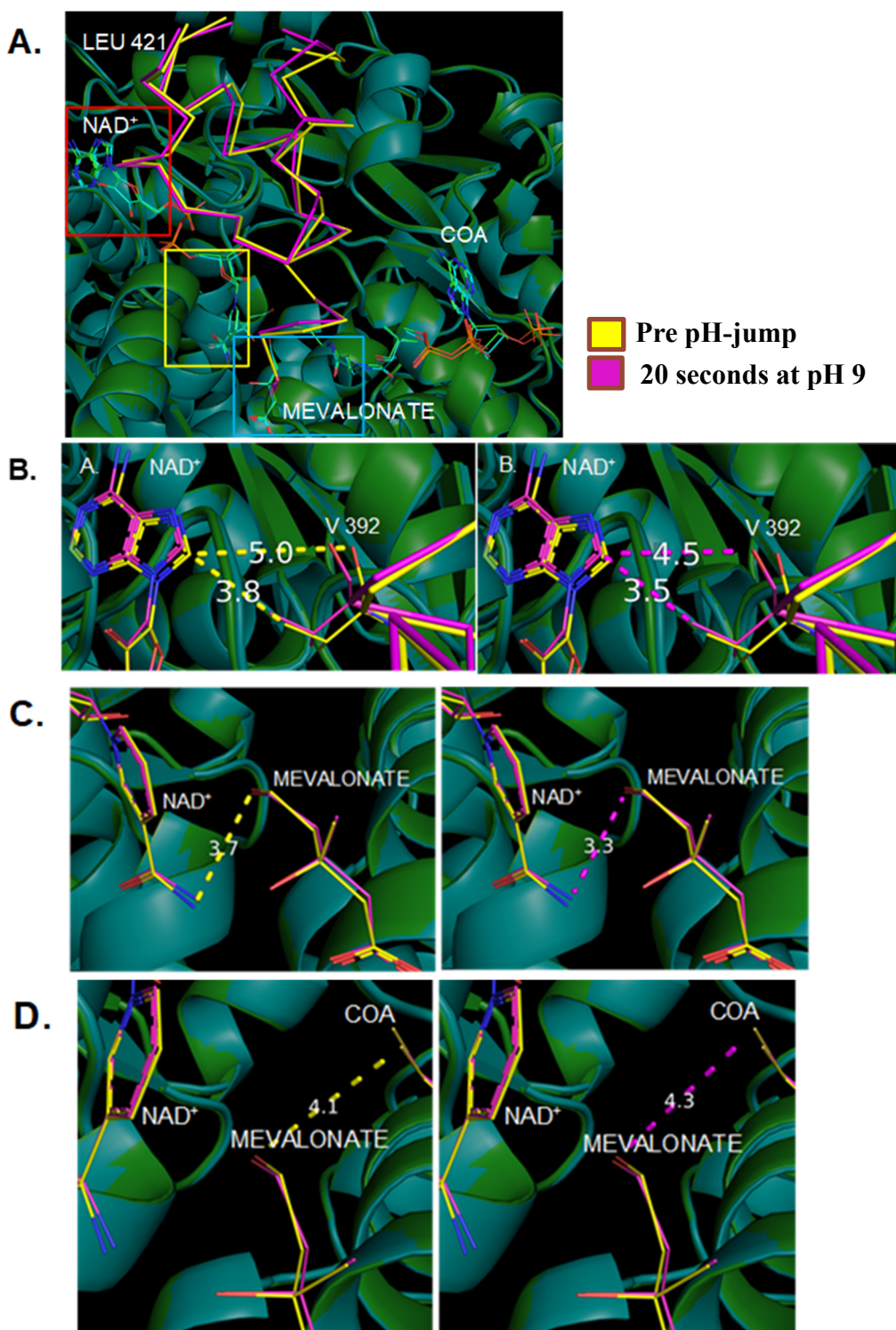


Figure 5.7 Structures showing A. Flap domain comparisons B. Distance between NAD (Adenine) and VAL 392, C. Distance between Nicotinamide and Mevalonate, D. Distance between Mevalonate and CoA at 20 (2.3 Å) sec (purple) and before a pH jump (yellow).

Continued movement of the enzyme continues to be observed in the flap domain 1 minute after the pH-jump in comparison to the crystallization environment at pH 6.7 (Fig 5.8A.). In the structure obtained at 1 min, regions of the flap domain (HIS 385 – VAL 392) were found to be closer to the control quaternary complex structure that was observed at 20 sec. The distance between the NAD<sup>+</sup> Adenine (C8A) and Val 392 in the *Pm*HMGR flap region is also not as short at 1 minute as it was at 20 seconds (Fig 5.8A – marked in red, Fig 5.8B). In the structure observed 1 minute after a change to pH 9, the distance between the NAD<sup>+</sup>-nicotinamide nitrogen and mevalonate hydroxyl oxygen wasn't as close (3.5 Å) as that observed at 20 seconds (3.3 Å) (Fig 5.8A – marked in green, Fig 5.8C.). The distance between mevalonate hydroxyl oxygen and CoA thiol was also observed to decrease from 4.1 Å to 4.0 Å.

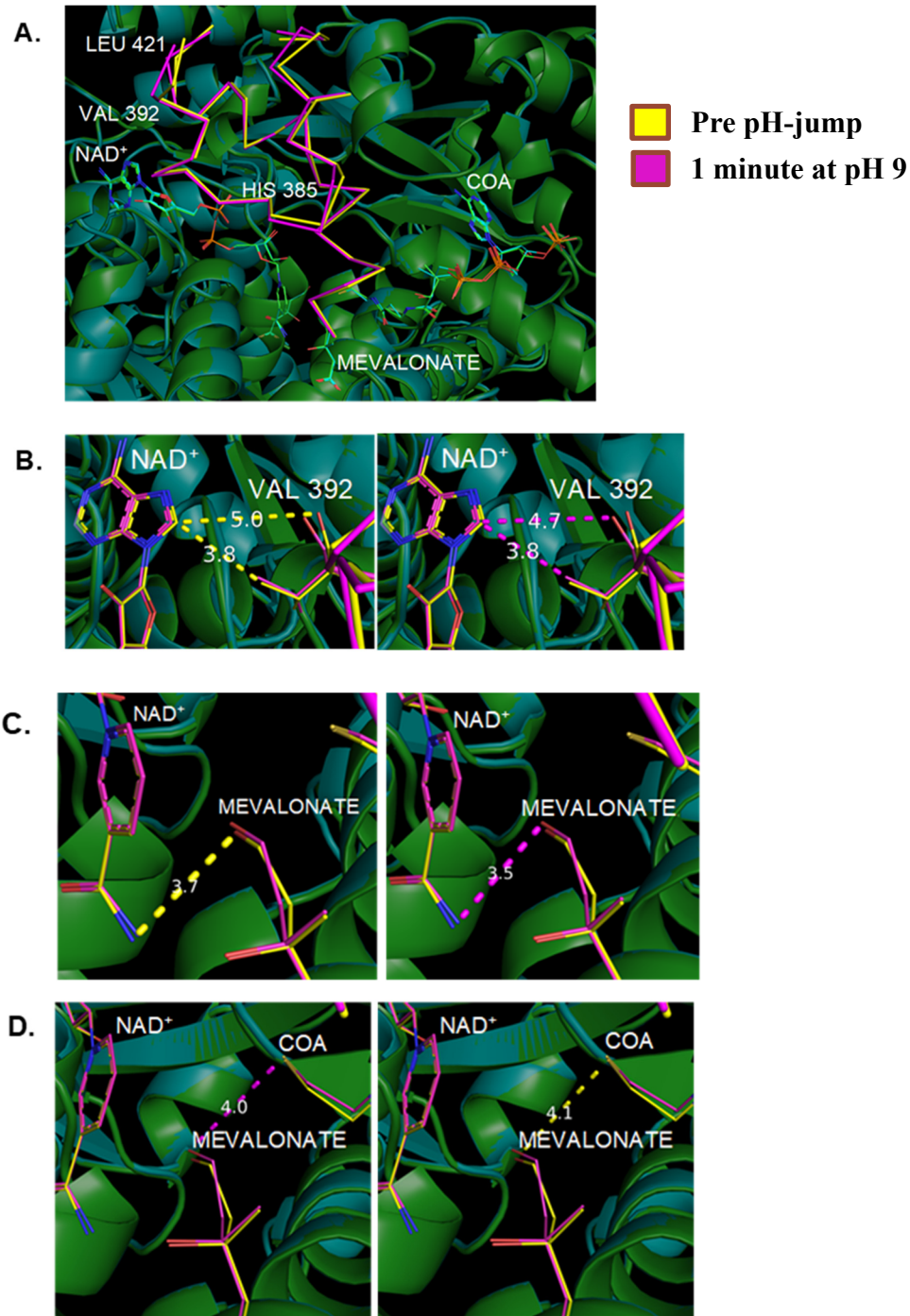


Figure 5.8 Structures showing A. Flap domain comparisons B. Distance between NAD (Adenine) and VAL 392, C. Distance between Nicotinamide and Mevalonate, D. Distance between Mevalonate and CoA at 1 min (2.5 Å) after a pH-jump (purple) and before a pH-jump (yellow).



At 2 minutes and 20 seconds, we observe a movement in the large domain residues 3-40 which can be linked to the movement of CoA. The adenine region of CoA is also observed to change its distance relative to the flap domain residue T 384 by 0.3 Å (Fig 5.9 B). The movement of the ribose-phosphate regions of CoA is also visible. While their distance from the neighboring large domain region (PRO 8) is observed to be the same, the sidechain itself is observed to move by 1.3 Å. At this time point, we also happen to visually observe changes in the configuration of the first helix of the flap domain (E 375 – A 386) in comparison to the pre-pH jump structure in the crystallization environment at pH 6.7 (Fig 5.9 A - marked in green) The difference in this region has also been documented via RMSD comparisons (Fig 5.9 C). A tilt in HIS 381 (12.5° for the amide nitrogen – Fig 5.9 D) towards CoA has been measured.

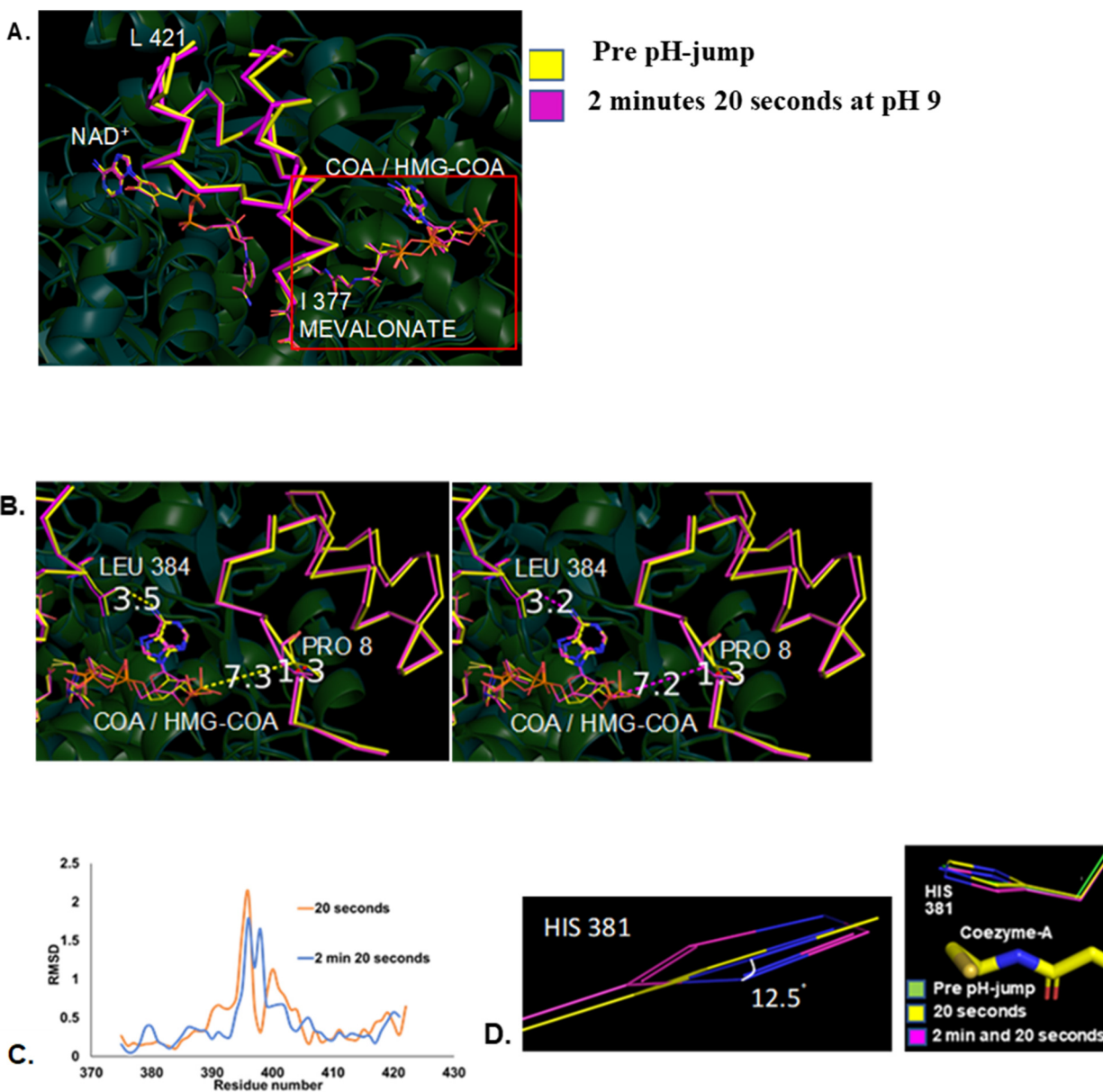


Figure 5.5.9 Structures showing A. Flap domain comparisons B. Distance between HMG-CoA / Mevaldyl-CoA (Phosphate) and Pro 8, C. RMSD comparisons of PmHMGR 20 seconds and 2 minutes and 20 seconds after being introduced to a pH 9 environment D. Change in the position of amide nitrogen in HIS 381 at 2 minutes 20 seconds (2.5 Å) after a pH jump (purple) and before a pH jump (yellow).



At 4 minutes after being introduced to a pH 9 environment, a movement in the large domain residues towards CoA continues to be observed (Fig 5.10 A – marked in red, B). A similar positional difference in the orientation of His 381 towards the thiol-atom in CoASH is also observed (Fig 5.10 C).

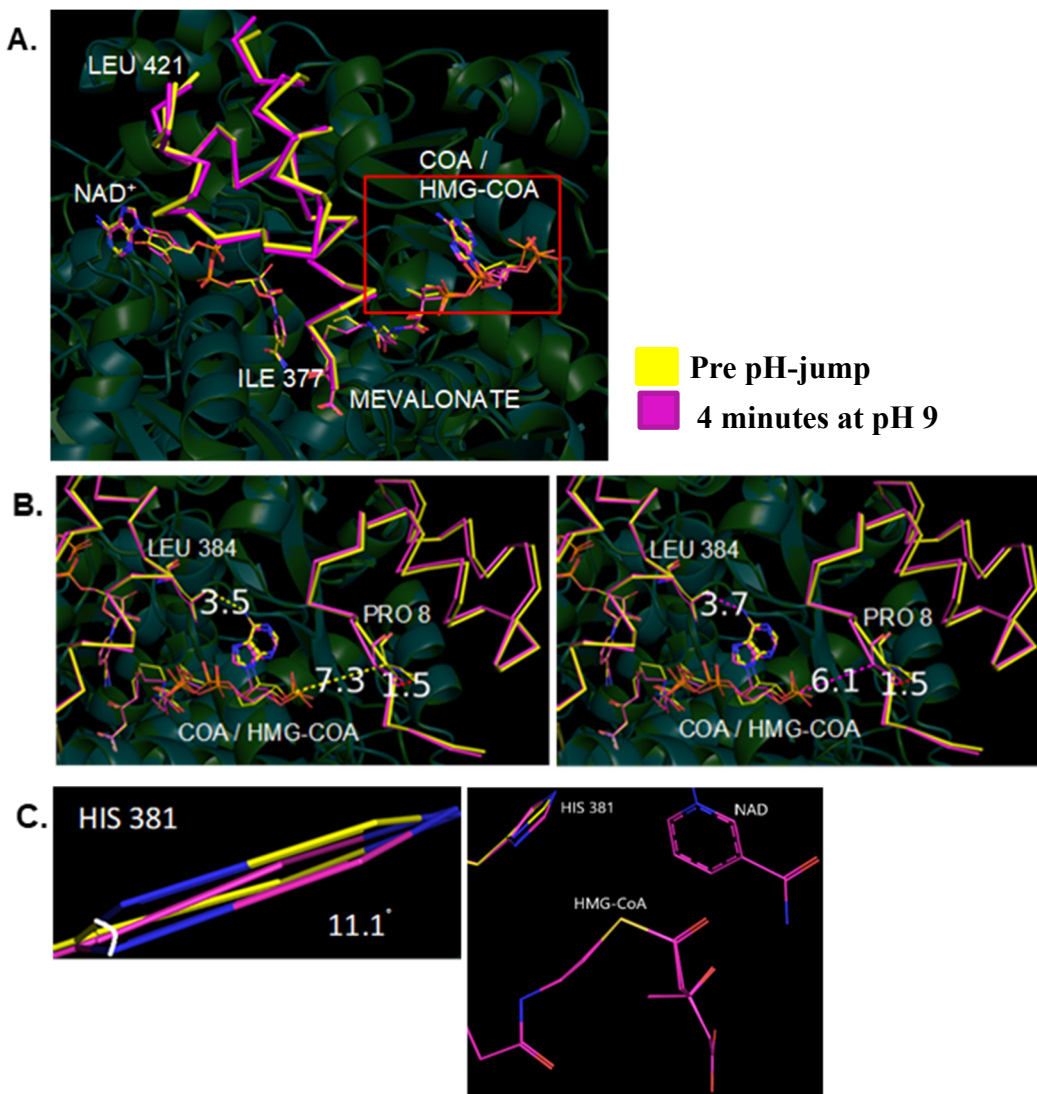


Figure 5.10 Structures showing A. Flap domain comparisons B. Distance between HMG-CoA / Mevaldyl-CoA (Phosphate) and Pro 8, C. RMSD comparisons of PmHMGR 20 seconds and 2 minutes and 20 seconds after being introduced to a pH 9 environment D. Change in the position of amide nitrogen in HIS 381 at 2 minutes 20 seconds (2.5 Å) after a pH jump (purple) and before a pH jump (yellow).

The position of NAD<sup>+</sup> doesn't fluctuate between 1 min – 4 min. However, at the 5-minute time point (2.06 Å), while the formation of the thioester bond was still observed (Fig 5.6.), we also observed the presence of an alternate position for the NAD<sup>+</sup>-adenine at 5 minutes. After comparing the distance of the adenines with the flap (VAL 392) and small domain (LEU 649), we observed 2 alternate configurations of NAD<sup>+</sup> adenine. In one, the adenine is placed closer to the flap domain and away from the small domain (Fig 37 A (marked in red), 5.11 B) and in another it is facing out into the solvent, away from the flap domain and closer to the small domain (Fig 5.11 A (marked in red), 5.11 B). The position of the CoA portion of HMG-CoA at 5 minutes with respect to the adjacent large domain (Fig 5.11. C) and HIS 381 (Fig 5.11. D) doesn't deviate significantly from that observed before the pH jump.

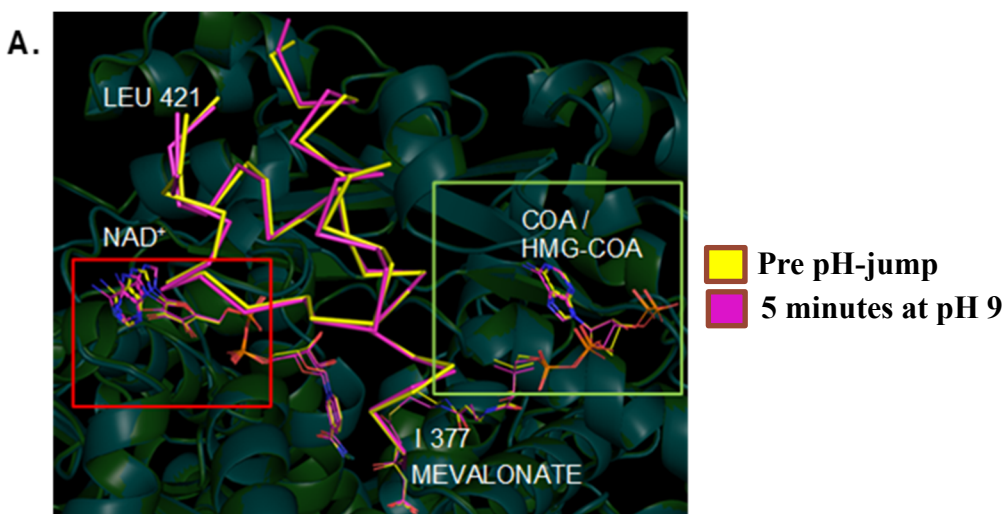
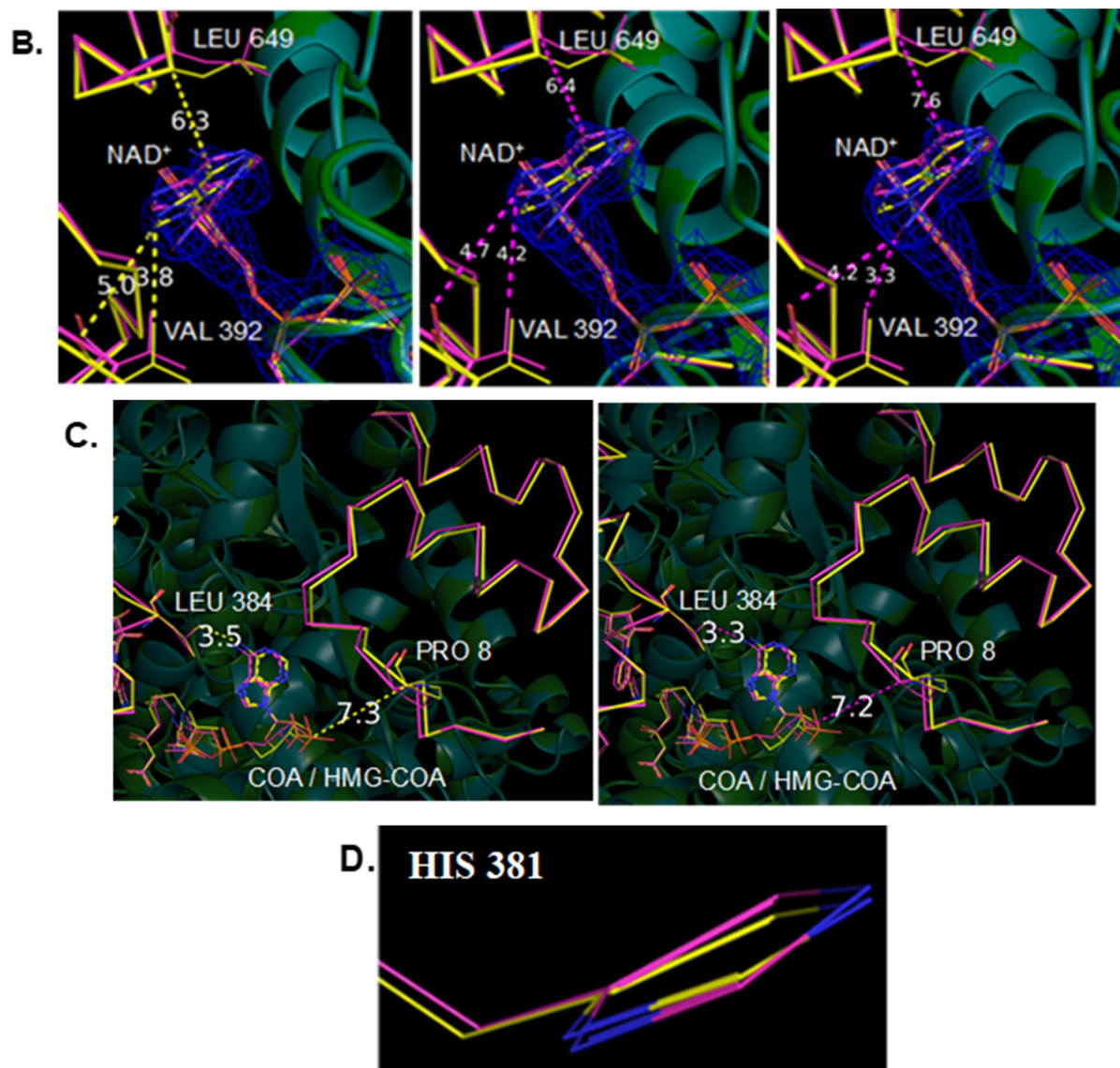


Figure 5.11 Structures showing A. Flap domain comparisons, Distance between NAD (Adenine) and Small domain (LEU 649) / Flap domain (VAL 392) for B. Control quaternary complex at pH 7 , Adenine (pos 1), Adenine (pos 2) for a structure obtained 5 min (2.06 Å) C. Distance between CoA (phosphate) and large domain (PRO 8) D. HIS 381 conformation after a pH jump (purple) and before a pH jump (yellow).

Figure 5.11 continued



At 8 minutes, the position of HMG-CoA is observed to move away from the active site with the distance between the HMG-CoA-phosphate and PRO 8 on the large domain significantly decreasing (Fig 5.12. A – marked in red, B). We also observe a change in the position of nicotinamide in NAD<sup>+</sup> with respect to the modelled HMG-CoA (Fig 5.12 B). While the distances of the nicotinamide amine group with respect to Mevalonate and the HMG-CoA O atoms remains the same in the crystallization buffer and 8 minute post-pH jump structure, the relative distance seems to have changed to allow for a re-orientation of NAD<sup>+</sup> after formation of Mevaldyl-CoA that could enable their interaction (Fig 5.12. A – marked in green, C). The position of the NAD<sup>+</sup>-Adenine is again found to be very close to that found in the control structure (5.12 D). This continued conversion of CoA into CoASH is observed with the residue involved in the proton transfer step – HIS 381, where the amine nitrogen changes conformation by 16.5°, which is the highest observed difference in HIS 381 so far (Fig 5.12 E.). We also observe a reduction in the density of Coenzyme-A in the adenine and ribose regions 8 minutes after being introduced into a pH 9 environment (Fig 5.12 F).

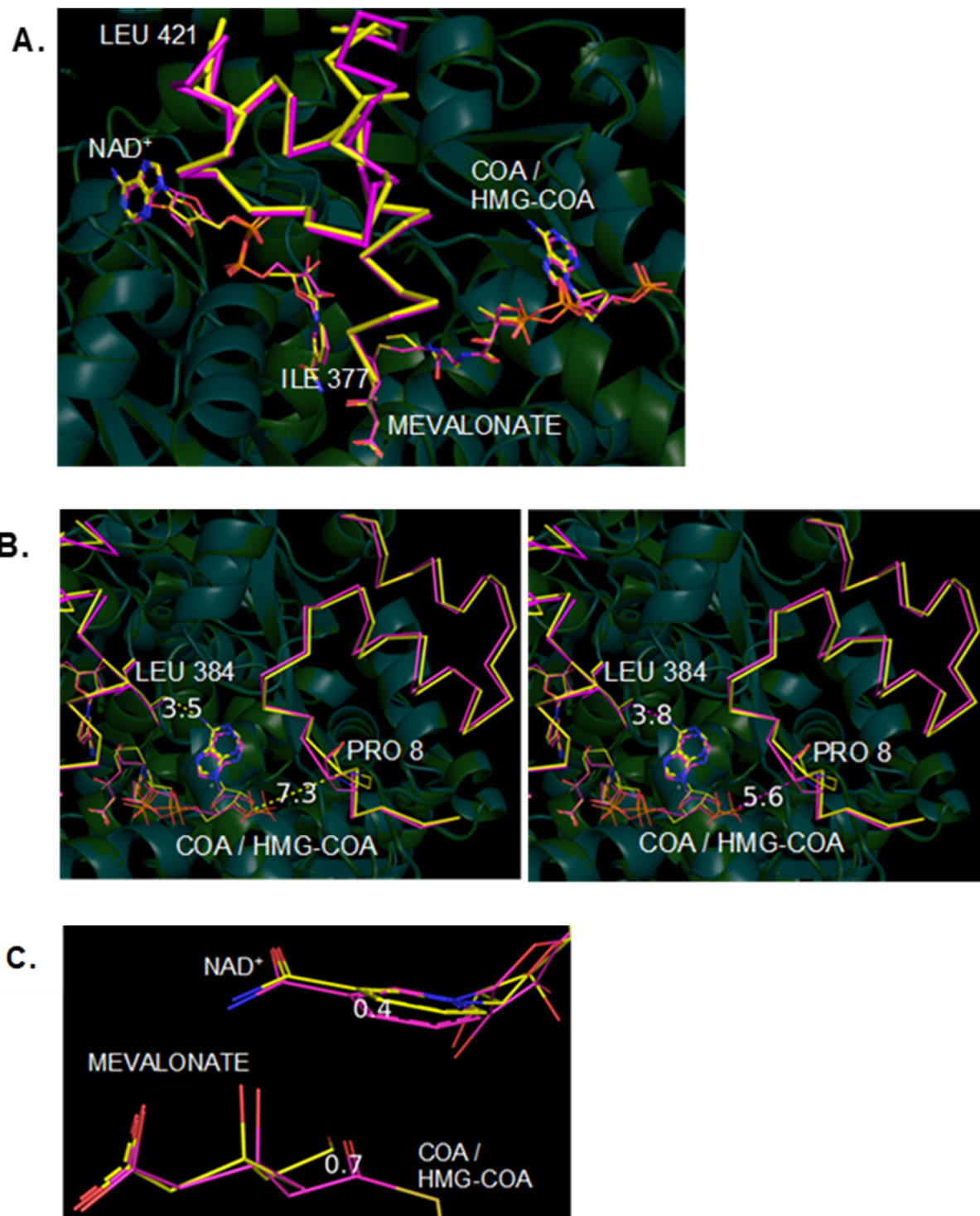
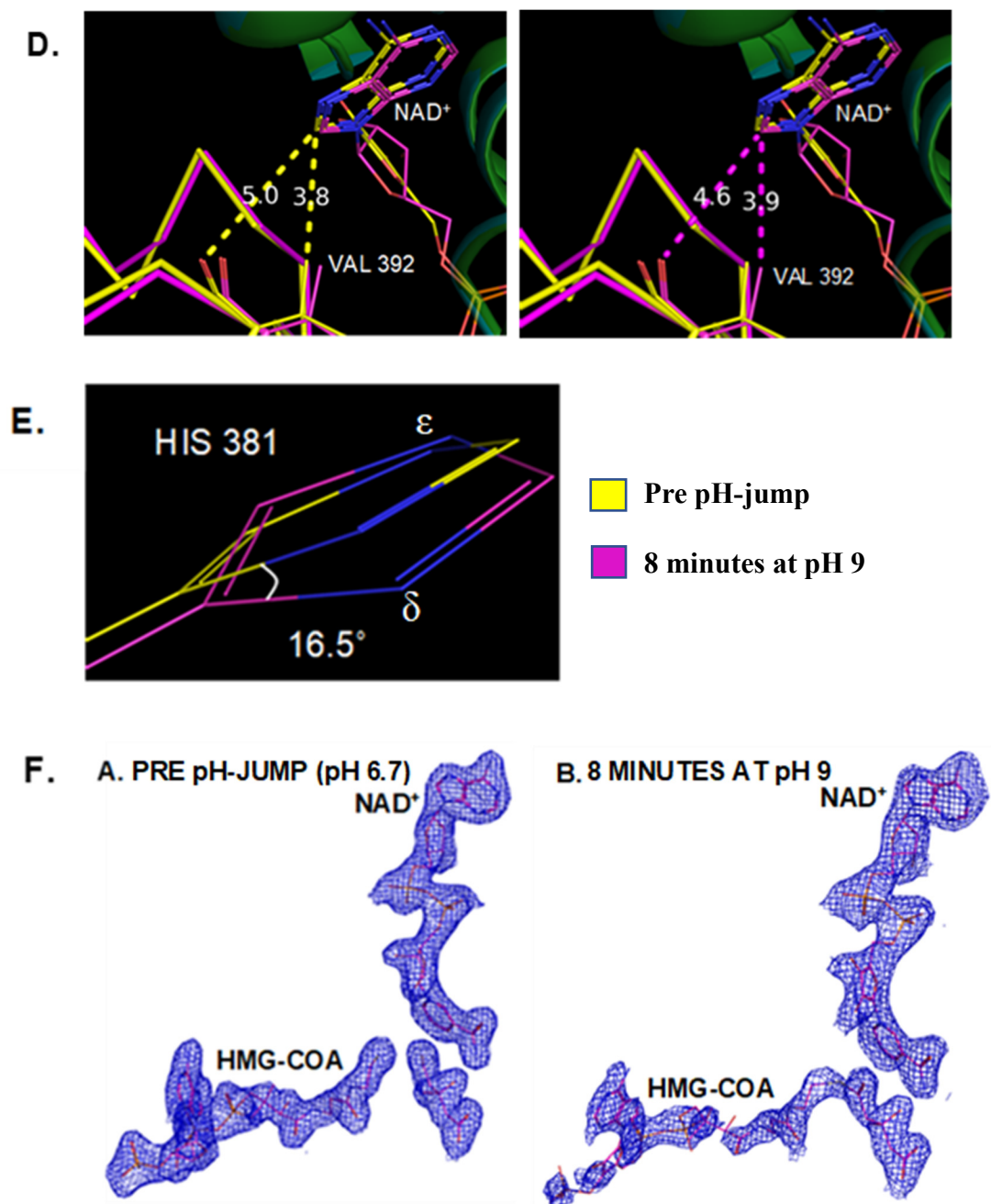


Figure 5.12 Structures showing A. Flap domain comparisons, B. Distance between CoA (phosphate) and large domain (PRO 8) C. Distance between NAD and Mevalonate / Mevaldyl-CoA D. Distance between NAD (Adenine) and flap domain (VAL 392) obtained 8 minutes after a pH jump (purple) and before a pH jump (yellow). E. HIS 381 conformations F. HMG-CoA and NAD<sup>+</sup> electron density in the pre pH-jump (pH 6.7) and 8 minutes after being introduced to a pH 9 environment.



Figure 5.12 continued



At 10 min, we see residue regions ALA 393 - TYR 410 of the flap domain lose density and residues from HIS 385 – VAL 392 show a drastic reduction in electron density (Fig 5.13 A, 5.15). We see a reduction of electron density of Coenzyme-A portion of HMG-CoA weaken in the crystal structure (Fig 5.14.) and observe a shift in the position of its adenine-ribose region with respect to the large domain (Fig 5.13 B, C). Movements in the flap domain in the region E 375 – M 382 is observed indicating a further change in the position of HIS 381 towards the active site (Fig 5.13 D). Movement of this flap domain could also be an outcome of product release at the active site. Lastly, we also observe a change in the conformation of the flap and small domain away from the active site and a different ribose-phosphate position of NAD<sup>+</sup> (Fig 5.13 E)

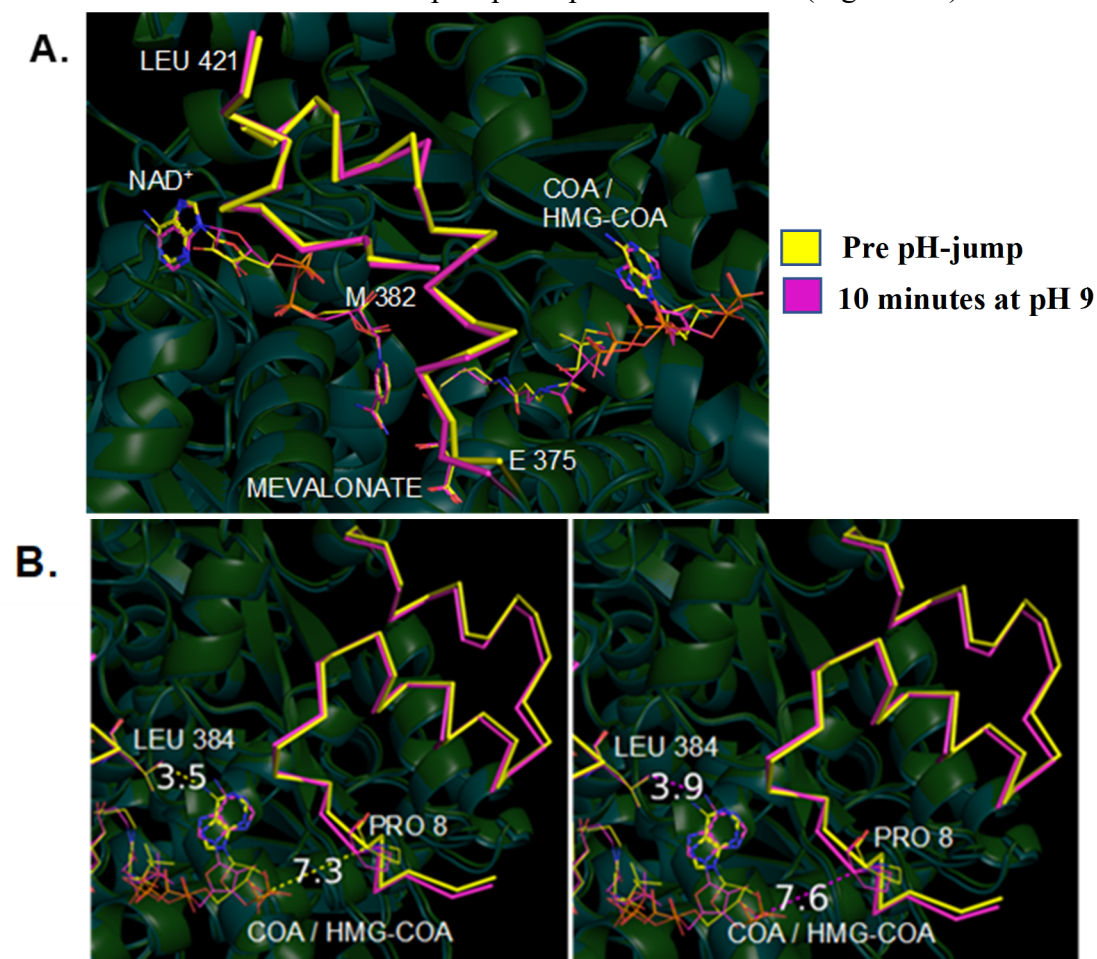
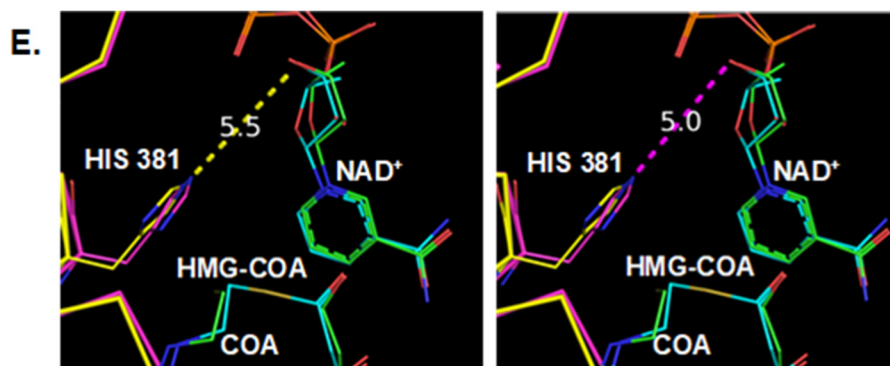
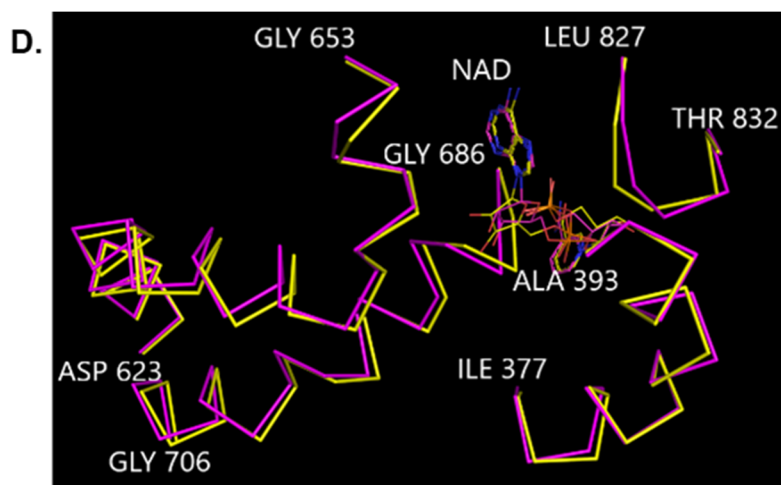
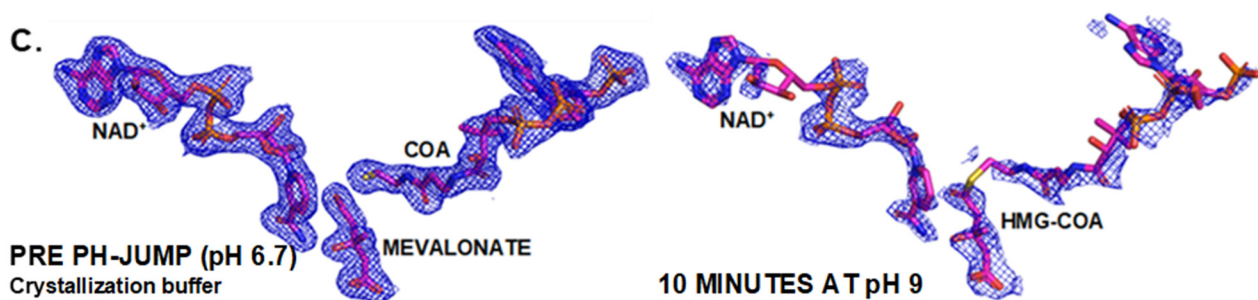


Figure 5.13 Structures showing A. Flap domain comparisons, B. Changing interactions between CoA and PRO 8 (Large domain) / LYS 384 (Flap domain) before and 10 minutes after a pH-change (pH 9), C. Changing 2Fo-Fc density (1 rmsd) before and 10 minutes after a pH-change (pH 9), D. Conformational changes in the small domain around NAD obtained 10 minutes after a pH jump (purple) and before a pH jump (yellow), E. HIS 381 conformation before (yellow) and after a pH-change (purple). Pre and post pH-change ligands shown in green and teal respectively.

Fig 5.13 Continued





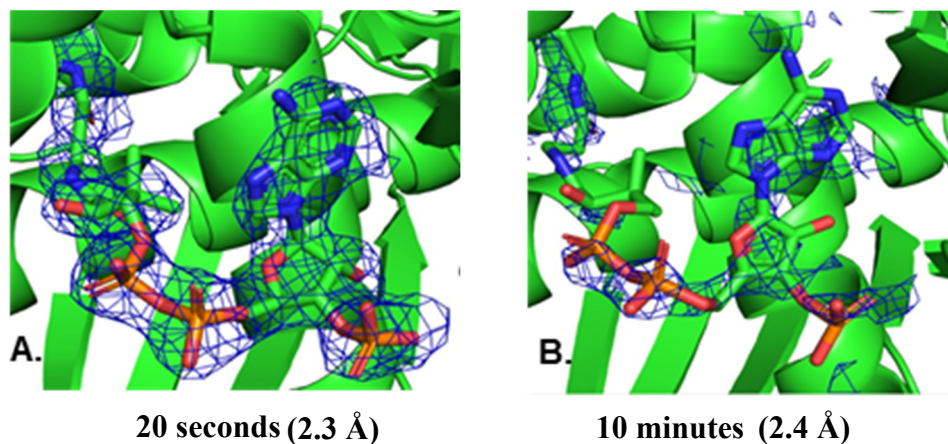


Figure 5.14 2Fo-Fc electron density observed in the CoA adenine region 20 seconds (A.) and 10 minutes (B.) after *Pm*HMGR crystals were soaked at pH 9.

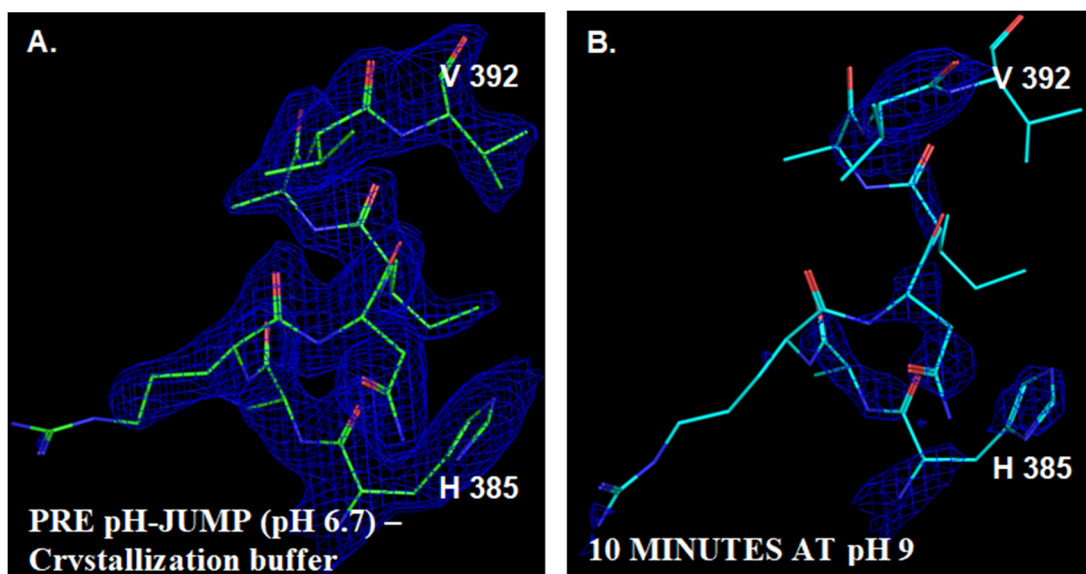


Figure 5.15 Changes in electron density in the residue region H 385 – I 389 before and after a pH-change (A.) at pH 9 at 10 minutes (B.).

#### 5.3.2.4 Conformational changes observed in the flap domain in post pH-jump structures

Conformations of the flap domain regions are also compared at different time points to identify corresponding movements in this region that are associated with biochemical changes at the enzyme active site.

The changes observed across various time points brings into focus the movements observed in the acquired structures that are mediated by the flap domain. Flap domain regions that are neighboring NAD<sup>+</sup> (A 386 – V 393 and R 414 – N 423) are observed to undergo an initial contraction away from NAD<sup>+</sup> 20 – 140 seconds after being introduced into a pH 9 environment (Fig 5.16 A, B). They are subsequently shown to undergo an expansion towards NAD<sup>+</sup> 4 – 5 minutes and contract again 8 – 10 minutes following a change to a pH 9 environment (Fig 5.16 A, B). However, regions near CoA (I 377 – H 385 and E 399 – H 411) are shown to expand 20 – 140 seconds after being introduced to a pH 9 environment (Fig 5.16 A, B).

The interhelical region between the first and second helix (ALA 393 – VAL 400) has been observed to show significantly increased rigidity in transition states of the first hydride transfer step converting mevaldehyde to mevalonate using a QM/MM-MD approach<sup>[94]</sup>. Therefore, we have also compared observed changes in this region at different time points after reaction initiation.

Changes in the electron density of the interhelical portions of *Pm*HMGR (G 394 – E 399) are observed over time with the electron density weakening significantly at 1 minute (Fig 5.17 C) in comparison to the 20 second and 140 second structures (Fig 5.17 B, D). In structures where we observe the formation of a thioester bond (140 seconds – 5 minutes), we observe a stronger electron density for all the mainchain atoms in this region (Fig 5.17 E-F). At the subsequent time point of 8 min that indicate the onset of ligand release, we observe a further reduction in the interhelical density of G 394 – E 399 and no density 10 minutes after a pH-jump (Fig 5.17 G).

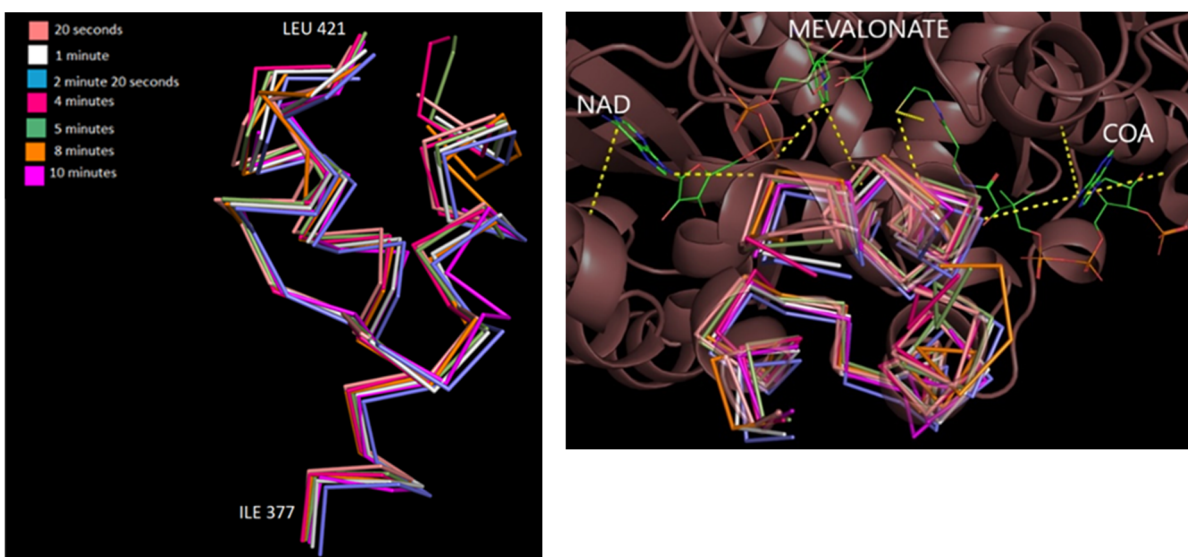


Figure 5.16 A. Flap domain conformations at different time points (20 seconds – 10 minutes), B. Network of interactions between flap domain and small / large domains mediated via the ligands bound at the active site.

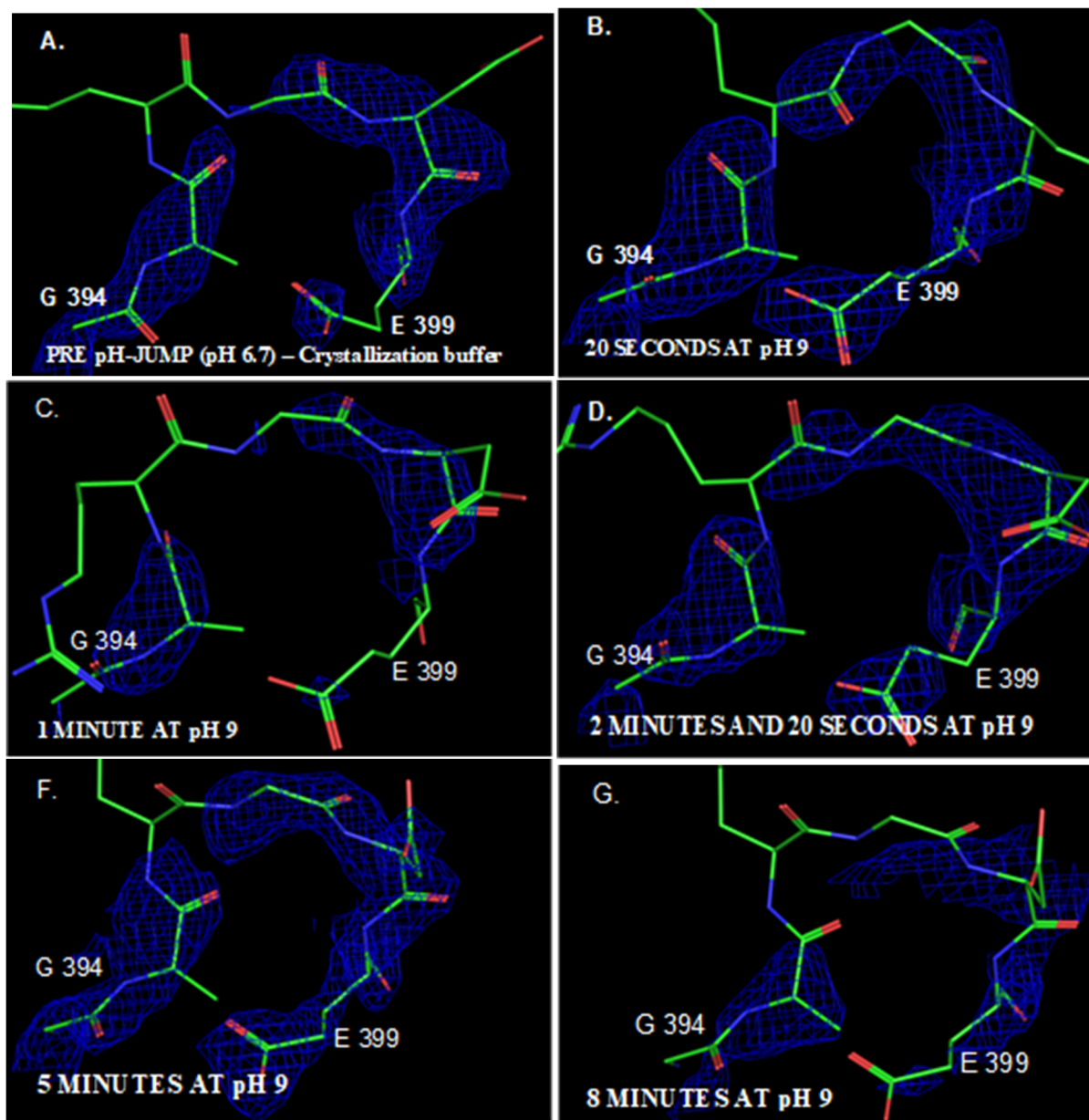


Figure 5.17 Electron density in the PmHMGR flap residue region G 394 – E 399 in (A.) the crystallization buffer environment (pH 6.), B. 20 sec, C. 1 minute, D. 2 min 20 sec, E. 4 min, F. 5 min and G. 8 minute after being introduced to a pH 9 environment

### 5.3.3 Changes in the NAD<sup>+</sup> and mevalonate interaction site

Movements between NAD<sup>+</sup> / NADH and mevalonate / mevaldehyde were compared within the first minute of reaction initiation. Given that we observe NADH production within the first minute as per measured UV-Vis spectra (Fig 4.4), we modelled the ligands NADH and mevaldehyde at the enzyme active site and compared the distance between the C4 atom of NAD<sup>+</sup>/NADH, the terminal carbon atom of mevalonate / mevaldehyde and a thiol atom for CoA. By comparing these distances, we wanted to see if the changes observed between the modelled ligands follow a trend that can be associated with a hydride transfer. While the models themselves do introduce a bias measurement, this comparison gives us an initial idea of what the changes at the active site with post hydride-transfer models would indicate.

On comparing the positioning of the cofactor at the active site, we observe a tilt in the nicotinamide ring with the amine group on nicotinamide tilting by 0.3 Å 20 seconds after the crystal has been soaked at pH 9 (Fig 5.18 A.). 1 minute after the soak, the nicotinamide portion of NAD<sup>+</sup> shows lesser deviation from the control structure with the amide region at the same position as that observed before the pH jump and carboxyl region only deviating by 0.2 Å (Fig 5.18 B).

We also observe a 0.4 Å movement of mevalonate that can be correlated with the changing position of nicotinamide in NAD<sup>+</sup> (Fig 5.19 A). The conformational change that would occur with the conversion of NAD<sup>+</sup> into NADH can also be correlated with the observed change in the mevalonate binding region that is modelled to be mevaldehyde (Fig 5.19 A.). This movement of the C1 atom in mevaldehyde in comparison to the structure obtained before the pH jump is observed to marginally reduce by 0.1 Å at 1 minute (Fig 5.19 B).

While the resolution also cannot resolve the differences between the substrate and intermediate, mevalonate and mevaldehyde, a change in the orientation of the carboxyl end of this molecule is observed where the carboxyl oxygen is found to shift by 0.5 Å in comparison to the pre-pH jump structure (Fig 5.20 A). At 1 min, we observe this distance to be 0.4 Å with the region from C2-C5 moving closer to CoA by 0.2 Å (Fig 5.20 B, 5.21 C).

We compared the distance between C4 atom of NAD<sup>+</sup>/NADH and terminal carbon of mevalonate / mevaldehyde which are involved in a hydride transfer for mevalonate oxidation. Our measurements indicate a marginal (0.2 Å) increase in this distance over time from the pre-pH-jump structure to that observed 1 minute after a pH-change (Fig 5.21 A-C). We also observe a small increase in the distance of the terminal carbon in mevaldehyde away from the CoA thiol 20

seconds after reaction initiation followed by a movement of 0.2 Å towards CoA after 1 minute (Fig 5.22 A-C).

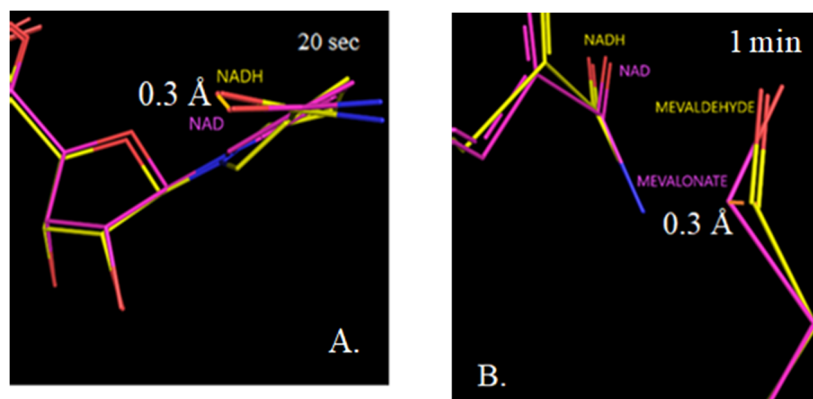


Figure 5.18 Nicotinamide region of *PmHMGR* observed (yellow) A. 20 seconds and B. 1 minute after the pH jump in comparison to the quaternary complex structure before the pH jump (violet).

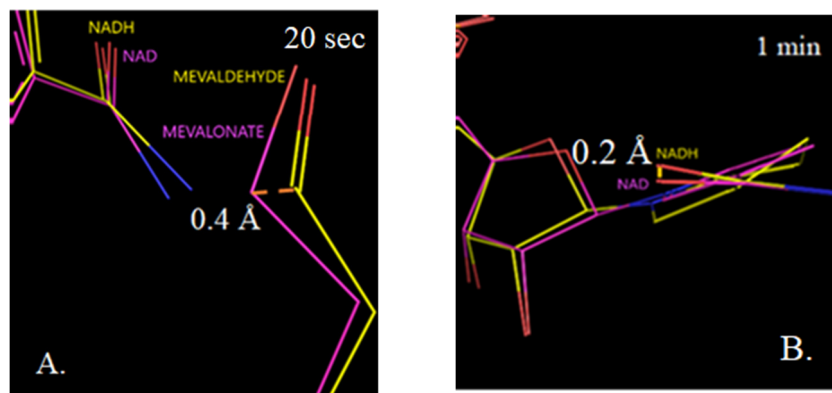


Figure 5.19 Mevalonate/Mevaldehyde region of *PmHMGR* observed (yellow) A. 20 seconds and B. 1 minute after the pH jump in comparison to the quaternary complex structure before the pH jump (violet).

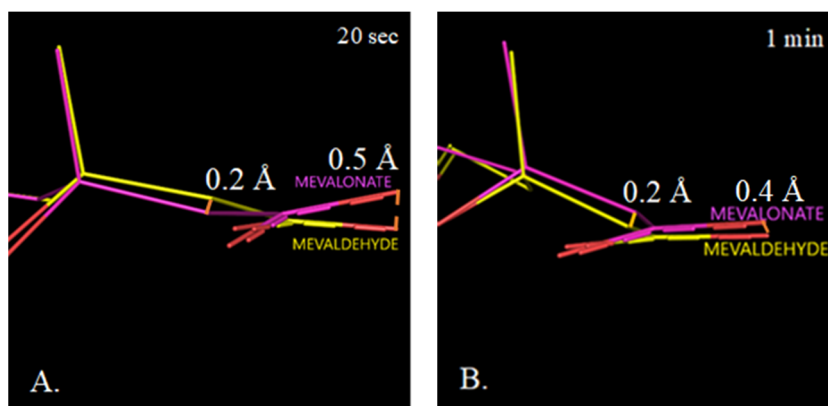


Figure 5.20 Carboxyl end of mevaldehyde modelled in the mevalonate binding region at A. 20 seconds, B. 1 minute after the pH jump in comparison to the mevalonate conformation in the quaternary complex structure before the pH jump.

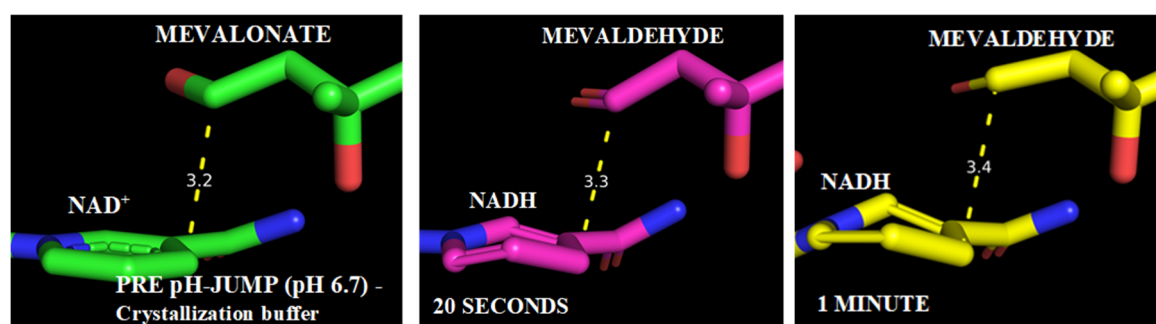


Figure 5.21 Active site in mevalonate / mevaldehyde and NAD<sup>+</sup>/ NADH bound structures A. before (green) B. 20 seconds (purple) C. 1 minute (yellow) after soaking ligand-soaked crystals at pH 9.

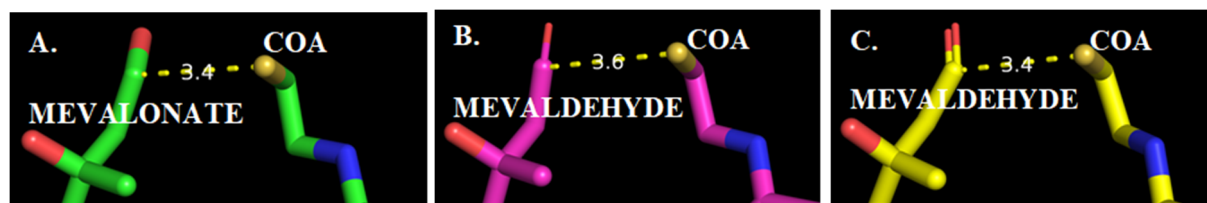


Figure 5.22 Active site in mevalonate / mevaldehyde and CoA bound structures A. before (green) B. 20 seconds (purple) C. 1 minute (yellow) after soaking ligand-soaked crystals at pH 9.

We observe the movement of the ligands at the active site in the manner that suggests the trapping of post hydride-transfer states. Additionally, we also observe an NADH absorbance peak around the first minute of pH change using UV-Vis spectra. Hence, we wanted to further study post pH-jump states of *PmHMGR* within the first minute of reaction initiation in crystals. In order to do so, we obtained additional post pH-jump datasets between 20 seconds – 1 minute in order to observe changes between more closely spaced time points separated by 10 seconds. We used a higher resolution 1 minute structure (2.12 Å) for this comparison instead of the previously used structure when comparing changes across 20 seconds – 10 minutes. We also obtained an additional control structure of *PmHMGR* pre-soaked in the pH-jump buffer before being bound to the ligands mevalonate, CoA and NAD<sup>+</sup> at pH 6.7 without any additional pH change.

Polder maps generated in the mevalonate, CoA and NAD<sup>+</sup> binding region before refinement with ligands were analysed to observe changes in the active site before and after the pH-jump. Utilizing this data to generate polder maps ensured that the models used were not biased by any refinements. The conversion of NAD<sup>+</sup> into NADH can be followed in these polder maps by observing changes in the C4 and C6 positions of the nicotinamide ring that is found to show puckering at these atoms in high resolution structures of NADH bound Horse Liver Alcohol Dehydrogenase. This change in NADH conformation has been further shown in DFT calculations<sup>[94, 109]</sup>.

Structures obtained with ligands soaked into the crystallization buffer environment (Fig 5.23 A.) and following an exchange into the pH- jump buffer (Fig 5.23 B.) showed flat and evenly distributed density over the NAD<sup>+</sup> ring, strong density for mevalonate and CoA with the CoA-SH thiol atom pointing away from mevalonate.

Polder maps generated in structures obtained 20 seconds after ligand bound *PmHMGR* crystals were transferred to a pH 9 environment showed electron density that appeared to be more spread out around the nicotinamide ring, in the CoA-SH thiol region and in mevalonate. The electron density continues to remain bulkier around the nicotinamide ring and is observed to fluctuate around the C4 and C6 positions of the nicotinamide ring 30 – 60 seconds after the enzyme is transferred to a pH 9 environment. This is particularly observed after 50 seconds at pH 9 where it is observed to merge with the density in the mevalonate bound region (Fig 5.23 F). These changes are accompanied with the appearance of density near the hydroxyl region of mevalonate in the direction facing the C4 atom of NAD<sup>+</sup> at 50 and 60 seconds.



Similar changes in electron density are also observed in simulated annealing composite omit maps generated at the mevalonate and NAD<sup>+</sup> binding site (Fig 5.24 A-G). These omit maps pick out the strongest signals by using simulated annealing refinement to reduce model bias. We continue to observe evenly distributed density around the nicotinamide ring before the pH jump (Fig 5.24 A-B). Subsequently, after 20 seconds at pH 9, the simulated annealing omit maps also show electron density that is more spread out around the nicotinamide ring (Fig 5.24 C). In structures obtained 30-60 seconds after the pH-jump at pH 9 we observe an uneven distribution of electron density at the C4-C6 positions with a significant increase in density around the C6 region (Fig 5.24 D-G). The position of the hydroxyl oxygen in the mevalonate bound region is also shown to have a conformation that is bent towards the nicotinamide ring at 50 seconds as is observed in the polder maps (Fig 5.24 F).

#### *5.3.3.1 Comparing changes in the electron density and distance between ligands at the PmHMGR active site within the first minute of reaction initiation*

Given the changing electron density of the ligands that is observed at the enzyme's active site with NAD<sup>+</sup> nicotinamide and mevalonate, we were also interested in following the changing placement of substrates and cofactor at the active site in structures obtained between 20 seconds – 1 minute after the mevalonate, CoA and NAD<sup>+</sup> bound crystals are transferred to a pH 9 environment. Comparing these movements would also help us determine conformational changes taking place during and after the hydride transfer step. To compare changing interactions between ligands at the active site we compared the distance between the terminal carbon on mevalonate / mevaldehyde and C4 atom on NAD<sup>+</sup>/NADH to determine the proclivity for a hydride transfer to take place. To determine the changing interactions between CoA and mevalonate / mevaldehyde for thioester bond formation, we compared the distance between the terminal carbon and the thiol atom. These comparisons were also assessed alongside changing Wilson B-factor values of these structures to assess an overall degree of movement at the active site and determine possible correlations.

Distance measurements between the hydroxyl (terminal) carbon atom of mevalonate and the C4 atom of NAD<sup>+</sup> and CoA-SH sulfur indicate a 0.2 Å and 0.1 Å reduction respectively (Fig 5.25 B, Table 5.3) after the crystals are soaked in pH-jump buffer in comparison to the crystallization buffer environment (Fig 5.25 A, Table 5.3). A comparison of Wilson B-factor

values from each of the structures (Table 5.2) also indicates a reduction in B-factor of the enzyme after it is transferred from the crystallized buffer (24.81) to the pH-jump buffer (16.8).

The distance between the ligands is observed to increase again following the pH-jump at 20 seconds (Fig 5.25 C-F., Table 5.3). Here the distance is measured between what is expected to be NADH, mevaldehyde and CoA based on the changing density and observed NADH peak in UV-Vis spectra after the first minute of pH change. The distance between C4 atom of NADH and the terminal carbon of mevaldehyde is observed to increase by 0.3 Å. The distance between the terminal carbon of mevaldehyde and thiol atom of CoA is also observed to increase by 0.2 Å. The B-factor values are observed to approximately double in the structure obtained 20 seconds (46.8) after a pH change (Table 5.3).

In structures obtained at subsequent time points after a pH change ranging from 30 – 40 seconds we also observe a gradual increase in distance between mevaldehyde and NADH of 0.3 Å and a reduction in distance between CoA-SH and mevaldehyde of 0.3 Å (Fig 5.25 D-E, Table 5.3). The Wilson B-factor values are observed to follow a decreasing trend from 20 seconds to 60 seconds where they reach a stable value at 50– 60 seconds (24.6 - 24.2) (Table 5.2). While the distance between NADH and mevaldehyde is observed to remain constant between 40 – 60 seconds (3.5 – 3.6 Å) after the pH change, we observe an expansion of 0.2 Å between CoA-SH and mevaldehyde at 50-60 seconds (Fig 5.25 F-G, Table 5.3).

While the observed distance changes in the captured structures is between 0.1 – 0.3 Å for the distances between mevalonate / mevaldehyde and NAD<sup>+</sup>/NADH and 0.1 – 0.2 Å between mevalonate / mevaldehyde and CoA, they display an overall range of motion that is 0.6 Å and 0.3 Å respectively.

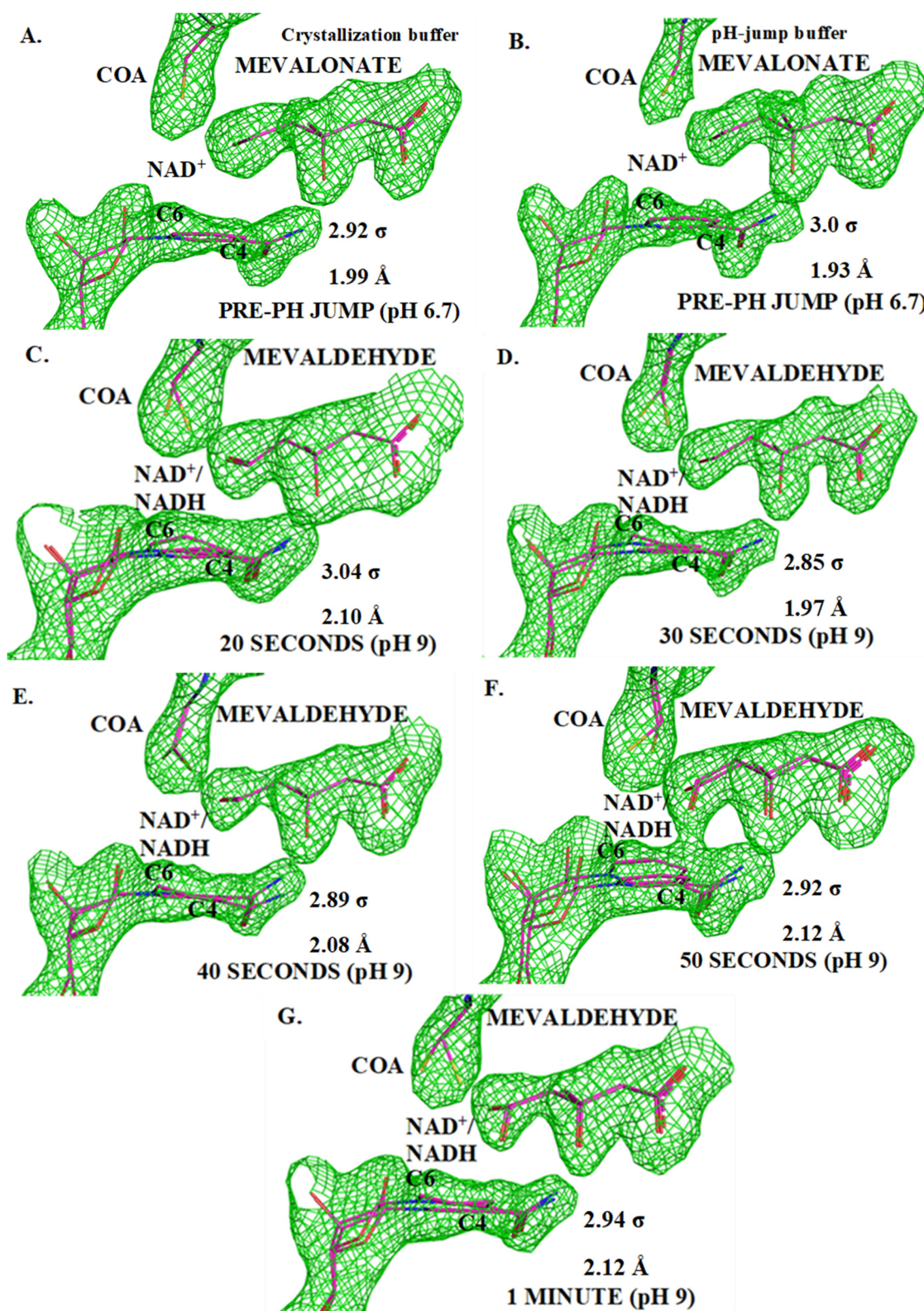


Figure 5.23 Polder maps generated for the ligands at the active site in mevalonate, CoA and NAD<sup>+</sup> soaked crystals A. after a slow-exchange with a pH-jump (ammonium acetate, ADA and PEG-400) buffer and (B-G) 20-60 seconds after soaking the ligand bound crystals in pH 9.

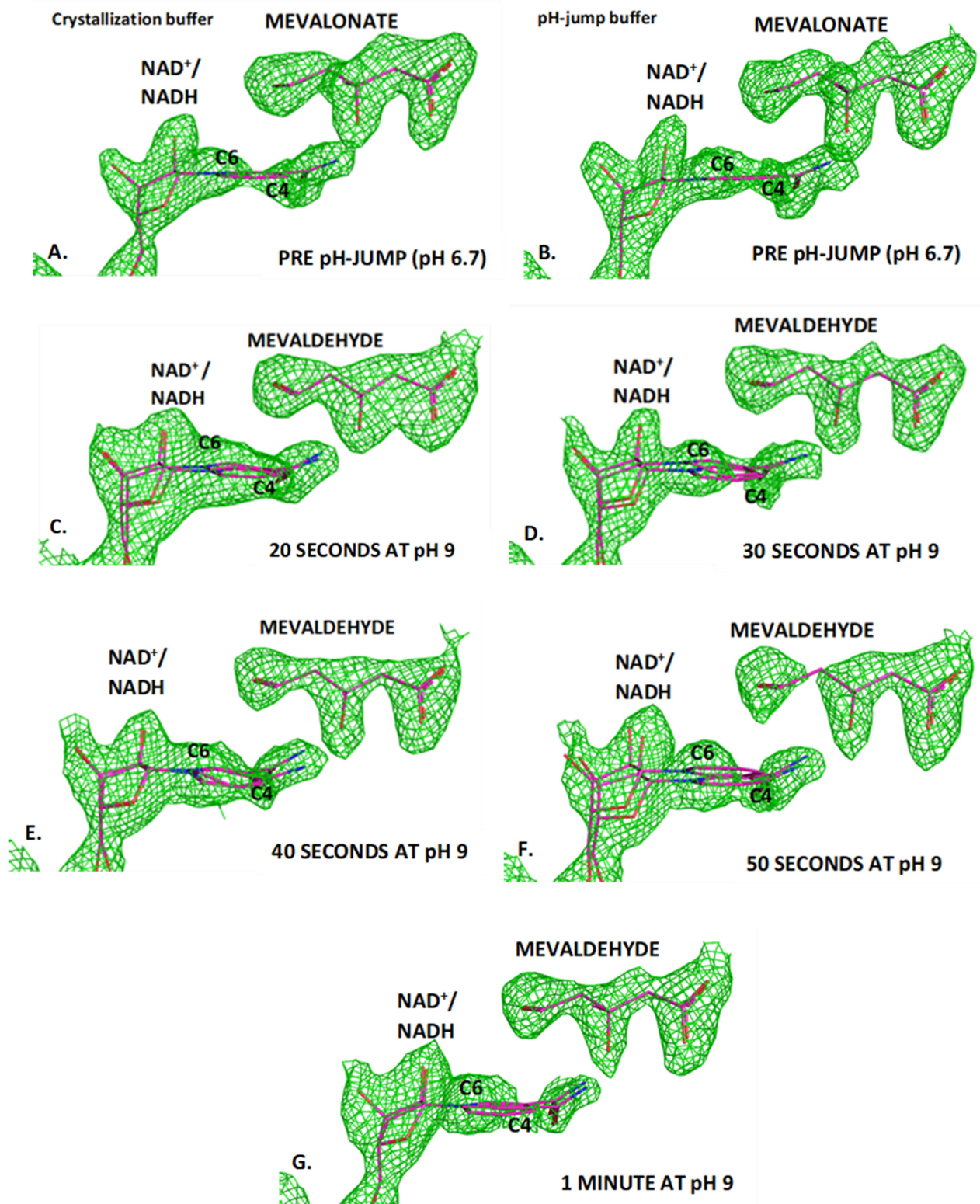


Figure 5.24 Simulated annealing composite omit maps showing changes in NAD<sup>+</sup> nicotinamide-ribose and mevalonate bound region before (Fig A-B) and after (Fig C-G) PmHMGR crystals are soaked at pH 9



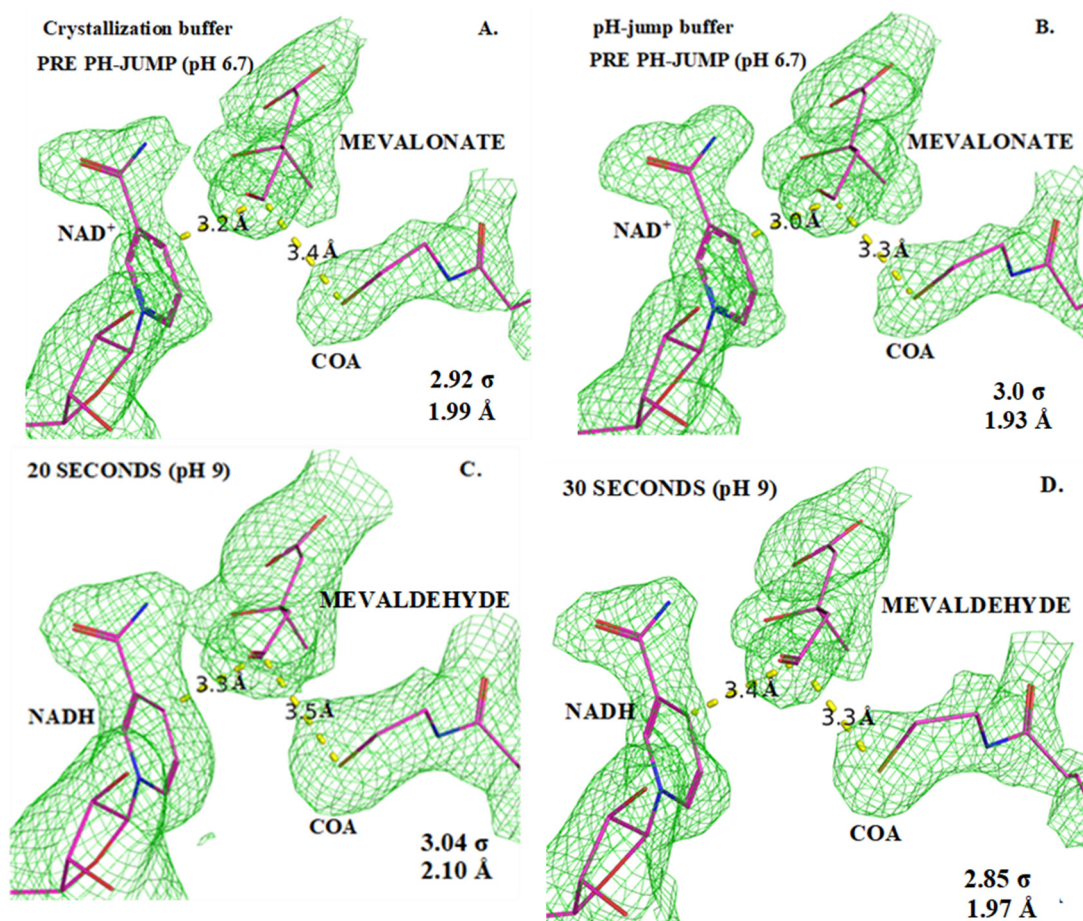


Figure 5.25 Distance between the ligands mevalonate, CoA and NADH at different before (A-B) and after (C-F) *PmHMGR* crystals are soaked at pH 9.

Figure 5.25 continued

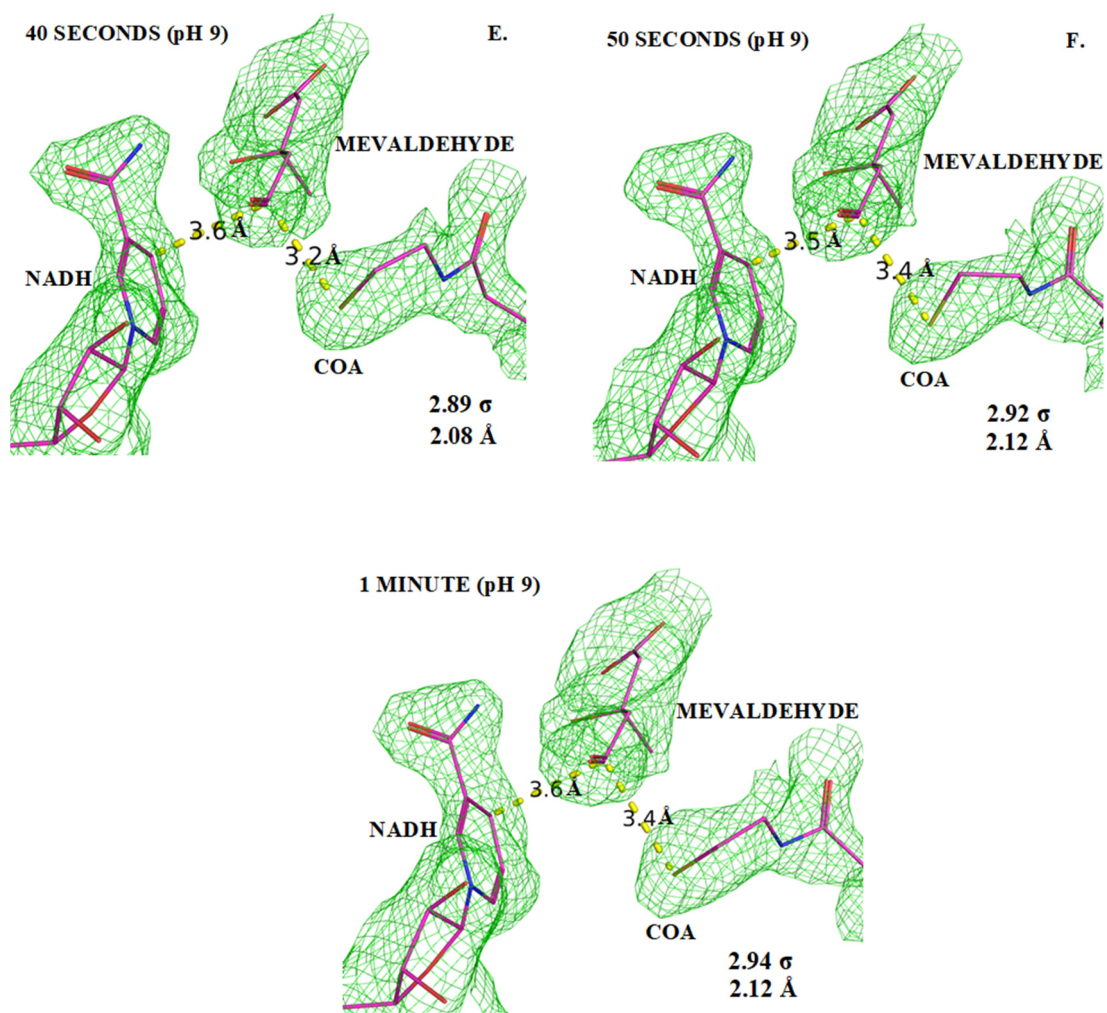


Table 5.2 Wilson Scale Factor obtained for the structures before and after a pH-jump.

<b>SAMPLE</b>	<b>WILSON B-FACTOR</b>
Control (No pH-change - Crys. buffer)	24.81
Control (No pH-change - pH-jump buffer)	16.8
20 seconds	46.8
30 seconds	32.6
40 seconds	27.2
50 seconds	24.6
60 seconds	24.2

Table 5.3 Distance observed between the hydroxyl C in mevalonate / mevaldehyde ,NAD+ C4 carbon and CoA-SH sulfur.

SAMPLE	DISTANCE (MEVALONATE C-OH – NAD C4)	DISTANCE (COA-S – MEV C4)
AMMONIUM SULFATE	3.17 Å	3.42 Å
AMMONIUM ACETATE	2.99 Å	3.33 Å
20 SECONDS	3.27 Å	3.51 Å
30 SECONDS	3.36 Å	3.29 Å
40 SECONDS	3.58 Å	3.24 Å
50 SECONDS	3.51 Å	3.42 Å
60 SECONDS	3.59 Å	3.42 Å



### 5.3.3.2 Changes in the adenine-ribose region of NADH in structures obtained within the first minute of reaction initiation:

We also compared the electron density in the NADH adenine-ribose region at different time points during the first minute since this region appeared to show movements before ligand release indicating that possible changes related to the cofactor exchange might also be initiated around this portion of NADH.

Electron density in the adenine-ribose region of  $\text{NAD}^+$  is observed to be more broadly spread out after the mevalonate, CoA and  $\text{NAD}^+$  bound crystals are soaked at pH 9 (Fig 5.26 C-F). This change in density is observed to increase after the pH change from 20 - 60 seconds.

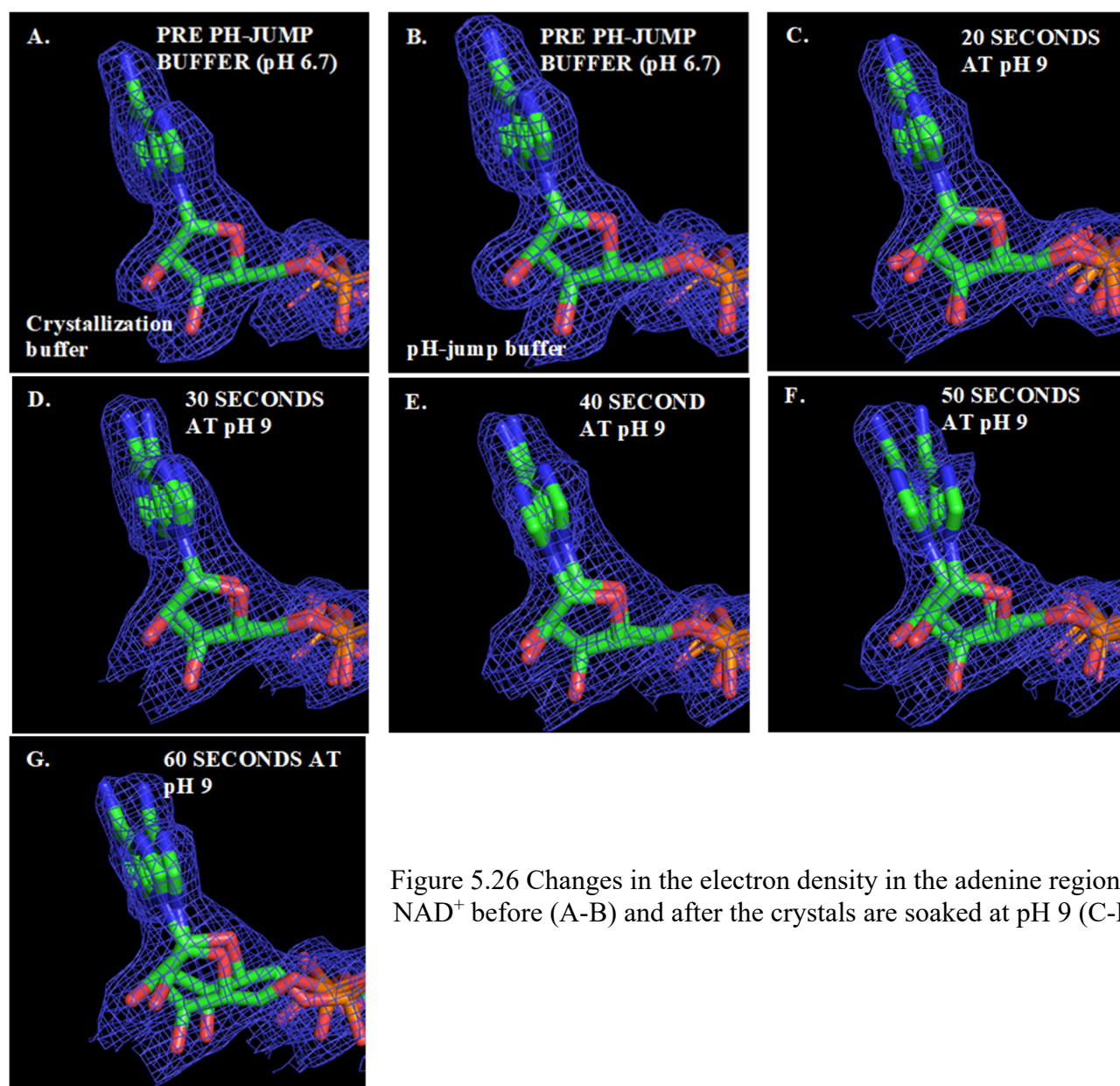


Figure 5.26 Changes in the electron density in the adenine region of  $\text{NAD}^+$  before (A-B) and after the crystals are soaked at pH 9 (C-F).

### 5.3.4 Movements observed in the *Pm*HMGR active site in structures obtained within the first minute of reaction initiation

With the electronic density changes that were observed corresponding to a hydride transfer between mevalonate and  $\text{NAD}^+$ , we were interested in observing any conformational changes that might take place at the enzyme's active site to facilitate the initiation of enzyme turnover and the subsequent steps in the biochemical reaction. The major residues forming contacts at the active site were GLU 83 and LYS 267 forming contacts with mevalonate and  $\text{NAD}^+$  to coordinate the first hydride transfer (Fig 1.1), HIS 381 which is involved in deprotonating CoA-SH for it to form a thioester bond with the first proposed intermediate mevaldehyde (Fig 1.1) and ASN 688, HIS 385, VAL 392 and SER 85 which are involved in forming contacts to position the ligands mevalonate, CoA and  $\text{NAD}^+$  at the enzyme's active site. Residues ASN 688, HIS 385 and VAL 392 are also involved in making contacts that result in the closure of the flap domain and in doing so could also regulate cofactor exchange. Among these residues we do not observe any significant movement between GLU 83 and LYS 267 after the enzyme is introduced to the pH-jump buffer and after it undergoes a change to a pH 9 environment (Fig 5.27 A-F). The distance between ARG 261 and mevalonate / mevaldehyde is also observed to be the same across the different time points (Fig 5.27 A-F). However, the residues that coordinate the binding and protonation state of CoA-SH (HIS 381 and SER 85) near the thiol and pantothenic acid amide region for thioester bond formation show movements of up to 0.3 Å in accordance with the changing position and conformation of the co-substrate (Fig 5.27).

Sidechains from VAL 392 and HIS 385 that are in contact with the  $\text{NAD}^+$ /NADH adenine-ribose and phosphate regions show a higher degree of movement within the range of 0.7 Å (Fig 5.27). This movement is observed with the changing position of the cofactor 40 and 50 seconds after a pH change where it also shows the most drastic changes in density (Fig 5.27 E-F). In the case of residues that are in contact with the ribose that is adjacent to the nicotinamide of  $\text{NAD}^+$ /NADH (ASN 688), we do not observe much movement in relation to the cofactor with the relative distance only varying by 0.2 Å (Fig 5.27 A-F). This region of the cofactor also shows very little movement.

We also looked at the changing B-factor values of the bound ligands in this pH-jump experiment after the first minute of a pH-jump. This comparison was done to assess the relative increase in B-factor of difference portions of the ligand to the average B-factor of the structure.

This helped correlate corresponding mobile regions of the bound substrates and cofactor with regions that are mobile near the ligand binding site.

In the NAD<sup>+</sup> and NADH bound region, the B-factor values associated with the active site for mevalonate and nicotinamide-ribose of NAD<sup>+</sup> are observed to be significantly lower in comparison to the regions spanning other portions of the ligands (Fig 5.28 A-F). In contrast, we also observe a higher B-factor in the adenine-ribose region of NAD<sup>+</sup> in comparison to the other portions of NAD<sup>+</sup> and mevalonate before and after a pH change.

In comparison to NAD<sup>+</sup> and mevalonate, CoA is shown to have a higher B-factor, particularly in the adenine-ribose regions (Fig 5.28 A-F). After introducing the enzyme to the pH-jump buffer environment at pH 6.7, we observe a further increase in the B-factor of the adenine-ribose region of CoA (Fig 5.28 B). However, we also observe a relative drop in the B-factor of the adenine and ribose region of NAD in the pH-jump buffer environment at pH 6.7 (Fig 5.28 B). After being introduced to a pH 9 environment, we observe a drastic increase in B-factor in the adenine and ribose regions of NAD<sup>+</sup> and the terminal carbon of mevalonate 20 seconds after a pH change (Fig 5.28 C). This increase in B-factor in portions of NAD<sup>+</sup> and mevalonate persists at 30 seconds after a pH change.

As we observe an increased density for alternate positions of the NAD<sup>+</sup>-adenine-ribose 40-50 seconds following a pH-change (Fig 5.26 E-F), we also observe that the relative B-factor in that region remains relatively higher. The relative B-factor in NAD<sup>+</sup> is initially observed to be higher in the adenine-ribose portions before any pH-change (Fig 5.28 A-B). However, after the enzyme is equilibrated in a new pH environment it is also observed to increase in the phosphate and nicotinamide-ribose regions after being introduced to a pH 9 environment for 20 – 50 seconds (Fig 5.28 D-F)

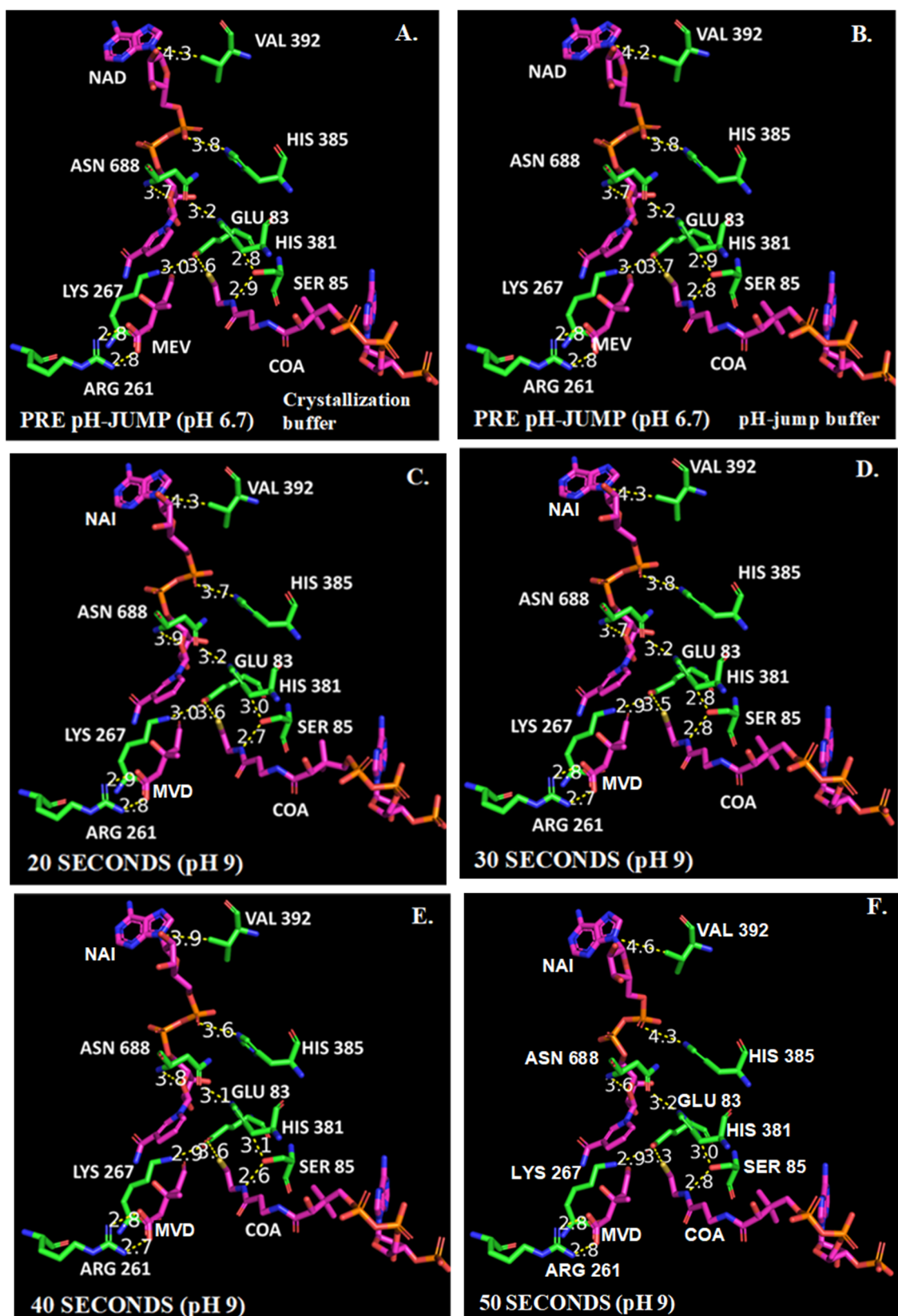


Figure 5.27 *PmHMGR* active site before a pH-change in the crystallization (A.) and pH-jump buffer (B.) and at different time points (C-E.) after the crystals are moved to pH 9.

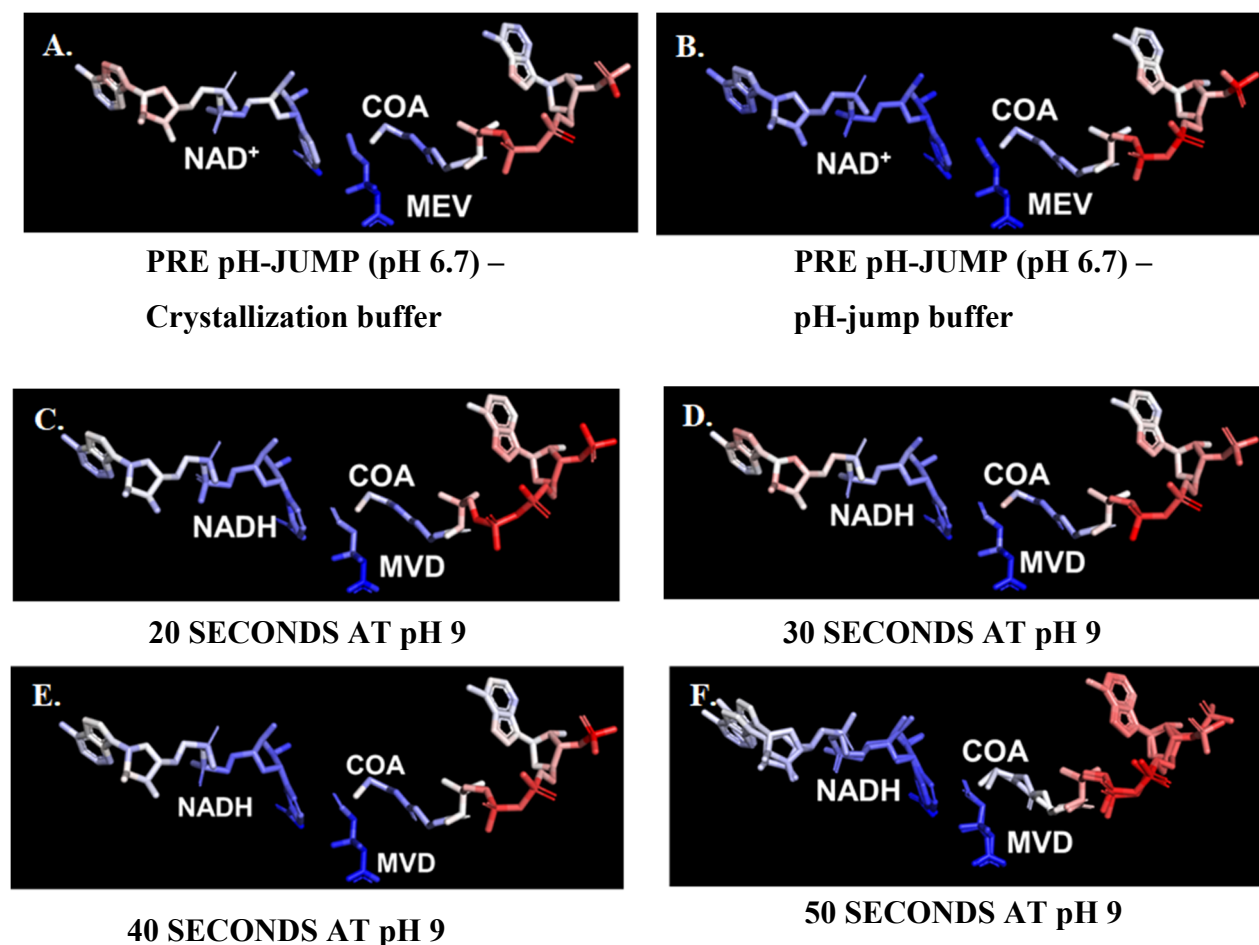


Figure 5.28 Changing B-factor of ligands in the mevalonate / mevaldehyde (MEV/MVD), CoA and NAD<sup>+</sup>/NADH binding site in the crystallization buffer (A), pH-jump buffer at pH 6.7 (B) and at different time points after being exposed to a pH 9 environment (C-F).

### 5.3.5 Movements observed in the *Pm*HMGR active site in structures obtained within the first minute of reaction initiation

Molecular dynamics and QM/MM studies by Quinn et. al have pointed to the long-range stabilization effects at the enzyme's transition state during hydride transfer on the flap domain residues R 396, E 399 and L 407<sup>[28]</sup>. This study pointed to the possibility of observing conformational changes in the flap domain at different time points following the pH-jump. To measure changes in the flap domain, we looked at structural comparisons of the flap domain region following the pH-jump buffer exchange and after the *Pm*HMGR crystals are transferred to a higher pH environment.

#### 5.3.5.1 Changing conformation of the PmHMGR flap domain

The observed flap domain in the mevalonate, CoA and NAD<sup>+</sup> bound structure can be broken into 3 helices with regions E 375 – V 392 that has an interhelix bend, W 402 – H 411 and D 416 – L 423. In comparison to the crystallization environment, we observed significant movement in the flap domain region between A 393 – D 401 (loop between helix 1 and 2), W 402 – H 411 (helix 2) and D 416 – L 422 (helix 3) (Fig 5.29 A.). Movement in the interhelix region between helix 1 and 2 (A 393 – D 401) continues to be observed 20 seconds after the crystals are transferred to a pH 9 environment (Fig 5.29 B.). We also observed the 2<sup>nd</sup> domain helix moving in the reverse direction along its helical axis 20 seconds after a pH change. Regions between A 393 – D 401 (loop between helix 1 and 2), W 402 – H 411 (helix 2) and D 416 – L 422 (helix 3) continue to move to a larger extent at 30 seconds (Fig 5.29 C.). At 40 and 50 seconds, we observe an increased movement in the first helix regions G 375 – V 392 (Fig 5.29 D-E.).

The RMSD of the flap residues was calculated between the pre-pH jump crystal structures in the crystallization and pH-jump buffer environment. It was also calculated between the post pH-jump structures at pH 9 with respect to the structure obtained at pH 6.7 in the pH-jump buffer. An increase in the RMSD of the first, second and third helices (Fig 5.30 A-C) is observed after the ligand-bound crystals are introduced to a higher pH. The RMSD of the regions spanning the 2<sup>nd</sup> and 3<sup>rd</sup> helices are observed to reach their maximum values 30 seconds after a pH change and start decreasing at 40 and 50 seconds. However, RMSD of the first helix is also observed to be the highest at 40 and 50 seconds in residues 386 - 390 (Fig 5.30 A).

The movements in the flap domain helices were also studied by measuring the angles between each flap domain helix. Like the changes in the RMSD of different helical regions of the flap, changes in the interhelical angles also helps us identify conformational changes in different regions of the flap domain. The changing conformation of the flap domain could also be instrumental in affecting the contacts of the flap domain residues that play a key role in catalysis (HIS 381) and coordinating ligands (HIS 385) thereby promoting an intermediate step along the reaction pathway. While the changes observed within the first minute of reaction initiation are largely centered around the first hydride transfer step of the reaction, our initial measurements of time points that show thioester bond formation also indicate significant helical movements across

the entire flap domain and a repositioning of HIS 381 to be closer to the CoA-SH thiol indicating that these movements might facilitate the intermediate steps of the *Pm*HMGR reaction (Fig 5.9).

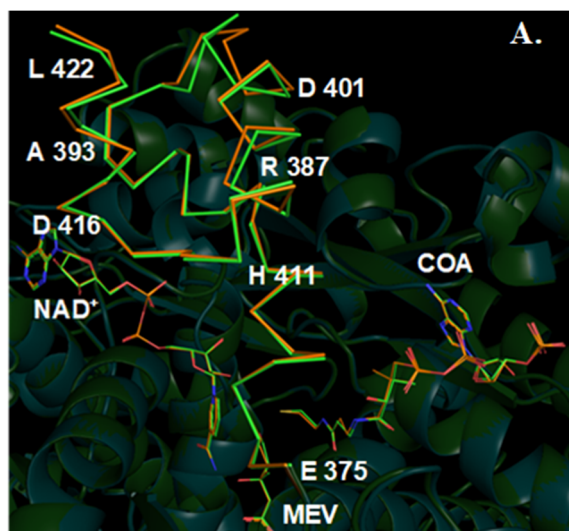
In measuring the changing angles between the different helical regions of the flap, we observe an 8.05° increase in the angle between helix 1 (region 387-395) and 2 appear right after the crystal is introduced to the pH-jump buffer environment (Table 5.4). We also observe that regions in helix 1 appear to show a 7.3° and 12.33° increase in angle at 40 and 50 seconds respectively in comparison to 30 seconds indicating the increase in movement in that region within this time frame (Table 5.4). With the observed movement of helix 2 in the opposite direction along the helical axis after the crystal is introduced in a pH 9 environment as opposed to its configuration at pH 6.7 in the pH-jump buffer (Fig 5.29 B-E.) and the increasing movement in helix 1, we observe this angle between these helices gradually decreasing over time (Table 5.4). While the position of helices 2 and 3 continue to change in contrast to that observed in the flap domain structure from the crystallization environment at pH 6.7, the angle between the helices returns to a similar value (Fig 5.29 B-E., Table 5.4). In comparing the angles between helices 2 and 3 which are observed to be the most mobile after the pH-jump, we observe a gradually decreasing value with an eventual reduction of 17.4° in this value 30 seconds after the crystals are transferred to a pH 9 environment indicating a possible contraction of this helical region in the flap domain (Table 5.4). With observed changes in helix 3 following the introduction of the enzyme to a pH 9 environment, we also observe a 9.5° increase in the angle between helix 1 (region 387-395) and helix 3 at 20 seconds (Table 5.4).

With indications of contraction and expansion of the different helices in the flap domain from our alignments and comparison of interhelical angle measurements, we wanted to test the possibility of a changing interhelical volume. The changing volume of the flap region would be another indication of change in the overall conformation of this subdomain. Such changes could be an effect or facilitator of cofactor exchange. In measuring the void volume which is as measurement of the internal volume in the flap domain, we observed an increase of 27 Å<sup>3</sup> going from the crystallization buffer environment to the pH-jump buffer environment (Table 5.5). Corresponding to the decreasing angle between the 2<sup>nd</sup> and 3<sup>rd</sup> flap domain helix at 30 seconds, we also observe a 19 Å<sup>3</sup> reduction in volume (Table 5.29 C, 5.4, 5.5). This contraction persists at 40

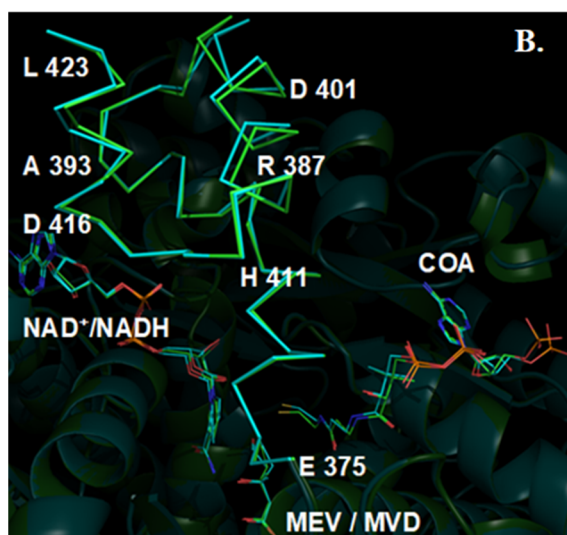
seconds where we observe a further 51 Å<sup>3</sup> reduction (Table 5.5). Lastly, we observe a 76 Å<sup>3</sup> increase in the flap domain 50 seconds after reaction initiation (Table 5.5).

Regions of the flap domain were color graded based on the average B-factor of the given structure to compare the relative difference in B-factor of different flap regions over time. In comparing B-factor values across the flap domain, we observe that the B-factor value in the interhelix region between helices 1 and 2 appears to be higher than the rest of the flap domain before reaction initiation and continues to remain relatively higher until 30 seconds after the enzyme is introduced into a pH 9 environment (Fig 5.31 A-C). The B-factor values also appear to be higher in the third helix of the flap domain 20 seconds after a pH change (Fig 5.31 B). The relative B-factor of the interhelix region is reduced in subsequent time points indicating a new stable conformation being achieved at 40 and 50 seconds (Fig 5.31 D-E) as has also been observed in Fig 5.29 D and E.

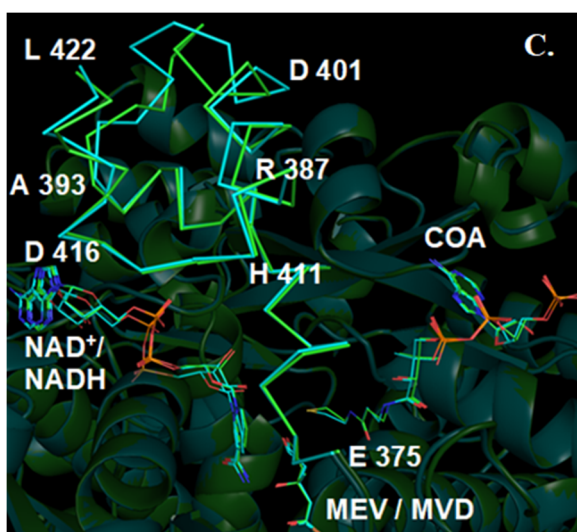




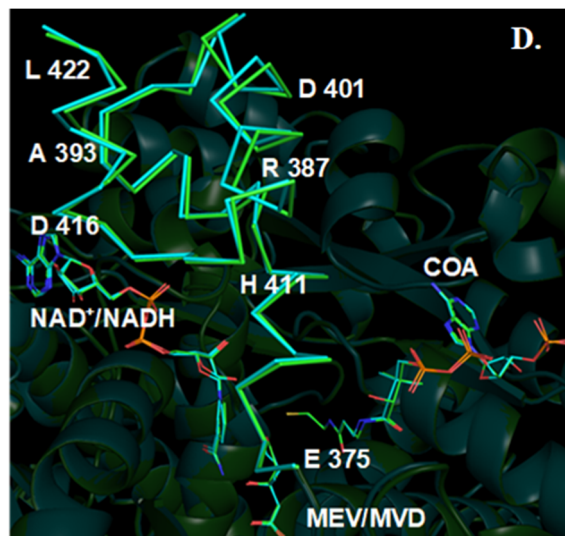
Ammonium Sulfate (pre pH-jump, pH 6.7)  
Ammonium Acetate (pre pH-jump, pH 6.7)



20 seconds at pH 9 (pH-jump buffer)  
Pre-pH jump at pH 6.7 (pH-jump buffer)



30 seconds at pH 9 (pH-jump buffer)  
Pre-pH jump at pH 6.7 (pH-jump buffer)



40 seconds at pH 9 (pH-jump buffer)  
Pre-pH jump at pH 6.7 (pH-jump buffer)

Figure 5.29 RMSD comparisons of the A. first, B. second and C. third flap domain helices before a pH-jump buffer exchange and after a pH-jump (at pH 9).

Figure 5.29 continued

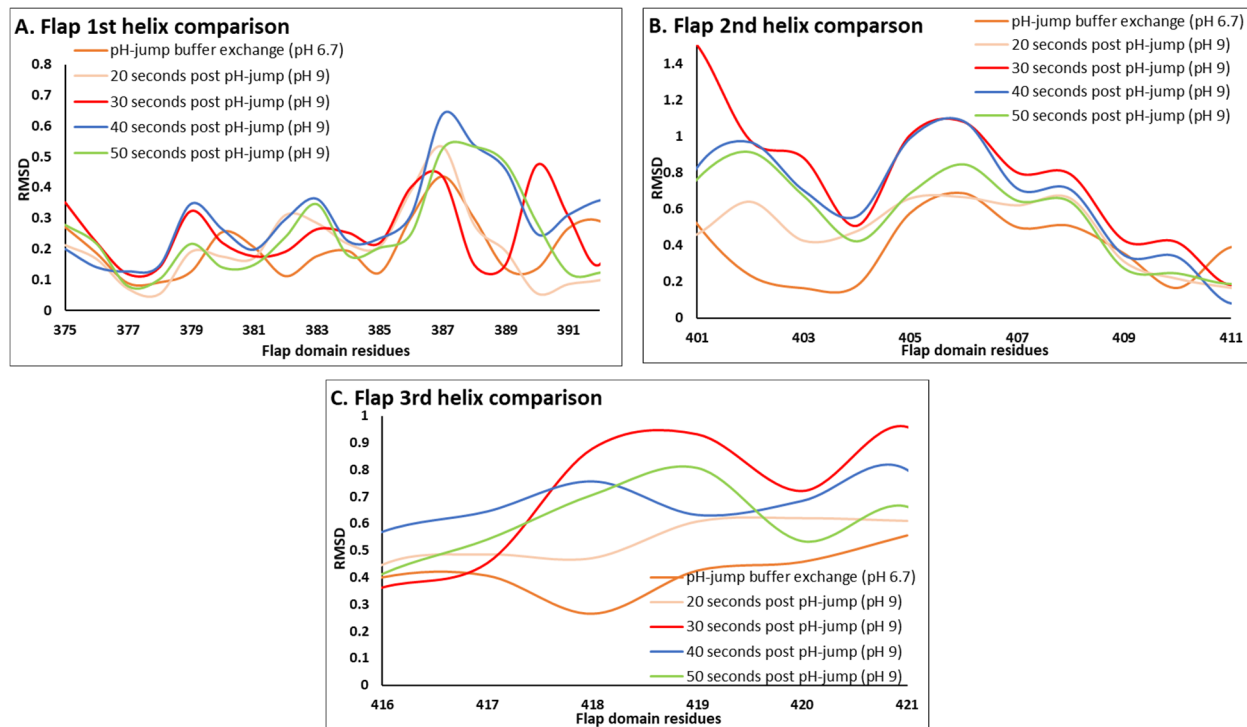
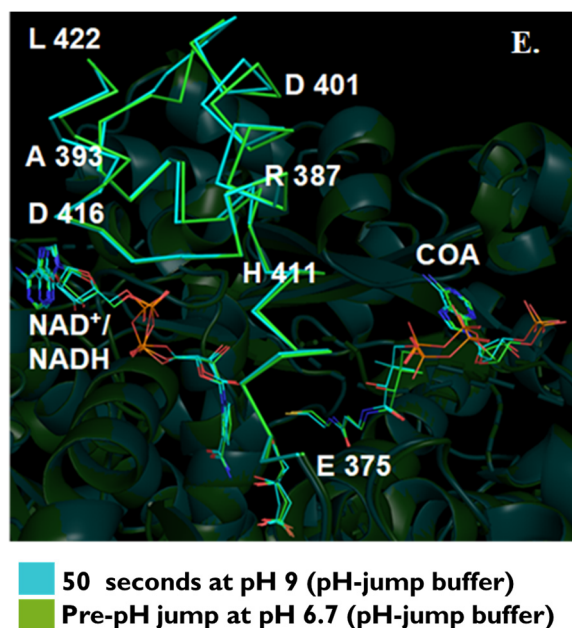


Figure 5.30 Conformational changes in the flap domain after being introduced in a pH-jump buffer environment (pH 6.7) and at different time points after the pH-jump (from 20 seconds - 50 seconds)

Table 5.4 Angle measurements between flap domain helices in pre-pH jump structures (pH 6.7) and at different time points after the crystal are introduced to pH 9.

Helices	Ammonium Sulfate (PRE PH-JUMP, pH 6.7)	Ammonium Acetate (PRE PH-JUMP, pH 6.7)	20 seconds at pH 9	30 seconds at pH 9	40 seconds at pH 9	50 seconds at pH 9
Helix 1-1 – Helix 1-2 (375-386 / 387-395)	59.02	57.48	59.21	56.90	64.23	69.11
Helix 1-2 – Helix 2 (387-395 / 399-410)	112.98	121.03	117.54	119.20	116.35	113.12
Helix 2 – Helix 3 (399-410 / 415-421)	125.11	125.82	119.85	108.47	121.82	124.76
Helix 1-2 – Helix 3(387-395 / 415-421)	51.26	53.48	62.94	55.53	55.34	57.33

Table 5.5 Volume measurements of the *Pm*HMGR flap domain before and after the crystals are transferred to a pH 9 environment.

Sample	Void Volume (Å <sup>3</sup> )
Pre pH-jump (pH 6.7) – crystallization buffer	1349.55
Pre pH-jump (pH 6.7) – pH-jump buffer	1376.75
20 seconds at pH 9	1379.02
30 seconds at pH 9	1360.00
40 seconds at pH 9	1309.46
50 seconds at pH 9	1385.23

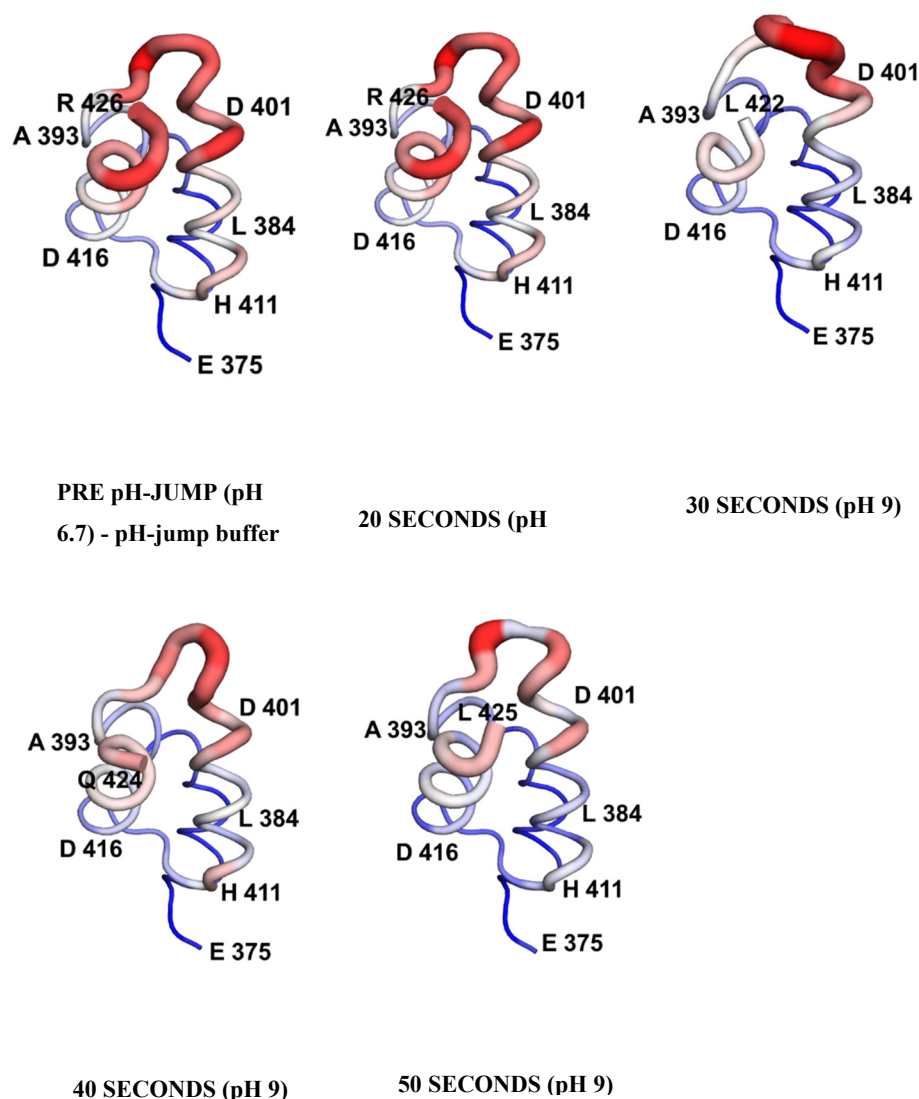


Figure 5.31 B-factor distributions in the *PmHMGR* flap domain in the range of 15-160 in the crystallization environment and pH-jump buffer environment at pH 6.7 (Fig 43. A-B) and after being introduced to a pH 9 environment (Fig 43. C-E).

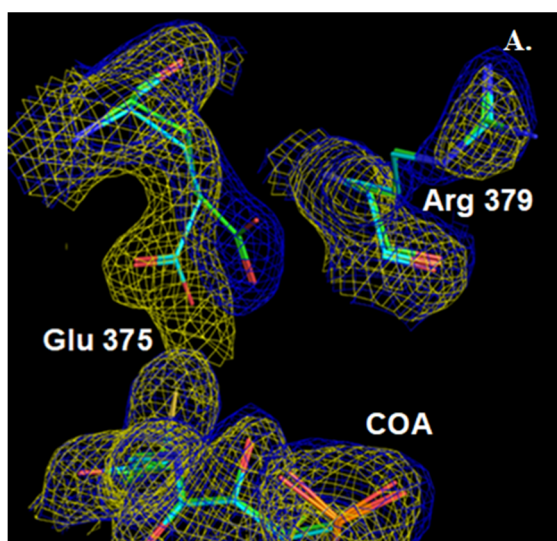
#### 5.3.5.2 Changing contacts between the *PmHMGR* flap domain and CoA binding site.

While comparing changes observed in the flap domain conformation after reaction initiation, we were also interested in identifying how the flap domain interactions at the ligand binding sites might be affected. This would help us identify if there happen to be any pH or reaction induced changes at the active site that also have an effect on the flap domain conformation.

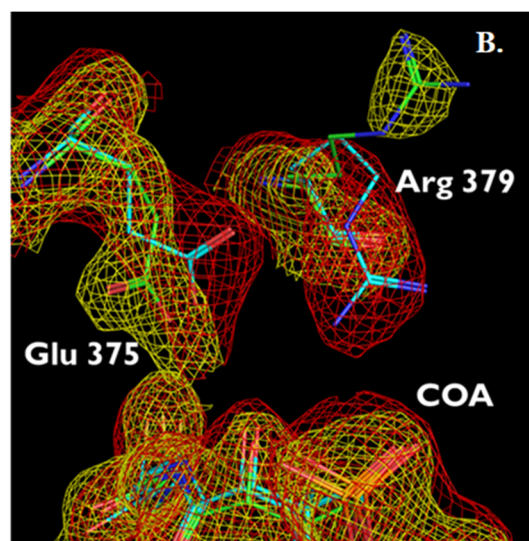
In comparing the movements in the flap domain, certain key regions were identified to change orientation before and after the pH jump. One of them happens to be in the first helix of

the *Pm*HMGR flap domain in residue Glu 375 which is in contact with CoA and is observed to change its conformation after the crystals have been slowly exchanged from a crystallization buffer to a pH-jump buffer environment (Fig 5.32 A.). A change in its conformation is again observed alongside a neighboring residue Arg 379 following a change in the pH-jump buffer environment from pH 6.7 to pH 9 also resulting in changing interaction between the 2 residues. After reaction initiation, this residue is observed to remain in the same state in all our comparisons from 20 seconds – 50 sec at pH 9 (Fig 5.32 B – E).

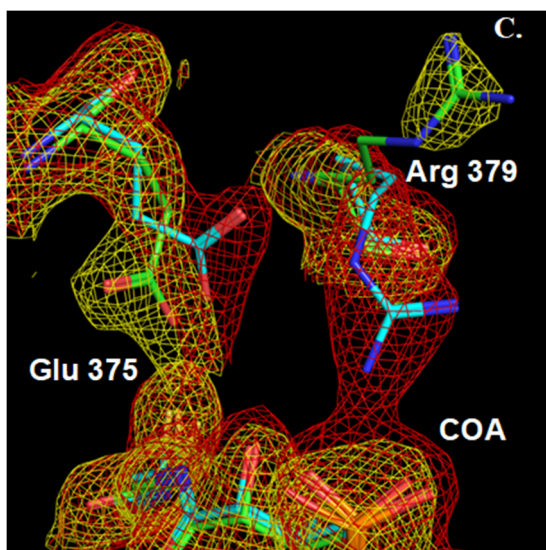




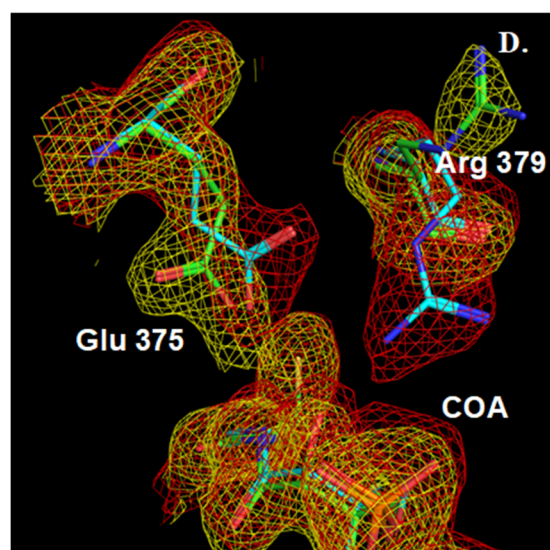
- Pre-pH buffer (pH 6.7) – Crystallization buffer
- Pre-pH buffer (pH 6.7) – pH jump buffer



- pH-jump buffer (pH 6.7)
- 20 seconds at pH 9 in pH-jump buffer



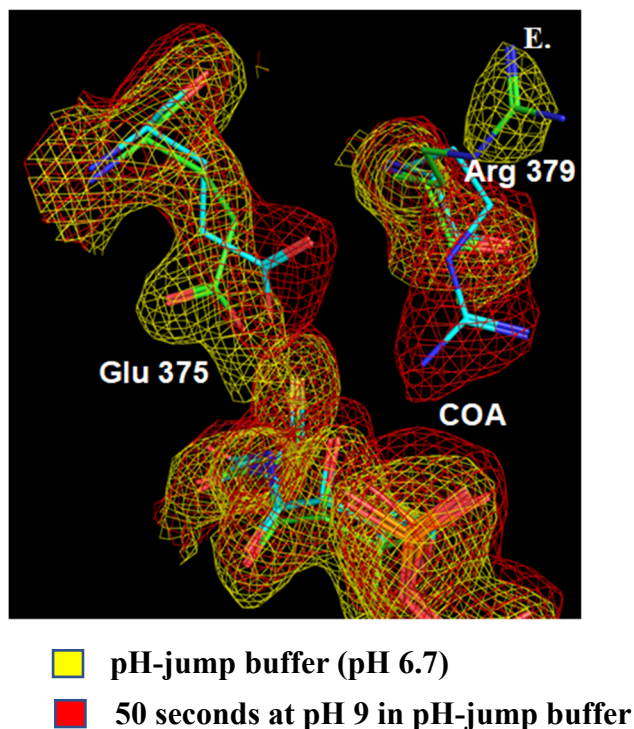
- pH-jump buffer (pH 6.7)
- 30 seconds at pH 9 in pH-jump buffer



- pH-jump buffer (pH 6.7)
- 40 seconds at pH 9 in pH-jump buffer

Figure 5.32 Changing coordination between the residues Glu 375 and Arg 379 in the Figure first helix of the *Pm*HMGR flap domain

Figure 5.32 continued



#### 5.3.5.3 Comparing contacts between the PmHMGR flap domain and the NAD<sup>+</sup> binding site

The distance between helix 1 of the flap domain and the adjacent ligands NAD<sup>+</sup> and CoA is also shown to be affected during the hydride transfer step in the enzymatic reaction. This is observed after the enzyme is introduced into the pH-jump buffer environment and a reduction of the distance by 0.3 Å is observed between the V 392 side chain and NAD<sup>+</sup> ribose (adenine) (Fig 5.33 B.). The distance between the I 389 sidechain and NAD<sup>+</sup> phosphate is then observed to reduce 20 seconds after the enzyme is introduced to a pH 9 environment (Fig 5.33 C.). Subsequently, the distance of the NAD<sup>+</sup> ribose and phosphate region from H 385, I 389 and V 392 sidechains appears to be the same distance 30 seconds after reaction initiation as that observed before the pH-jump (Fig 5.33 D). We then observe the distance between V 392 and NAD<sup>+</sup> ribose decrease by 0.3 - 0.4 Å 40 and 50 seconds after the pH-jump (Fig 5.33 E-F). We also observe a significant reduction of 0.7 Å between the L 384 sidechain and the CoA adenine region 50 seconds after reaction initiation.

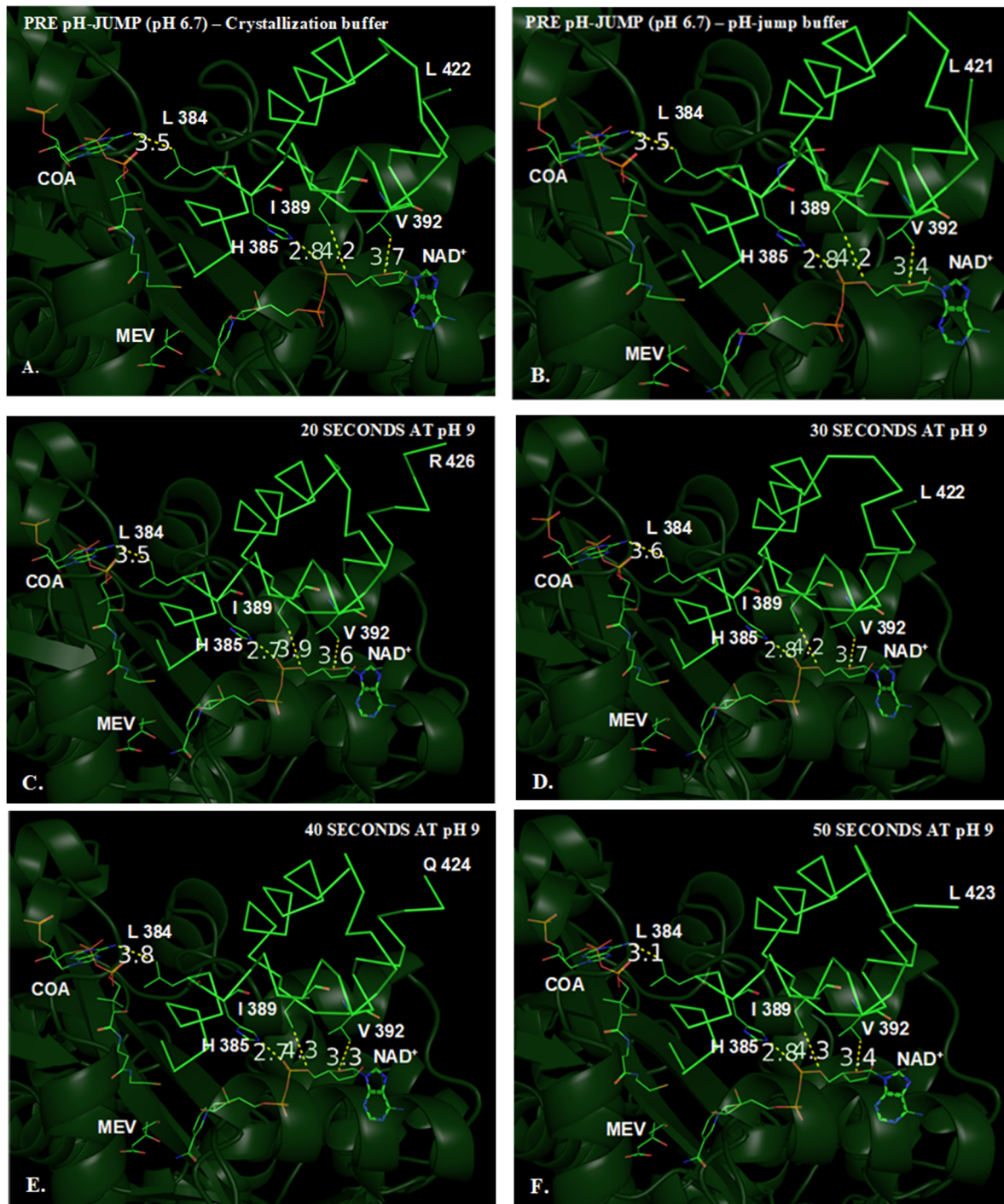


Figure 5.33 Changes in the contacts formed between the *Pm*HMGR flap domain and NAD<sup>+</sup> and CoA in the crystallization and pH-jump buffer environment (A-B) and after the enzyme is moved into a pH 9 environment (C-E).



#### 5.3.5.4 Interhelical movements in the flap domain

After identifying local changes in the conformation of GLU 375 and ARG 379 near the CoA binding site, we were interested in investigating whether these conformational changes also influence the interhelical contacts in the flap domain. The movement of residues near the ligand binding site also results in changes in interhelix interaction. The distance between residues R 379 and H 411 sidechains is observed to increase by 1.2 Å after the enzyme is introduced in the pH-jump buffer environment with the changing conformation of GLU 375 (Fig 5.32 A, Fig 5.34 A-B). Subsequently, it is observed to increase by 2.7 Å after the enzyme has been introduced to a pH 9 environment for 20 seconds after which the interhelical distance between ARG 379 and HIS 411 shows a slight reduction of 0.9 – 1.3 Å but remains significantly higher than that observed before the pH-jump (Fig 5.34 C-F). With the pH-change we also further observe a reduction in interhelical C $\alpha$  distance between helix 1 (A 386) and helix 2 (V 408) by 0.4 Å 20 seconds (Fig 5.35 C) after a pH-change and an expansion of 0.2 Å (Fig 5.35 E) at 40 seconds. This distance is expected to change with the overall movement of helix 2.

The effect of the changing distance and orientation between helices 1 and 2 in the flap domain is also observed in the changing density in the region between ALA 395 – GLU 399 (Fig 5.36 A-E). This irregular region between the 2 helices 1 and 2 is also shown to have weaker density where we can only place the mainchain atoms and a few sidechains. Due to its flexibility, we find that the continuity of the electron density in this region fluctuates after the enzyme is introduced to the pH-jump buffer and at different time points at higher pH. This is first observed with the significantly reduced density between R 396 – D 398 in the pH-jump buffer environment at pH 6.7 in comparison to the crystallization buffer environment (Fig 5.36 A). Similarly, a change in density is observed 20 seconds after the enzyme is introduced to a higher pH where stronger density is observed from G 397 – E 399 (Fig 5.36 B.). We also observe a significant reduction in electron density 30 seconds after a pH change. A re-appearance of density in this region is observed 40 and 50 seconds after the pH-change without significant difference in the mainchain density between these two time points (Fig 5.36 D-E).

The conformation of the interhelical residues present on the loop connecting helices 2 and 3 is also observed to change. This is indicated by the changing electron density around R 417 after the enzyme is introduced to the pH-jump buffer indicating a mobile side chain and thus changing distance between D 412 and R 417 which are neighboring residues (Fig 5.37 A-B). This distance

is expected to reduce after the enzyme is introduced to a pH 9 environment given the change in electron density (Fig 5.37 C.). This changing conformation also affects the distance between the contacting residue pairs D 412 - R 414 with an increase of 0.3 Å being observed between the sidechain guanidino group and carboxylic acid after being exposed to the pH-jump buffer at pH 6.7 (Fig 5.37. A-B). Subsequently, the same distance between R 416 – D 416 sidechains is observed to increase by 0.3 Å in comparison to the crystallization buffer environment after being introduced to a pH-jump buffer at pH 9 (Fig 5.37 A-C).

With the movement of helices 2 and 3 after the enzyme is introduced into a pH-jump buffer and subsequently at higher pH (Fig 5.29 B-E, Fig 5.30 B-C), we observe a corresponding increase in  $C_{\alpha}$  distance between the interhelical hydrophobic residues L 407 and A 418 by 0.2-0.3 Å (Fig 5.38 B-F).

With the changing conformation of the flap domain, we also observe a further change in distance between the  $C_{\alpha}$  atoms of the hydrophobic residues V 403 and L 422 from flap domain helices 2 and 3 respectively. We observe this  $C_{\alpha}$  distance between the 2 residues expand by 0.3 Å after being introduced into a pH-jump buffer and then go through phases of expansion and contraction after being introduced into a pH 9 environment with distance measurements ranging from 8.7 Å to 7.1 Å (Fig 5.39 A-F).

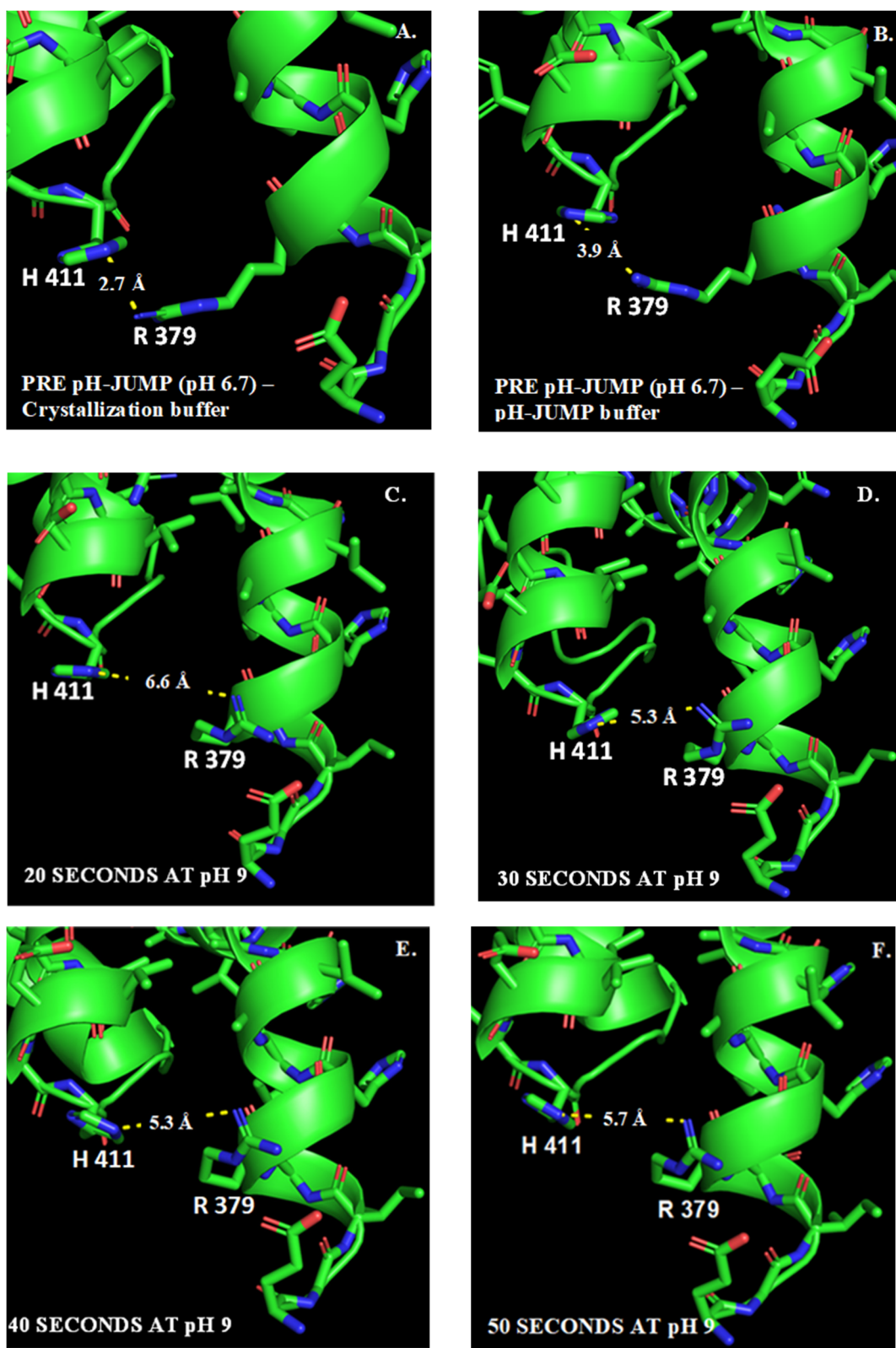


Figure 5.34 Changing interactions between the flap domain helices at pH 6.7 in the crystallization (A.) and pH-jump buffer (B.) and following a change to pH 9 (C-F.)

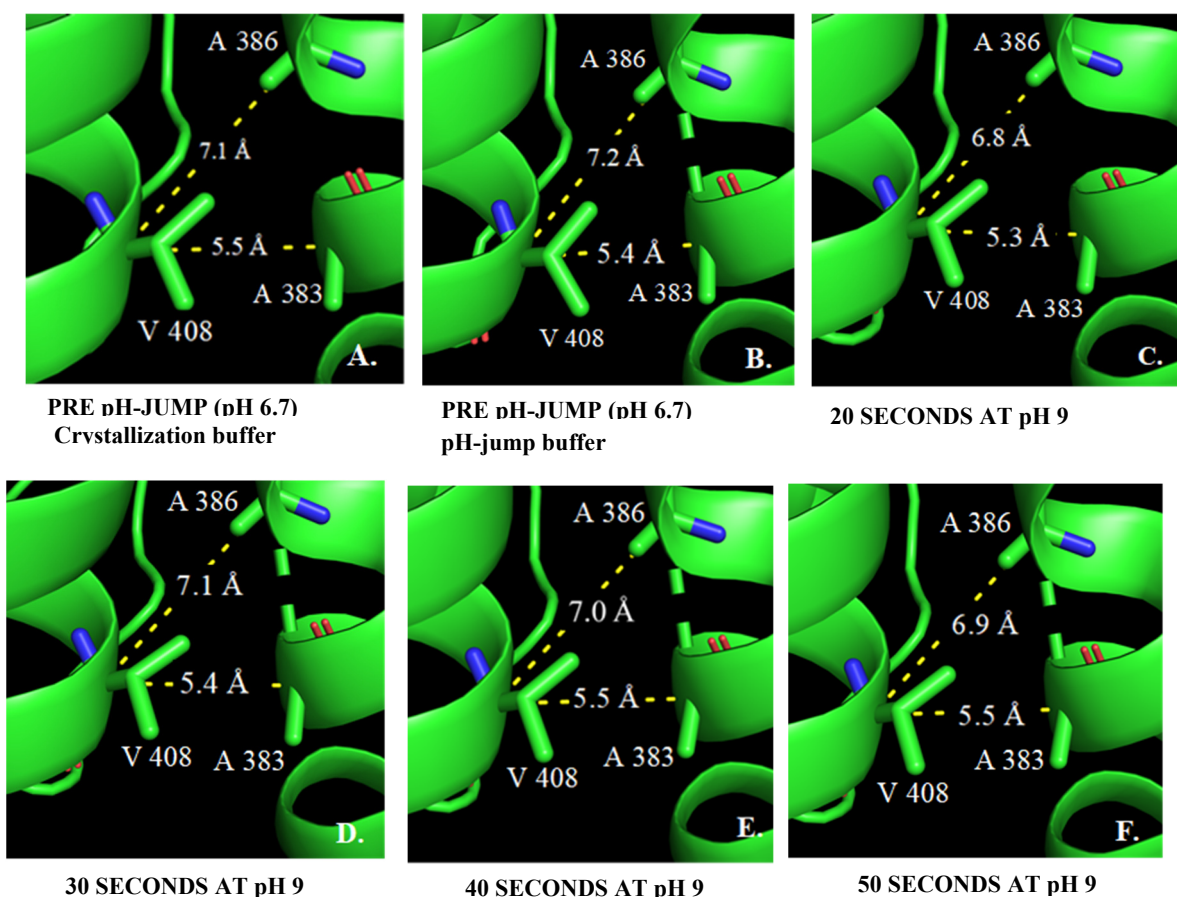
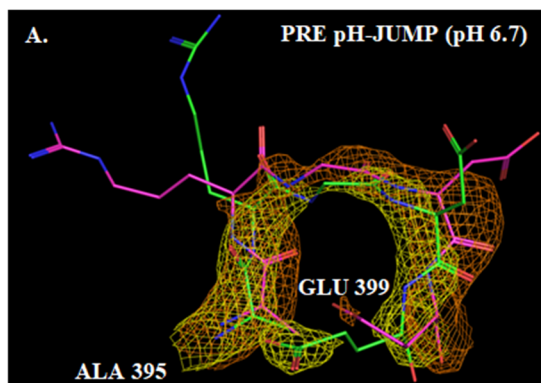

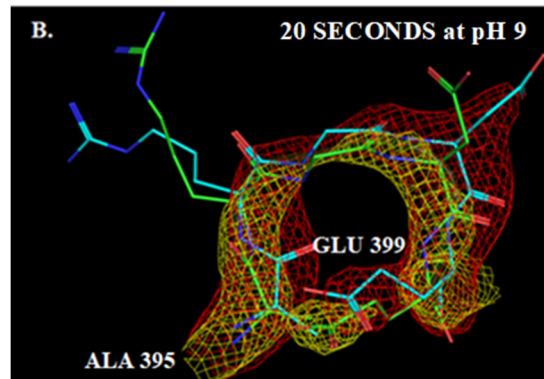


Figure 5.35 Interhelical distance between A 383 / A 386 (helix 1) and V 408 (helix 2) in the crystallization and pH-jump buffer (pH 6.7) and after the enzyme is introduced to a higher pH (pH 9) (C-F.).



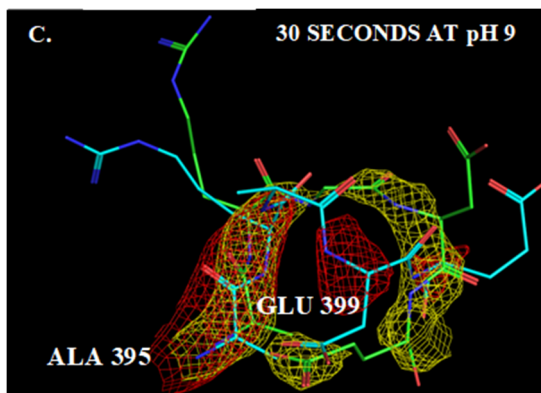
 pH-jump buffer (pH 6.7) – Crystallization buffer


 pH-jump buffer (pH 6.7) – pH-jump buffer



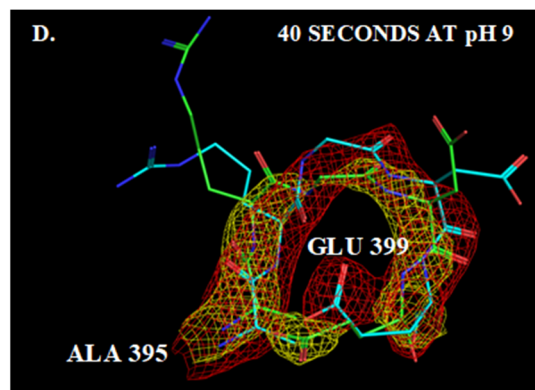
 20 seconds at pH 9 in pH-jump buffer


 pH-jump buffer (pH 6.7)



 30 seconds at pH 9 in pH-jump buffer

 pH-jump buffer (pH 6.7)

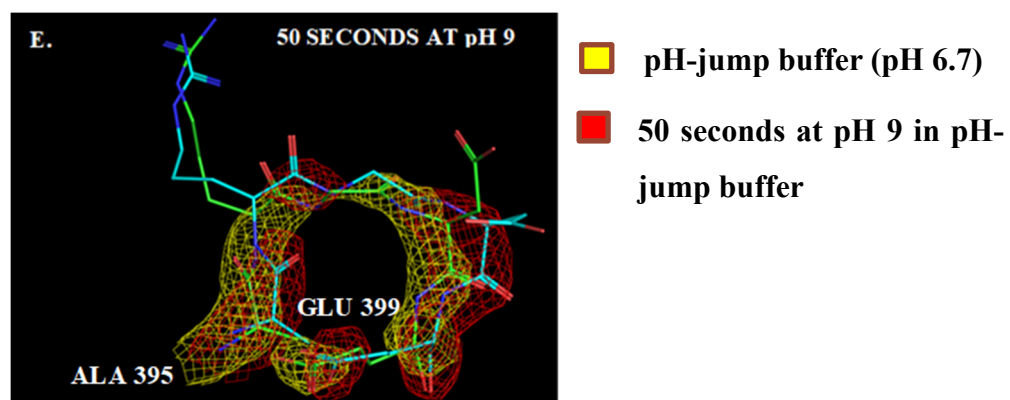


 40 seconds at pH 9 in pH-jump buffer

 pH-jump buffer (pH 6.7)

Figure 5.36 Changing density in the region 395-399 between the first and second helix of the *PmHMGR* flap domain.

Figure 5.36 continued



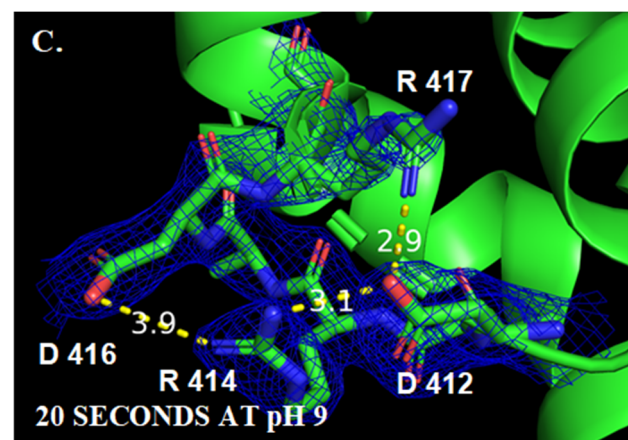
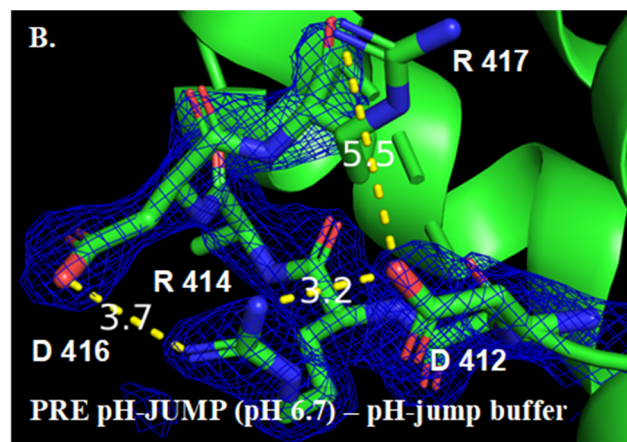
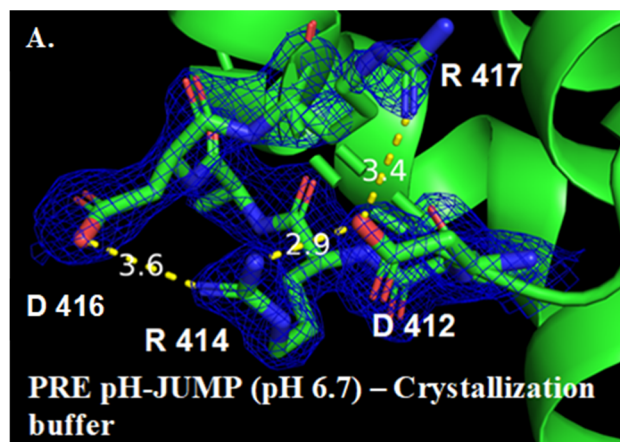


Figure 5.37 Conformational changes in the orientation of interhelical residues spanning from D 412 – R 417 in *Pm*HMGR in the crystallization buffer environment (A), pH-jump buffer environment (B) and at pH 9 (C).



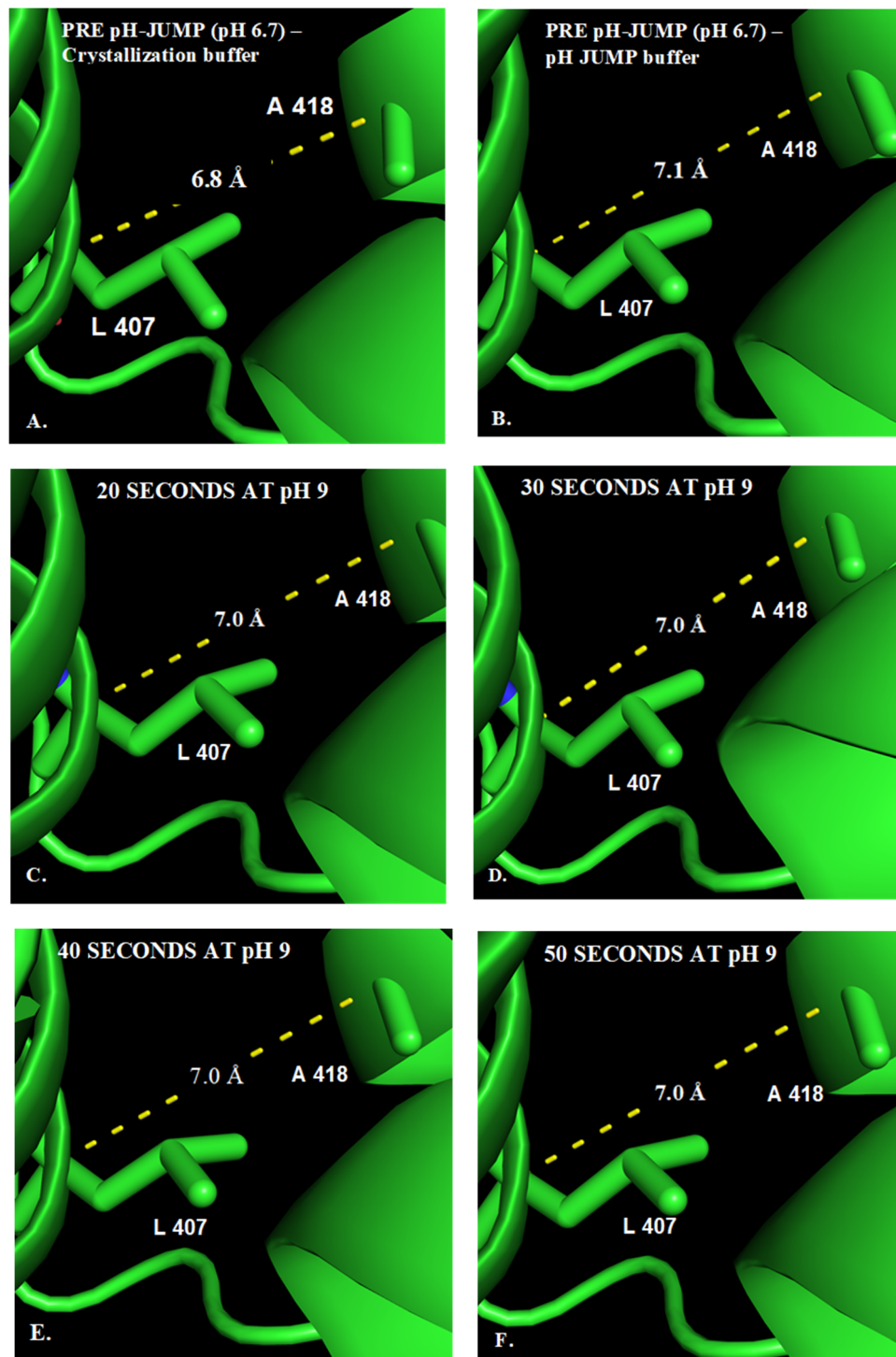
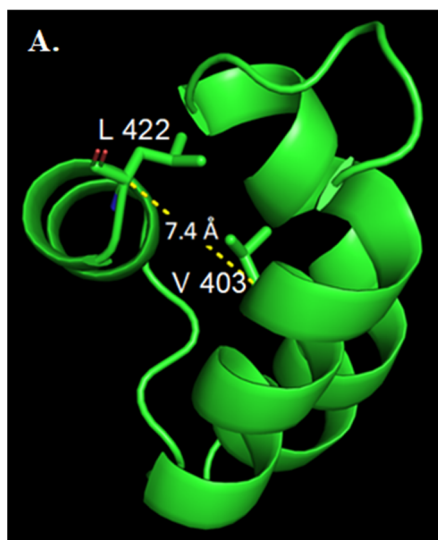
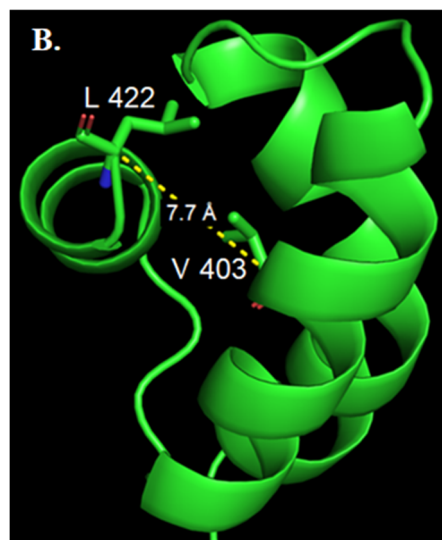


Figure 5.38 Changing interhelical distance between L 407 and A 418 on helices 1 and 2 respectively in the crystallization and pH-jump buffer environments (A-B) and after undergoing a pH-jump (pH 9) (C-F).

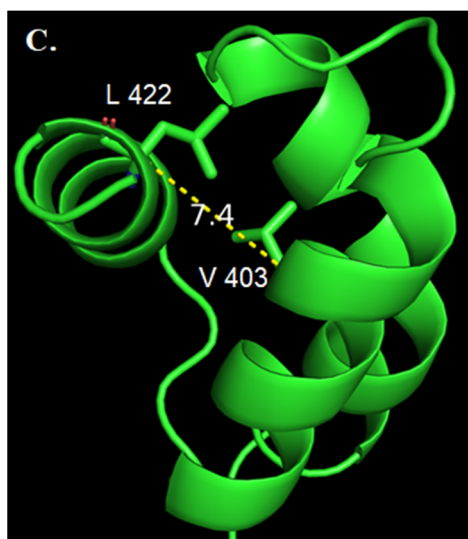




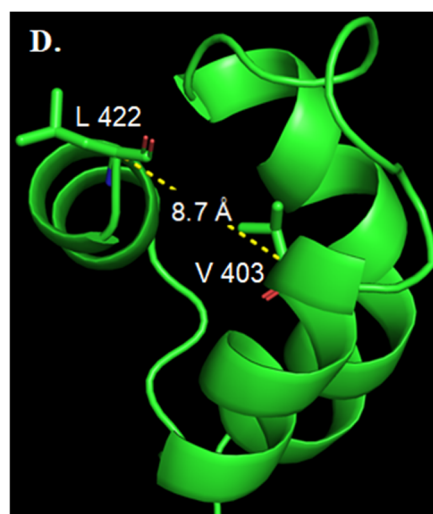
**PRE pH-JUMP (pH 6.7) –  
Crystallization buffer**



**PRE pH-JUMP (pH 6.7) –  
pH-jump buffer**



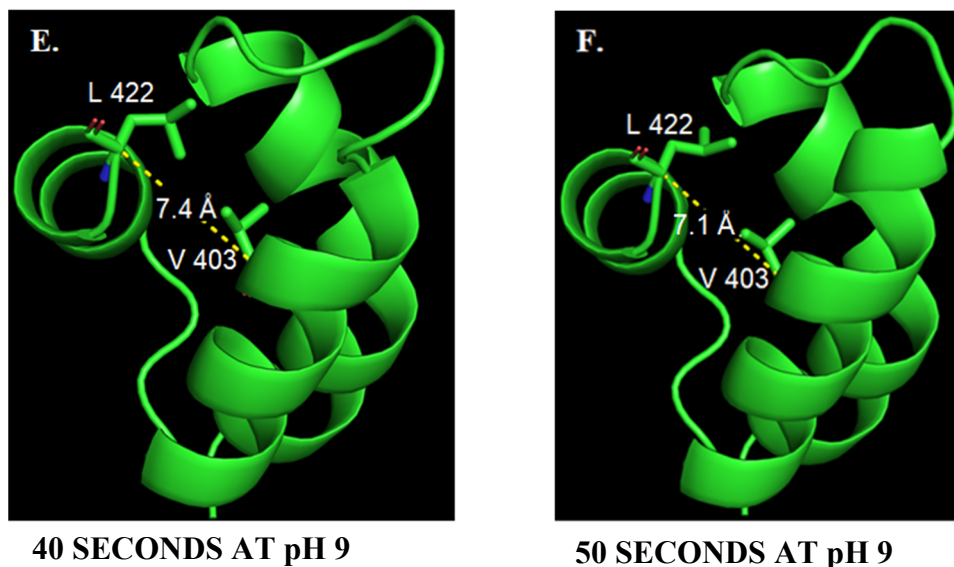
**20 SECONDS AT pH 9**



**30 SECONDS AT pH 9**

Figure 5.39 Changing distance between L 422 and V 403 in the second and third helix of the *PmHMGR* flap domain in the crystallization (A) and pH-jump buffer (B) environment and at pH 9 (C-F).

Fig 5.39 continued



### 5.3.6 Effect of *Pm*HMGR flap mutations on ligand-binding and flap closure

Simulations done using the transition force fields through the quantum-guided molecular mechanics method (Q2MM) indicated that the 3 residues R396, E399 and L407 had the most fluctuations between their ground and transition states and hence were expected to influence enzyme activity. Further experiments were performed by Quinn et. al where these mutants were purified, and their specific activity was measured in the presence of Mevalonate, CoA and NAD<sup>+</sup>. These experiments showed that while the R396A mutant did not have a significant effect on the enzyme's activity, E399A and L407S showed 43% and 31% specific activity respectively in comparison to the wild type enzyme<sup>[109]</sup>. The region where the residues showed reduced motion in the transition state were also found to have variable mobility after being introduced to the pH-jump buffer and at different time points after reaction initiation at higher pH (Fig 5.17, 5.36). To observe changes in the mutant enzyme's structure and how it leads to a reduction in enzymatic activity, all the mutant enzymes were crystallized and soaked with mevalonate, CoA and NAD<sup>+</sup>. Their structures were compared to the wild-type quaternary complex enzyme structure. The RMSD of the mevalonate, CoA and NAD<sup>+</sup> bound E399A mutant structure was calculated with respect to the wildtype *Pm*HMGR complex bound to the same ligands (Shown in Fig 5.40).

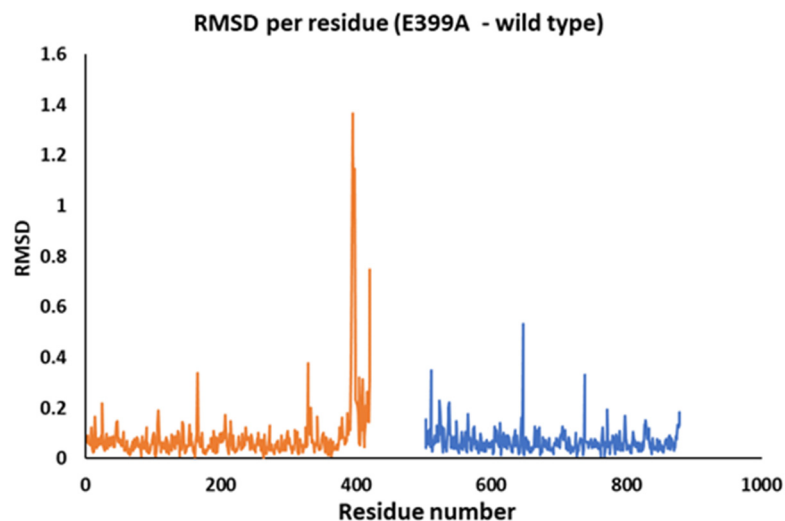


Figure 5.40 A. Plot of RMSD per residue between an E399A mutant and the wild type *Pm*HMGR soaked with Coenzyme A, NAD<sup>+</sup> and Mevalonate

Minimal changes in RMSD (0-0.2) were observed across one of the E399A enzyme structures except for in certain residues that were solvent exposed where the RMSD ranged from 0.3-0.5 or with unresolved electron density like in the case of ALA 395-GLU399 where the RMSD is greater than 1. Since the electron density for E399 side chain is never fully observed in any of the *Pm*HMGR structures, it is currently difficult to decipher the contacts that it makes with the rest of the enzyme. The conformation of the rest of the flap domain is found to closely match the wild-type enzyme (Fig. 5.41 A.). The catalytic residues GLU 83 and LYS 267 are observed to have the same conformation as the wild-type enzyme and HIS 381 is shown to have minimal deviation from the wild type enzyme in the mutant structure (Fig 5.41 B, D). The cofactors and substrates are also observed to have the same conformation in the wild type and mutant enzymes (Fig. 5.41 C).

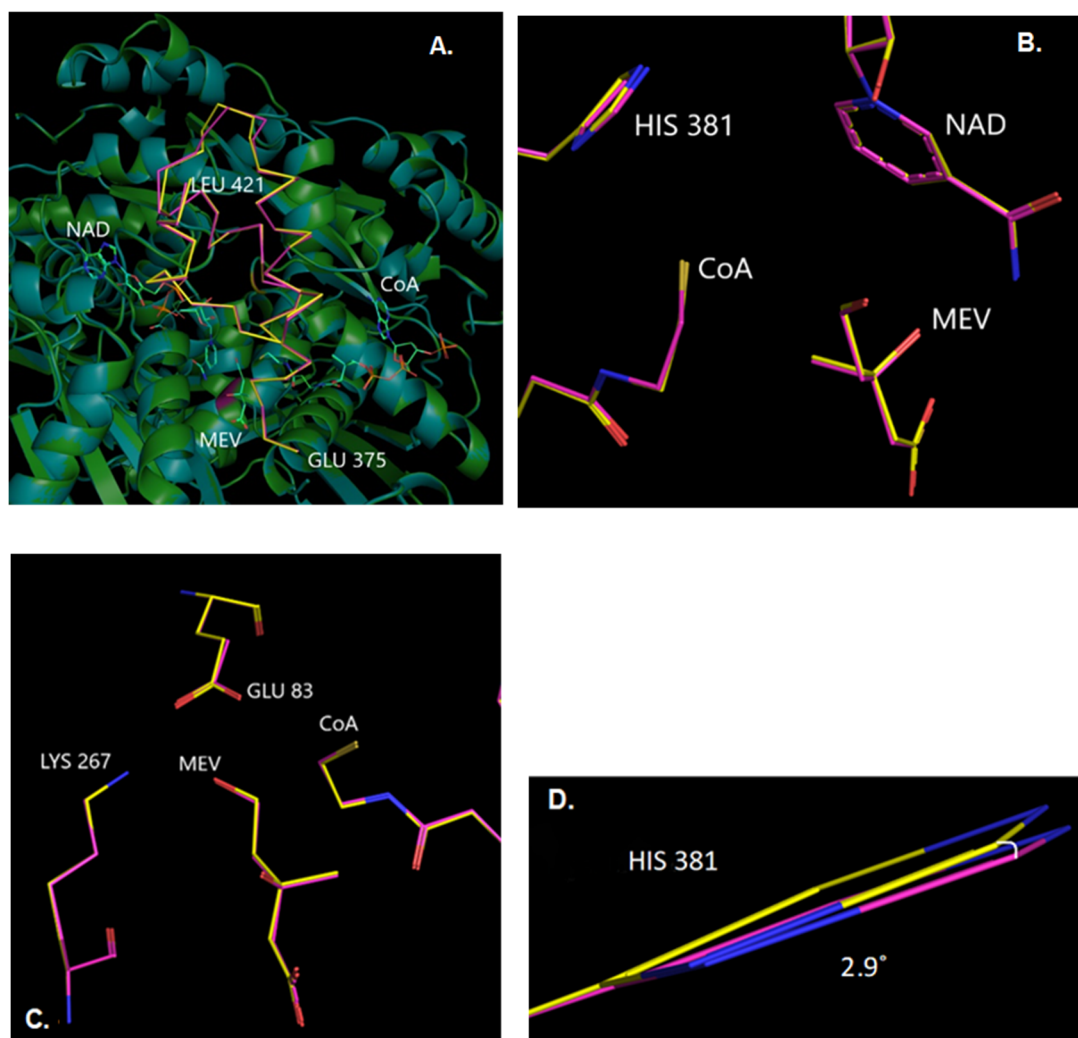


Figure 5.41 A. Comparison of wild type (violet) and E399A mutant (yellow) *PmHMGR* flap domain regions. B. Active site showing conformation of HIS 381 C. GLU 83 and LYS 267 in E399A (violet) and Wild type *PmHMGR* (yellow). D. Close-up view of changes in HIS 381 conformation in E399A (violet) and wild type *PmHMGR* (yellow).

However, in an additional E399A structure, the flap domain after ILE377 was not observed. Only mevalonate was found to bind at the active site. The structure obtained was observed to match closely with the binary complex with mevalonate (PDB ID: 4I6Y) with no significant RMSD deviation (RMSD: 0.4-0.7) until the flap region ILE 375-ILE377 where the RMSD is greater than 7 (Shown in Fig 5.42.). In contrast to the structure obtained with mevalonate (4I6Y), the flap region between GLU 375-ILE 377 in the E399A mutant is observed to fold in the same direction as the quaternary complex flap domain (Shown in Fig. 5.43). However, the flap domain is still not observed in this mutant structure.

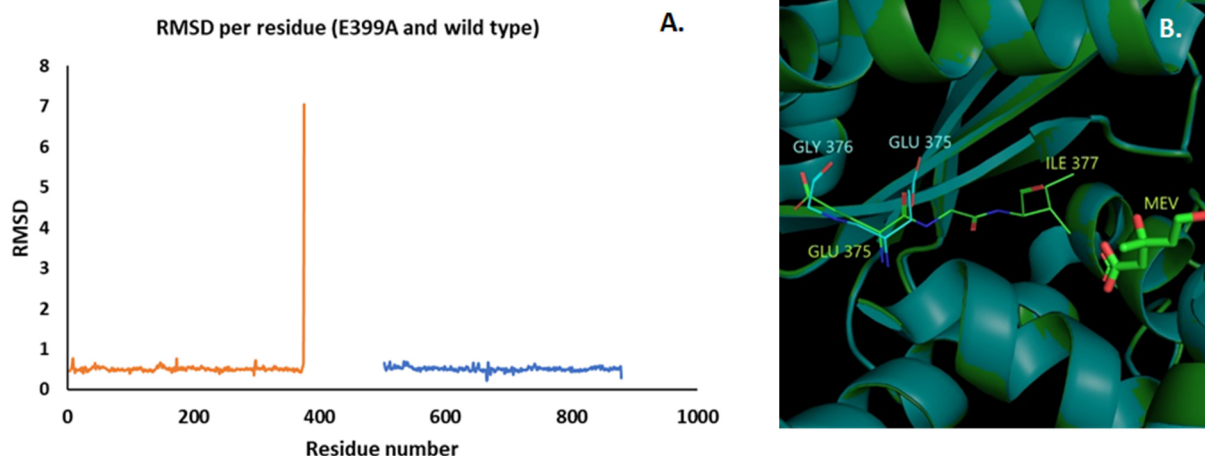


Figure 5.42 A. RMSD per residue between an E399A mutant and wild type pM. HMGR bound to Mevalonate B. First helix flap domain residue GLU 375-ILE 377 for E399A mutant (teal) and the wild type (green) pM. HMGR bound to Mevalonate.

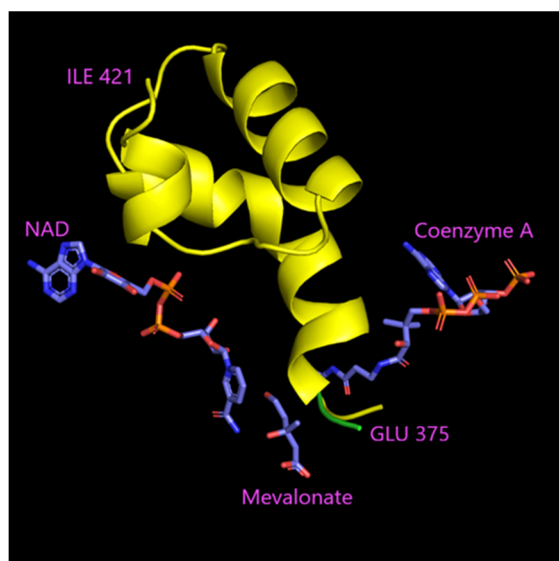


Figure 5.43 Flap domain region from GLU375 - ILE377 in E399A (green) shown in contrast to the flap region from GLU 375 - ILE 421 in the wild type quaternary complex (yellow). Mevalonate, Coenzyme A and NAD<sup>+</sup> are shown from the quaternary structure for reference.

In the case of the L407S mutant, the flap region was also not visible after ILE 377 in the structure obtained. Only mevalonate was observed at the active site. The structure of the enzyme was compared to the structure obtained with just mevalonate. The RMSD of the structures was plotted and minimal variation was observed across the enzyme (RMSD – 0.3-0.5; Shown in Fig 5.44 A.). The only prominent change was observed in the flap domain region between GLU 375-ILE377 where the conformation of the L407S had the flap domain oriented closer to the mevalonate binding region and showed density for ILE 377 whereas no density for ILE 377 was observed in the wild type enzyme bound to mevalonate (Shown in Fig 5.44 B.).

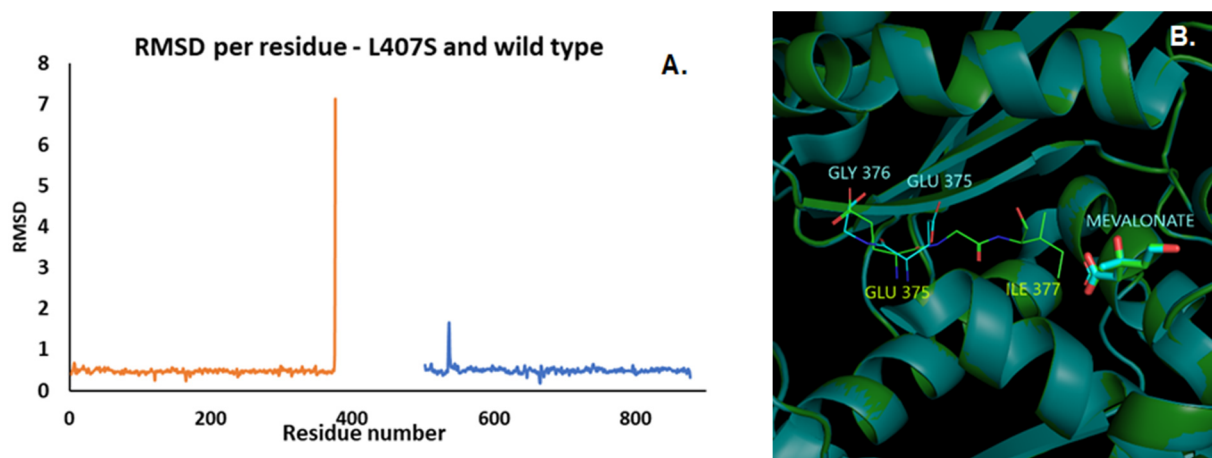


Figure 5.44 A. RMSD per residue between a L407S mutant and wild type *PmHMGR* bound to Mevalonate B. First helix flap domain residue GLU 375-ILE 377 for L407S mutant (teal) and the wild type (green) *PmHMGR* bound to Mevalonate.

### 5.3.7 Movement in the *PmHMGR* small domain

Movement in regions of the small domain spanning from residue D 646 – L 652 was observed 20 and 30 seconds after the enzyme was introduced to a pH 9 environment (Fig 5.45 B - C, F). This movement is observed to reduce subsequently at longer time points at higher pH (40 – 50 seconds) and become localized in residues closest to the NAD<sup>+</sup> adenine and ribose binding sites (Fig 5.45 D - E, F). Movements in the residue region D 646 – L 652 are observed to occur in tandem with movements observed in the third helix of the flap domain (D 416 – A 418) (Fig 5.45 G). Subsequently at longer soaking times at higher pH (50 seconds), we observe movements of the ligands also initiate movement in the first helix of the flap domain (I 389) (Fig 5.45 H).

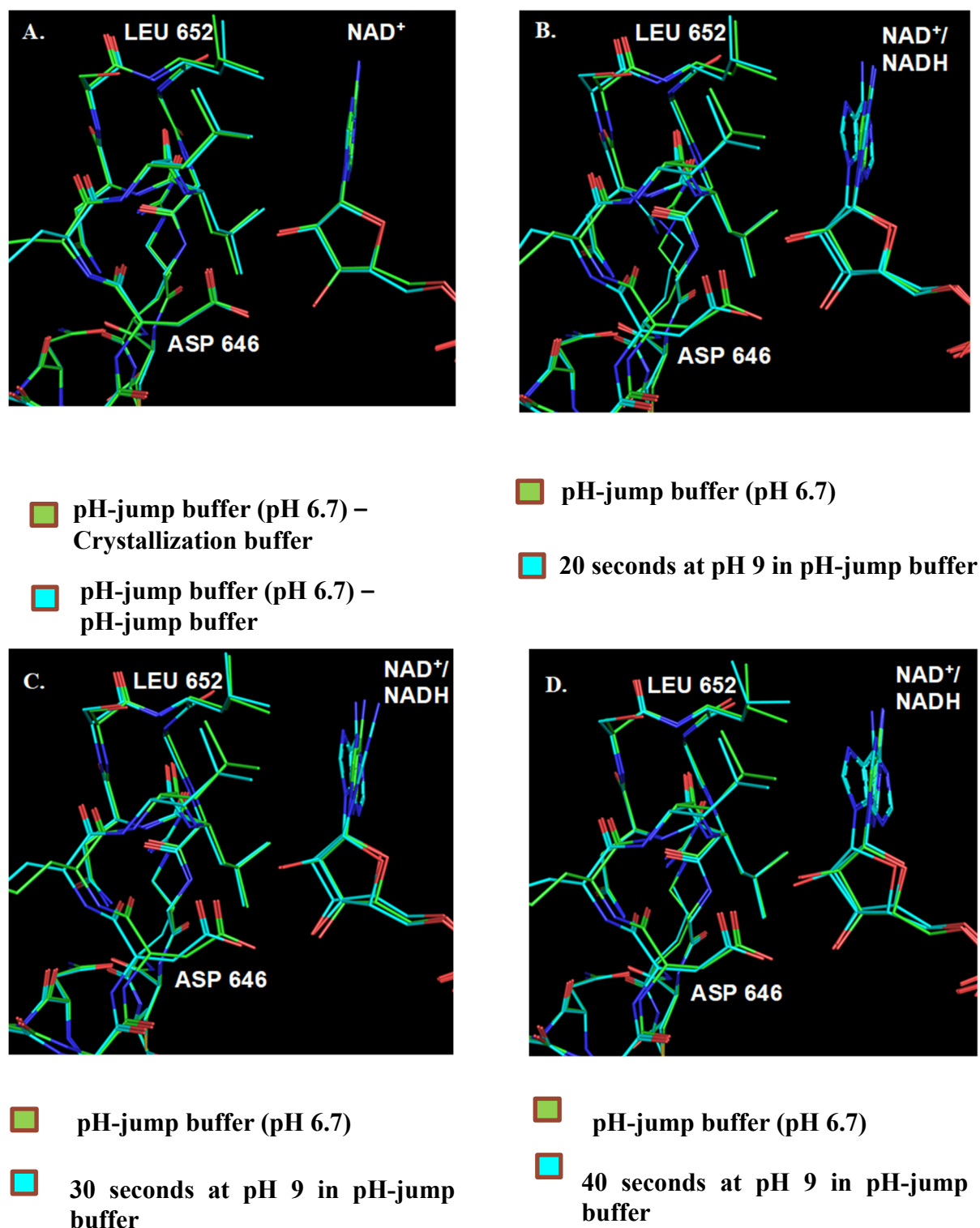
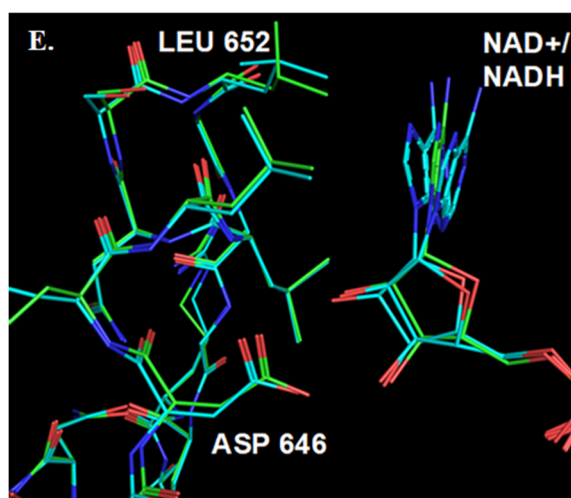


Figure 5.45 A. Movement in the small domain region adjacent to NAD-adenine-ribose after a pH-jump buffer exchange and at different time points at pH 9 (B-E), F. RMSD comparisons of the residue region 640-658 in the *Pm*HMGR small domain. F. Movements in the neighboring regions of the flap and small domains adjacent to the NAD<sup>+</sup> / NADH-adenine-ribose binding site 20 seconds (G.) and 50 seconds (H.) at pH 9 in comparison to a pH 6.7 environment.

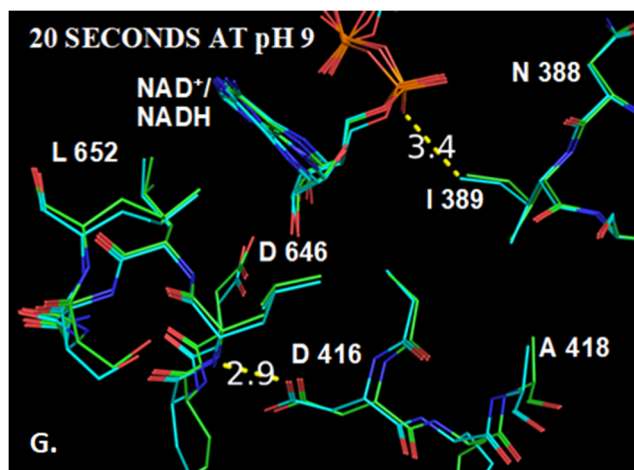
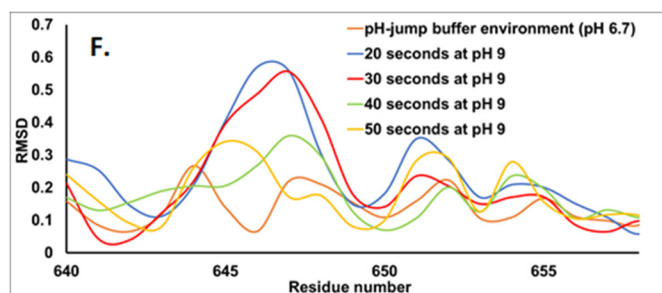


Figure 5.45 continued



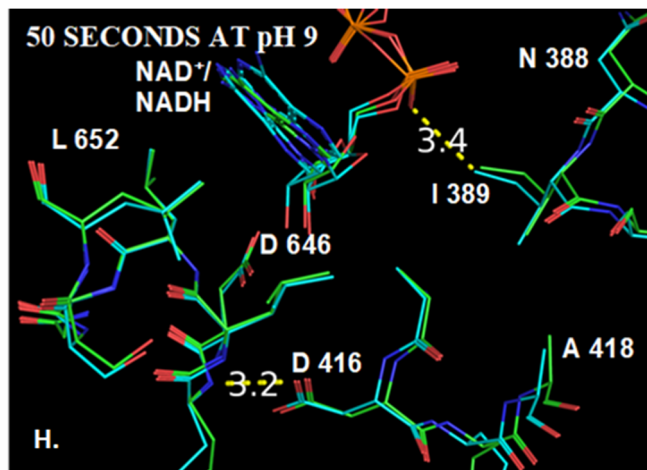
■ pH-jump buffer (pH 6.7)

■ 50 seconds at pH 9 in pH-jump buffer



■ pH-jump buffer (pH 6.7)

■ 20 seconds at pH 9 in pH-jump buffer



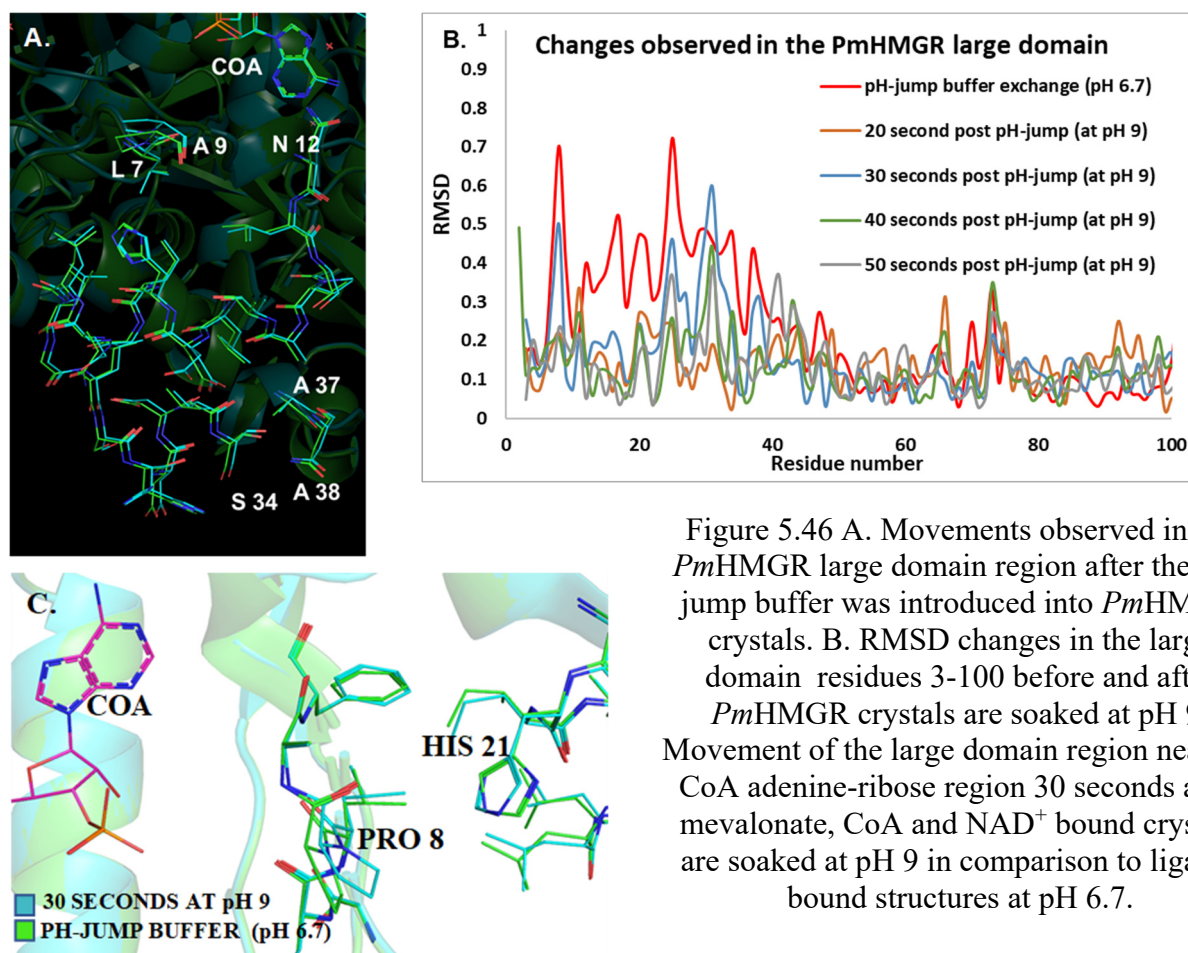
■ pH-jump buffer (pH 6.7)

■ 50 seconds at pH 9 in pH-jump buffer



### 5.3.8 Movement in the *Pm*HMGR large domain

Significant movements in the large domain region of *Pm*HMGR were observed in crystals after the pH-jump buffer constituents ammonium acetate, ADA and PEG-400 were introduced into the crystallization environment. While the large domain residues LEU 3 – MET 50 show significant movement (RMSD 0-0.7) after being introduced to a pH-jump buffer environment, the movements in this region are not as significant after the crystals are transferred to a pH 9 environment (Fig 5.46 A.). Following the pH-jump the movements are observed to be more localized between residues SER 5 – PHE 10 and ASP 20 – GLY 40 and to varying degrees with the largest movement observed 30 seconds after the pH-jump (Fig 5.46 B.). The movement in the large domain that is observed after the introduction of the pH-jump buffer exchange appears to be a result of changing domain conformation in response to the surrounding environment. However, in the case of the post pH-jump structure, the observed movement appears to be a response to changing conformation of Coenzyme-A at the active site (Fig 5.46 C.).



## 5.4 Discussion

Our studies of the effects of ions and pH in the crystallization environment led to the development and testing of the pH-jump reaction triggering method (Chapter 3). The utilization of ionic inhibition and pH-dependent kinetic properties of the enzyme for reaction triggering in *PmHMGR* crystals has also been demonstrated using spectroscopic methods (Chapter 4). As per UV-Vis spectroscopic measurements, it appears that the enzyme is inactive at pH 6.7 in a pH-jump buffer environment. Transferring the enzyme to a pH 9 environment initiates enzyme activity in crystals. Subsequent work with this method has been focused on its application in acquiring time-resolved crystallographic diffraction data.

After testing the application of this method in reaction initiation, we wanted to utilize this approach to observe untapped transitory states along the *PmHMGR* reaction pathway using crystallographic structures. While our spectroscopic measurements and calculations of the reaction progressing in the *PmHMGR* crystal environment have indicated that the reaction is progressing over a minutes time scale, we need to determine the time course within which we can expect to trap various intermediate states of the reaction. Additionally, while our spectroscopic experiments show the occurrence of a hydride transfer reaction step, we also need to observe the formation of thioester bond between mevalonate and CoA to confirm the full progression of the *PmHMGR* reaction in crystals.

To establish the time-course within which we can expect to observe various intermediate states of the *PmHMGR*, an experiment was designed where *PmHMGR* crystals bound to mevalonate, CoA and NAD<sup>+</sup> after being exchanged with pH-jump buffer at pH 6.7 were introduced to a pH 9 environment for several widely spaced time points ranging from 20 seconds – 10 minutes. The goal of this study was to determine if thioester bond formation can be observed between the ligands mevalonate and CoA and to determine the time points within which we can expect the hydride transfer, NAD<sup>+</sup> / NADH exchange and product (HMG-CoA) release to occur. After doing so our studies have focused on studying several closely spaced structures obtained within 1 minute of reaction initiation in *PmHMGR* crystals where we focus on biochemical and conformational changes that occur during the hydride transfer step.

The pH-jump method was applied to trigger reaction initiation in a mevalonate, CoA and NAD<sup>+</sup> bound complex. Trapped intermediates that are captured using this method are expected to show changes near ligand-binding and allosteric regions that facilitate turnover. Hence, by

comparing the quaternary complex to other static ligand-bound binary, ternary and apoenzyme structures that mimic various reaction states, we can identify various regions influenced by ligand-binding and intermediate / product formation. This information is beneficial in understanding the changes associated with reaction initiation in post pH-jump structures.

#### **5.4.1 Comparison of the *Pm*HMGR quaternary complex to various ligand-bound structures**

The binding of the ligands mevalonate, CoA and NAD<sup>+</sup> is shown to move neighboring regions in the small and large domain of the bound NAD<sup>+</sup> closer to the ligand-binding site (Fig 5.3 A). Additionally, the binding of these ligands also results in the closure of the flap domain. Such changes are not observed at the CoA binding large domain site perhaps due to the increased accessibility of that region to the solvent. However, the binding in the mevalonate, CoA region is also observed to influence movements in the small domain near the NAD<sup>+</sup> binding site as has been observed in the HMG-CoA, mevalonate and thiohemiacetal bound structures in the absence of NAD<sup>+</sup> (Fig 5.3 B, 5.3 C, 5.3 D). This indicates that the interactions formed with mevalonate and the enzyme in the mevalonate, mevaldyl-CoA and HMG-CoA complexes are enough to move the small domain close to the conformation observed in the mevalonate, CoA and NAD<sup>+</sup> complex (Fig 5.3 B, 5.3 C, 5.3 D). The interactions formed with the helix adjacent to mevalonate in the small domain (GLY 686 – THR 705) appear to affect regions of the small domain further away, thereby pulling them closer to the active site than the apo enzyme. The effect of mevalonate binding interactions on the small domain conformation is further observed in the absence of the substrate in the NADH bound structure (Fig 5.3 E). While the cofactor does influence the small domain conformation bringing neighboring regions closer to the active site, there are still helical regions neighboring the mevalonate binding site that do not fully achieve the conformation observed in the quaternary complex. This difference can be attributed to the lack of mevalonate. Additionally, a small variation in the large domain region neighboring the NADH binding site is also observed (Fig 5.3 E). This could be attributed to minor differences in cofactor positioning in the absence of the substrate. However, its movement in comparison to the apo, HMG-CoA and mevalonate bound structures indicates the effect of NAD<sup>+</sup> binding on the adjacent large domain region.

In comparison to the NAD<sup>+</sup> and mevalonate bound binary complex structures, we observe a greater degree of movement away from the active site in the presence of a CoA bound structure in comparison to the quaternary complex (Fig 5.3 F). However, it doesn't appear to be as great as the difference between the quaternary complex and the apo enzyme indicating that CoA binding does have some effect on the small domain conformation. This has been previously pointed out in structural comparisons by Duncan et. al where the range of roll in motion of the NAD<sup>+</sup> and CoA bound *Pm*HMGR was analyzed in comparison to the apo enzyme<sup>[2]</sup>. The binding of CoA was shown to result in a roll-in movement of small domain regions spanning MET 685 – LEU 720 and ALA 627 - PHE 664. The orientation of the thiol region of CoA in the quaternary complex is shown to be reoriented in the presence of mevalonate towards its terminal hydroxyl region (Fig 5.47 A). This indicates that the presence of both substrates in the quaternary complex also results in their rearrangement to initiate turnover.

The comparison of the mevalonate-NAD<sup>+</sup> structure that lacked the presence of CoA to that of the quaternary complex also illustrated the effect of CoA binding on the structure (Fig 5.3 G). Interestingly, both the structures showed flap domain closure with observed density for flap residues between GLU 375 – ALA 418. This indicated that the conformational changes in the small and flap domain brought about by contacts formed between the ligands NAD<sup>+</sup> and mevalonate respectively is enough for flap domain closure. The binding of CoA, however, is found to readjust the conformation the flap domain, the large domain neighboring CoA and the small domain neighboring NAD<sup>+</sup>. The binding of CoA does not appear to change the conformation of any of the residues near the active site. This indicates that while the entry of CoA rearranges the flap region, it should not affect the initiation of enzymatic activity. The observed conformational changes brought about after CoA binding might also play a significant role in coordinating changes in subsequent steps of the reaction pathway. However, the movements visually appear to be slight readjustments after ligand binding and might have no effect on the reaction. In the mevalonate-NAD<sup>+</sup> complex structures where the flap domain is not observed to close due to reduced binding of the ligands because of lower soaking time and ligand concentrations, small differences in the small domain conformation neighboring NAD<sup>+</sup> are observed (Fig 5.3 H). This difference indicates that it is the flap closure that results in the full movement of the NAD<sup>+</sup> binding small domain observed in the quaternary complex. These flap-small domain contacts also observed in CoA-NAD bound structure (Fig 5.47 A and B.).

The lack of significant changes observed in the absence of CoA with respect to the formation of the active site indicate the easy accessibility of the CoA binding site. The CoA binding region should allow entry and release of the cosubstrate without significantly affecting the enzyme conformation while mevalonate and NAD<sup>+</sup> binding resulting in flap closure which is crucial for active site formation and regulating cofactor exchange.

The structures of *Pm*HMGR bound to both NAD<sup>+</sup> and CoA in the absence of mevalonate adopt a conformation very similar to that of quaternary complex with subtle negligible variations in conformations of regions of the small domain (Fig 5.3 I). In comparison to the quaternary complex, the CoA and NAD<sup>+</sup> bound structure also shows differences in the conformation of certain solvent exposed and flexible regions of the flap domain.

These results indicate that while the binary complex of *Pm*HMGR with mevalonate brings about movements in the region between GLY 630 – ARG 721 that are closer to the conformation observed in the quaternary complex in comparison to the binary complexes with CoA or NAD<sup>+</sup>, the ternary complex of CoA and NAD<sup>+</sup> can facilitate conformational changes across the enzyme that are very close to the pre-turnover state without mevalonate through the closure of the flap domain. The movements observed in the small domain and the contacts formed between NAD and the flap domain (Fig 1.7.) and between the small and flap domains through mevalonate (Fig 5.48 B) could be instrumental in flap closure. The flexibility of this region could also be instrumental in coordinating NAD<sup>+</sup>/NADH movement and cofactor exchange.

The presence of the flap domain in both CoA-NAD<sup>+</sup> and mevalonate-NAD<sup>+</sup> complexes and its absence in the mevaldehyde-CoA complex indicates that the nucleotide is essential for locked flap configuration observed in crystal structures. The closed position formed between the *Pm*HMGR flap and small domain with NAD<sup>+</sup>-enzyme interactions could regulate the exchange of NAD<sup>+</sup> since the only observed factor controlling flap closure is the entry and release of NAD<sup>+</sup>, the mechanism of which is unknown.

The HMG-CoA and NAD<sup>+</sup> bound non-productive structure which closely resembles what would be the post-turnover complex after reaction initiation with a mevalonate, CoA and NAD<sup>+</sup> bound enzyme, has a conformation very similar to the quaternary complex (Fig 5.3 J). The lack of change is expected since the mevalonate, CoA and NAD<sup>+</sup> binding regions are fully occupied in this structure. Differences in the conformation are only observed in certain regions of the *Pm*HMGR flap domain. These regions happen to be more solvent exposed, and the movements

are shown to occur majorly in flexible connecting regions between the first, second and third helices. Differences in the orientation of the thiol atom and mevalonate binding region of HMG-CoA are also observed in comparison to the quaternary complex (Fig 5.48 C). However, with the absence of movement in the neighboring small, large and flap domain regions, it cannot be inferred that these differences in ligand placement affect the distant flap domain conformations since there are no observable connecting interactions. The position of the  $\text{NAD}^+$  cofactor in the HMG-CoA and  $\text{NAD}^+$  structure is found to be very close to that of the  $\text{NAD}^+$  cofactor in the quaternary complex. The terminal carboxyl region of HMG-CoA is also found to be placed in a position close to that observed in mevalonate in the quaternary complex. This would explain the lack of movement in the small domain. It can be speculated from this observation that the difference in small domain configuration and flap domain closure observed in the absence of mevalonate and / or  $\text{NAD}^+$  is a result of missing interactions with the cofactor and substrate with the small and flap domain respectively with both the ligands (Fig 5.48 B). In the case of HMG-CoA and  $\text{NAD}^+$  bound complexes, if the substrate region can preserve the same interactions in its terminal hydroxyl and methyl carbon atom with the small and flap domain, then the placement of the rest of HMG-CoA does not appear to affect the conformation of the molecule (Fig 5.48 B, C). The similar conformations of the non-productive and quaternary complexes also indicate that we cannot expect much variability between pre and post turnover states going from the mevalonate, CoA and  $\text{NAD}^+$  to HMG-CoA and NADH unless there are significant differences in the placement of the reduced cofactor. The conformational changes observed across the reaction pathway would hence largely be a result of changes at the active site associated with possible substrate and cofactor movement during intermediate formation and cofactor exchange.

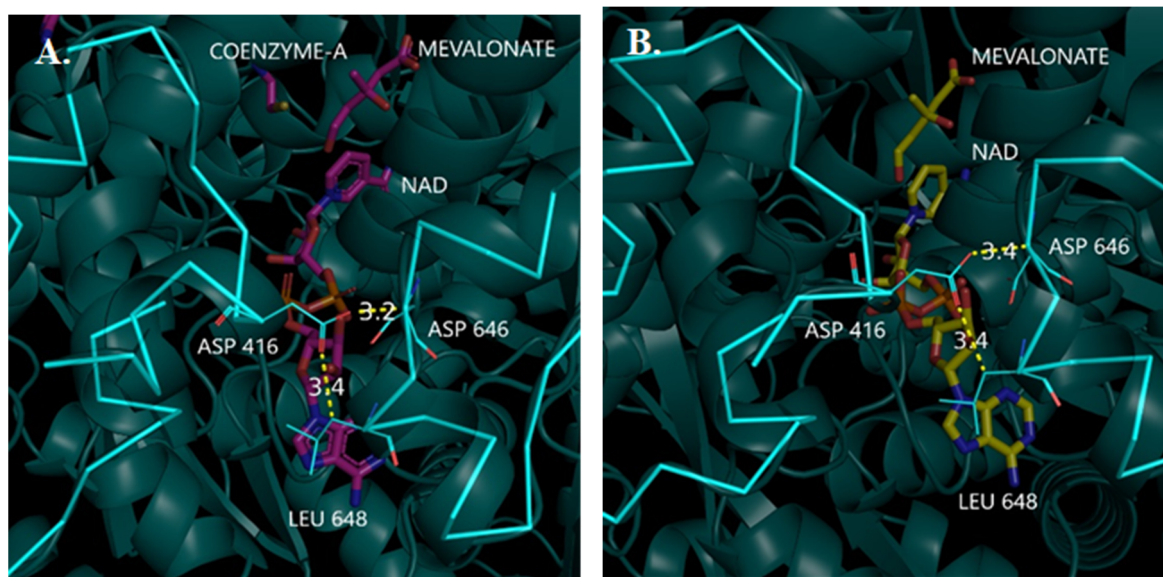


Figure 5.47 Interactions between flap and small domain in the structure bound to A. CoA and  $\text{NAD}^+$  and B. Mevalonate and  $\text{NAD}^+$ .

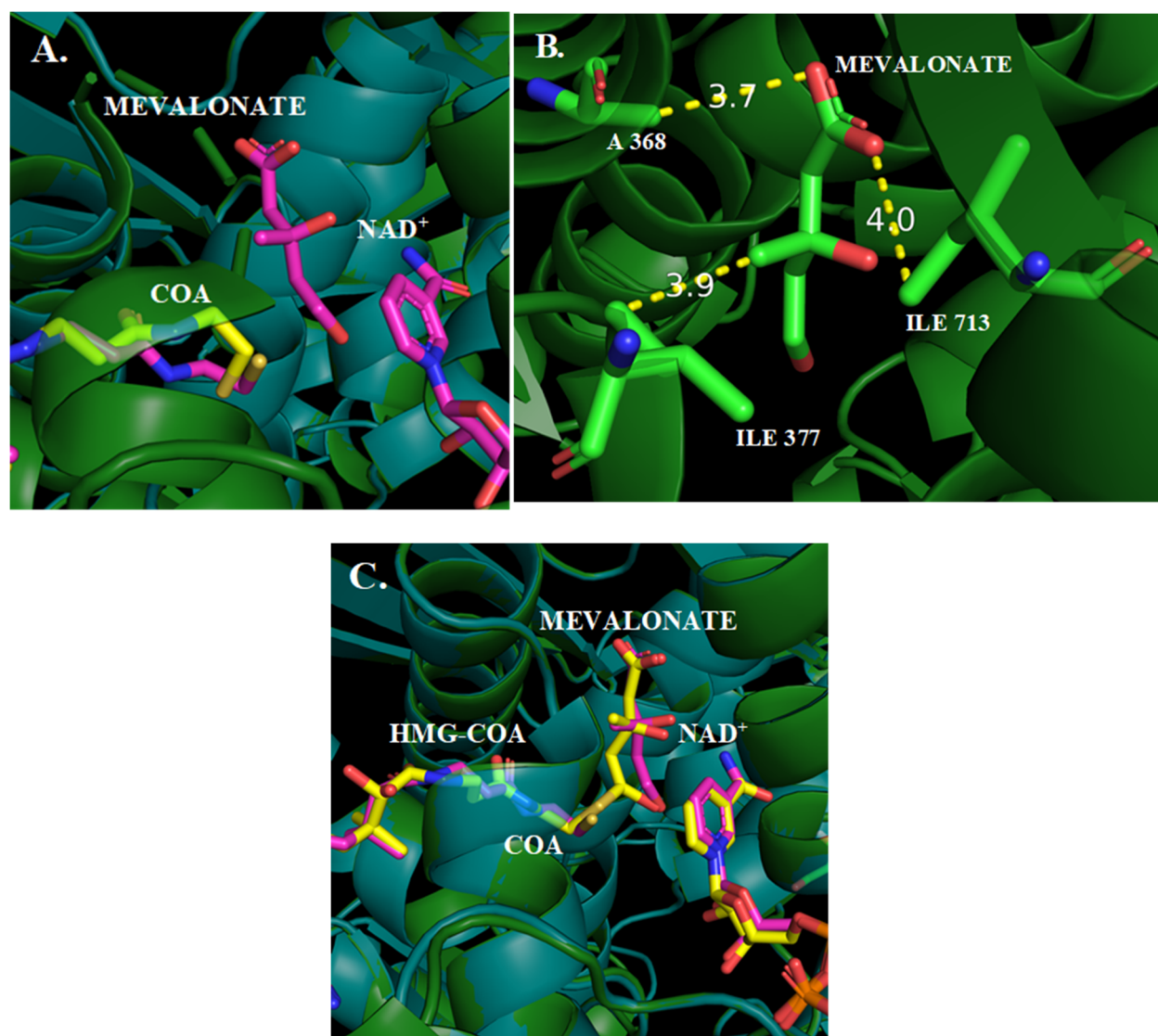


Figure 5.48 A. Mevalonate, CoA and NAD<sup>+</sup>(purple) and the CoA bound region in the *PmHMGR* active site, B. Mevalonate bound region showing contacts with ALA 368, a region adjacent to the flap domain, ILE 377 on the flap domain and LEU 713 on the small domain and C. Mevalonate, CoA and NAD<sup>+</sup>(purple) and the HMG-CoA bound region in the *PmHMGR* active site.



Inferences about the effect of ligand binding on enzyme conformation, domain interaction and positioning of other ligands at the active site that were deduced from this structural comparison were subsequently applied to further understand changes taking place along the *Pm*HMGR reaction pathway. While the static ligand-bound structures can capture some of the stages along the reaction pathway, there are several intermediary stages in the reaction mechanism that have been unexplored. These include the steps associated with mevalonate oxidation, changes facilitating conversion of mevaldehyde into mevaldyl-CoA, cofactor ( $\text{NAD}^+/\text{NADH}$ ) exchange and product (HMG-CoA) release (Illustrated in Fig 2.8). The use of time-resolved methods allows us to capture these intermediary states and understand the conformational and biochemical changes associated with them.

#### **5.4.2 Application of the pH-jump triggering method to observe reaction initiation in *Pm*HMGR crystals**

The pH-jump reaction triggering method was applied on mevalonate, CoA and  $\text{NAD}^+$  crystals to trap reaction intermediates after turnover initiation. Initial structural studies looked at sparse time points separated between 20 seconds – 10 minutes after reaction initiation with the pH-jump.

Based on polder maps generated for the ligands in the pre-pH jump structure of *Pm*HMGR crystals soaked in the pH-jump buffer with mevalonate, CoA and  $\text{NAD}^+$  at pH 6.7, we can determine that there is no change in electron density that indicates thioester bond formation between mevalonate and CoA (Fig 5.6 B). Additionally, based on the lack of absorbance at 340 nm observed in pre-pH jump ligand-bound *Pm*HMGR crystals at pH 6.7 and the flat density observed around the nicotinamide ring in  $\text{NAD}^+$ , we can tell that there is no NADH formation before the pH-jump (Fig 4.2-4.4). This indicated that electron density changes associated with turnover would only be present at pH 9.

After a soaking time of 5 minutes following reaction initiation at pH 9, we observe the appearance of density in our generated omit maps between the mevalonate and CoA binding region between the two ligands (Fig 5.6 F). This change indicated that at sufficiently long soaking times at higher pH, we do observe the formation of the second intermediate with the formation of a thioester bond. A gradual build-up of this thioester density was also observed when comparing 2Fo-Fc maps of this region in structures obtained 1 minute – 5 minutes after reaction initiation via

a pH jump (Fig 5.6 I - L). Subsequently, at even longer soaking times of 10 minutes we observe a drastic reduction in electron density of all the bound ligands (Fig 5.6 H). This change is indicative of the product being released as has also been previously observed in time-resolved spectroscopic absorbance measurements of NAD<sup>+</sup> to NADH conversion (Fig 4.3). The lack of changes associated with thioester bond formation until 2 minutes and 20 seconds following a pH change (Fig 5.6 D, 5.6 J) in addition to the lack of NADH absorbance at pH 6.7 further indicates that the pH-jump buffer environment (At pH 6.7) appears to keep the enzyme in an inactive state and that the changes associated with mevaldyl-CoA formation are only observed after the ‘pH-jump’ (Fig 5.6 A-D).

Initial structures following a pH-jump were studied more closely and movements of different regions following a pH change were identified. One of these identified movements was found to be adjacent to the adenine portion of NAD<sup>+</sup> in the flap domain (Fig 5.7 A, B). Movement of the flap domain observed 20 seconds following a pH change was initially speculated to be a result of pH, environment or reaction initiation.

Initial alignments also indicated changes in the distance between NAD<sup>+</sup>, mevalonate and CoA. The distance changes between mevalonate and NAD<sup>+</sup> were measured between the amide on the NAD-nicotinamide ring and the hydroxyl oxygen of mevalonate (Fig 5.7 C). While these two atoms are not directly involved in the hydride transfer step, the decrease in their distance indicated a changing placement of the substrate / intermediate and the nicotinamide ring. An increasing distance was also measured between the oxygen on the terminal end of the substrate / intermediate and CoA indicating a movement of the substrate mevalonate closer to the cofactor and away from CoA (Fig 5.7 D). These changes were the first structural indication of rearrangements at the enzyme active site that would be associated with the hydride transfer step.

The structural changes in the *Pm*HMGR flap domain in comparison to the control pre-pH jump structure are not as prominent at 1 minute following a pH-jump as they are observed to be 20 seconds in a pH 9 environment (Fig 5.8). This difference is observed particularly in regions spanning between HIS 411 – LEU 421 that are closer to NAD<sup>+</sup> (Fig 5.8 A). The shift back to the pre-pH jump configuration over time as is observed in the 1-minute post pH-jump structure in comparison to the one acquired 20 seconds after a pH change could be due to the relative position of NAD<sup>+</sup> being closer to that in the control structure than the NAD<sup>+</sup> observed at 20 seconds.

The position of NAD<sup>+</sup> nicotinamide is observed to move further away from the hydroxyl region in mevalonate (Fig 5.8 C). Similarly, the hydroxyl region in mevalonate is observed to

move closer to CoA (Fig 5.8 D). These changes show that the structure obtained at 1 minute after a pH-jump is capturing changes after a hydride transfer has taken place between Mevalonate and  $\text{NAD}^+$ , where the enzyme is now beginning to promote an interaction between  $\text{NAD}^+$  and CoA.

The observation of these changes before and after reaction initiation indicated the possibility of trapping both pre and post hydride transfer states before observing changes associated with thioester bond formation. It also informed us about the time range (20 seconds – 1 minute) within which we could capture further structural information about the hydride transfer reaction step. The observation of an NADH absorbance peak 65 seconds after a pH-jump in 0.1 mm crystals and 80 seconds after a pH-jump in 0.4 mm crystals further indicates the possibility of observing post hydride transfer changes within this time frame. While one quantifies the population immediately after a pH jump, the other captures the state right before a bond between the substrate and cofactor start to appear.

2 minutes and 20 seconds following a pH change, we observe movements in the flap domain that would promote thioester bond formation. This has been documented with a rotation of HIS 381 towards the thiol region of CoA-SH and movement of the large domain towards CoA-adenine-phosphate (Fig 5.9 D). The interaction between a deprotonated HIS 381 and CoA-SH at high pH would result in a proton transfer between CoA-SH and HIS 381 resulting in the formation of  $\text{CoA-S}^-$ .  $\text{CoA-S}^-$  would then be able to interact with mevaldehyde to form a thioester bond resulting the formation of mevaldyl-CoA.

A rearrangement of the adenine-ribose phosphate and pantothenic acid portion of CoA is also observed with neighboring movements in the large and flap domain. This movement would be associated with HMG-CoA bond formation (Fig 5.9 B).

This movement of the large domain region neighboring CoA-SH and flap domain residue HIS 381 towards the CoA-SH thiol atom is observed to become more prominent 4 minutes after a pH change (Fig 5.10 B, C) during which time we also start observe the appearance of a thioester bond density between the mevalonate and CoA binding regions (Fig 5.6 E, 5.6 K). These movements are hence speculated to enable the formation of a thioester bond between mevaldehyde and CoA and the *Pm*HMGR active site.

At 5 minutes where we observe a strong thioester bond density (Fig 5.6) between mevalonate and CoA binding indicating significant mevaldyl-CoA formation in the *Pm*HMGR crystal environment (Fig 1.1). The density of the adenine portion of  $\text{NAD}^+$  indicates two alternate

conformations of the ligand in this region, one pointing towards and the other away from the flap domain (Fig 5.11 B). The presence of two conformations and the relative change in the flap and small domain conformations indicates that the state captured is showing movement of NAD<sup>+</sup>/NADH after the thioester bond formation step. Given that NAD<sup>+</sup>/NADH binding has been shown to affect the conformation of the adjacent small and flap domain regions (Fig 5.3 E), we would expect to observe a conformational change in adenine bound region of the enzyme with movement of the cofactor.

After the formation of HMG-CoA, it is speculated that changing interactions of the NAD<sup>+</sup>-adenine-ribose regions with the flap and small domains could initiate the release of ligands from the enzyme's active site. Given the solvent exposure of this site, the same interactions could also play a role in mediating cofactor exchange along the reaction pathway. Considering that this cofactor is involved in the second hydride transfer that converts Mevaldyl-CoA into HMG-CoA, the movement can be presumed to be after HMG-CoA formation. We observe both the adenine-phosphate-ribose of CoA and the neighboring large domain again adopting the conformations observed in the crystallization buffer conditions at pH 6.7 (Fig 5.11 C). If we are indeed observing HMG-CoA formation, this movement could be a post-turnover rearrangement in the CoA binding site to facilitate the product release. We also observe the catalytic HIS 381 returning to its original configuration in the pre pH-jump structure indicating a possible change in the flap conformation after HMG-CoA formation (Fig 5.11 D). As was also observed in the HMG-CoA and NAD<sup>+</sup> bound structure, the conformation of the enzyme was found to resemble the quaternary complex very closely in the large domain region (Fig 5.3 J).

At 8 minutes, we observe significant movement of the ligands at the active site that indicate changes associated with their release (Fig 5.12). This could be initiated after HMG-CoA formation. This is further shown by the drastic reduction in density of the adenine-ribose-phosphate regions of CoA 8 minutes after being introduced into a pH 9 environment (Fig 5.12 F). The reduction in this density indicates that this region of the co-substrate has increased mobility potentially from leaving the enzyme active site which is also indicated from its changed configuration with respect to the adjacent large domain (Fig 5.12 B). Unlike what is observed 5 minutes after a pH change, the structure observed 8 minutes after a pH change does not have alternate conformations of NAD<sup>+</sup> which is now observed to be back in a configuration matching that of the pre pH-jump structure (Fig 5.12 D). This could indicate the possibility of obtaining a post turnover state in the enzyme

following the formation of HMG-CoA with a new cofactor molecule now being present at the active site. In correlation with the changes observed at 8 minutes, the reason for NAD<sup>+</sup>/NADH movement at 5 minutes is speculated to either initiate the process of ligand release or indicate a cofactor exchange taking place before NADH reduction. Obtaining more closely spaced time points between 5 minutes – 10 minutes would allow us to closely follow the changes in the cofactor that take place following thioester bond formation. A conformational change in the position of HIS 381 is also observed with the  $\delta$  N of HIS 381 pointing towards CoA (Fig 5.12 E). The change in HIS 381 conformation could be a result this flap domain residue readjusting to a population of CoA leaving the active site in the crystal.

10 minutes following a pH-change, we observe a drastic reduction in electron density and movement of ligands that indicates their release from the enzyme's active site (Fig 5.13 C, 5.14 B). Regions of the first and second helices (HIS 385 – VAL 410) of the flap domain are also observed with much weaker density or not observed at all indicating that there is an increased mobility in this interhelical region (Fig 5.13 A, 5.15 B). The increased mobility in the flap domain could be a result of movements observed at the active site. This movement would bring changes in the ligand-flap domain interactions in residues of the first helix that is near NAD<sup>+</sup> and HMG-CoA thereby affecting the flap domain configuration (Fig 5.13 D). The reduction in electron density of NAD<sup>+</sup> and HMG-CoA at the active site has also been observed (Fig 5.13 C). In the case, of NAD<sup>+</sup>, we find weaker density in the adenine-ribose regions whereas in the case of HMG-CoA, the density appears to be weaker from the adenine to the thiol region of the molecule. These density changes in comparison to the electron density for the ligands observed at 8 minutes indicate further movement of HMG-CoA out of the active site (Fig 5.12 F, 5.13 C). This can be determined from the density first weakening in the adenine, ribose and phosphate regions of the molecule at 8 minutes and then extending across the pantothenic acid region at 10 minutes. In contrast to the electron density observed for the ligands at 8 minutes, we also happen to see a weakening of the NAD<sup>+</sup> density in the adenine and ribose region. This change in NAD<sup>+</sup> density indicates that the release of ligands is first initiated by HMG-CoA which subsequently results in NAD<sup>+</sup> release (Fig 5.12 F, 5.13 C). We find small and flap domain regions around NAD<sup>+</sup> to also be moving indicating the regions that change conformation during the release of NAD<sup>+</sup>.

We also do not observe the thioester bond density at the active site. This could indicate that in addition to release of HMG-CoA, we might have CoA and mevalonate re-entering the *PmHMGR* active site (Fig 5.13 C).

In addition to the release of ligands, we also observe corresponding changes in the flap domain residue HIS 381 that is observed to move out of its initial configuration towards the NAD<sup>+</sup> ribose hydroxyl atom (Fig 5.13 E). This change in conformation appears to follow from its initial conformational change observed at 8 minutes and appears to be a readjustment of the residue upon ligand release.

### **5.4.3 Conformational changes in the flap domain associated with ligand and small domain movements**

Comparing movements in the flap domain with changes in electron density at the active site (Fig 5.6) – we can break the observed datasets into 3 reaction stages: 20 seconds – 1 minute after a pH change where we expect to observe the occurrence of a hydride transfer step, 2 minutes 20 seconds – 5 minutes where we observe the formation of a thioester bond and 8 – 10 minutes where we observe the release of the product and cofactor from the enzyme's active site. Additionally, changes in the *PmHMGR* flap NAD and adenine distance 20 seconds after a pH change (Fig 5.7 B) indicate the possibility of a cofactor exchange step occurring immediately after the mevalonate oxidation step.

Regions of the interhelical region between the first and second helices of the flap domain are also observed to show stronger electron density at 20 seconds. This change in density (Fig 5.17 B) is in agreement with the lower mobility of the residues E 399 and E 396 that is observed in QM/MM-MD simulations of the mevaldehyde reduction transition state (going towards mevalonate formation) performed by Quinn et. al<sup>[94]</sup>. Our structures indicate that this region also appears to obtain a more rigid conformation for the reaction going in the reverse direction during the time points where we expect to observe the hydride transfer between NAD<sup>+</sup> and mevalonate. The changing flexibility of this region is expected to influence the conformation of the rest of the flap domain.

Following the 20 second time point, we see a drastic reduction in the density of this interhelical region 1 minute after a pH change (Fig 5.17 C). This intermittent change in electron density indicates a possible conformational change in the flap domain that would allow cofactor

exchange. Subsequently, we observe this region having stronger density at time points (Fig 5.17 D – F) where we do observe thioester bond density from 2 minutes 20 seconds to 5 minutes after a pH change (Fig 5.6 F, J-L). The changing conformation and rigidity of the interhelical region could possibly be allowing the placement of the flap domain in a conformation that allows the correct placement of ligands at the active site for the hydride transfer and thioester bond formation steps. However, during intermittent steps that require ligand release, the increased mobility of this region could facilitate a partial movement of the flap domain away from the enzyme's active site to accommodate the release of the bound cofactor for the  $\text{NAD}^+/\text{NADH}$  exchange step.

In addition to affecting the placement of the flap domain during the hydride transfer step, the changing conformation of this interhelical region between helix 1 and 2 in the flap domain is also expected to affect the conformation of the flap domain during the thioester bond formation steps. The adopted conformation of the flap domain is expected to facilitate an interaction with the catalytic residue H 381 with CoA-SH to form a deprotonated co-substrate and subsequently form a thioester bond. Following the time points where we observe thioester bond formation, we again observe a changing electron density of this interhelical region between helices 1 and 2 of the flap domain 8 minutes after a pH change (Fig 5.17 G). After the formation of a thioester bond and the subsequent hydride transfer to form a product, we could expect a release of bound ligands at the active site before binding of new mevalonate, CoA and  $\text{NAD}^+$  molecules. Therefore, this change in conformation here is expected to allow the movement of the flap domain residues away from the active site to allow product release.

In observing the movement of the different flap domain helices, we find movements associated with  $\text{NAD}^+/\text{NADH}$  cofactor exchange from 20 sec – 140 sec after a pH-jump resulting in a contraction of helices in the flap residue region H 385 – A 393 and R 414 – N 423 (Fig 5.16 A, B). These regions are observed to contract at time points where we would expect release of the  $\text{NAD}^+/\text{NADH}$  cofactor (8 – 10 min) as well.

While the previous movement is expected to allow for the cofactor exchange step along the reaction pathway, the latter could be accommodating the eventual release of the cofactor. This is further supported by the observation of alternate  $\text{NAD}^+/\text{NADH}$  positions observed in the adenine-ribose region 5 minutes after a pH change indicating a movement in the cofactor after thioester bond formation (Fig 5.11 B). Given that this portion of the cofactor is solvent exposed allowing greater mobility, we would also expect to observe the cofactor exchange being initiated

in this part of the enzyme. Therefore, the subsequent contraction of the flap domain away from the NAD<sup>+</sup> binding site 8 minutes after a pH change is expected to accommodate cofactor exchange / release by allowing more room for ligand movement out of the enzyme (Fig 5.16 A, B).

Similarly, the flap domain regions neighboring CoA (I 377 – H 385 and E 399 – H 411) are found to contract at time points where we would expect thioester bond formation (4-5 min) possibly to accommodate room for CoA repositioning at the active site for thioester bond formation (Fig 5.16 A, B). In contrast to the NAD<sup>+</sup> / NADH binding site, these regions are found to expand at time points (8 – 10 minutes) where we observe product release. This movement could be indicating a flap-readjustment with HMG-CoA leaving the active site (Fig 5.16 A, B). While we have observed the enzyme remain largely unaffected in the large domain CoA-binding region upon entry and release of the cofactor subtle changes in the N-terminal portion of the large domain (LEU 3 – GLY 40) and the flap domain could be an indication of changes in CoA configuration and HMG-CoA release.

Extending these comparisons to the changes in contacts made by the flap domain at the active site at different time points can further elucidate its effect on the mechanism of *Pm*HMGR. Interdomain contacts mediated by ligands positioned between the flap and small or flap and large domains could facilitate a domain sensing mechanism that triggers individual steps of the enzymatic reaction (Shown in Fig 5.16 B).

A pH-change would thus kick off a biochemical or conformational change that initiates a cascade of movements and chemical changes at each step of the *Pm*HMGR reaction. Further studies that observe these sparse data points in more detail by obtaining more closely time steps would help elucidate the mechanistic changes that facilitate the hydride transfer step, the formation of mevaldyl-CoA from the proposed mevaldehyde intermediate and NAD<sup>+</sup>/NADH exchange. Since, very little is known about the first hydride transfer step and we have spectroscopic and crystallographic information (Fig 4.3, 4.4, 5.6) indicating its occurrence in the first minute of the reaction, we decided to obtain more time-resolved data points within the first minute of the pH-jump experiment.

Initial comparisons of structures obtained 20 seconds – 1 minute after a pH change indicated slight movements at the active site that indicated changes in cofactor and substrate during hydride transfer (20 seconds after a pH change) and after a hydride transfer to position the mevaldehyde intermediate for thioester bond formation with coenzyme-A.



This change is indicated by a change in the nicotinamide carboxyamide conformation, increasing distance between modelled NADH and mevaldehyde and readjustment of the ligand (modelled as mevaldehyde) in substrate binding region (Fig 5.18 A, 5.19 A, 5.21 A-B). This conformational change could indicate a conversion of mevalonate into mevaldehyde after a hydride transfer and a shift in orientation for mevaldehyde to interact with CoA (Fig 5.19 A-B, 5.22 A-C).

A reduction in the distance between the CoA-thiol atom and modelled mevaldehyde oxygen observed at 1 minute also indicates the reconfiguration of the co-substrate CoA at the active site to allow thioester bond formation (Fig 5.18 A, 5.22 C).

The initial movements captured at the active site were very small in magnitude and between very scarce time points to confirm that they were indeed corresponding to changes associated with the hydride transfer. However, the observation of an NADH absorbance peak within 65 seconds after a pH-jump and the thioester bond formation indicating the production of mevaldyl-CoA in mevalonate, CoA and NAD<sup>+</sup> soaked crystals indicated the possibility of capturing post hydride-transfer changes within the first minute of transferring ligand-soaked crystals to a pH 9 environment.

Hence, to further verify the changes observed at the active site and to determine more structural information centered around the hydride transfer steps, we decided to obtain several closely spaced time points between 20 seconds – 1 minute after transferring *Pm*HMGR crystals to a pH 9 environment.

#### **5.4.4 Comparison of polder maps at the mevalonate-NAD<sup>+</sup> interaction site within the first minute of reaction initiation**

To determine if post hydride transfer changes are observed at the mevalonate and NAD<sup>+</sup> binding site, the polder maps of the nicotinamide region of NAD<sup>+</sup> and in the mevalonate binding region were compared. By excluding the bulk solvent around the omitted region that is observed around the ligand-binding site, these polder maps are able to pick up the weakest signals and hence can indicate the presence of NADH or mevaldehyde density even if these reaction intermediates and biproducts are present at lower occupancy than the substrates<sup>[101]</sup>.

The flat and evenly spread-out polder map density (Fig 5.23 B) across the nicotinamide ring before the pH-jump indicating the presence of NAD<sup>+</sup> is congruent with the lack of NADH

absorbance observed in ligand-bound crystals that have been soaked in pH-jump buffer at pH 6.7 (Fig 4.2-4.4).

After the crystals are introduced into a pH 9 environment for 20 seconds, this density appears to be bulkier along the nicotinamide ring and mevalonate binding region indicating increased movement of the ligands at the active site and the possibility of having a mixture of the substrate (mevalonate), intermediate (mevaldehyde) and both the cofactors ( $\text{NAD}^+/\text{NADH}$ ) at the enzyme's active site (Fig 5.23 C).

Formation of NADH from  $\text{NAD}^+$  has been previously shown to result in a puckering of the pyridine ring in NADH-bound structures of Liver Alcohol Dehydrogenase and in DFT calculations of the reduced nicotinamide with the C4 and C6 atoms being out of plane<sup>[99]</sup>. Hence, in order to detect the formation of NADH in our structures we were looking for changes that indicated an emerging asymmetry in the distribution of electron density in the cofactor nicotinamide ring.

At subsequent time points following a pH change ranging from 30 seconds – 60 seconds after the crystals are introduced into a pH 9 environment, we observe a change in the distribution of density particularly around the C4 and C6 atoms of the nicotinamide ring (Fig 5.23 D-G). Based on previous studies that have shown a bend in these atomic positions of a nicotinamide ring in NADH, the changing distribution of electron density suggests the reduction of  $\text{NAD}^+$  to NADH<sup>[110]</sup>. Given that this density appears to bulkier around the  $\text{NAD}^+$  ring in comparison to the structure obtained at pH 6.7, it can be speculated that these maps also indicate the presence of a heterogenous population of substrate and intermediate, with one ( $\text{NAD}^+$ ) adopting a flat and the other adopting a bent (NADH) position. The increased redistribution of density around C4 and C6 position, particularly observed in polder maps obtained 50 to 60 seconds after a pH change indicates an increasing population of NADH in the *PmHMGR* crystals.

At 50 and 60 seconds following a pH change, we also observe a new density near the terminal carbon and hydroxyl atoms of mevalonate that is pointed towards the nicotinamide ring (Fig 5.23 F-G). While it is uncertain what interaction this rearrangement would facilitate, it appears that this changing density near mevalonate could also indicate a rearrangement of the substrate or its oxidized intermediate during or immediately after the first hydride transfer step of the enzymatic reaction.

#### 5.4.5 Comparison of simulated annealing omit maps at the mevalonate-NAD<sup>+</sup> interaction site within the first minute of reaction initiation

In addition to comparing polder maps of the nicotinamide portion of NAD<sup>+</sup> and in the mevalonate binding site, we also compared these regions using simulated annealing omit maps. In contrast to the polder maps, these omit maps can pick out only the strongest density signals by using a simulated annealing refinement prior to generating omit maps in a region, thereby removing residual bias from any atoms present at partial occupancy<sup>[88]</sup>.

The simulated annealing omit maps also show the same changes observed in polder maps with the density appearing to be more spread out in the ligand-binding region 20 seconds after the pH change indicating an increase in movement at the enzyme's active site and possible a mixture of substrate (mevalonate) / intermediate (mevaldehyde) and both the cofactors (NAD<sup>+</sup>/NADH) present at the enzyme's active site (Fig 5.24 B).

Subsequently from 30 – 60 seconds, we observe the electron density to be appearing spread out disproportionately at the C4 and C6 positions with very weak density between the C4 and C5 atoms (Fig 5.24 C-G). This change also indicate a bent conformation of the nicotinamide ring that is present in NADH.

At 50 seconds, the simulated annealing omit maps also indicate a configuration of the terminal hydroxyl atom in the mevalonate binding site that is now placed closer to the cofactor (Fig 5.24 F). Since the electron density changes and UV-Vis spectra of post pH-jump crystals indicate a reduction of NAD<sup>+</sup> we can expect this crystal sample to at least have a small population of mevaldehyde intermediate formed at the active site. We observe a disproportionately more skewed density at the C4 and C6 positions 50 – 60 seconds after a pH change as compared to previously acquired time points after reaction initiation (Fig 5.23, 5.24). Hence, we could even have a much larger concentration of mevaldehyde in comparison to mevalonate at the active site in *PmHMGR* crystals. The alternate position of mevalonate / mevaldehyde at the enzyme's active site 50 seconds after a pH change could indicate substrate movement that is captured during its interaction with the cofactor during the hydride transfer step. This alternate configuration could also indicate the onset of a reconfiguration of the intermediate leading up to its interaction with CoA to form mevaldyl-CoA.

#### 5.4.6 Movement of ligands at the *Pm*HMGR active site within the first minute of reaction initiation

Along with comparing the changes in electron density in the cofactor nicotinamide and substrate which indicated changes associated the first hydride transfer, we were also interested in comparing the distances between the ligands at the active site. By comparing the distances between the ligands, we expected to capture the changes associated with the hydride transfer step after the pH change and subsequent movements after mevaldehyde formation. The placement of the ligands here is based on a real space refinement of the ligand molecules in polder maps generated for these ligands from fully refined structures. With single models of mevalonate / mevaldehyde, NAD<sup>+</sup>/NADH and CoA at the active site we aim to capture an average change in the distance between what should be a mixture of substrates and intermediates.

In comparing the pre pH-jump structures in the crystallization and pH-jump buffer environments, we find that there is a reduction of distances between the terminal carbon of mevalonate and the C4 atom of NAD<sup>+</sup> and the thiol atom of CoA indicating a contraction between the ligands at the active site. This reduction could indicate a strained conformation of the enzyme after being introduced to the pH-jump buffer environment at pH 6.7 (Fig 5.25 A, B). In addition to the reducing distance between the ligands at the active site, we also observe a drop in the Wilson B-factor value of the acquired structure after being soaked in the pH-jump buffer environment in comparison to the crystallization buffer (Table 5.2). This difference indicates a reduced thermal motion of the enzyme after being introduced to the pH-jump buffer environment.

What seems to be an environmental effect restricting the enzyme's movement after a transfer to a pH-jump buffer environment appears to dissipate following a transfer to a pH 9 environment. This is reflected in the increased distance between what is modelled as mevaldehyde, CoA and NADH at the active site. The B-factor values are also observed to approximately double in comparison the pre pH-jump crystallization environment (Table 5.3).

The sudden rise in Wilson B-factor 20 seconds after a pH change could be a response of the enzyme to a sudden increase in the surrounding pH. This B-factor value is observed to gradually decrease from 20 seconds – 50 seconds and obtain a constant value between 50 – 60 seconds after a pH change. The B-factor observed 1 minute after a pH change closely matches that of the structure obtained in the crystallization buffer at pH 6.7 (Table 5.2). The decreasing B-factor at subsequent time points after a pH change indicates the overall enzyme conformation readjusting

over time to a change in pH. This gradual reduction in B-factor could occur if the pH induced effects were percolating from the outer regions of the crystal environment to the core of the enzyme.

After the pH-jump, we observe a continuous increase in the distance between mevaldehyde and NADH from 20 – 60 seconds after the enzyme is introduced to a pH 9 environment. The distance between the modelled mevaldehyde and NADH increase by 0.6 Å within the first 60 seconds in comparison to the pre pH-jump structure in the pH-jump buffer (at pH 6.7) (Fig 5.25). This change indicates a switch at the enzyme's active site from facilitating the first hydride transfer step towards coordinating the formation of the thioester bond for the second intermediate. It also indicates the possible movements of the enzyme leading up to the hydride transfer occurring before the first 20 seconds of the pH jump since no time point after the pH change shows a movement of the substrate and cofactor to be closer. On the contrary, the mevaldehyde and NADH only appear to move further away from 20 – 60 seconds after a pH change. What we do observe from 30 – 60 seconds based on the skewed distribution of electron density at the C4 and C6 positions is the presence of NADH at the active site indicating that what we might be largely capturing within the first minute of reaction initiation are the changes occurring post-hydride transfer.

While we observe an incremental increase in the distance between mevaldehyde and NADH after the pH change within the first minute, the distance between mevaldehyde and CoA does not follow a particular trend. This distance is measured between the thiol atom of CoA and the terminal carbon of mevaldehyde and appears to decrease by 0.3 Å going from 20 seconds – 40 seconds (Fig 5.25 C-E). However, this distance is again observed to increase by 0.2 Å from 50 – 60 seconds (Fig 5.25 F-G). The overall distance between mevaldehyde and CoA appears to be the same as the pre pH-jump structures and doesn't appear to change.

The incremental increase in the distance between NADH and mevaldehyde might in fact be a result of the cofactor starting to leave the active site following the hydride transfer to allow for another  $\text{NAD}^+$  molecule to enter the active site (Fig 5.25 A-G). This change in the cofactor positioning at the active appears to be what follows the hydride transfer step.

Given the significantly reduced rate of turnover in this crystal environment, we only observe thioester bond formation several minutes after a pH change. Therefore, these changing distances also indicate that we could be capturing movements in the mevaldehyde and NADH bound enzyme that might eventually facilitate cofactor exchange and initiating thioester bond formation within the first minute of the reaction.

#### **5.4.7 Observed changes in the NAD<sup>+</sup> adenine-ribose binding region within the first minute of reaction initiation**

In addition to comparing the changes observed in the NAD<sup>+</sup> nicotinamide region, we were also interested in comparing changes in the adenine and ribose bound regions of the cofactor to document any changes that might occur that are associated with cofactor exchange. Movement in this region was also in the structure obtained 5 minutes after the pH change indicating changes in the cofactor conformation before ligand release.

Hence, changes within this region were followed within the first minute of reaction initiation to detect possible movements in the cofactor immediate after mevalonate oxidation. We observe the density of the cofactor to be bulkier in the adenine region following the pH jump after the crystal has been in a pH 9 environment for 20 seconds. Subsequently at time points ranging from 40 – 60 seconds after reaction initiation, we also observe the density to be more spread out in the adenine, ribose and phosphate binding region indicating further movements in this cofactor binding site with time (Fig 5.26 C-G).

This change in electron density is indicative of this region of the ligand adopting multiple conformations. Movement of this portion of NAD<sup>+</sup> could be indicative of potential changes in the enzyme that would accommodate the exchange of NAD<sup>+</sup> and NADH at the active site after the first hydride transfer step resulting in the oxidation of mevalonate. Structural changes in the regions surrounding the adenine-ribose portion of NAD<sup>+</sup> could highlight flexible regions that facilitate the release of the reduced cofactor for the enzyme to carry out its second hydride transfer step.

#### **5.4.8 Movement of *Pm*HMGR active site residues within the first minute of reaction initiation**

In addition to comparing the movement of ligands, we were also interested in comparing the changes in the distance between the key residues involved in placing the ligands at the active site for catalysis, driving reaction steps and in the full formation of the active site with the closure of the flap domain.

When comparing changes in the conformation of the catalytic residues GLU 83 and LYS 267 we observed no difference in the distance between them (Fig 5.27 A-F). Given that they act as a proton acceptor and oxyanion hole for the mevalonate oxidation step, it implies that the active

site in the inactive quaternary complex (At pH 6.7) is positioned to advance the first hydride transfer step of the *PmHMGR* reaction. Given that we observe NADH production after pH change, we can deduce that the initiation of the first hydride transfer step is only dependent on a pH increase to initiate the reaction.

In addition to comparing distances between these residues and bound ligands, we also compared the relative B-factor values of different regions of the bound ligands to determine the effect of changing crystal environment, pH and reaction initiation on the overall thermal motion of different regions of the ligand. We find an increase in the B-factor values of CoA after introducing the enzyme into a pH-jump buffer environment after transferring it from a crystallization buffer. This could possibly be due to movement of this ligand and subsequent movement of the neighboring large domain region (Fig 5.28 B).

We also observed an increase in the B-factor of all the ligands after a pH change. This change is expected given the overall increase in the Wilson B-factor in these crystal samples (Fig 5.28 C). Like with the Wilson B-factor values, we also observe the B-factor of the individual ligands drop significantly between 20 to 30 seconds after a pH change (Fig 5.28 C-D). The permeation of the higher pH-buffer into the *PmHMGR* crystal appears to result in an initial increase in thermal motion and the eventual stability once the pH-induced conformation has been attained across the entire crystal. While the Wilson B-factor of the structures acquired after a pH change is observed to lower over time, the relative B-factor of the certain regions in the ligand-bound region continue to remain higher (Fig 5.28 C-F). The subsequent changes in the ligand B-factor at higher pH indicate movements in specific regions of bound ligands that can be associated with changes occurring after reaction initiation.

We find that across all the structures obtained before (pH 6.7) and across time points after a pH change (pH 9) within the first minute, the B-factors of the NAD<sup>+</sup> nicotinamide and mevalonate binding region are significantly lower than the other parts of the cofactor and substrate (Fig 5.28). This is indicative of a highly stable active site region where there is minimal movement of the ligands after reaction initiation. The increased rigidity at the active site could be a result of the increased electrostatic contacts and hydrogen bonds that are involved in the positioning of the interacting region of the ligands to facilitate the hydride transfer and thioester formation steps. The relative lack of room in the active site cavity after flap domain closure in comparison to the solvent facing portions of the ligand is an additional factor that could result in reduced movement.

We also compared the placement of the residues SER 85 and HIS 381 that are involved in forming contacts with CoA-SH at the active site with HIS 381 also acting as a proton acceptor for the deprotonation of the co-substrate to initiate thioester bond formation with mevaldehyde. In contrast to the residues GLU 83 and LYS 267 we observe a change in these residues indicating small (up to 0.3 Å) near the CoA binding site (Fig 5.27 A-F).

In comparison to NAD<sup>+</sup> and mevalonate, the B-factor of CoA is also observed to be higher in both the pre and post pH-jump structures (Fig 5.28 A-F). We also find this value increasing with time from 30 seconds – 50 seconds after a pH change including the relative B-factor values in the pantothenic acid and thiol regions (Fig 5.28 D-F). This indicates that while the portion of the active site associated with the hydride transfer step does not require movement to initiate the reaction step, subsequent intermediate steps are enabled by corresponding movement of CoA. The thiol region that has a relatively higher B-factor compared to the adjacent mevaldehyde carbon and nicotinamide region (Fig 5.28 E-F) could also have a higher range of motion as is observed by the electron density after the pH-jump (Fig 5.25 C). While a changing distance between the thiol atom and mevaldehyde is not captured in average distance comparisons, this movement could eventually facilitate the interaction of CoA with mevaldehyde.

Further time points need to be obtained using pH-jump experiments to look at possible interaction between the mevaldehyde and CoA between the post hydride transfer time points (60 seconds) and before we start observing thioester bond density (2 minutes 20 seconds). While the residues in contact with cofactor nicotinamide appear to be rigidly placed, we found significant movement (up to 0.7 Å) in the flap residues (VAL 392 and HIS 385) placed next to the adenine and phosphate region of NADH (40 – 50 seconds after a pH change) (Fig 5.27 E-F). This movement is also observed at time points where we start to observe a significant change in density in the adenine, ribose and phosphate region indicating 2 alternate conformations of the cofactor indicating a significant change in its position.

We observe a similar trend in the changing B-factor values of NADH once the enzyme has re-equilibrated in a new pH environment. In the case of NADH, we observe the B-factor to be higher in the adenine-ribose region before the pH jump (Fig 5.28 A-B). These B-factor values continue to increase after the enzyme has been equilibrated in a new pH environment (Fig 5.28 C-F). However, we also observe an increase in the B-factor values from the NADH phosphate to nicotinamide regions (Fig 5.28 B-F). This indicates the motion that is initially localized in the



adenine-ribose region before a pH-change is greater in this region after reaction initiation and is eventually also increasing in the other regions of NADH that are closer to the active site after sufficiently long soaking times at higher pH (Fig 5.28 E-F). This increase in movement in the cofactor could be indicative of movements associated with its exchange at the enzyme's active site.

The range of motion observed in all the *Pm*HMGR residues in contact with NAD<sup>+</sup> / NADH is also indicative of the overall difference in degree of motion in the adenine-ribose, phosphate, and nicotinamide-ribose regions of the cofactor. Given that the cofactor nicotinamide and adjacent ribose regions have a much smaller B-factor (albeit slowly increasing over time) in comparison to the adjacent phosphate, ribose and adenine regions, we also find the ASN 688 residue that is adjacent to the nicotinamide (ribose) region to be largely stationary across the different time points captured after reaction initiation (Fig 5.28 A-F).

Glu 83 has been shown to be involved in the hydride transfer steps involving the oxidation of mevalonate and reduction of HMG-CoA in site-directed mutagenesis and computational studies<sup>[23, 24]</sup>. However, mutants of the catalytic glutamate (Glu 558) in Syrian hamster HMGR have shown that the enzyme retains 40 % of its wild type activity while producing HMG-CoA from mevaldyl-CoA<sup>[26]</sup>. This indicates a possibility of a different mechanism involved in the second hydride transfer step involving the formation of HMG-CoA from mevalonate. Additional time points capturing HMG-CoA formation from 2 minutes 20 seconds to 8 minutes would be beneficial in determining potential differences in the role of the Glu 83 and Lys 267 pair for HMG-CoA production.

#### 5.4.9 Changes in flap domain configuration

The flap domain conformation was compared in structures obtained after the crystal was introduced to a pH-jump buffer environment and at different time points after reaction initiation. Changes in the flap domain would determine possible effects of observed cofactor movement, changing environment and pH. It would also determine changing effects of the flap domain at the active site, where the HIS 381 residue is involved in the catalytic step resulting in the deprotonation of CoA-SH for thioester bond formation. The helices in the flap domain were broken into four segments for this comparison two of which spanned helix 1 (E 375 – A 386, R 387 – A 395) and one segment each for helix 2 (E 399 – Y 410) and 3 (A 415 – L 421).

In comparing the three helical regions of the flap domain, we find the initial movement after introducing the enzyme to the pH-jump buffer environment and a higher pH to be localized in the regions between helix 1 and 2 (ALA 393 – ASP 401) and on helices 2 (TRP 402 – HIS 411) and 3 (ASP 416 – LEU 422) (Fig 5.29 B-C). In the case of helix 2 we also observe it shift its conformation before and 20 seconds after a pH change (Fig 5.29 B-C). The initial movements observed could be a result of the changing external environment and pH given that the flap region of the enzyme is solvent exposed and would be affected by the surrounding solvent molecules. Like other parts of the enzyme, we also expect its conformation to be affected by any changes in the protonation states of the flap domain residues.

In comparing the RMSD values between structures we find that the overall difference in conformation of the 2<sup>nd</sup> and 3<sup>rd</sup> flap domain helix from the pre-pH-jump structure is observed to reach its maximum value 30 seconds after a pH change (Fig 5.30 B – C). This movement is reflected in the intermittent contraction between helix 2 and 3 at 30 seconds and an intermittent expansion between helix 1 and 3 at 20 seconds as measured by changing angles (Table 5-2). Our alignments shown that both these changes are only a result of the initial movements observed in the 2<sup>nd</sup> and 3<sup>rd</sup> helix.

In contrast, we observe the region of the 1<sup>st</sup> helix have its maximum RMSD at 40 and 50 seconds (Fig 5.30 A). The increased movement of the 1<sup>st</sup> helix is also reflected in our measurement of interhelical angle measurements that show an increasing value between the 2 separate regions spanning helix 1 and decreasing value between helix 1 and helices 2 and 3 40 and 50 seconds after reaction initiation (Table 502). This change over time indicates the possibility of the movement that is originating in the 2<sup>nd</sup> and 3<sup>rd</sup> helix eventually affecting the position of the residues in the 1<sup>st</sup> helix near the enzyme active site.

The movement of the first helix can be also correlated with the observed movement of the adenine-ribose region of NAD<sup>+</sup> / NADH at 40 and 50 seconds that is also in contact with the third helix of the flap domain (ASP 416) and the small domain region (ALA 642 – ASP 646). As, we have observed in structures of *Pm*HMGR with the CoA and NAD<sup>+</sup> binding site occupied, contacts of the first helix with these regions are observed near ILEU 389 (Fig 5.47). Given that we start to observe movements NADH adenine and ribose region adjacent to the 3<sup>rd</sup> helix of the flap domain after a pH change, it is possible that movements in the 2<sup>nd</sup> and 3<sup>rd</sup> helix are affected by changes in the cofactor binding region. The changing angles of the helices of the flap domain also allude to

possible movements that are a result of neighboring small domain regions that could facilitate NAD<sup>+</sup>/NADH exchange (Table 5-2).

We also observe changes in the void volume calculations of the flap domain indicating conformational changes that are a result of changing environment and cofactor exchange. After introducing the *Pm*HMGR crystal to a pH-jump buffer environment, we observe an increase in volume of 27 Å<sup>3</sup> indicating a possible readjustment of the flap domain in the presence of new buffer constituents (Table 5-3). After reaction initiation with a pH change, we also observe an eventual decrease in the flap domain volume of 51 Å<sup>3</sup> 40 seconds after reaction initiation. This contraction can be explained by following changes in the interhelical angles between helix 1 (region 387-395) and 2 and helix 2 and 3 at 40 seconds. These changes indicated that the observed increase in interhelical angles can also result in an overall contraction of the flap domain. The contracting of the flap domain can hence be viewed as an intermittent response to changing buffer environments, pH and post-reaction states that could facilitate NAD<sup>+</sup>/NADH exchange by rearranging the flap helices and subsequently allow thioester formation (Table 5-3, Fig 5.29 E). We subsequently observe a 76 Å<sup>3</sup> expansion in the flap domain region 50 seconds after reaction initiation even though the interhelical angles have values close to that observed at 40 seconds (Table 5-3). This change indicates that while the changes interhelical angles are largely preserved subtle changes in the conformation of all the helices and movement in the interhelical region between helix 1 and 2 of the flap domain allow for its re-expansion (Table 5-3, Fig 5.29 F). This rearrangement of the flap domain could therefore accommodate movement of NAD<sup>+</sup>/NADH.

This change in the mobility of the interhelical region between *Pm*HMGR flap domain helices 1 and 2 is also captured in the B-factor comparisons where the B-factor values are observed to be the highest within this interhelical region across time points. It is observed to be particularly high after the pH change from 20 seconds – 30 seconds alongside residue residues the follow it is ranging from ASP 401 to LEU 424 (Fig 5.31 C-D). The increase in B-factor in this region also corresponds to the increased movement observed at 20 and 30 seconds (Fig 5.29 B – C). It is possible that changing conformation of this interhelical region (as is observed in earlier obtained time resolved structures in the structures obtained 1 minute – 10 minutes) after the pH change also initiates observed movement in helices 2 and 3. We also observe a slight increase in the B-factor of the first helix 40-50 seconds after reaction initiation in comparison to the pre pH-jump structure

which also further indicates an increased movement in this region at these time points (Fig 5.31 E-F).

#### **5.4.10 Changing contacts of the flap domain at the ligand binding site**

In addition to understanding changes in the flap domain conformation, we also wanted to understand if these conformational changes are observed near a ligand-binding site. Changes observed with flap and ligand contacts could also affect the ligand conformation.

In the case of the CoA bound region, we observed a change in the residues GLU 375 and ARG 379 wherein after the pH-jump buffer exchange, we found the conformation of GLU 375 to move away ARG 379 and towards the CoA binding site (Fig 5.32 A). This conformation of GLU 375 is observed to persist in the post pH-jump structure after reaction initiation (Fig 5.32 B-E). However, in addition to having a new GLU 375 conformation, we also find the conformation of ARG 379 changing and pointing towards CoA after a pH-change (Fig 5.32 B). This new conformation of GLU 375 and ARG 379 is found to persist at all the observed time points after reaction initiation (Fig 5.32 B-E). Given that the new conformation of both these residues is preserved after a pH change, it appears to be due to a changing protonation state in this region because of increased pH. It remains to be determined exactly which residue is initially affected in a manner that would bring about this change. Further comparisons of the pKa values and expected protonation states in this CoA binding region of the enzyme would be useful in determining the factors that directly impact this changing conformation. However, the newly adopted conformation of GLU 375 and ARG 379 could subsequently impact the conformation and placement of CoA. This conformational change could be playing a role in the increased B-factor values observed for the adenine, ribose and phosphate regions of CoA in comparison to the other ligand bound regions after a pH-jump buffer exchange and at several time points after reaction initiation.

We also observe changes in flap conformation with respect to NAD<sup>+</sup> within the first minute of reaction initiation. With the flap readjustment observed after transitioning the enzyme from a crystallization environment to the pH-jump buffer environment, we observe a reduction in the distance (0.3 Å) between V 392 and NAD<sup>+</sup> ribose at the adenine end (Fig 5.33 A). This is followed by a 0.3 Å reduction in distance between NADH phosphate and I 389 and a 0.2 Å increase in distance between V 392 and NADH adenine 20 seconds after a pH change (Fig 5.33 C). 30 seconds after a pH-change we observe distances between H 385, I 389 and V 392 on the first helix and

NADH phosphate, ribose and adenine readjusting to the distances observed in the crystallization buffer environment at pH 6.7 (Fig 5.33 D). However, since we don't see any significant movement of the first helix until 40 seconds after a pH change (Fig 5.29 A-E), the changing distance of the flap observed at 20 and 30 seconds could simply be an effect of changes in the configuration of NAD after a pH change.

However, 40 and 50 seconds after reaction initiation, we once again observe a reduction in the distance between the flap domain (VAL 392) and NAD ribose (adenine) regions. This reduction is also between 0.3 – 0.4 Å (Fig 5.33 E-F). It is also accompanied by a greater reduction (0.7 Å) in distance between LEU 384 and CoA adenine (Fig 5.33 F). The changing distances observed at 40 and 50 seconds (Fig 5.33 E-F) with respect to the ligands NADH and CoA in addition to the movements observed in the first helix (Fig 5.29 D-E, Fig 5.30 B-C) indicate a possible effect on the flap domain conformation due to observed movement of CoA and NADH.

#### **5.4.11 Changes in interhelical contacts in the flap domain region**

With the changing conformation of ARG 379 which is a flap domain residue in the first helix forming contacts with the flap residue on the second helix, HIS 411, we observe a changing interhelical distance. This distance is observed to increase after the enzyme is introduced in a pH-jump buffer (1.2 Å) and increase further after it has undergone a pH-change (By 2.7 Å) (Fig 5.34 B-C). Similarly, we find that the interhelical hydrophobic distances between the residues ALA 386, VAL 408 and ALA 383 are also reduced after the pH jump ( Up to 0.4 Å, Fig 5.35 B-E) . This is also apparent in the interhelical angle contraction between helix 1 and 2 after reaction initiation that is observed (Table 5-2).

We observe changes in the interhelical density between helices 1 and 2 as has been observed after reaction initiation across time points that capture thioester bond formation and product release (1 minute – 10 minutes). This change in electron density is also indicative of the changing rigidity and placement of these residues and therefore, the changing distance between helices 1 and 2 (Fig 5.36 A-E).

We find the density in this region to get weaker going from the crystallization buffer to a pH-jump buffer but become stronger again immediately after reaction initiation (Fig 5.36 A-B). It is then observed to intermittently fluctuate with a weaker density at 30 seconds (Fig 5.36 C) and regain a stronger density 40 and 50 seconds after reaction initiation (Fig 5.36 D-E). The changing

flexibility of this region would explain the change in orientation of the 2nd helix after the pH-jump buffer exchange step (Fig 5.29 A.). Movement of this helical region can be viewed as a rearrangement of its helical axis depending on the changing position of the adjacent flexible interhelical residues.

Therefore, the changes in placement of residues in the interhelical region 20 and 30 seconds (Fig 5.36 B-C) after the pH-change also explains the movements observed along the axis in helix 2 that is observed at these time points (Fig 5.29 B-C). The reappearance of stronger electron density at 40 seconds and the lack of subsequent movement 50 seconds (Fig 5.36 D-E) after reaction initiation could indicate the eventual re-stabilization of a new conformation of helix 2 after what seems like a readjustment period 20 - 30 seconds after a pH jump. This is also indicated by the changing B-factor in this interhelical region which increases after a pH change at 20 - 30 seconds and subsequently decreases at 40 and 50 seconds (Fig 5.31). The stabilization of this region could be effective in regulation the hydride transfer step by locking the flap domain in a configuration where the  $\text{NAD}^+$  cofactor is situated at the active site to initiate the hydride transfer step. It could also regulate the cofactor exchange by changing the closed conformation of the flap domain while being extremely flexible to accommodate the release of the reduced cofactor and re-entry of  $\text{NAD}^+$ . Observing changes in this region using closely spaced time points leading up to the HMG-CoA bond formation step could be helpful in further investigating the role of this region in cofactor exchange.

Due to conformational changes in helices 2 and 3, we observe changing distances in the interhelical residue region with a changing conformation that is observed between ARG 417 and the surrounding residues that make electrostatic contacts in this interhelical region (D 416, R 414 and D 412) (Fig 5.37). The changing conformation of the residues in this region could affect the conformation of helix 2 with respect to helix 3.

We also observe changing distances between helix 2 and 3 with a small expansion of 0.3 Å in the  $C_\alpha$  distance between LEU 407 and ALA 418 after the enzyme is introduced to a pH-jump buffer at pH 6.7 (Fig 5.38 B). The distance between the 2 helices is also observed to change by 0.3 Å between the  $C_\alpha$  atoms of LEU 422 and VAL 403 after they enzyme is introduced into the pH-jump buffer (Fig 5.38 B). After reaction initiation, we observe significant expansions and contractions in this distance at different time points with a range of 7.1 – 8.7 Å (Fig 5.38). This

movement indicates the changing conformation of helices 2 and 3 with changes in the buffer environment, pH and neighboring movements of ligands and the small domain.

#### 5.4.12 Exploring key *Pm*HMGR flap mutant structures

With the movements observed in the *Pm*HMGR flap domain region, particularly in helix 2 and with the changing density in the interhelical region between helix 1 and 2, we wanted to investigate the changes in mutant structures in this residue region that have been shown to affect turnover of the enzyme. Based on QM/MM-MD simulations conducted by Quinn et. al, we identified residues ARG 396, GLU 399 and LEU 407 to have a long range effect on the hydride transfer step of the enzymatic reaction<sup>[94]</sup>. This region has been shown to influence turnover by what is speculated to be a stabilization of these residues in the transition state that affects the conformation of the flap domain which plays a key role in regulating enzyme activity. Evidence for these residues achieving a relatively more rigid state has also been observed in time-resolved structures obtained in a high pH (pH 9) environment at different stages of hydride transfer between mevalonate and NAD<sup>+</sup> and thioester bond formation between mevaldehyde and CoA (Fig 5.36, 5.17).

We were able to obtain crystal structures of the mutants E399A and L407S after soaking their crystals with the ligands mevalonate, CoA and NAD<sup>+</sup>. While one of the observed structures of E399A showed flap closure, mevalonate, CoA and NAD<sup>+</sup> binding and a conformation very similar to that observed in the wild type quaternary complex (Fig 5.40, 5.41), we also observed the lack of flap domain closure and NAD<sup>+</sup> / CoA binding in 2 other structures of E399A and L407S (Fig 5.42, 5.44).

In the case of both the mutants (E399A and L407S), the lack of flap domain density in these structures indicates that the mutation could reduce the probability of flap domain closure by affecting the flap domain conformation. Structural studies with the wild type enzyme have also indicated the lack of flap domain closure in the absence of NAD<sup>+</sup><sup>[2]</sup>. Therefore, it is possible that the conformation of the flap domain in the mutant structures has a lesser propensity to form contacts with NAD<sup>+</sup> and other flap domain interactions required for its closure at the active site. This change could simultaneously also affect the binding of NAD<sup>+</sup> and CoA at the concentrations used for this soaking experiment.

The structural insight gained from the structural studies of flap domain mutants indicates that the E399 residue on the interhelical loop between helix 1 and 2 and L407 on helix 2 of the flap domain are involved in stabilizing interactions that allow flap domain closure. Microsecond molecular dynamics simulations of *PmHMGR* have demonstrated that the stabilization of these residues also plays a key role in the progression of the transition state converting mevaldehyde into mevalonate in an HMG-CoA and NADH bound complex<sup>[109]</sup>. Therefore, it can be speculated that the stabilizing interactions that ensure flap domain closure and ligand binding at the active site could also further transition state changes that result in the oxidation of mevalonate. The stability in this region between helix 1 and 2 of the flap domain therefore has a long-range effect on the progression of the reaction. The variation of its density at different pH-induced time points goes further to show that it results in different flap and small domain configurations during intermediate stages of the reaction (Fig 5.17 and 5.33).

#### **5.4.13 Movements observed in the small domain region adjacent to the NAD<sup>+</sup>/NADH binding site**

While identifying changes in the flap domain configuration that were correlated with readjustments in the NAD<sup>+</sup>/NADH configuration, we were also interested in identifying changes in the adjacent small domain region that might also play a role in regulating dynamics required for enzyme function. As was observed in the initial time points studied across 10 minutes the adjacent flap domain, NAD<sup>+</sup> and small domain regions can affect each other's conformations depending on the conformation of a particular region (Fig 5.47).

In our comparisons of the small domain region within the first minute, we observe a significant change in the conformation of this region 20 seconds after reaction initiation in comparison to the pre-pH jump structure (Fig 5.45 B). We observe this difference in conformation reducing over time but increasing in the NAD<sup>+</sup>/NADH adenine-ribose region as has been observed with the change in electron density of the cofactor indicating the presence of alternate configurations of the cofactor (Fig 5.45 B-F, 5.26 C-F).

Conformational changes are observed 20 seconds after the enzyme is introduced to a pH 9 environment in the small domain (ASP 646 – LEU 652) and the 3<sup>rd</sup> helix region of the flap domain (ASP 416 – LEU 422). These movements precede the changes observed in the NAD<sup>+</sup>/NADH adenine-ribose region (Fig 5.26). While it is not clear which movement occurs initially and what



initiates that change, it appears that these interacting regions of the flap and small domain influence each other (Fig 5.45 G-H.).

The flexibility at the  $\text{NAD}^+$  /  $\text{NADH}$  bound region that is a result of these movements at the flap and small domain could facilitate the exchange of the cofactor (Fig 5.45 G). This is further indicated by the changing B-factor along the  $\text{NAD}^+$ / $\text{NADH}$  molecule which starts increasing near the adenine-ribose portion 20 seconds after the enzyme is introduced to pH 9 and then appears to also increase in the phosphate and nicotinamide-ribose region at subsequent time points following a pH-change (Fig 5.31).

Changes in the protonation state of flap and small domain residues in contact with  $\text{NAD}^+$  phosphate such as HIS 385 and ASN 688 if affected by the change in pH or the changing protonation state of active site residues such as GLU 83, LYS 267 and HIS 381 during turnover might influence the hydrogen bonding effects of neighboring regions resulting in a change in flap / small domain and  $\text{NAD}^+$ / $\text{NADH}$  interactions. Since several  $\text{NAD}^+$  bound ternary structures with CoA, HMG-CoA and mevalonate have also shown the effect of cofactor binding on the small domain conformation and flap-small domain interactions, it is possible that these regions could also regulate the exchange and release of the cofactor.

#### **5.4.14 Movements observed in the large domain region adjacent to the CoA binding site**

With the mobile regions of CoA observed from B-factor comparisons of ligands, alternate CoA conformations observed after reaction initiation and movement in flap regions in contact with CoA, we were also interested in comparing changes in the large domain region (LEU 3 – MET 50) that is in contact with this co-substrate. In our comparisons, we identified specific portions of the large domain that show significant movement after the enzyme is introduced into a pH-jump buffer environment. While it appears to adopt this conformation even after reaction initiation, it also shows an intermittent contraction after 30 seconds post reaction initiation in the SER 5 – PHE 10 and ASP 20 – GLY 40 residue region (Fig 5.46 A-C).

The movement in the large domain that is observed after the introduction of the pH-jump buffer exchange appears to be a result of changing domain conformation in response to the surrounding environment. However, in the case of the post pH-jump structure, the observed movement appears to be a response to changing conformation of Coenzyme-A at the active site (Fig 5.46 C.).

The changes in the flap, small and large domain configuration that are a result of changing external environment as the enzyme is moved to the pH-jump buffer at pH 6.7 indicate possible movements and changes in flexibility of the enzyme that might facilitate turnover not observed in the crystallization environment.

## 5.5 Limitations in our application of the pH-jump method

While this project can highlight significant changes in the population of enzymes going from a pre-reaction state towards reaction initiation and can subsequently show the formation of reaction intermediates, it is limited in being unable to capture small incremental changes between intermediate steps. This inability is due to the fact that the time-resolved experiment currently depends on the use of multiple crystals, each of which have undergone multiple steps of buffer exchange, ligand-soaking, pH change and freeze-trapping. The variability that is a natural consequence of human error and expected within each crystal sample could influence the captured trends over the course of the enzymatic reaction in *PmHMGR* crystals.

To address this issue, some measures were taken to reduce variability between post reaction-triggered measurements. The size of the crystals used was chosen to be between 0.3-0.4 mm for all the diffraction measurements and the initial ligand soaking time was kept to 4 hours to ensure maximum binding. This soaking time was previously tested by Tim Schmidt to determine the time needed to produce saturated binding of ligands at the enzyme active site. This reduced variability in ligand concentrations in the *PmHMGR* crystals upon saturation and so the rate of post-reaction changes within the *PmHMGR* crystals.

While we do not have an exact estimated value for the diffusion of  $\text{OH}^-$  ions for a pH change inside a *PmHMGR* crystal, there are experimental and calculated estimates to predict the diffusion of ammonium and sulfate ions inside ribonuclease crystals of the size 0.3 x 0.3 x 0.3 mm which are within 90 – 220 seconds<sup>[111]</sup>. Similarly, studies observing isocitrate binding saturation in 0.5 mm isocitrate dehydrogenase crystals have shown a saturation time of 10 seconds<sup>[112]</sup>. Given that the influx of  $\text{OH}^-$  can be expected to be faster, we expect the *PmHMGR* crystals to be equilibrated within 20 seconds of pH change. In addition, we can expect the diffusion of  $\text{OH}^-$  to result in a cascade of changing protonation states mediated through several hydrogen bond networks across the enzyme thereby further increasing the rate of pH change in the *PmHMGR*

crystals. The *PmHMGR* crystals have also been shown to have a significantly large pore size that would allow for an increased diffusivity.

Hence, it is reasonable to expect that the crystals to be equilibrated at a higher pH within 20 seconds of pH change.

As described earlier in Chapter 5, we observed drastic changes in the population of the enzyme with the formation of a thioester bond and subsequent release of product over large time points ranging up to 10 minutes after reaction initiation. Coupled with the increase in UV-Vis absorbance measured at 340 nm after a pH change, we can determine that these changes are associated with the progression of the reaction and the conversion of  $\text{NAD}^+$  to NADH. Our measurements of absorbance in 0.4 mm *PmHMGR* crystals between 1.3 – 8.5 minutes after reaction initiation also indicate a rate of NADH production that is 0.00019 M/min (Fig 4.3). Given that we can approximate the concentration of  $\text{NAD}^+$  soaked into the crystal to be 1 mM, we can expect that the time taken for all the added concentration of  $\text{NAD}^+$  to be converted to be 5.3 min. While noise introduced from experimental variability in samples and ice formation does affect these spectroscopic measurements, they can still reliably determine that the expected timescale of reaction-initiated changes in *PmHMGR* crystals is in the order of several minutes.

Seeing how we observe a continued increase in absorbance within this timescale and our crystal structures indicate changes associated with ligand release from 8-10 minutes, we can determine that our structures indicate changes associated with HMG-CoA formation within 5 minutes of pH change and product release at later time points. It also points to the reliability of utilizing *PmHMGR* absorbance data to quantify changes in crystal structures. However, given the sparsity in data points acquired over the span of 10 minutes in our absorbance and diffraction measurements, it is difficult to identify time points that would be associated specifically with thiohemiacetal formation and cofactor exchange. Additional closely spaced time points need to be acquired after reaction initiation to study crystallographic and absorbance changes to further distinguish the time periods where we can expect to observe different reaction intermediates and quantify these changes with greater certainty.

The crystallographic changes that are observed over the span of the first minute are obtained by freeze-trapping methods between closely spaced time points that are separated by 10 seconds between 20 – 60 seconds. Given the variability in the samples and assuming human error with the timing of the freeze-trapping steps, it can be expected that these changes might not be

perfectly separated and that there would be some overlap in differences between the different time points studied. Obtaining complementary UV-Vis absorbance spectra from 20 – 60 seconds would help further determine the extent of expected changes post-hydride transfer within this time frame.

One thing, however, is clear in, our comparison of electron densities observed after the pH-change. These comparisons indicate a stark change in the distribution of electron density in the nicotinamide region of the cofactor from 30 – 60 seconds after the pH change. The obtained absorbance in 0.4 mm crystals at 80 seconds (Fig 4.3) indicates that it is reasonable to assume NADH formation within the first minute. Simulated annealing maps in structures of resolution 1.9 – 2.4 Å have been utilized to assign the puckering of proryl rings in the unnatural amino acid 4-fluoroproline<sup>[113]</sup>. Therefore, the resolution range and analysis method used to compare the conformation of the nicotinamide ring of NADH in our structures appears to be suitable. The density shift that is observed in the C4 and C6 atoms in our simulated annealing omit and polder maps indicates a build-up of the reduced cofactor at the enzyme's active site (Fig 5.23 and 5.24). A suitable way to further confirm the formation of the reduced cofactor would be to obtain replicated datasets of structures obtained from 20 – 60 seconds. This is an ongoing effort for the future of this project. However, the reproducibility of expected electron density changes associated with NADH formation in each of the structures obtained from 30 – 60 seconds after reaction initiation further exhibits that they are all associated with the formation of NADH at the active site. The lack of 2Fo-Fc density observed between mevaldehyde and CoA until 2 minutes and 20 seconds after a pH change also indicates that the structures captured within the first minute are showing enzyme populations that have undergone the first hydride transfer but not thioester bond formation (Fig 5.6).

Following a pH change, we expect to have a varying mixture of both substrate and intermediate present in *PmHMGR* crystals where the concentration of NADH is gradually increasing over time. This increase in NADH concentration would also result in an increase in this cofactor occupancy in *PmHMGR* crystals post reaction-initiation. Unlike mevalonate and mevaldehyde, the new configuration of NADH with its C6 atom pointed towards mevalonate / mevaldehyde makes it easy to distinguish from the NAD<sup>+</sup> cofactor in electron density maps. A comparison of the changing occupancies of the two cofactors is however still found to be unreliable in these measurements. This is largely due to the merging of density between NAD<sup>+</sup> and NADH

at the cofactor binding site. Given that we cannot reliably distinguish between the changing populations of substrate and intermediates from our current refined electron density maps, we are not able to fully quantify the observed changes in NADH formation over the first minute with crystallographic data alone. Acquiring complementary absorbance data to quantify the expected NADH concentration changes and utilizing additional analysis techniques to determine changes in intermediate population would help us further understand the extent of overlap between the acquired time points in the first hydride transfer step.

Given that the changes between the discrete time steps obtained within the first minute of reaction initiation cannot always be understood to linearly follow one after another, it is useful to look for larger trends that might occur over the span of the first minute after reaction triggering. We observe a continued trend of movement for the reduced cofactor nicotinamide away from mevaldehyde after reaction initiation, where the distance between the C4 atom of NADH and the terminal carbon of mevaldehyde increases by 0.6 Å (Fig 5.25). This rearrangement of the cofactor is also apparent at the adenine end where we observe the presence of alternate conformations for NADH indicating movement of the reduced cofactor away from the active site after reaction initiation. We also observed a 0.7 Å movement in VAL 392 in the flap domain adjacent to the adenine of NADH 60 seconds after a pH change (Fig 5.27). Since this change is strikingly more apparent 50 and 60 seconds after a pH change in comparison to the pre pH-jump structure, we can ascertain that there is a clear difference in the placement of the NADH bound in this enzyme and its surrounding regions within 60 seconds of reaction initiation.

Another potential source of error in this experiment comes from the expectation that movements induced by a pH-change occur in tandem with changes associated with reaction initiation. However, we have developed approaches and identified metrics to separate the effects of a pH change and reaction initiation. The changes in the overall conformation of *Pm*HMGR that we could associate with the change in pH were indicated with the changing B-factor after a pH-change and are followed over several time points after reaction initiation. We find the biggest increase in the Wilson B-factor of the structures to be immediately after a pH change at the time points obtained 20 seconds after a pH change and that this value subsides rapidly at later time points. The drop in B-factor from 30-60 seconds is indicative of a general readjustment of the crystals to a higher pH (Table 5.2). There are additional readjustments in the enzyme that appear immediately after the pH change. One example is a re-positioning of residues GLU 375 and ARG

379 near the phosphate binding regions of CoA, which then persists over the rest of the time points examined after an increase in the crystal pH. Given that the reaction is blocked at low pH and is only observed to go forward at higher pH in the pH-jump buffer environment, we can assume that conformational changes in the enzyme such as these play an important role in facilitating the catalytic mechanism.

The separation of pH and reaction induced movements that can be determined from the observed trend in Wilson B-factor values and the conformational changes adopted at higher pH allow us to assign reaction induced changes. An example of this includes a readjustment of helices 2 and 3 in the flap domain and an increased motion in helix 1 adjacent to the mobile NADH phosphate 30 - 50 seconds after a pH change (Fig 5.29, 5.30). We also observe an increased stabilization of small domain regions (ASP 646 – LEU 652) adjacent to the NADH adenine and the interhelix flap domain regions between helices 1 and 2 (A 395 – E 399) from 40-60 seconds after reaction initiation (Fig 5.31, 5.36, 5.45).

The range of movements in the small and flap domain are within an RMSD range of 0.6 – 1.4. While the range of movements is not drastic, it appears to be significantly higher than the movements observed in the control structures at pH 6.7 which have an RMSD range of 0.3 - 0.6. Given that this trend in movements is only observed in the ligand bound monomer and can be correlated with changes in different regions (adenine, ribose and phosphate) of the bound cofactor tells us that they are interconnected. Given that the cofactor needs to be exchanged to allow for another hydride transfer in the *Pm*HMGR reaction mechanism, we can expect movement in NADH after the first hydride transfer step. Therefore, this range and sequence of movements points to a rearrangement of this region after reaction initiation and not stochastic motion.

## 5.6 Future Directions

With the extensive testing and application of the pH-jump reaction triggering method, we have been able to capture various bound intermediate states of the *Pm*HMGR enzyme along its reaction pathway. However, several stages of the reaction such as the conversion of mevaldehyde to mevaldyl-CoA, additional changes associated with cofactor exchange and product release

remain unexplored. Therefore, applying this method to look at intermediates captured further along the reaction pathway would be beneficial in further understanding its mechanism.

With the development of several new methods to introduce chemical triggers in crystals such as the use of on-chip crystallization, microfluidic channels and liquid droppers to introduce the pH change in ligand bound *Pm*HMGR we can expect to adapt this experiment for serial and Laue crystallography experiments<sup>[46, 114, 115]</sup>. This would allow us to capture changes after reaction initiation within a single crystal instead of relying on datasets obtained from several samples using the freeze-trapping approach. Obtaining diffraction data at different stages along the reaction pathway from a single crystal could improve the variability between repeated measurements that might otherwise be introduced from differences in the bound ligand concentrations and internal pH between different crystals. It would also allow us to collect data at much faster timescales ( $\mu$ s – ms) which would be essential in observing immediate biochemical changes leading up to the hydride transfer step in mevalonate, CoA and NAD<sup>+</sup> bound complex. Potential use of *Pm*HMGR microcrystals that are within the 0.01 mm size range for a pH-jump experiment might be beneficial in the utilization for mix-and-diffuse setups on tape drives that can also introduce chemical triggers like high pH buffers into their crystal stream before collecting diffraction data<sup>[48]</sup>. The drastically smaller size of the crystal might enable a much faster pH-change and would therefore have to be diffracted at significantly faster time-scales to capture relevant changes associated with the reaction mechanism.

Adapting this pH-jump experiment to faster timescales would be crucial for trapping structures showing electronic changes at the active site associated with the transition states of the first hydride transfer step. Our data suggests that changes associated with mevalonate oxidation occur before we capture any pH-induced reaction intermediates and by utilizing an automated and faster data collection approach, we could study changes associated with the hydride transfer step in greater detail.

Seeing that we observe half reaction steps occur in the presence of dithio-HMG-CoA with NADH and mevaldehyde with CoA at pH 6.7, time-resolved approaches looking at enzyme-ligand

interactions at faster timescales after introducing these ligands into the crystal can also allow us to capture other transition states along the reaction pathway.

Utilizing new approaches of single value decomposition and cluster analysis, we aim to identify variations in the population of bound intermediates in *Pm*HMGR crystals in the structures we have studied post reaction initiation<sup>[116, 117]</sup>. These techniques would allow us to obtain time-independent structures from a set of pH-triggered crystallographic datasets each of which contains an ensemble of different populations of substrate, intermediate and product. They would also allow us to characterize the change in these populations over time. By determining changing populations of intermediates, we would be able to specifically determine biochemical and conformational changes associated with each reaction step.

Structural information about these transitory states can be utilized to develop new inhibitors that are particularly engineered using structure-guided drug design methods to target intermediate bound states of the enzyme. This could be done by engineering them to selectively bind post-reaction conformations of the enzyme that might exist during cofactor exchange. New inhibitors could also be engineered to bind near regions identified in time-resolved structures to have a long-range effect on the reaction mechanism such as portions of the flap domain. By selectively targeting regions that influence the reaction mechanism far away from the active site, we could also potentially develop novel inhibitors for class II HMG-CoA reductases in antibiotic resistant bacteria.



## REFERENCES

1. Steussy, C.N., et al., *A novel role for coenzyme A during hydride transfer in 3-hydroxy-3-methylglutaryl-coenzyme A reductase*. Biochemistry, 2013. **52**(31): p. 5195-205.
2. Duncan, C., *Analysis of the HMG-CoA reductase reaction mechanism by x-ray crystallography*, S. Purdue University. Biological, Editor. 2009, Thesis (Ph.D.)--Purdue University, 2009.
3. Feng, L., et al., *Specific inhibitions of annonaceous acetogenins on class II 3-hydroxy-3-methylglutaryl coenzyme A reductase from Streptococcus pneumoniae*. Bioorganic & medicinal chemistry, 2011. **19**(11): p. 3512-3519.
4. Wilding, E.I., et al., *Identification, evolution, and essentiality of the mevalonate pathway for isopentenyl diphosphate biosynthesis in gram-positive cocci*. J Bacteriol, 2000. **182**(15): p. 4319-27.
5. Jordan-Starck, T.C. and V.W. Rodwell, *Pseudomonas mevalonii 3-hydroxy-3-methylglutaryl-CoA reductase. Characterization and chemical modification*. J Biol Chem, 1989. **264**(30): p. 17913-8.
6. Gill, J.F., M.J. Beach, and V.W. Rodwell, *Mevalonate utilization in Pseudomonas sp. M. Purification and characterization of an inducible 3-hydroxy-3-methylglutaryl coenzyme A reductase*. The Journal of biological chemistry, 1985. **260**(16): p. 9393-9398.
7. Gill, J.F., M.J. Beach, and V.W. Rodwell, *Transport of mevalonate by Pseudomonas sp. strain M*. J Bacteriol, 1984. **160**(1): p. 294-8.
8. Bochar, D.A., C.V. Stauffacher, and V.W. Rodwell, *Sequence Comparisons Reveal Two Classes of 3-Hydroxy-3-methylglutaryl Coenzyme A Reductase*. Molecular Genetics and Metabolism, 1999. **66**(2): p. 122-127.
9. Wilding, E.I., et al., *Essentiality, expression, and characterization of the class II 3-hydroxy-3-methylglutaryl coenzyme A reductase of Staphylococcus aureus*. J Bacteriol, 2000. **182**(18): p. 5147-52.
10. Hedl, M., et al., *Enterococcus faecalis Acetoacetyl-Coenzyme A Thiolase/3-Hydroxy-3-Methylglutaryl-Coenzyme A Reductase, a Dual-Function Protein of Isopentenyl Diphosphate Biosynthesis*. Purdue University.
11. Schwarz, B.H., et al., *Kinetic characterization of an oxidative, cooperative HMG-CoA reductase from Burkholderia cenocepacia*. Biochimica et biophysica acta. Proteins and proteomics, 2014. **1844**(2): p. 457-464.
12. Theivagt, A.E., et al., *Characterization of an HMG-CoA Reductase from Listeria monocytogenes That Exhibits Dual Coenzyme Specificity*. Biochemistry (Easton), 2006. **45**(48): p. 14397-14406.
13. Takahashi, S., T. Kuzuyama, and H. Seto, *Purification, Characterization, and Cloning of a Eubacterial 3-Hydroxy-3-Methylglutaryl Coenzyme A Reductase, a Key Enzyme Involved in Biosynthesis of Terpenoids*. Journal of Bacteriology, 1999. **181**(4): p. 1256-1263.
14. Hamano, Y., et al., *Cloning of a gene cluster encoding enzymes responsible for the mevalonate pathway from a terpenoid-antibiotic-producing Streptomyces strain*. Bioscience, biotechnology, and biochemistry, 2001. **65**(7): p. 1627-1635.
15. Kim, D.-Y., C.V. Stauffacher, and V.W. Rodwell, *Dual coenzyme specificity of Archaeoglobus fulgidus HMG-CoA reductase*. Protein science, 2000. **9**(6): p. 1226-1234.

16. Lawrence, C.M., V.W. Rodwell, and C.V. Stauffacher, *Crystal structure of Pseudomonas mevalonii HMG-CoA reductase at 3.0 angstrom resolution*. Science, 1995. **268**(5218): p. 1758-62.
17. Lawrence, C.M., et al., *Crystallization of HMG-CoA reductase from Pseudomonas mevalonii*. Acta Crystallogr D Biol Crystallogr, 1995. **51**(Pt 3): p. 386-9.
18. Purohit, V., et al., *pH dependent inhibition from ammonium ions in the Pseudomonas mevalonii HMG-CoA Reductase crystallization environment*. bioRxiv, 2020: p. 2020.06.03.132290.
19. Tabernero, L., et al., *Substrate-induced closure of the flap domain in the ternary complex structures provides insights into the mechanism of catalysis by 3-hydroxy-3-methylglutaryl-CoA reductase*. Proc Natl Acad Sci U S A, 1999. **96**(13): p. 7167-71.
20. Qureshi, N., et al., *Kinetic analysis of the individual reductive steps catalyzed by beta-hydroxy-beta-methylglutaryl-coenzyme A reductase obtained from yeast*. Biochemistry, 1976. **15**(19): p. 4191-07.
21. Rétey, J., et al., *A probable intermediate in the enzymic reduction of 3-hydroxy-3-methylglutaryl coenzyme A*. Eur J Biochem, 1970. **15**(1): p. 72-6.
22. Bochar, D.A., et al., *Aminoethylcysteine can replace the function of the essential active site lysine of Pseudomonas mevalonii 3-hydroxy-3-methylglutaryl coenzyme A reductase*. Biochemistry, 1999. **38**(28): p. 8879-83.
23. Wang, Y., B.G. Darnay, and V.W. Rodwell, *Identification of the principal catalytically important acidic residue of 3-hydroxy-3-methylglutaryl coenzyme A reductase*. J Biol Chem, 1990. **265**(35): p. 21634-21641.
24. Haines, B.E., et al., *Molecular modeling of the reaction pathway and hydride transfer reactions of HMG-CoA reductase*. Biochemistry, 2012. **51**(40): p. 7983-95.
25. Darnay, B.G., Y. Wang, and V.W. Rodwell, *Identification of the catalytically important histidine of 3-hydroxy-3-methylglutaryl-coenzyme A reductase*. J Biol Chem, 1992. **267**(21): p. 15064-15070.
26. Frimpong, K. and V.W. Rodwell, *Catalysis by Syrian hamster 3-hydroxy-3-methylglutaryl-coenzyme A reductase. Proposed roles of histidine 865, glutamate 558, and aspartate 766*. J Biol Chem, 1994. **269**(15): p. 11478-11483.
27. Darnay, B.G. and V.W. Rodwell, *His865 is the catalytically important histidyl residue of Syrian hamster 3-hydroxy-3-methylglutaryl-coenzyme A reductase*. J Biol Chem, 1993. **268**(12): p. 8429-8435.
28. Quinn, T.R., et al., *Microsecond timescale MD simulations at the transition state of PmHMGR predict remote allosteric residues*. Chemical science (Cambridge), 2021. **12**(18): p. 6413-6418.
29. Alber, T., G.A. Petsko, and D. Tsernoglou, *Crystal structure of elastase-substrate complex at -- 55 degrees C*. Nature (London), 1976. **263**(5575): p. 297-300.
30. Hajdu, J., et al., *Catalysis in the crystal: synchrotron radiation studies with glycogen phosphorylase b*. The EMBO journal, 1987. **6**(2): p. 539-546.
31. Rapp, G., et al., *Time-resolved X-ray crystallographic study of the conformational change in Ha-Ras p21 protein on GTP hydrolysis*. Nature (London), 1990. **345**(6273): p. 309-315.
32. Stoddard, B.L., et al., *Millisecond Laue structures of an enzyme-product complex using photocaged substrate analogs*. Nat Struct Biol, 1998. **5**(10): p. 891-7.

33. Genick, U.K., et al., *Structure of a Protein Photocycle Intermediate by Millisecond Time-Resolved Crystallography*. Science (American Association for the Advancement of Science), 1997. **275**(5305): p. 1471-1475.
34. WÖhrli, A.B., et al., *Light-Induced Structural Changes in a Photosynthetic Reaction Center Caught by Laue Diffraction*. Science (American Association for the Advancement of Science), 2010. **328**(5978): p. 630-633.
35. Srajer, V., et al., *Photolysis of the Carbon Monoxide Complex of Myoglobin: Nanosecond Time-Resolved Crystallography*. Science (American Association for the Advancement of Science), 1996. **274**(5293): p. 1726-1729.
36. Knapp, J.E., et al., *Allosteric Action in Real Time: Time-Resolved Crystallographic Studies of a Cooperative Dimeric Hemoglobin*. Proceedings of the National Academy of Sciences - PNAS, 2006. **103**(20): p. 7649-7654.
37. Moffat, K., [22] *Laue diffraction*. Methods in Enzymology, 1997. **277**: p. 433-447.
38. van Thor, J.J., *Advances and opportunities in ultrafast X-ray crystallography and ultrafast structural optical crystallography of nuclear and electronic protein dynamics*. Structural dynamics (Melville, N.Y.), 2019. **6**(5): p. 50901-050901.
39. Arthur, J., et al., *First lasing and operation of an ångström-wavelength free-electron laser*. Nature photonics, 2010. **4**(9): p. 641-647.
40. Weierstall, U., et al., *Lipidic cubic phase injector facilitates membrane protein serial femtosecond crystallography*. Nature communications, 2014. **5**(1): p. 3309-3309.
41. Monteiro, D.C.F., et al., *3D-MiXD: 3D-printed X-ray-compatible microfluidic devices for rapid, low-consumption serial synchrotron crystallography data collection in flow*. IUCrJ, 2020. **7**(2): p. 207-219.
42. Sherrell, D.A., et al., *A modular and compact portable mini-endstation for high-precision, high-speed fixed target serial crystallography at FEL and synchrotron sources*. Journal of synchrotron radiation, 2015. **22**(6): p. 1372-1378.
43. *A modular and compact portable mini-endstation for high-precision, high-speed fixed target serial crystallography at FEL and synchrotron sources*. 2015, Washington, D.C: United States. Dept. of Energy. Office of Science.
44. Fuller, F.D., et al., *Drop-on-demand sample delivery for studying biocatalysts in action at X-ray free-electron lasers*. Nature methods, 2017. **14**(4): p. 443-449.
45. Ishigami, I., et al., *Crystal structure of CO-bound cytochrome c oxidase determined by serial femtosecond X-ray crystallography at room temperature*. Proceedings of the National Academy of Sciences - PNAS, 2017. **114**(30): p. 8011-8016.
46. Mehrabi, P., et al., *The HARE chip for efficient time-resolved serial synchrotron crystallography*. J Synchrotron Radiat, 2020. **27**(Pt 2): p. 360-370.
47. Schulz, E.C., et al., *The hit-and-return system enables efficient time-resolved serial synchrotron crystallography*. Nature methods, 2018. **15**(11): p. 901-904.
48. Beyerlein, K.R., et al., *Mix-and-diffuse serial synchrotron crystallography*. IUCrJ, 2017. **4**(Pt 6): p. 769-777.
49. Salerno, C.P., et al., *Synthesis of Caged NAD(P)<sup>+</sup> Coenzymes: Photorelease of NADP*. Journal of the American Chemical Society, 1997. **119**(14): p. 3403-3404.
50. Istvan, E.S. and J. Deisenhofer, *The structure of the catalytic portion of human HMG-CoA reductase*. Biochim Biophys Acta, 2000. **1529**(1-3): p. 9-18.

51. Bourbon, P., et al., *Synthesis, Photophysical, Photochemical, and Computational Studies of Coumarin-Labeled Nicotinamide Derivatives*. Journal of organic chemistry, 2012. **77**(6): p. 2756-2762.
52. Salahi, F., et al., *pHP-Tethered N-Acyl Carbamate: A Photocage for Nicotinamide*. Org Lett, 2018. **20**(9): p. 2547-2550.
53. Cohen, B.E., B.L. Stoddard, and D.E. Koshland, *Caged NADP and NAD. Synthesis and Characterization of Functionally Distinct Caged Compounds*. Biochemistry (Easton), 1997. **36**(29): p. 9035-9044.
54. Pacaud, K., et al., *Determination of the transglycosidation activity of NAD + glycohydrolases with 4-(2'-alkyl-sulfanyl-vinyl)-pyridine derivatives generating chromophoric NAD + analogs*. Bioorganic chemistry, 2003. **31**(4): p. 288-305.
55. Salahi, F. and O. Wiest, *Regioselective Alkylation of Pyridinium Riboses*. European journal of organic chemistry, 2020. **2020**(4): p. 446-449.
56. Salahi, F., *Attempts towards Total Synthesis of Photocaged Nicotinamide Adenine Dinucleotide (NAD+) and Its Analogues*. 2019, ProQuest Dissertations Publishing.
57. Singer, P.T., et al., *The hydrolytic water molecule in trypsin, revealed by time-resolved Laue crystallography*. Science, 1993. **259**(5095): p. 669-73.
58. Donten, M.L., et al., *pH-Jump Induced Leucine Zipper Folding beyond the Diffusion Limit*. The journal of physical chemistry. B, 2015. **119**(4): p. 1425-1432.
59. Rimmerman, D., et al., *Revealing Fast Structural Dynamics in pH-Responsive Peptides with Time-Resolved X-ray Scattering*. The journal of physical chemistry. B, 2019. **123**(9): p. 2016-2021.
60. Rimmerman, D., et al., *Probing Cytochrome c Folding Transitions upon Phototriggered Environmental Perturbations Using Time-Resolved X-ray Scattering*. The journal of physical chemistry. B, 2018. **122**(20): p. 5218-5224.
61. Abbruzzetti, S., et al., *Fast Events in Protein Folding: Structural Volume Changes Accompanying the Early Events in the N→I Transition of Apomyoglobin Induced by Ultrafast pH Jump*. Biophysical journal, 2000. **78**(1): p. 405-415.
62. Hekstra, D.R., et al., *Electric-field-stimulated protein mechanics*. Nature (London), 2016. **540**(7633): p. 400-405.
63. Thompson, M.C., et al., *Temperature-jump solution X-ray scattering reveals distinct motions in a dynamic enzyme*. Nature chemistry, 2019. **11**(11): p. 1058-1066.
64. Keedy, D.A., et al., *Mapping the conformational landscape of a dynamic enzyme by multitemperature and XFEL crystallography*. eLife, 2015. **4**.
65. Henry, L., et al., *Real-time tracking of protein unfolding with time-resolved x-ray solution scattering*. Structural dynamics (Melville, N.Y.), 2020. **7**(5).
66. Li, S., et al., *Thermal-triggered proteinquake leads to disassembly of DegP hexamer as an imperative activation step*. Scientific reports, 2014. **4**(1): p. 4834-4834.
67. Wirth, A.J., et al., *Comparing Fast Pressure Jump and Temperature Jump Protein Folding Experiments and Simulations*. Journal of the American Chemical Society, 1900. **137**(22): p. 7152-7159.
68. Wright, P.A., et al., *'pH-jump' crystallographic analyses of gamma-lactam-porcine pancreatic elastase complexes*. Biochemical journal, 2000. **351 Pt 2**(2): p. 335-340.
69. Jeong, B.-S. and R.B. Dyer, *Proton Transport Mechanism of M2 Proton Channel Studied by Laser-Induced pH Jump*. Journal of the American Chemical Society, 2017. **139**(19): p. 6621-6628.

70. Warren, J.C. and S.G. Cheatum, *Effect of Neutral Salts on Enzyme Activity and Structure*. Biochemistry (Easton), 1966. **5**(5): p. 1702-1707.
71. Doscher S., M.a.R.M.F., *Journal of Biological Chemistry*, in 238 : 2399. 1963.
72. Winstead, J.A. and F. Wold, *The effect of high concentrations of salt on kinetic properties of pancreatic ribonuclease*. J Biol Chem, 1965. **240**(9): p. 3694-6.
73. Fedorov, A.A., et al., *Ionic interactions in crystalline bovine pancreatic ribonuclease A*. Biochemistry, 1996. **35**(50): p. 15962.
74. Chatzileontiadou, D.S.M., et al., *The ammonium sulfate inhibition of human angiogenin*. FEBS Letters, 2016. **590**(17): p. 3005-3018.
75. Park, C. and R.T. Raines, *Quantitative analysis of the effect of salt concentration on enzymatic catalysis*. J Am Chem Soc, 2001. **123**(46): p. 11472-9.
76. Otwinowski, Z. and W. Minor, *Processing of X-ray diffraction data collected in oscillation mode*. Methods Enzymol, 1997. **276**: p. 307-26.
77. Winn, M.D., et al., *Overview of the CCP4 suite and current developments*. Acta Crystallogr D Biol Crystallogr, 2011. **67**(Pt 4): p. 235-42.
78. Murshudov, G.N., A.A. Vagin, and E.J. Dodson, *Refinement of macromolecular structures by the maximum-likelihood method*. Acta Crystallogr D Biol Crystallogr, 1997. **53**(Pt 3): p. 240-55.
79. McCoy, A.J., et al., *Phaser crystallographic software*. Journal of Applied Crystallography, 2007. **40**(4): p. 658-674.
80. Brünger, A.T., et al., *Crystallography & NMR system: A new software suite for macromolecular structure determination*. Acta Crystallogr D Biol Crystallogr, 1998. **54**(Pt 5): p. 905-21.
81. Liebschner, D., et al., *Macromolecular structure determination using X-rays, neutrons and electrons: recent developments in Phenix*. Acta Crystallogr D Struct Biol, 2019. **75**(Pt 10): p. 861-877.
82. Kleywegt, G.J., et al., *Pound-wise but penny-foolish: How well do micromolecules fare in macromolecular refinement?* Structure, 2003. **11**(9): p. 1051-9.
83. Terwilliger, T.C., et al., *Ligand identification using electron-density map correlations*. Acta crystallographica. Section D, Biological crystallography., 2007. **63**(1): p. 101-107.
84. Terwilliger, T.C., et al., *Automated ligand fitting by core-fragment fitting and extension into density*. Acta Crystallogr D Biol Crystallogr, 2006. **62**(Pt 8): p. 915-22.
85. Afonine, P.V., et al., *Towards automated crystallographic structure refinement with phenix.refine*. Acta crystallographica. Section D, Biological crystallography., 2012. **68**(4): p. 352-367.
86. Williams, C.J., et al., *MolProbity: More and better reference data for improved all-atom structure validation*. Protein Sci, 2018. **27**(1): p. 293-315.
87. Urzhumtseva, L., et al., *Crystallographic model quality at a glance*. Acta Crystallogr D Biol Crystallogr, 2009. **65**(Pt 3): p. 297-300.
88. Hodel, A., S.H. Kim, and A.T. Brünger, *Model bias in macromolecular crystal structures*. Acta crystallographica. Section A, Foundations of crystallography, 1992. **48**(6): p. 851-858.
89. Terwilliger, T.C., et al., *Decision-making in structure solution using Bayesian estimates of map quality: the PHENIX AutoSol wizard*. Acta crystallographica. Section D, Biological crystallography., 2009. **65**(6): p. 582-601.

90. Bensch, W.R. and V.W. Rodwell, *Purification and properties of 3-hydroxy-3-methylglutaryl coenzyme A reductase from Pseudomonas*. J Biol Chem, 1970. **245**(15): p. 3755-62.
91. Rostkowski, M., et al., *Graphical analysis of pH-dependent properties of proteins predicted using PROPKA*. BMC Struct Biol, 2011. **11**: p. 6.
92. Søndergaard, C.R., et al., *Improved Treatment of Ligands and Coupling Effects in Empirical Calculation and Rationalization of pKa Values*. J Chem Theory Comput, 2011. **7**(7): p. 2284-2295.
93. Korolev, S., et al., *Using surface-bound rubidium ions for protein phasing*. Acta Crystallogr D Biol Crystallogr, 2001. **57**(7): p. 1008-1012.
94. Quinn, T., *Microsecond simulations of the PmHMGR second hydride transfer transition state and investigations into molecule and enzyme dynamics*, in *Chemistry and Biochemistry*. 2020, University of Notre Dame.
95. Rodwell, V.W., et al., *3-Hydroxy-3-methylglutaryl-CoA reductase*. Methods in Enzymology, 2000. **324**: p. 259-280.
96. Spilburg, C.A., J.L. Bethune, and B.L. Vallee, *Kinetic properties of crystalline enzymes. Carboxypeptidase A*. Biochemistry, 1977. **16**(6): p. 1142-1150.
97. Wheeler, M.J., et al., *Measurement of the equilibrium relative humidity for common precipitant concentrations: facilitating controlled dehydration experiments*. Acta crystallographica. Section F, Structural biology and crystallization communications, 2012. **68**(1): p. 111-114.
98. Ziegenhorn, J., M. Senn, and T. Bücher, *Molar absorptivities of beta-NADH and beta-NADPH*. Clinical Chemistry, 1976. **22**(2): p. 151-160.
99. Moriarty, N.W., R.W. Grosse-Kunstleve, and P.D. Adams, *electronic Ligand Builder and Optimization Workbench (eLBOW): a tool for ligand coordinate and restraint generation*. Acta Crystallogr D Biol Crystallogr, 2009. **65**(Pt 10): p. 1074-80.
100. Karplus, P.A. and K. Diederichs, *Assessing and maximizing data quality in macromolecular crystallography*. Curr Opin Struct Biol, 2015. **34**: p. 60-8.
101. Liebschner, D., et al., *Polder maps: improving OMIT maps by excluding bulk solvent*. Acta Crystallogr D Struct Biol, 2017. **73**(Pt 2): p. 148-157.
102. Urzhumtsev, A., et al., *Metrics for comparison of crystallographic maps*. Acta Crystallogr D Biol Crystallogr, 2014. **70**(10): p. 2593-2606.
103. Lunin, V.Y., *Use of the information on electron density distribution in macromolecules*. Acta crystallographica. Section A, Foundations of crystallography, 1988. **44**(2): p. 144-150.
104. Lunin, V.Y., *Electron-density histograms and the phase problem*. Acta crystallographica. Section A, Foundations of crystallography, 1993. **49**(s1): p. c28-c29.
105. Main, P., *A formula for electron density histograms for equal-atom structures*. Acta crystallographica. Section A, Foundations of crystallography, 1990. **46**(6): p. 507-509.
106. Main, P., *The use of Sayre's equation with constraints for the direct determination of phases*. Acta crystallographica. Section A, Foundations of crystallography, 1990. **46**(5): p. 372-377.
107. Terwilliger, T.C., et al., *Iterative-build OMIT maps: map improvement by iterative model building and refinement without model bias*. Acta Crystallogr D Biol Crystallogr, 2008. **64**(5): p. 515-524.

108. Chen, C.R. and G.I. Makhatadze, *ProteinVolume: calculating molecular van der Waals and void volumes in proteins*. BMC bioinformatics, 2015. **16**(1): p. 101-101.
109. Taylor, Q., et al., *Microsecond Timescale Simulations at the Transition State of PmHMGR Predict Remote Allosteric Residues*. 2019.
110. Meijers, R., et al., *On the Enzymatic Activation of NADH*. The Journal of biological chemistry, 2001. **276**(12): p. 9316-9321.
111. Geremia, S., et al., *Simulation of Diffusion Time of Small Molecules in Protein Crystals*. Structure (London), 2006. **14**(3): p. 393-400.
112. O'Hara, P., P. Goodwin, and B.L. Stoddard, *Direct measurement of diffusion rates in enzyme crystals by video absorbance spectroscopy*. Journal of applied crystallography, 1995. **28**(6): p. 829-834.
113. Holzberger, B., et al., *Structural insights into the potential of 4-fluoroproline to modulate biophysical properties of proteins*. Chemical Science, 2012. **3**(10): p. 2924-2931.
114. Mueller, C., et al., *Fixed target matrix for femtosecond time-resolved and in situ serial micro-crystallography*. Structural dynamics (Melville, N.Y.), 2015. **2**(5): p. 054302-054302.
115. Mehrabi, P., et al., *Liquid application method for time-resolved analyses by serial synchrotron crystallography*. Nat Methods, 2019. **16**(10): p. 979-982.
116. Schmidt, M., et al., *Application of Singular Value Decomposition to the Analysis of Time-Resolved Macromolecular X-Ray Data*. Biophysical journal, 2003. **84**(3): p. 2112-2129.
117. Kostov, K.S. and K. Moffat, *Cluster Analysis of Time-Dependent Crystallographic Data: Direct Identification of Time-Independent Structural Intermediates*. Biophysical journal, 2011. **100**(2): p. 440-449.

## APPENDIX

The data processing statistics for all the structures documented in Chapters 3 and 5 shown below.

Table I – Data processing statistics for structures acquired in the crystallization and pH-jump buffer environment at pH 6.7 and 20 seconds after a pH change at pH 9

	PRE pH-jump (Crystallization buffer, pH 6.7)	PRE pH-jump (pH-jump buffer, pH 6.7)	20 seconds at pH 9
Wavelength	1.033	1.033	1.033
Resolution range	46.14 - 1.994 Å	46.07 - 1.932 Å	44.26 - 2.103 Å
Space group	I 4(1)3 2	I 4(1)3 2	I 4(1)3 2
a, b, c (Å)	226.043	225.674	225.67
$\alpha = \beta = \gamma$ (deg)	90	90	90
Unique reflections	66670 (312)	72760	55516
Multiplicity	16.4 (13.4)	19.9 (19.2)	7.3 (2.5)
Completeness (%)	83.37 (4.75)	85.80 (4.53)	97.88 (87.30)
Mean I/sigma(I)	15.43 (0.64)	14.75 (0.89)	12.32 (0.71)
Wilson B-factor	26.27	20.16	48.55
R-merge	2.1 (27.4)	3.17 (35.23)	1.2 (9.8)
CC1/2	0.997 (0.322)	0.995 (0.312)	0.992 (0.387)
CC*	0.999 (0.698)	0.999 (0.69)	0.998 (0.747)
R-work (%)	18.22	17.82	18.71
R-free (%)	22.54	21.95	22.23
Protein residues	800	799	802
RMS(bonds)	0.008	0.01	0.01
RMS(angles)	1.07	1.46	1.36
Ramachandran favored (%)	96.48	96.23	95.86
Ramachandran allowed (%)	3.52	3.77	4.14
Ramachandran outliers (%)	0	0	0
Rotamer outliers (%)	0	0	0
Clashscore	4.06	4.81	5.4
Average B-factor	32.19	26.26	59.42
macromolecules	31.81	25.73	59.5
ligands	34.37	34.26	63.73
solvent	36.48	31.17	50.21



Table II – Data processing statistics for structures acquired in the pH-jump buffer environment from 30 seconds – 50 seconds after a pH change at pH 9

	30 seconds at pH 9	40 seconds at pH 9	50 seconds at pH 9
Wavelength	1.033	1.033	1.033
Resolution range	48.3 - 1.973 Å	48.2 - 2.082 Å	44.22 - 2.122 Å
Space group	I4(1)3 2	I4(1)3 2	I4(1)3 2
a, b, c (Å)	226.546	226.068	225.481
$\alpha = \beta = \gamma$ (deg)	90	90	90
Unique reflections	69214	58668	55033
Multiplicity	38.1 (34.2)	25.8 (25.5)	35.6 (15.3)
Completeness (%)	83.75 (3.89)	85.22 (5.62)	91.67 (24.83)
Mean I/sigma(I)	17.91 (0.69)	14.61 (1.01)	17.51 (0.92)
Wilson B-factor	26.94	26.47	26.14
R-merge	3.9 (64.36)	4.01 (43.81)	3.17 (30.54)
CC1/2	0.998 (0.319)	0.996 (0.377)	0.995 (0.294)
CC*	0.999 (0.696)	0.999 (0.74)	0.999 (0.674)
R-work (%)	20.45	19.38	20.64
R-free (%)	24.73	23.7	24.92
Protein residues	798	800	801
RMS(bonds)	0.009	0.008	0.008
RMS(angles)	1.24	1	0.97
Ramachandran favored (%)	95.97	96.73	95.73
Ramachandran allowed (%)	4.03	3.27	4.27
Ramachandran outliers (%)	0	0	0
Rotamer outliers (%)	0	1.3	1.13
Clashscore	5.01	5.74	5.62
Average B-factor	37.37	39.45	39.33
macromolecules	37.33	39.47	39.38
ligands	37.09	41.1	39.94
solvent	38.29	37.6	37.42

Table III – Data processing statistics for structures acquired in the pH-jump buffer environment from 60 seconds – 4 minutes after a pH change at pH 9

	1 minute at pH 9	2 minutes 20 seconds at pH 9	4 minutes at pH 9
Wavelength	1.033	1.033	1.033
Resolution range	44.28 - 2.062 Å	43.96 - 2.502 Å	46.03 - 2.25 Å
Space group	I4(1)3 2	I4(1)3 2	I4(1)3 2
a, b, c (Å)	225.766	224.162	225.477
$\alpha = \beta = \gamma$ (deg)	90	90	90
Unique reflections	60096	33265	46277
Multiplicity	30.9 (24.0)	9.4 (8.5)	9.6 (9.6)
Completeness (%)	89.86 (21.21)	98.05 (82.78)	98.72 (89.15)
Mean I/sigma(I)	15.77 (0.61)	16.45 (2.26)	16.41 (2.03)
Wilson B-factor	26.57	34.21	29.85
R-merge	3.22 (43.44)	1.37 (10.05)	1.34 (11.75)
CC1/2	0.997 (0.218)	0.997 (0.717)	0.998 (0.693)
CC*	0.999 (0.599)	0.999 (0.914)	0.999 (0.905)
R-work (%)	21.88	17.54	18.92
R-free (%)	24.94	23	22.93
Protein residues	802	795	800
RMS(bonds)	0.002	0.006	0.004
RMS(angles)	0.51	0.9	1.018
Ramachandran favored (%)	95.99	96.46	96.1
Ramachandran allowed (%)	4.01	3.54	3.9
Ramachandran outliers (%)	0	0	0
Rotamer outliers (%)	0.49	0	0
Clashscore	3.83	5.63	5.93
Average B-factor	42.36	41.6	40.66
macromolecules	42.36	41.69	40.55
ligands	47.25	42.29	40.55
solvent	40.37	38.2	42.72

Table IV – Data processing statistics for structures acquired in the pH-jump buffer environment from 5 – 10 minutes after a pH change at pH 9

	5 minutes at pH 9	8 minutes at pH 9	10 minutes at pH 9
Wavelength	1.033	1.033	1.033
Resolution range	44.32 - 2.07 Å	47.99 - 2.2 Å	45.97 - 2.4 Å
Space group	I4(1)3 2	I4(1)3 2	I4(1)3 2
a, b, c (Å)	225.988	225.078	225.203
$\alpha = \beta = \gamma$ (deg)	90	90	90
Unique reflections	59611	49214	38129
Multiplicity	9.5 (8.9)	9.5 (9.7)	9.6 (9.2)
Completeness (%)	99.04 (93.76)	99.32 (94.41)	98.86 (90.39)
Mean I/sigma(I)	20.44 (2.73)	17.36 (2.19)	12.25 (2.37)
Wilson B-factor	23.47	29.55	35.02
R-merge	1.05 (7.51)	1.2 (10.15)	1.5 (8.41)
CC1/2	0.998 (0.785)	0.998 (0.744)	0.996 (0.741)
CC*	1 (0.938)	1 (0.924)	0.999 (0.923)
R-work (%)	19.94	18.5	18.95
R-free (%)	24.28	20.94	21.9
Protein residues	797	797	779
RMS(bonds)	0.006	0.004	0.006
RMS(angles)	0.922	0.88	0.82
Ramachandran favored (%)	95.83	96.09	96.64
Ramachandran allowed (%)	4.17	3.91	3.36
Ramachandran outliers (%)	0	0	0
Rotamer outliers (%)	0	0	0
Clashscore	4.47	5.57	7.48
Average B-factor	34.59	38.09	44.55
macromolecules	34.06	37.66	43.81
ligands	36.2	62.58	94.12
solvent	40.87	38.3	41.58

Table IV – Data processing statistics for *Pm*HMGR flap domain (E399A and L407S) mutants soaked with mevalonate, CoA and NAD<sup>+</sup> and pH 6.7

	E399A	E399A-2	L407S
Wavelength	0.9794	0.9794	0.9794
Resolution range	46.14 - 2.2 Å	36.71 - 1.52 Å	35.76 - 1.79 Å
Space group	I4(1)3 2	I4(1)3 2	I4(1)3 2
a, b, c (Å)	226.039	226.278	226.193
$\alpha = \beta = \gamma$ (deg)	90	90	90
Unique reflections	49050	149206	91836
Multiplicity	25.6 (26.1)	22.3 (22.7)	22.2 (22.6)
Completeness (%)	98.41 (95.45)	99.45 (94.81)	99.81 (98.56)
Mean I/sigma(I)	58 (24.67)	17.69 (2.17)	18.03 (2.26)
Wilson B-factor	29.59	13.72	20.01
R-merge	6.8 (21.2)	1.641 (16.68)	1.63 (14.8)
CC1/2	0.999 (0.993)	0.999 (0.733)	0.999 (0.754)
CC*	49045 (4680)	148406 (13982)	91682 (8960)
R-work (%)	2439 (236)	7459 (712)	4720 (476)
R-free (%)	18.34 (32.13)	17.98	16.69
Protein residues	20.98 (38.28)	19.48	19.41
RMS(bonds)	0.003	0.007	0.007
RMS(angles)	0.72	0.93	0.9
Ramachandran favored (%)	96.34	97.2	97.05
Ramachandran allowed (%)	3.66	2.67	2.95
Ramachandran outliers (%)	0	0.13	0
Rotamer outliers (%)	0.65	0.17	0.51
Clashscore	3.83	3.65	3.32
Average B-factor	36.49	18.88	23.61
macromolecules	35.96	16.88	22.21
ligands	49.99	25.56	23.86
solvent	39.73	30.98	34.78

Table V – Data processing statistics *Pm*HMGR crystals soaked in Rb<sub>2</sub>SO<sub>4</sub>, ADA and PEG-400 buffer to determine a potential NH<sub>4</sub><sup>+</sup> binding site using anomalous diffraction

	Rb <sub>2</sub> SO <sub>4</sub> soaked crystal
Wavelength	1.52E+04
Resolution range	48.37 - 2.23 Å
Space group	I4(1)3 2
a, b, c (Å)	226.863
$\alpha = \beta = \gamma$ (deg)	90
Unique reflections	48399
Multiplicity	19.3 (18.4)
Completeness (%)	98.07 (82.05)
Mean I/sigma(I)	18.80 (2.13)
Wilson B-factor	28.85
R-merge	2.06 (16.8)
CC1/2	0.999 (0.941)
CC*	47476 (3921)
R-work (%)	2374 (189)
R-free (%)	17.63
Protein residues	22.18
RMS(bonds)	0.008
RMS(angles)	1.04
Ramachandran favored (%)	97.19
Ramachandran allowed (%)	2.81
Ramachandran outliers (%)	0
Rotamer outliers (%)	0
Clashscore	3.38
Average B-factor	34.72
macromolecules	34.22
ligands	65.73
solvent	40.44